THE UNIVERSITY *of* EDINBURGH

The Discovery of Novel Prognostic Tools to Stratify High Risk Stage II Colorectal Cancer Patients utilising Digital Pathology

Peter David Caie

Thesis Presented for the degree of Doctor of Philosophy

The University of Edinburgh

2015

Declaration

I hereby state that this thesis was composed by me. All experimental and analysis work was carried out by me and any aid in sample preparation or analysis has been acknowledged where appropriate. This work has not been submitted for any other degree or professional qualification.

Thesis Presented for the degree of Doctor of Philosophy

The University of Edinburgh

2015

Contents

Table of Figures & Tables

List of Figures **Page**

List of Tables. **Pages**

Acknowledgements

I would like to wholeheartedly thank my supervisor David Harrison for his support and for facilitating this entire study as well as my future career. His thought provoking discussions, assistance, encouragement, humour and never ending patience are all very much appreciated.

My thanks also go to Dr Anca Oniscu for her support and encouragement over the last three years and for her helpful discussions on many aspects of clinical pathology.

I would also like to thank Mr Grant Stewart and Dr Simon Langdon for their insightful discussions on clinical research.

It has been a pleasure working alongside the members of the Division of Pathology laboratory, many of whom helped me over my time at Edinburgh. Thank you also to Frances Rae for her help in the tissue governance and ethics approval for the study. John O'Connor and Shirley Johnstone were a constant help with tissue preparation and a source of great patter. I am also grateful to Ying Zhou for her assistance in assembling the validation cohort and creation of the training cohort TMA. In hwa Um's help was invaluable over the years, especially with fluorescence imaging and the creation of the tumour bud TMA. Arran Turnbull's assistance with the statistical analysis was constructive for which I thank him. Thank you also to Ghassan and Chrysi for making the office a fun environment in which to work and for their friendship alongside Fiach, Carlos, Kyle, James, Romina, Jenny and Alex.

I would also like to thank my family for their encouragement, patience and support over the last three years. My mother and father were always ready to help, feed, water and calm me before banishing me to my word processor, when the need arose. Thank you also to my sister and John for their support and reassurance.

Finally, I would like to thank my wife, Mira. She has sacrificed much in order for me to complete this journey. She has always stood by me, inspired me, comforted me and brought me endless love and joy for which I will be eternally grateful. During the final year of my PhD she brought even more joy and love to our family in the form of our son, Roshan. Roshan, as his name suggests, fills our life with light.

I dedicate this thesis to my son, Roshan.

Abbreviations

4P medicine	Predictive, Preventive, Personalised and Participatory
aCGH	Array comparative genomic hybridisation
ALTB	Sum Area Large Tumour Bud
au	Arbitrary units
BRAF	B-Rapidly Accelerated Fibrosarcoma protein
CAP	College of American Pathologists
CART	Classification and regression tree
CASyM	Coordinating Action Systems Medicine
CAVE	Cyclophosphamide, Adriamycin, Vincristine, Etoposide
CI	Confidence interval
CIMP	CpG-island methylator phenotype
CIN	Chromosomal instability
CK	Cytokeratin
CRC	Colorectal cancer
CSC	Cancer stem cell
DAB	3, 3 -diaminobenzidine
DNA	Deoxyribonucleic acid
ECM	Epithelial to mesenchymal transition
ECM	Extra cellular matrix
EGFR	Epidermal growth factor receptor
EVG	Elastic Verhoeff-Van Geison stain
FAP	Familial Adenomatous Polyposis
FDA	Food and Drug Administration
FDR	False discovery rate
FISH	Fluorescence in situ hybridisation
FOLFIRI	Folinic acid, Fluorouracil, Irinotecan
FOLFOX	Folinic acid, Fluorouracil, Oxaliplatin
H&E	Haematoxylin & Eosin
HER2	Human epidermal growth factor receptor 2
HNPCC	Hereditary Non-Polyposis Colorectal Cancer
HR	Hazard ratio
HRP	Horse radish peroxidase
IF	Immunofluorescence
IHC	Immunohistochemistry
IPS	Integrative pathology signature
KM	Kaplan-Meier
KRAS	Kirsten rat sarcoma protein
LCM	Laser capture microarray

LTB	Large tumour buds
LVA	Lymphatic vasculature analyser
LVD	Lymphatic vessel density
LVI	Lymphatic vessel invasion
MMPs	Matrix metalloproteinases
MMR	Mismatch repair
MSI	Microsatellite instability
MSS	Microsatellite stability
NGS	Next generation sequencing
NRAS	N-rat sarcoma protein
panCK	Pan Cytokeratin antibody
PBST	Phosphate buffer saline with Tween
PCA	Principal component analysis
PCR	Polymerase chain reaction
PIK3CA	Phosphoinositide-3-Kinase, Catalytic, Alpha Polypeptide
RCPath	Royal College of Pathologists
RNA	Ribonucleic acid
ROC	Receiver operator curve
ROI	Region of interest
ROI	Region of interest
RPPA	Reverse phase protein arrays
TB	Tumour budding
TBA	Tumour Bud Analyser
TMA	Tissue Microarray
TNM	Tumour, Node and Metastasis
TPA	Tissue Phenomics Analyser
VEGF	Vascular endothelial growth factor
WSI	Whole slide imaging

Glossary of terms

Adenoma

A benign tumour originating from epithelial glandular structures.

Adenocarcinoma

A cancer that originates in the cells that form glands (to lubricate) in tissue such as the colon or gut.

Angiogenesis

The development of new blood vessels.

Area large tumour bud (ALTB)

The sum area of all objects across the digital tissue section which are classified as a ‘Large tumour bud’. The area is calculated in pixels.

Carcinoma

A malignant cancer which originates from epithelial cells.

Classification and regression tree (CART)

A decision tree model for classification and regression analysis which is commonly used in data mining. It can be used to identify the optimal combination of parameters, and their associated cut-offs at each ‘branch point’, within a decision tree which best answer a binary question. Its goal is to predict the answer to a question based on multiple input variables.

Differentiation/Grade

Differentiation is the grade of the cancer and it is based on how abnormal the cells look under the microscope. It reflects the ability of the cancer cells to form glandular structures or not. It is categorised in the pathology report as low, medium and high grade.

Digital pathology

The digitising of a pathological specimen mounted on a microscope slide and viewed on a computer screen instead of under a traditional microscope.

Dukes staging

A method of staging cancers which is considered old fashioned compared the TNM staging. Dukes staging, as TNM staging, is based on the extent of the local or distant tumour spread. See Appendix B.

EMLVI

Extramural lymphovascular invasion is when the cancer has invaded either blood or lymphatic vessels located beyond the muscularis propria (see diagram in Appendix B).

Epithelium

The thin tissue forming the outer layer of a body's surface and lining the alimentary canal.

Extra cellular matrix

Molecules in the tissue which are secreted by cells and form a scaffold and support network between the cells.

False discovery rate

The rate of type I errors which occur when cutting your continuous data multiple times in order to identify a statistically relevant cut-off where each cut-point represents an opportunity to find significance by chance. This can be corrected for through multiple statistical methods such as the Miller-Siegmund and Benjamini-Hochberg calculations.

Integrative pathology signature (IPS)

The integrated features of pT stage, differentiation and ALTB into a novel prognostic signature which improved upon current clinical practice.

Invasive margin pattern

The histological pattern that the colorectal cancer forms at the invasive front. It is either a pushing border where the cancer advances as a solid margin or an infiltrative border where the cancer invades in finger-like protrusions. The pattern is correlated to prognosis.

Lymphatic vessel density

Lymphatic vessel density is the area of the stroma which is taken up by lymphatic vessels.

Lymphatic vessel invasion

Lymphatic vessel invasion is when the cancer has invaded into the lymphatic vessels.

Lymphangiogenesis

Formation of new lymphatic vessels.

Lymph node involvement (pN0, 1, 2)

Depends on if the cancer has metastasised to the lymph nodes and reflects the number of nodes affected: pN0 = no lymph nodes affected, pN1 = 1-3 lymph nodes affected and pN2 = 4 or more lymph nodes affected.

Metastasis

The spread of cancer from one organ of origin to another distant one.

Occult LVI

1-5 cancer cells which have invaded a lymphatic vessel and would therefore be obscure under traditional H&E observation.

Poorly differentiated clusters

Clusters of cancer cells disseminated from the neoplastic glands at the invasive front of CRC and contain more than 5 cells but are non-gland forming.

Principal component analysis (PCA)

Allows dimensional reduction of a multi-parametric data set and thereby its visualisation in graph form. It transforms the data within the multi-parametric set into a new coordinate system such that the greatest variance by some projection of the data comes to lie on the first coordinate or 'component'. The 1st component will describe the most variation in the data, the 2nd the next etc.

Random forest

Random forests are an ensemble learning method for classification and regression that operate by constructing a multitude of decision trees at training time and outputting the class that is the mode of the classes (classification) or mean prediction (regression) of the individual trees. The associated Gini score for each parameter relates to how large its overall discriminative value was for the classification problem under study and therefore its importance in the overall forest model. Out of the bag validation is performed where the original forest is created with a training set of the data (usually 2/3rds of the data) and the resultant model is validated with the remainder of the data.

Stroma

The supportive tissue of the epithelium consisting of cells of the connective tissue and vasculature.

Tissue datafication

The capture of fully quantified and continuous data from features and objects, or parameters associated with objects, within a digital tissue section and through image analysis.

Tissue Microarrays (TMA)

Consist of small cores of tissue taken from potentially hundreds of entire paraffin embedded tissue blocks and arrayed across a single new paraffin block. This allows multiple patient samples to be analysed across a single section of the TMA once mounted on a microscope slide.

Tissue phenomics

The capture of multiple, hierarchical and often co-registered image-based parameters across a digital pathology specimen to fully explain or 'datafy' it. Each feature captured from each classified object (be it a biomarker or histopathological feature) is termed a 'phene'. The 'phenome' is the entire collection of 'phenes' which describes the full pathological specimen.

TNM staging (see Appenidx B)

The classification of tumours into categories which are correlated with prognosis and treatment regimens. TNM stands for Tumour, Node, and Metastasis and is linked to the local depth of a tumour's invasion, whether it has invaded the lymph nodes or metastasised to a distant organ. TNM staging is the international gold-standard for staging CRC.

Tumour budding

Clusters of 1-5 cells disseminated from neoplastic glands at the invasive edge of a tumour.

Tumourigenesis

Formation of a new tumour at the site of origin or at a distant metastatic site.

Virtual machine

A virtual machine (VM) is an operating system or application environment that is installed on software which imitates dedicated hardware

Whole slide imaging

The digital capture of a whole tissue section through digital pathology

Abstract

Colorectal cancer (CRC) patients are stratified by the Tumour, Node and Metastasis (TNM) staging system for clinical decision making. Additional genomic markers have a limited utility in some cases where precise targeted therapy may be available. Thus, classical clinical pathological staging remains the mainstay of the assessment of this disease. Surgical resection is generally considered curative for Stage II patients, however 20-30% of these patients experience disease recurrence and disease specific death. It is imperative to identify these high risk patients in order to assess if further treatment or detailed follow up could be beneficial to their overall survival. The aim of the thesis was to categorise Stage II CRC patients into high and low risk of disease specific death through novel image based analysis algorithms.

Firstly, an image analysis algorithm was developed to quantify and assess the prognostic value of three histopathological features through immunofluorescence: lymphatic vessel density (LVD), lymphatic vessel invasion (LVI) and tumour budding (TB). Image analysis provides the ability to standardise their quantification and negates observer variability. All three histopathological features were found to be predictors of CRC specific death within the training set (n=50); TB (HR =5.7; 95% CI, 2.38-13.8), LVD (HR =5.1; 95% CI, 2.04-12.99) and LVI (HR =9.9; 95% CI, 3.57-27.98). Only TB (HR=2.49; 95% CI, 1.03-5.99) and LVI (HR =2.46; 95% CI, 1 - 6.05), however, were significant predictors of disease specific death in the validation set (n=134). Image analysis was further employed to characterise TB and quantify intra-tumoural heterogeneity. Tumour subpopulations within CRC tissue sections were segmented for the quantification of differential biomarker expression associated with epithelial mesenchymal transition and aggressive disease.

Secondly, a novel histopathological feature ‘Sum Area Large Tumour Bud’ (ALTB) was identified through immunofluorescence coupled to a novel tissue phenomics approach. The tissue phenomics approach created a complex phenotypic fingerprint consisting of multiple parameters extracted from the unbiased segmentation of all objects within a digitised image. Data mining was employed to identify the significant

parameters within the phenotypic fingerprint. ALTB was found to be a more significant predictor of disease specific death than LVI or TB in both the training set (HR = 20.2; 95% CI, 4.6 – 87.9) and the validation set (HR = 4; 95% CI, 1.5 – 11.1).

Finally, ALTB was combined with two parameters, ‘differentiation’ and ‘pT stage’, which were exported from the original patient pathology report to form an integrative pathology score. The integrative pathology score was highly significant at predicting disease specific death within the validation set (HR = 7.5; 95% CI, 3 – 18.5).

In conclusion, image analysis allows the standardised quantification of set histopathological features and the heterogeneous expression of biomarkers. A novel image based histopathological feature combined with classical pathology allows the highly significant stratification of Stage II CRC patients into high and low risk of disease specific death.

Lay Summary

There exists a subset of colorectal cancer (CRC) patients where surgery is considered curative and where no chemotherapy or further treatment is recommended. There is, however, a high risk subpopulation within this subset that experience disease recurrence and die of CRC. It is important to be able to identify these high risk patients in order to assess if further treatment or detailed follow up could be beneficial.

The literature reports that there are three microscopically observed features within tissue which have been correlated to disease recurrence and disease specific death: lymphatic vessel invasion, lymphatic vessel density and tumour budding. They have not been included into official clinical guidelines for the reporting of CRC due to variation in results between pathologists when carrying out manual quantification.

This thesis utilises computer based image analysis to help standardise the quantification of these features and reports on their significance to categorise CRC patients into high and low risk of disease specific death. This work was carried out on a training set (n=50) and validation set (n=134) of patients. Although all the features were significant in predicting disease specific death in the training set only tumour budding and lymphatic vessel invasion were significant when assessing the larger validation set.

Although tumour buds are significantly prognostic there is less known about their characteristics which make them an indicator of aggressive disease. In this thesis, image analysis is not only used to segment tumour buds for quantification but to identify proteins displayed by them and not by other parts of the cancer. These proteins once identified could be used as a drug target to inhibit cancer invasion.

The thesis further discovers a previously unidentified feature, through novel image based methodology, and which predicts poor patient outcome. This novel feature is more significant at the prediction of disease specific death than those previously described for both the training and validation set.

Novel tools within pathology will most likely not replace classical pathology but augment it and therefore the thesis reports an integrative pathological score which is compiled of the novel image based feature and two parameters from the original clinical report. This integrative pathology score is highly significant at stratifying high risk colorectal patients and in the prediction of disease specific death.

Chapter 1: Introduction

1.1 Cancer Heterogeneity

1.1.1 Neoplasia

Cancer is amongst one of the leading causes of disease related mortality in the world with 14 million new cases diagnosed each year and 8.2 million cancer related deaths in 2012(1). Lung, colorectal and either prostate in men or breast in women are the most common diagnosed cancers worldwide. Despite advances in early detection, surgery and treatment, these numbers are likely to rise due to, among other reasons, pollution, an aging population and poor lifestyle choices: smoking, alcohol, poor diet and lack of exercise(1). Cancer is not one disease but an umbrella term for many diseases originating from many tissue types and from heterotypic cells of origin. The one common theme of all cancers is malignant neoplasia. Neoplasia, meaning a new growth, is the unregulated and autonomous proliferation of cells outwith homeostatic control(2).Neoplasms may be either benign or malignant and are also referred to by their more common name of tumour. Malignant tumours, unlike benign ones, have the capability to invade into neighbouring tissue borders and structures as well as metastasise(3).Metastasis occurs when cancer cells obtain the ability to invade from the primary tumour of origin and spread, usually through the vasculature, to a distant organ where they form a new proliferating neoplastic colony(4). In around 90% of cancer cases it is the secondary metastatic neoplasm which kills the patient(5). Malignant tumours are usually spawned from a single cell of origin which, through multiple steps of mutation or epigenetic aberration, termed the metastatic cascade, creates a heterogeneous malignant tumour; where at least a subpopulation of which is capable of metastasis(6). Metastasising adenocarcinoma cells, for example, must not only be able to lose aspects of their epithelial phenotype in order to break contact and migrate away from their neighbouring cells but also acquire driver mutations enabling them to intravasate the vasculature, survive within the blood or lymphatic vessels, extravasate into and colonise a foreign organ(5, 7). Vogelstein characterised this multi-

step progression to neoplasia in 1993(8) and malignancy is now characterised by a cancer's evolution to encompass the six major hallmarks of cancer: undergoing uncontrolled proliferation, replicative immortality, evading growth suppressors, resisting cell death, inducing angiogenesis and being able to invade and metastasise(9).

1.1.2 Cancer evolution

Primary tumours contain heterogeneous subpopulations of cancer cells which display differential genotypes and phenotypes, some of which may confer proliferative and metastatic advantages to the tumour. These subpopulations evolve through a Darwinian natural selection process which may also be affected by a response to attack from the host or insult by therapy(10). These populations of heterogeneous cells may also perform differing functions within the tumour depending on their lineage and evolutionary hierarchy. These functions could involve angiogenic, proliferative and Extra cellular remodelling (ECM) remodelling properties to sustain neoplastic growth and tumour survival(11). This heterogeneity may stem from several sources; clonal evolution, cancer stem cells, the microenvironment, host interactions or a response to the chemotherapy itself(12).

The clonal evolution theory states that cancers build up heterogeneous subpopulations after concurrent mutations over multiple rounds of cell division due to the plasticity of the cells through chromosomal and replicative instability or exogenous insults(6, 10). These heterogeneous subpopulations are under the influence of natural selection where they may acquire mutations which ultimately lead to cell death while others accumulate a specific set of driver mutations allowing the cancer cells to metastasise.

There are multiple hypotheses on the existence of the cancer stem cell (CSC) model and the CSCs' multipotency. CSCs may originate from healthy tissue stem cells(5, 13) or may have attained their stem-like phenotype through epigenetic alterations of the genome or through stromal cell interaction from their microenvironmental niche(14). The stem-like attributes associated with CSCs would confer a certain amount of plasticity upon it in order for it to evade aggressive treatment regimens or commit to the metastatic cascade(15). CSCs may have the ability to produce hierarchical heterogeneous cell subpopulation progenies of which only some are tumourigenic and

others differentiated(12). CSCs are thought to initiate tumourigenesis, have the ability to propagate the cancer after chemotherapy and a cure for the patient depends on the eradication of such self-renewing cells. CSCs also appear to be more resistant to radiation and chemotherapeutic treatment and may incur tumour recurrence even after a long period of remission and dormancy(13). The plasticity of CSCs also potentially allows them not only to undergo an epithelial to mesenchymal transition (EMT) in order to invade in the first instance, but also to revert back to an epithelial phenotype and propagate a secondary tumour upon metastasising to a distant organ (15, 16).

1.1.2.1 Epithelial to mesenchymal transition

The epithelial to mesenchymal transition (EMT) is the first step of the metastatic cascade for adenocarcinomas such as colorectal cancer(5). During EMT cells lose certain characteristics of an epithelial cell and express a more mesenchymal-like phenotype(17). This not only enables the cell to disseminate from their epithelial neighbours through disassembly of cell-cell adhesions and loss of cell polarity, but allows it to migrate through the extra cellular matrix(18). Loss of E-cadherin, a major component of cell-cell adhesion complexes and cell polarity, is considered an essential factor of the EMT (18, 19), and can occur at the invasive edge of colorectal cancer (Figure 1)(20). The stabilisation of β-Catenin and its subsequent nuclear translocation is a hallmark of colorectal cancers(21). β-Catenin loss at the cell membrane, where it binds to E-cadherin in cell-cell adhesion complexes, further disrupts the epithelial phenotype(19). Upon nuclear translocation β-Catenin acts as a transcription factor for proliferation, mesenchymal and invasion oncogenes. Zeb1, Snail and Twist proteins transcriptionally repress E-cadherin and are associated with the mesenchymal phenotype (15, 18, 19). These families of proteins are also activated by nuclear β-Catenin either directly or indirectly. Zeb1 also acts as a transcriptional repressor of EpCAM, another epithelial cell adhesion molecule, to induce EMT(22). A further inducer of the mesenchymal phenotype is TGF-β which upregulates Snail, Zeb and Twist protein expression(23). Interestingly it has been shown that the source of EMT inducers such as TGF-β and TNFα come from the stromal cells of the microenvironment, such as cancer-associated fibroblasts, and from inflammatory cytokines respectively(23-25). After the cancer cells have disassociated from the

neoplastic glands they may express enzymes involved in the remodeling of the extra-cellular matrix (ECM) in order to migrate toward sites of invasion such as the matrix metalloproteinases (MMPs)(26). Cancer cells may undergo a further transformation in the form of mesenchymal to amoeboid transition, which is regulated by Rac and Rho protein expression, whereupon they migrate through the ECM without breaking it down through proteolysis(11).

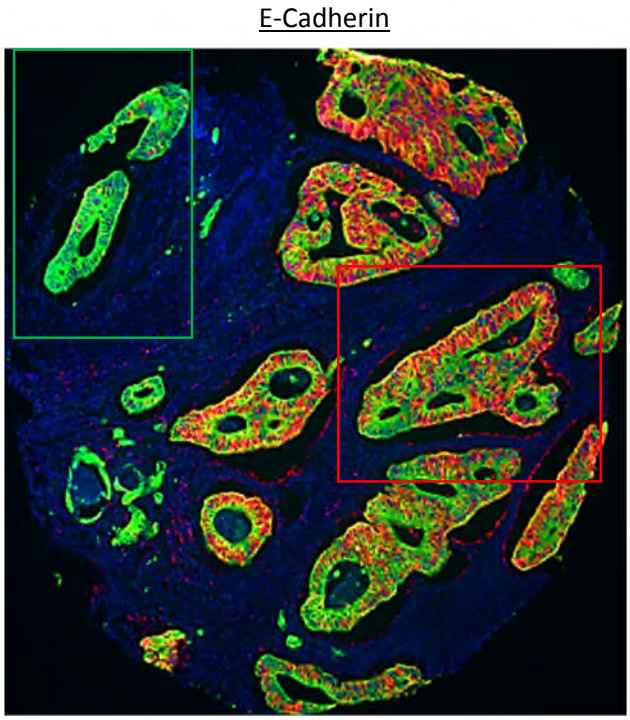

Figure 1. Loss of E-Cadherin at the invasive front of CRC. TMA core taken from the invasive front of a CRC patient tumour block. Neoplastic glands are visualized with antibody against panCK (green) and counterstained with DAPI (blue). E-Cadherin (red) is not expressed in neoplastic glands at the edge of the cancer invasion (green box) but is expressed in well differentiated glands located closer to the tumour centre (red box). Image taken with a x10 objective.

Although the EMT process can become complicated with many interacting proteins and pathways, it results in a cell which decreases its epithelial cell polarity, its ability to adhere to neighbouring epithelial cells and increases cell survival and migratory characteristics. The EMT process also adds to the intra-tumour heterogeneity. In CRC, for example, well-differentiated neoplastic glands near the centre of the tumour may display an epithelial phenotype whereas cells at the invasive edge can undertake EMT.

1.1.3 Tumour microenvironment

Within the tumour and interacting with it is the cancer microenvironment. This is made up of a heterogeneous colony of cancer cells as well as a complex milieu of non-cancerous host cells and scaffold proteins including immune and inflammatory cells, stroma (fibroblasts, myofibroblasts, muscle cells and extra cellular matrix) and lymphatic and venous vasculature all of which further adds to the inherent heterogeneous make-up of tumourigenesis(3). The stromal aspect of cancers is thought to play a role in EMT and to induce stem-like properties in the cancer cell, where the cancer cells at the invasive front react to mesenchymal stimuli from host cells and not from within the tumour itself(15). A novel CRC grading system for patient prognosis has recently been proposed which combines a tumour's invasive pattern with stromal desmoplastic reaction(27). Understanding the microenvironment is therefore important to understand the cancer's progression as its interaction with the tumour can aid or hinder the tumour's evolution to autonomous survival as well as its metastatic and invasive potential(11, 24, 28). The majority of anti-cancer therapies, either cytotoxic e.g. FOLFOX (Folinic Acid, Fluorouracil and Oxaliplatin) for colorectal cancer(29) and CAVE (Cyclophosphamide, Adriamycin, Vincristine, Etoposide) for lung cancer(30) or targeted trastuzumab for breast cancer(31) and gefitinib for non-small cell lung cancer(32), are designed against the cancer cell with an attempt to stop one of the six hallmarks stated above. As the knowledge of the tumour microenvironment and its role in tumourigenesis grows there has been a shift in effort within pharmaceutical strategies to target its characteristics rather than the tumour's (33-35) in an attempt to stifle the tumour and its invasive capacity. Examples of such strategies are: bevacizumab(36) and sunitinib(37) which target VEGF and are anti-angiogenic, induced apoptosis of T_{reg} cells by agonistic anti-OX40 mAb(38) and repolarization of macrophages by agonistic CD40 mAb(39), marimastat(40) and neovastat(41) which block matrix metalloproteinases and inhibit the breakdown or remodelling of ECM. Microenvironmental features such as; microvessel density and angiogeneisis (42-44), vasculature invasion(45-47) and immune and inflammatory cell infiltration(44, 46, 48) are being investigated for their clinical use. The prognostic importance of the immune infiltrate in CRC is becoming ever more apparent(49, 50). The immune response is not only being utilised as a prognostic tool but also to identify

novel drug targets such as anti-PD1 to stimulate the anti-tumour immune response of the patient(51).

When investigating the difference in deregulation of significant pathways involved in CRC between the epithelium and the stroma Abba *et al*. showed that epithelial active pathways were involved mainly in proliferation, while the stromal expression favoured invasive and angiogenic related pathways(52). They state that the tumour related stroma is the major determinant of cancer phenotype adding further weight to the argument that the stroma as well as the primary tumour should be investigated for prognosis and therapeutically targeted.

1.1.4 Inter-patient heterogeneity

Inter-patient heterogeneity can be classified as patients with the same cancer type but whose disease differs in molecular, morphological and phenotypic characteristics. Inter-patient heterogeneity is demonstrated in Figure 2 where two stage II CRC patient samples express differential Cytokeratin 7.

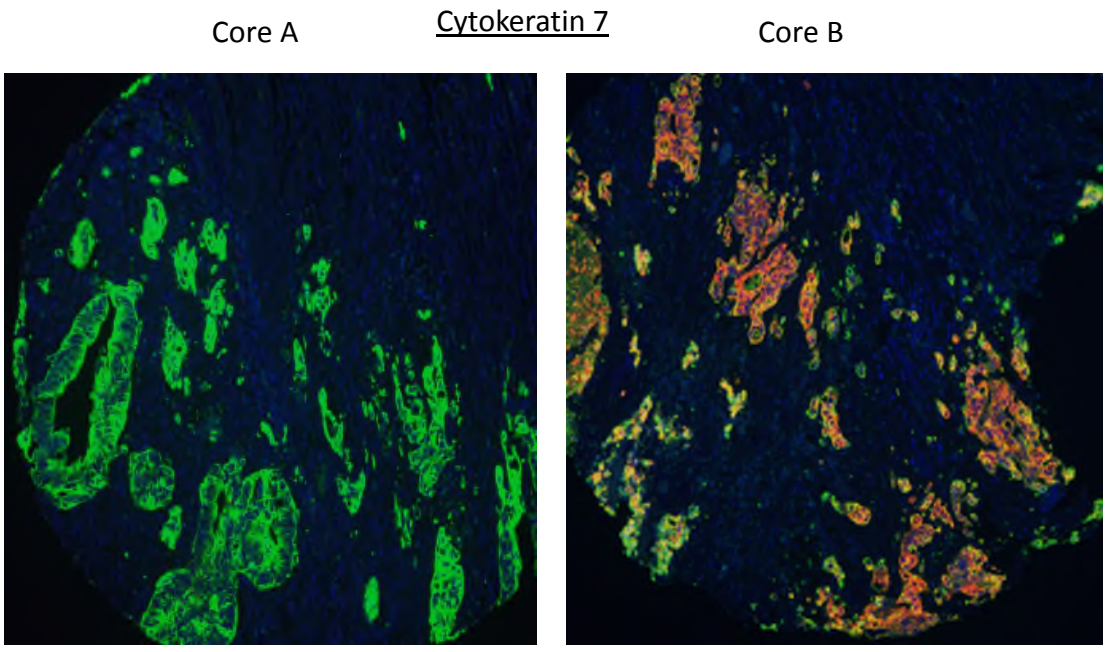

Figure 2. Cytokeratin 7 inter-patient heterogeneity. TMA cores taken from blocks from 2 different patient: core A and core B. Core B shows high expression Cytokeratin 7 (red) in the neoplastic cells (green) and Core A shows no Cytokeratin 7 expression. Image taken with a x10 objective.

Driver mutations leading to tumourigenesis can be somatic and sporadic or of germline descent. They can be caused by genetic or epigenetic aberrations or from exogenous sources such as viruses(10). Depending on the type of mutagen, morphology, phenotype and organ or cell type of origin, cancers can be divided into subgroups. Since the dawn of molecular pathology these subgroups can be further subdivided depending upon specific molecular characteristics(53, 54). In theory, patients with similar characteristics may therefore have similar prognosis and be treated with similar therapy regimens(55, 56). Knowledge of inter-patient heterogeneity, through clinical and molecular pathology, arms the oncologist with a much more exacting data repertoire to consult in order to treat the patient successfully. This pathological knowledge of the difference between patients' cancer and treatment strategies bears a much higher success rate in treating patients and their overall quality of life than a "one treatment fits all". This is eloquently exemplified in the treatment of CRC over the last decade. Previous to targeted biological treatment, advanced colorectal patients were commonly treated with FOLFOX or FOLFIRI (Folinic Acid, Irinotecan and Fluorouracil)(57, 58). Targeted therapy against EGFR through administration of cetuximab has since shown promising results with increased progression-free survival compared to chemotherapy(59). EGFR inhibition, however, only shows benefit to patients with wild-type KRAS(60, 61) and those patients with mutations downstream of EGFR such as KRAS, BRAF(62, 63), PIK3CA(64) and NRAS(65) show poor response or predicts resistance to targeted EGFR therapy such as cetuximab or panitumumab. In fact it has been shown that monoclonal antibody inhibition of EGFR in combination with FOLFOX may actually have detrimental effects on patients with mutant KRAS CRC(66). KRAS and BRAF mutations are also informative concerning prognosis and disease specific death(53, 67). Although there are multiple heterogeneous subgroups of colorectal cancer(68) aside from KRAS mutation status, there are relatively few prognostic and predictive biomarkers routinely used in the clinic. Further research continues within this field to identify biomarkers for anti-EGFR therapy resistance(69).

Although colorectal and has been used here as an example, most cancers can be sub-grouped depending on histological and pathological criteria. This subsequent

subgrouping can offer information on prognosis and optimal treatment options or novel drug targets in, for example, breast(70, 71) prostate(72, 73), ovarian(74, 75) and renal cell carcinoma(76, 77). A reason for recent successes over the past decade in the targeted treatment of certain cancers is therefore due to accurately identifying subgroups of patients which are susceptible or resistant to chemotherapy and targeted treatments, thereby not only guiding the optimal combinatorial therapy, but avoiding unpleasant or harmful side effects by withholding drugs from patients which will have little to no advantageous effect for them.

1.1.5 Intra-patient heterogeneity

The ability to stratify patients into subgroups for more efficacious treatment and prognosis, depending on the characteristics of their whole tumour, has seen recent advancement and benefit to the patient in terms of progression-free survival. However, systemic therapy frequently fails and, moreover, highly effective targeted therapies are not resulting in long term benefits in terms of patient outcome in spite of initial response(78). There is a danger in treating an individual's cancer as an entity with uniform molecular and phenotypic properties. Doing so could be the cause of recurrence of disease and the reason why some members of a subgroup respond better than others to their designated treatment(79). The fact that a cancer's evolution plays a major role in tumourigenesis is not novel (8, 10, 80), however, it is only more recently that knowledge is being gathered on how this manifests as intra-tumoural heterogeneity(12, 14, 15, 79). Quantifying the tumour's inherent intra-heterogeneity provides hierarchical data into the molecular, phenotypic and functional properties of an individual's cancer and as to whether they will respond positively in the long term to targeted or personalised therapy.

Molecular pathology has the ability to subgroup patients not only on inter-patient heterogeneity but also on intra-patient heterogeneity. Intra-patient heterogeneity may be classed as either intra-tumour heterogeneity or heterogeneity between the primary tumour and secondary distant metastasis. As the cells in the primary tumour evolve toward malignancy and express the six major hallmarks of cancer (81), it becomes ever more heterogeneous. Figure 3 shows the decrease in epithelial-associated markers at

the invasive front of CRC compared to neoplastic glands closer to the centre of the tumour. This intra-tumour heterogeneity may confer metastatic and invasive properties to the cells at the invasive edge(82-84), while the cells nearer the core possess differential expression patterns(85, 86) and can retain some properties to the differentiated cells from which they originated.

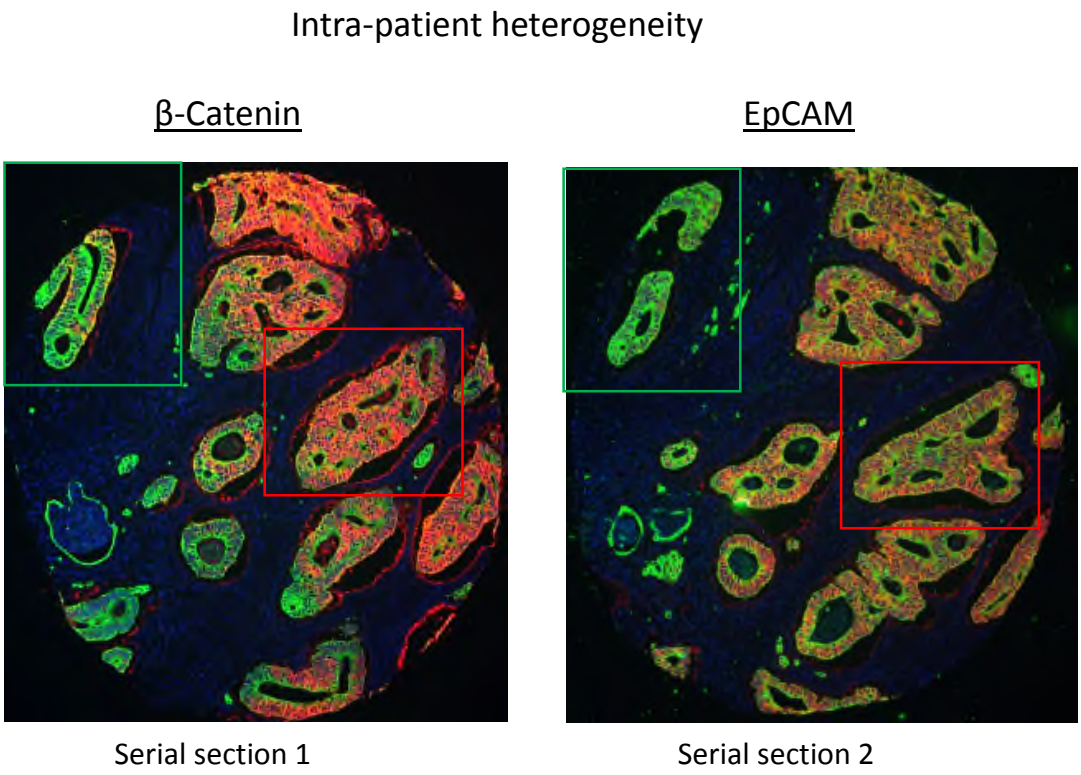

Figure 3. Examples of subpopulations within the same tissue sample expressing differential protein signatures. Serial sections of a TMA core taken from the invasive front of a CRC patient tumour block. Neoplastic glands are visualized with antibody against panCK (green) and counterstained with DAPI (blue). Membranous β-Catenin (red in section 1) and EpCAM (red in section 2) are not expressed in neoplastic glands at the edge of the cancer invasion (green box) but are expressed in the well differentiated glands located closer to the tumour centre (red box). Image taken with a x10 objective.

The activating mutations in the EGFR pathway of KRAS, BRAF and PIK3CA in CRC are shown to be differentially detected between the tumour core and invasive front after macrodissection of primary tumour (87) . In a separate CRC study KRAS and BRAF heterogeneity was shown when two tissue blocks were sampled per patient

instead of just one(88). High grade expression of Laminin-5 gamma chain 2 (LN-5γ2)(82) and nuclear beta-catenin(21) expression in CRC is predominantly expressed at the invasive front rather than at the centre of the primary tumour and the grades of expression in these distinct areas hold prognostic value. Conversely VEGF and RKIP expressing cells were found predominantly in the tumour core(86) and not the invasive front. After discordant results of $BRAF^{V600E}$ mutation status using conventional sequencing and mutant-specific PCR in melanoma tumours Yancovitz *et al*., laser-capture microdissected primary tumours and found most to contain subpopulations of BRAF mutant and wild type cells(89). These results may explain why some melanoma patients do not respond well or show disease recurrence when treated with BRAF inhibitors such as vemurafenib.

As with intra-tumour heterogeneity within the primary tumour there is also discordance between the molecular profile of the primary tumour and distant metastasis. In CRC mutant and wild-type KRAS, BRAF and PIK3CA heterogeneity varies from primary tumour, lymph node metastasis and distant metastasis(87). EGFR pathway related intra-tumoural heterogeneity could lead to the reporting of false positive KRAS wild-type status, especially if only the primary tumour is tested, and could explain why these patients may not respond well to cetuximab and panitumumab and experience disease recurrence(60, 61). Patients with primary melanomas when tested for mutational BRAF also carried metastasis with wild-type BRAF and in 5 cases separate metastasis from the same patient carried either wild-type or BRAF mutations(89).

It is not only molecular differences which confer heterogeneity but morphology and cell differentiation may vary from tumour core, invasive edge and metastatic sites. The cells at the invading edge of CRC may be more mesenchymal and undifferentiated as they undergo EMT and disseminate from the neoplastic glands (20, 27, 90). Although there is an underlying molecular phenomenon associated with morphological change, the pathologist need not know the exact mechanism driving this to recognise a heterogeneous invasive pattern related to poor or good prognosis(91-93). Levels of necrosis(94, 95), apoptosis(96, 97) and mitosis(98, 99) may also vary across the primary tumour and be correlated to patient prognosis.

The importance of the heterogeneous molecular and morphological tumour and its interaction with the cancer microenvironment is apparent. It is also therefore important to be able to capture this complex and hierarchical data in a meaningful way in order to glean as much useful information on an individual's tumour and thus inform clinical decision making. The understanding of patient-wide heterogeneity may inform oncologists on the optimal combination of therapies needed for the patient at a personalised level rather than at a population based level.

1.2 Tissue Datafication

A wealth of prognostic and predictive information lies within the patient's tissue sample. Classical histopathology strives to infer dynamical prediction of disease progression from the static artefact which is the tissue section. The pathologist directly observes microscopically the complex diseased tissue and its interaction with the host microenvironment in order to mentally compute these multiple signals into a prognosis. This has long been the gold standard in clinical prognosis. Although multiple novel prognostic methodologies for CRC have been developed to replace or augment classical pathology, and while some show promise, for example the gene expression signatures ColoPrint(100) and Oncotype DX® in colon cancer(101), none have become established within routine CRC clinical prognosis. The classical Dukes and TNM morphological and histological staging of the disease remains steadfast in clinical pathology (102-104). One reason for this is standardisation and the imperfection of tissue. The human eye can account for the variation and artefacts that occur between surgical removal of the tissue through to mounting sections onto microscope slides for analysis. Poor and small sample size, imperfection and damage to tissue as well as poor tissue orientation can be easily disregarded by the pathologist while they can glean the pertinent information from the final stained tissue section. Automated quantification, spanning the CRC omics fields(105) of the tissue section which is not able to be so selective, may return variable results and where standardisation is a very real problem.

Advances in extracting data in a meaningful and robust manner could add value to classical histopathology methodologies and provide greater impact and accuracy of

patient stratification at a more personalised level than current population statistics. This is increasingly relevant when the quantification techniques take into account the heterogeneity of the disease and report on it. 'Datafication' of tissue is the extraction of information in a fully quantifiable and standardised manner. This can take the form of quantifying a single biomarker to capturing a complex and hierarchical multi-modal omics signature. A single read-out may be extracted from a single tissue sample or multiple readouts taken across distinct subpopulations identified through morphometric or biomarker expression.

1.2.1 Quantifying inter-tumour heterogeneity

Understanding tumour heterogeneity is important in striving toward an intelligent and individualised treatment strategy which translates to clinical impact. To truly fulfil a personalised medicine approach and select the correct combination therapy for a patient, it is essential to know which mutational or epigenetic aberrations their cancer carries in both primary and distant disease and what the subsequent phenotypic and functional effect on the cells and their microenvironment are.

Since the post omics era scientists have been armed with a suite of new tools to identify biomarkers to subgroup a patient's cancer at the molecular level. Using these tools a raft of data and new biomarkers have been discovered over the last few decades and allowed genome scale analysis and comparisons (105-108). The three main disciplines to bear the wealth of the results are genomic, transcriptomic and proteomic studies whereas work is also on going in epi-genetics. A recent epi-genetic example in CRC showed hypermethylation of TWIST 1 and TWIST 2 in the stromal compartment of the microenvironment in well differentiated tumours, whereas there was no methylation of the gene promoters in tumours with an infiltrative invasive pattern(109). Epigenetics is especially relevant to CRC where a patient's cancer can be subtyped by DNA methylation and correlated to genetic mutations(68, 107).

1.2.1.1 Genomics

The two main technologies at the disposal of investigators into genomic biomarkers from patient tissue samples are: next-generation sequencing (NGS) and array comparative genomic hybridization (aCGH). NGS allows cost-effective large scale

genome wide DNA sequencing of the cancer genome and has led to the discovery of at least one clinically relevant genetic alteration in 59 % of a group of colorectal and non-small cell lung cancers revealing two gene fusions *C2orf44-ALK* and *KIF5B-RET* respectively(110) and that the tumour suppressor gene *ARID1A* is mutated in more than half of clear-cell ovarian cancer tumours tested(111). NGS' integration into clinical practice is comprehensively reviewed by Kohlmann *et al*(112). aCGH allows the analysis of gene copy number loss or amplification across the genome. This can directly translate to driver aberrations in cancers and the heterogeneity of copy number in a patient population can give rise to patient subgrouping(113). Genetic intra-tumour heterogeneity was found in cervical cancer after analysing core biopsies from 4 quadrants of the patient's tumour with aCGH(114). In CRC copy number profiles were related to stages and metastatic spread where Dukes D patients showed genomic losses and Dukes C patients showed genomic gains(115). Detection and investigation of subpopulations using aCGH can therefore identify resistant and sensitive cancer signatures with prognostic and predictive outcomes. aCGH and its role in cancer research is reviewed in detail by Micheuls *et al* (116).

1.2.1.2 Transcriptomics

Quantifying the mutation status at the genomic level alone does not portray the full picture of how driver mutations affect cellular dysregulation and cancer progression. Investigating how the genes are expressed through transcription allows insight into the mutation's effect on overall cellular control and protein production. Transcriptomics follows the assumption that patterns of gene expression correlate to cellular function at the proteomic level(105). Two technologies which allow gene expression profiling are RNA microarray analysis and high throughput RNA sequencing (RNA-seq), termed deep sequencing(117). RNA microarray analysis, allowing the genome-wide analysis of gene-expression, was used to discover a 70 gene expression signature which identified a poor prognosis signature in lymph node negative breast cancer patients as well as identifying tumours from BRCA1 carriers(118) leading to MammaPrint© the first commercial microarray assay used in the breast cancer clinic(119). Oncotype DX® is also routinely used in the clinic for prognostic value and looks at a 21 gene signature to predict which patients are at risk of disease

recurrence(120). Similar approaches in the field of CRC have shown some prognostic value, however little predictive value, and are currently without FDA approval(121). A recent study applied gene expression microarrays to discover RNA biomarker patterns in colorectal patients which can be detected in blood plasma for use in a point of care companion diagnostic. KIAA1199 transcripts were found to be more abundant in the plasma of patients with colorectal cancer than the control group(122). Deep sequencing directly sequences the RNA transcripts from tissue samples, which are mapped to a reference genome and quantified to assess level of gene expression. Overexpression of CD151 in all stages of epithelial ovarian cancer was found by RNA-seq and could become a new anti-invasive target for drug discovery(123). These studies could result in a predictive test in which patients overexpressing CD151 are chosen to receive treatment. Both transcriptomic technologies and how they can complement each other are discussed in more detail by Malone *et al*(117).

1.2.1.3 Proteomics

Although transcriptomics report valuable information on the pattern of gene expression, studying the proteome allows the understanding of functional proteomics. Proteomics research quantifies the transcribed gene's end product, the protein. The way that proteins interact in complex signalling pathways, their cellular sub-localisation and post-translational modification (such as conformation change and on/off states controlling signal transduction pathways) has impact on cellular control. In short, proteomics and not simply the gene expression provides insight into the functional phenotypic effect of the genomic mutation or silencing and what this effect has on cellular regulation or deregulation. The two technologies employed to analyse multiple proteins and their interactions from a patient sample are Reverse Phase Protein Arrays (RPPA) and mass spectrometry. RPPAs allow the quantification of multiple signalling pathway responses and post-translational modifications where the proteome can be spotted and analysed on a single chip(124). Each spot comprises the entire lysed protein pool of the tissue sample in question and entire patient cohorts can thus be quantified for heterogeneous total and phospho-state protein expression in a highly comparable manner(125). RPPA was utilised to identify a prognostic proteomic signature associated with the PI3k/AKT pathway for stage II CRC patients(126).

Recently this technology has moved out of the research laboratory and into the clinical setting and the technology is reviewed in more detail by Mueller *et al*(127). Mass spectrometry has been utilised to profile the proteome from not only tissue but also from blood and urine(105). Mass spectrometry was utilised to identify protein signatures which correlated to the morphometry of the CRC glands and could identify well, moderate and poorly differentiated tumours(128). This work provides some insight into which proteins may be involved in tumour progression and malignancy.

The aim of all 'omics' research is to identify biomarkers which can lead to targeted drug discovery programmes or companion diagnostics which will allow the clinician and pathologist to make rapid informed decisions on the prognosis of the disease and to predict which treatment will offer the greatest efficacy and best outcome possible for the patient.

1.2.2 Quantifying intra-patient heterogeneity

Although the above methodologies to quantify the molecular mode of action driving cancer subtypes have added significant value, they also hold disadvantages to assaying such complex material. To extract DNA, RNA and protein molecules these assays usually homogenise and destroy the tissue integrity. The tissue is literally "mashed and measured" mixing together any subpopulations of cancer and host cells expressing differential properties while losing spatial resolution. This results in one end-point being reported for the whole tumour. Due to the nature of these applications, intra-tumoural heterogeneity of the tissue may be under-detected where the dominant or most abundant genotypes or phenotypes mask signal from smaller cell populations within the tumour. Healthy tissue and host cells from the tumour microenvironment are both also added to the molecular sample creating a further source of noise to the signal and could increase the reporting of false positive or negative results. Under-detection of tissue heterogeneity therefore leads to an urgent and difficult problem when treating a patient with combination therapy, as resistant subgroups could go unnoticed and untreated. There are, however, tools to overcome this problem which attempt to better quantify, and thus comprehend, the complexity of heterogeneous tumours.

1.2.2.1 Laser capture microdissection

One such tool is laser capture microdissection (LCM) which isolates and analyses cells and sections of the tissue of interest, usually those displaying morphological differences(129). This technique allows the separate analysis of distinct subpopulations as well as comparing the tumour's core, invasive edge and the stromal microenvironment. From these distinct sections DNA, RNA and protein can be isolated and studied resulting in a cleaner profile of the difference between regions of interest and their heterogeneity. Yancovitz *et al* performed LCM on distinct subpopulations within primary melanomas and utilised SNaPshot® technology (which allows the multiplexing of up to 10 single nucleotide polymorphisms in a single test) to detect mutations from within them. They showed that subpopulations from within the same tumour contained heterogeneity for BRAF mutations which were undetected when sampling the whole tissue(89). LCM was further employed to segregate stroma from epithelium in CRC and compare the differential expression signatures from each using a microarray gene expression assay(52). LCM is also commonly used alongside RPPA in proteomic studies for the molecular profiling of cancer specific signalling networks and specific subpopulations or regions of interest(130). This technique was utilised in a study where LCM and subsequent RPPA analysis of normal, intraepithelial neoplasia and invasive prostate tissue showed an increase in phosphorylated Akt, decrease in phosphorylated ERK and a decrease in apoptotic signals, respectively, displaying increasing metastatic hallmarks through cancer progression(131). There are drawbacks to LCM as the procedure can damage the molecular material of interest and spatial integrity is still lost when performing destructive homogenising assays. Recent technological advances such as Ion Torrent sequencing(132) and RPPA using fully optimised platforms, for example Zeptozens' ZeptoCHIP technology(133), allow molecular genomic and proteomic profiling respectively with small sample sizes amenable to ever smaller tissue samples in the study of heterogeneity. Background signals from complex tissue can still create noise in these assays and robust and sensitive data depends on the LCM technique as well as the specificity of probes, antibodies and detection technology used.

1.2.2.2 *In situ* labelling

To avoid contamination of signals, from heterogeneous subpopulations within tissue, *in situ* imaging of protein through Immunohistochemistry (IHC) and genomics through fluorescence in situ hybridisation (FISH), may be applied. This has advantages over destructive assays as the tissue structure, spatial orientation and sub-localisation of molecules are retained and heterogeneity can be visualised, compartmentalised and quantified while providing insight into cellular interactions within the tumour and its microenvironment. IHC further allows the visualisation of morphological status of the cells expressing the biomarker of interest and allows the observer to correlate morphometric and proteomic signatures at the cellular resolution. IHC by has been the gold standard for the detection of *in situ* protein expression and sub localisation for many decades(134). Identifying and quantifying the heterogeneous patterns of the invasive edge in CRC, for example, benefits greatly from cytokeratin immunohistochemistry in order to identify the epithelial cells when compared to H&E staining (135, 136). Semi-quantitative scoring of ER, PR and HER2 in breast cancer samples by pathologists is the recommended clinical methodology practiced for prognosis and prediction of effective drug combinations (137, 138). FISH, similarly to IHC, allows the *in situ* visualisation and quantification of mutation status of genes of interest and gene amplification analysis. This is performed by probing the chromosome with fluorescent oligonucleotides which hybridise and bind to specific regions of interest, such as a common mutation which could report on a prognostic or predictive biomarker(139). Commonly IHC and FISH will be utilised together in a study to understand the correlation of amplification and expression patterns of genes of interest. HER2/neu gene amplification using FISH showed correlation with strongly positive protein expression of the same gene using IHC in oesophageal squamous cell carcinoma(140). Patients with gene amplification of HER2/neu showed poor prognosis. Furthermore, heterogeneity was found within a CRC patient cohort when analysing EGFR and Cyclin-D1 over expression and cellular localisation as well as EGFR gene amplification using IHC and FISH respectively(141). The heterogeneity could stratify patients into resistant or susceptible subgroups in response to anti-EGFR therapy. Intratumoural heterogeneity was also found to be present in a high percentage of Gastric cancer patients when assessed for HER2 gene expression and amplification

using IHC and FISH respectively(142). This intratumoural heterogeneity could create false positive or negative HER2 status and be the reason why subgroups of patients do not respond well to HER2 targeted therapy. As with RPPA the specificity of the antibody or probe and the use of correct controls are paramount to the success of these assays.

Mass spectrometry has the ability to analyse the proteome of single cells and to assess cell-to-cell heterogeneity(143) as well as *in situ* imaging mass spectrometry which can analyse an area of tissue at the lateral resolution of ~150nm(144). The resolution of formalin-fixed paraffin embedded (FFPE) tissue is usually in the order of 150-200µm in diameter(145). These advances in mass spectrometry allow detailed interrogation of the proteome of tumour subpopulations and the interface between the tumour and the microenvironment.

There are currently certain drawbacks to analytical IHC, and international clinical standardisation is still to be reached including standardisation of fixation, antigen retrieval and staining. Reproducible semi-quantitative scoring by pathologists for predictive testing is subjective and can lead to inter-observer variability while low levels of staining may be hard to identify. These difficulties are further complicated when analysing highly heterogeneous samples.

1.2.3 Image analysis

Although the field of high content analysis is not new(146, 147), where multiple parameters and biomarkers are measured from fluorescently labelled cells(148), the discipline has been slow to translate to histopathology and the clinic. This has been in part due to the complexity of tissue and its imperfection compared to *in vitro* cell studies and the need for extensive validation and standardisation for clinical use(149, 150). This is now changing and digital pathology as well as automated image analysis for tissue-based studies is rapidly emerging into the realm of clinical research(151, 152).

1.2.3.1 Digital pathology

Digital pathology is the high resolution, whole-slide imaging (WSI) of slide mounted tissue sections. This can be undertaken with brightfield and immunofluorescence illumination. The resultant virtual slide may be viewed and navigated on a computer monitor and shared with remote parties for, amongst other things, secondary opinions and research validation studies. Reporting for primary diagnosis has not passed UK or US regulation where further validation is needed to ensure standardised quality control(152, 153). The FDA has recently published a draft guidance for the technical performance needed in WSI devices(154). Countries, where there may be large distances between specialist pathologists have passed regulatory clearance for primary diagnosis, for example, most recently approved in Canada and Sweden. The Canadian Association of Pathologists has published its guidelines on establishing clinical WSI(155).

There are multiple advantages of WSI in the reporting of histopathology. The most obvious in clinical impact is rapid remote reporting on an urgent patient sample when specialist pathologists may be geographically remote(156). Similarly if a second opinion is needed or the hospital has no access to a subspecialist the virtual slide can be shared between institutes almost instantaneously(157). This advantage also facilitates international collaborative research into histopathology and drug discovery(158). Further cost is saved in replacing and servicing of expensive microscopes for each pathologist in an institute. The user interface of mouse and screen is arguably more ergonomically friendly than traditional microscopy and multiple persons may view the slide in one room without the need of multi-header microscopes. Further advantages include ease of slide retrieval from the archive, teaching of medical students and lack of slide breakage, loss and photobleaching of fluorescence samples(159, 160). The assessment of FISH in WSI by image analysis was found to be a robust alternative to traditional fluorescence microscopy which returns variable results between observers(160). Although high concordance exists between glass and digital reporting (unless there is an inconsistency of image quality) (161) there still remain barriers to the technology. These barriers include reluctance of pathologists to change, need for high speed IT infrastructures and storage for large file types(162).

Widespread adoption will most likely occur once image quality can be robust and standardised and the retrieval of sample from archive to screen is faster than mounting glass slides onto a physical microscope.

1.2.3.2 Computer based image analysis

The integration of digital pathology with automated image analysis brings further advantages to the field. These include the standardisation of quantification where observer variability is excluded and the robust analysis of rare or complex features is captured. Traditionally image analysis in histopathology concentrated on the quantification of protein expression through IHC and IF(163). This was to overcome the subjective manual and semi-quantitative scoring of a 1+, 2+, 3+ system. Upon employing IF image analysis software can perform fully quantified continuous data-export from which cut-offs can be calculated in order to stratify patient subgroups(150, 164).

Computer based quantification of nuclear morphometry, however, has been practiced for over a decade(165-167). Continuous improvements to image analysis software now allow the simultaneous export of morphometric parameters of cells and histopathological features alongside biomarker quantification associated to this feature. In this co-registering methodology it is possible to identify surrogate morphological features which correlate with molecular phenotype.

The market leading tissue imaging platform manufacturers provide their own image analysis solutions for chromogenic and fluorescence assays such as Perkin Elmer (http://www.perkinelmer.co.uk/Catalog/Category/ID/InForm-Advanced-Image-Analysis-Software), Zeiss (http://www.zeiss.co.uk/microscopy/en_gb/products/microscope-software/zen.html#features) and Leica (http://www.leicabiosystems.com/pathology-imaging/aperio-epathology/analyze/). This allows segmentation of cells and subcellular compartments and subsequent biomarker quantification within heterogeneous tissue. These software packages are designed to work in connection with the images captured from their own platforms and can sometimes be restrictive to the quantification of set assays, biomarkers and parameters. Definiens

(http://www.definiens.com/), Indica lab (http://indicalab.com/) and Visiopharm (http://www.visiopharm.com/) offer image analysis packages which can import images from most microscopes and allow a more flexible image analysis environment. Definiens, for example, offers two main software packages for the automated image analysis of tissue samples; Tissue Studio® and Developer XD™. Tissue Studio® is an "out-of-the-box" software package which allows the quick application and tuning of a set of sophisticated analysis algorithms to segment and quantify biomarker expression profiles and morphometrics on an object by object basis. Their Developer XD™ software involves additional programming but allows the user to build their own customised image analysis solutions and provides greater flexibility to exploit contextual information in heterogeneous tissue and to determine reliably the quantitative readouts required.

1.2.3.2.1 Quantification of multiplexed biomarkers

While imaging a single biomarker can yield predictive or prognostic information the ability to multiplex two or more markers on a single tissue section becomes a much more powerful tool. An advantage of IF based image analysis is the ability to multiplex, co-register and quantify biomarkers at the cellular resolution(168). Multiplexing reports on protein interactions, pathway activation and multiple cellular events. Accurate co-localisation and spatial resolution of multiple biomarkers or histological features on the same section of tissue reports a richer high content and functional data than serial sections of one biomarker while saving the precious resource which is the tissue sample. Researchers can quantify multiple proteins on a per cell basis or accurately quantify multiple cell types within a heterogeneous population. Traditional multiplexing is limited by bleed through of fluorophores and chromogens as well as antibody cross-reactivity of secondary host-species. Multi-spectral imaging and un-mixing of chromogens and fluorophores allows an accurate spectral readout for each biomarker of interest, increases the multiplexing capacity and negates any autofluorescence(150, 169, 170).The additional use of Quantum Dots with multi-spectral imaging increases the amount of multiplexing available to the researcher(171), however limits must still be reached. The Toponome Imaging System (TIS)(172) allows the ability to spatially map over 100 proteins with subcellular resolution. This is done by sequential rounds of incubating, imaging and bleaching of

fluorescently tagged antibodies building up a spatial map of hundreds of protein interactions and whole protein networks on a single tissue section. Not only does this technology give rise to *in situ* protein network signatures of different subpopulations of heterogeneous healthy and diseased tissue, it also paves the way for next-generation biomarkers for combinatorial drug discovery strategies(173).

1.2.3.2.2 Image analysis of Tissue Microarrays

Tissue microarray (TMA) cores can be punched out of a region of interest from the original tumour block and spotted onto microscope slides for digital image analysis post biomarker labelling(174, 175). Whole slide image analysis may also be employed in order to identify regions of interest (ROI) to select for TMA construction(176). This creates the ability to select samples from areas of distinct morphological and histopathological interest from multiple patients onto a single slide for standardised comparative analysis. The major advantage of using TMAs is the ability to image and quantify protein and genetic heterogeneity *in situ* for entire cancer cohorts under identical, and so fully comparable, IHC and IF. The majority of automated image analysis packages can import TMA images for quantification. Utilising IHC or IF with image analysis makes it possible to quantify the protein expression levels from full cohorts as well as report spatial information relating to the heterogeneity within the TMAs and also between TMAs sampled across the primary tissue and distant metastasis. Image analysis has been performed on TMAs from breast(177), mantle cell lymphoma(178) and ovarian cancer(75) as well as a proposed novel score for predicting metastasis in adrenocortical carcnimoas(179). *In situ* genomics can also be studied using TMAs and FISH technology making it possible to quantify the heterogeneity of mutations or amplification of genes(180, 181).

1.2.3.2.3 Image analysis of whole slide images

While TMAs allow a large number of samples to be analysed in a time and cost efficient manner, imaging entire tissue sections to quantify biomarkers and histopathological features across them yields objective and standardised assessment of intra-tumour heterogeneity(182, 183). Imaging the whole tissue section coupled with automated image analysis allows the investigator to quantify differential protein expression and sublocalisation for biomarker identification across the entire

sample(184). Classical pathology reporting of histopathological events in H&E stained tissue can yield high inter-observer variability and is subjective. Whole slide image analysis may be applied to quantify such events in a more reproducible manner, for example, reporting mitotic index in breast cancer(185). The tumour microenvironment and its interaction with the tumour may also be quantified where spatial heterogeneity and density parameters are reported such as for lymphocytic infiltration and(186) the vasculature(187). Although image analysis of whole slide imaging features predominantly within cancer research other fields of histopathology, such as transplant pathology, are beginning to utilise the same technology(188). Quantitative whole slide imaging of omics based biomarkers has distinct advantages over the more traditional quantification through 'mash and measure' homogenisation of the tissue. The homogenisation of tissue for e.g. NGS, mass spectrometry and RPPAs destroys information on spatial heterogeneity and does not report on heterogeneous subpopulations within the tissue sample. The image analysis of WSI can capture these heterogeneities across the sample and extract information regarding even small subpopulations while the traditional methods will only report the most abundant signal.

1.2.3.3 Tissue phenomics

Although big-data is now associated with the post-omics era of clinical medicine(189, 190), advances in image analysis allow the approach to be adopted in the field of morphometrics and tissue histopathology. Tissue phenomics is the term which describes the big-data capture from image analysis based segmented tissue sections to quantify the data-rich histopathology and the interactions and spatial heterogeneity of the cancer microenvironment's phenotypic features. This involves the extraction of complex and hierarchical data pertaining to a single segmented feature or set of features across the segmented tissue section. This data may be captured through co-registering of biomarkers as proteomic or genomic signals, as multiple morphometric and texture parameters or a combination of both; essentially extracting as much data as possible from each single segmented object within the image(191). A multi-parametric signature is therefore built up for each tissue sample which may be compiled of multi-omic image based features. Sophisticated data mining is required to

identify the significant single or combination of parameters within the signature in order to stratify patients for prognostic or predictive purposes. Data mining techniques previously applied to identify significant parameters have been logistic regression analysis and ensemble decision tree models(192-194).

Advances in imaging technology, such as next-generation IHC, which combines mass spectrometry with IHC, provide an ideal methodology to be incorporated into tissue phenomics. Next-generation IHC enables the exportation of highly multiplexed proteomic data at sub-cellular resolution(195). This data can also be combined with spatial information(196). Image analysis software such as from Visiopharm and Definiens allow hundreds of morphometric and texture parameters to be exported on every single segmented object and spatial statistics calculated between them. These can be co-registered to multi-plexed biomarker data for the same object; which can be a nucleus, a cell or a histopathological feature. By applying a multi-parametric morphometric data capture approach Beck *et al* were able to identify a novel prognostic stromal signature in breast cancer(192). This signature was distilled from over 6000 features relating to intensity, shape, texture and neighbouring objects. More recently a study in glioblastoma correlated a nuclear morphometric signature with clinical and genomic data, which would allow a simplistic morphometric measurement to act as a surrogate for expensive genomic testing(193).

Tissue phenomics may identify novel phenotypic features which may be too subtle to observe by the naked eye. Image analysis can also reproducibly quantify these features in a continuous data manner. Mapping multiple spatial and morphometric heterogeneous parameters in whole tissue sections brings a new dimension to histopathology and can map its intrinsic architecture(197). These features can be used for prognostic purposes, understanding the role of the microenvironment and acting as surrogates for underlying molecular pathways.

1.3 Integrative pathology

Traditional omics research attempts to identify single molecular or histopathological features which could be utilized for prognosis or prediction of response to drug therapy. Cancer is, however, a very complex disease with multiple molecular

interactions within the cell and multiple cellular interactions within the microenvironment(105). Many single biomarkers never translate to the clinic, as they do not take into account the complexity and heterogeneity of the disease. Integrating large scale data from multiple omics fields may help to address this problem as it will create a better understanding of the multiple molecular interactions occurring within the cell and how these translate to disease progression. The diagnosis and prognosis of CRC has been recently re-assessed by subgrouping patients on their epigenetic and genetic profiles(198). A further study in CRC integrated histopathological subtypes with molecular features to assess their correlation and impact on prognosis(56). Integrative large scale pathology has been implemented in breast cancer where cellular resolution of *in situ* and co-registered genotype and phenotype was utilised to study intra-tumoural heterogeneity between primary and distant metastasis for prognostic and potential drug target studies(199). A further breast cancer study integrated a multi-omics signature and discovered JAK-STAT and TNF signalling pathways to be significant in triple negative disease which could lead to novel and personalised drug treatments(200).There is a wealth of data collected during classical histopathology which largely remains unused in clinical decision making. This clinical data is beginning to be integrated with the modern datafication modalities as a further hierarchical level of understanding of the disease from the tissue. In mucoepidermoid carcinoma, histopathology, immunophenotypic and cytogenetic parameters were integrated to identify a signature which was able to identify the pulmonary disease from other subtypes of lung cancer(201). Clinical and molecular data is now also being integrated with the complex and data-rich image-based phenotypic signatures to investigate cancer heterogeneity and its interaction with the microenvironment. The morphometric signatures can also be correlated to the genomic profile and clinical outcome(191). Computational IT solutions are becoming available which allow the incorporation of multiscale omics data(202, 203) as well as to integrate it with clinical information(204).

1.3.1 Systems pathology

Modern pathology is no longer hampered by a lack of large-scale hierarchical data encompassing multi-omics and morphometrics. This data, however, must be integrated

in a meaningful way which makes best use of its complexity and is robust enough to be clinically relevant. Systems medicine, and more recently systems pathology, takes a holistic view of tissue, the cell and its multitude of interactions(205). Systems pathology requires a large amount of high-quality multi-scale data to be extracted from tissue and which acts as input for predictive mathematical models(206). Although systems pathology has predominantly concentrated on molecular profiling of the genome, transcriptome or proteome, tissue phenomics and morphometry is perfectly matched to add to the hierarchical data within a systems model.

Essentially, a modern integrative pathology would adopt the principles of 4P medicine in a systems pathology approach. 4P medicine consists of Prediction, Personalisation, Prevention and Patient participation(207). Although many definitions of systems medicine exist CASyM (https://www.casym.eu/what-is-systems-medicine/), a European consortium tasked to develop an implementation strategy for clinical systems medicine, defined it as the following:

> Systems Medicine is the implementation of Systems Biology approaches in medical concepts, research and practice. This involves iterative and reciprocal feedback between clinical investigations and practice with computational, statistical and mathematical multiscale analysis and modelling of pathogenetic mechanisms, disease progression and remission, disease spread and cure, treatment responses and adverse events as well as disease prevention both at the epidemiological and individual patient level. As an outcome Systems Medicine aims at a measureable improvement of patient health through systems-based approaches and practice.

The principle of systems pathology is to predict a dynamic pathological response from static data sets. Systems pathology is complex with the implementation of multiple differential equations into a multiscsale dynamic model to predict a drug effect on a patient or inform how that patient will respond over time(206, 208, 209). Systems pathology, under this definition, was utilised to confirm the role of PTEN in trastuzumab drug resistance(210). Systems pathology can also be implemented to track tumour evolution post chemotherapy through intra-tumour heterogeneity and spatial

distribution of phenotype and genotype at the cellular level(211). In CRC a systems pathology approach was employed to identify a disease recurrence signature in early stage patients from a multi-omics data set where parameters associated with immune response were found to be the most significant predictors(212).

The ultimate goal of integrative and systems pathology is to make use of hierarchical data captured across multiple modalities from an imperfect and static tissue sample, in order to better understand both disease progression and a patient's personalised response to treatment.

1.4 Colorectal cancer

1.4.1 Epidemiology

Colorectal cancer (CRC) is the third most common cancer in the world(213) and in Scotland, with 3849 new cases being diagnosed and 1578 deaths recorded in 2013 in Scotland alone(214). Incidence and mortality rates are lower amongst women than men. Although incidence rate has decreased only slightly in the last decade, the change in mortality has decreased significantly by 20.7% in males alone, between 2000 and 2010, with 55% of all patients surviving after 5 years post diagnosis (215). Reasons for the decrease in mortality include early detection of disease(216), targeted therapy borne through omics research (217), novel prognostic factors coupled with more accurate pathological and clinical staging of disease (104) and advances in surgical technique. These factors culminate in more effective treatment of patients at an early stage and at a personalised level. Survival rates in early stage cancer, where the tumour is localised, are good with ~90% of patients experiencing 5 year disease free survival. Upon spread to localised lymph nodes survival decreases to 50-70% and if distant metastasis has occurred survival is only 12%(216, 218).

CRC may develop through either hereditary or sporadic origins. The two most common types of hereditary CRC are Familial Adenomatous Polyposis (FAP) and Hereditary Non-Polyposis Colorectal Cancer (HNPCC) which is also referred to as Lynch syndrome; the hereditary cancers account for 1% and 2-3% of all CRC respectively. It is thought that up to 35% of all CRCs have associated hereditary factors

although these are poorly understood(219). The majority of cancers are termed as sporadic CRC cancer and result in mutation or epigenetic aberration. Lifestyle affects CRC and a higher incidence is associated with a sedentary lifestyle, diet, alcohol, obesity, diabetes and smoking(219).

1.4.2 Adenoma to carcinoma sequence

Sporadic colorectal tumours are generally thought to evolve from an adenomatous polyp through a multi-step process where mutations or epigenetic silencing in critical genes accumulate toward malignant neoplasia. This somatic evolutionary process was termed the adenoma to carcinoma sequence by Fearon and Vogelstein in 1990(220) who describe a set of genetic aberrations which are needed for a precursor lesion to mature toward malignancy (Figure 4). These are thought to generally occur in a specific order; however it is their temporal accumulation which is essential for metastasis. The most simplistic model proposed begins with a mutation in the APC gene, involves constitutive activation of KRAS (a signal transducer in the EGFR pathway), aberrant TGFβ signaling through loss of 18q and finally TP53 mutation.

Figure 4. Fearon and Vogelstein's adenoma carcinoma sequence, expanded to illustrate current knowledge of chromosomal (CIN) and microsatellite instability (MSI).

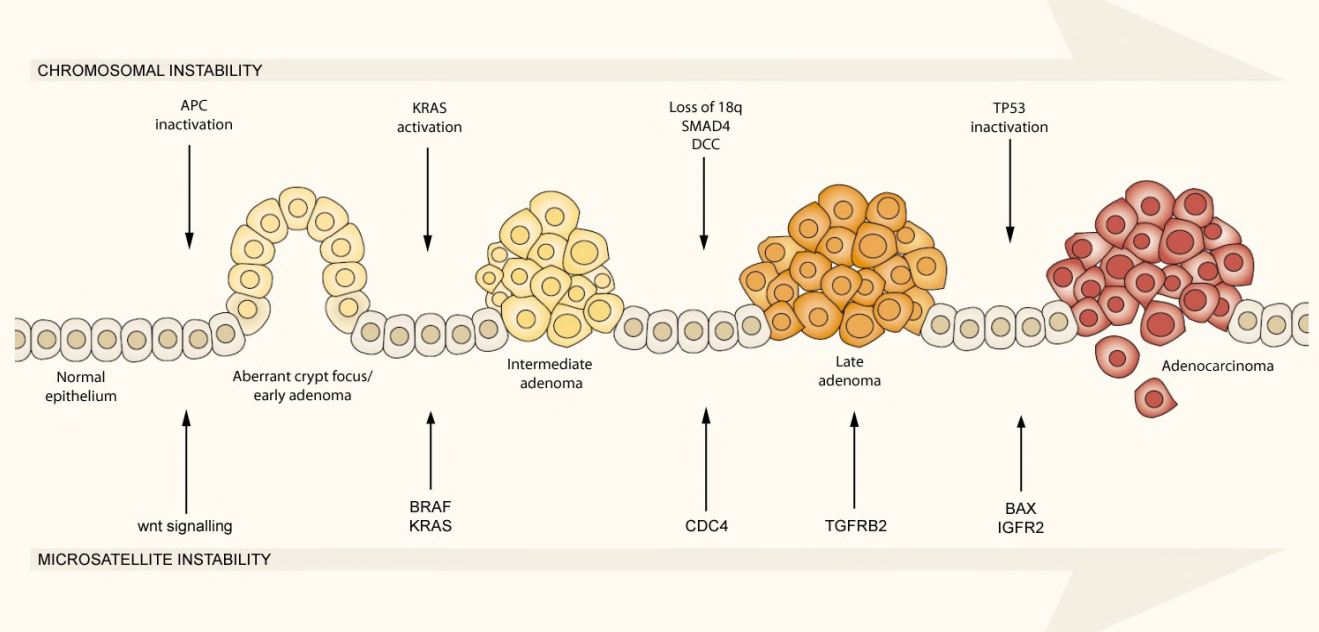

The earliest detectable abnormality is the aberrant crypt focus (ACF), characterised by hyperproliferation and resistance to apoptosis. In the CIN pathway, these are seen to derive following bi-allelic inactivation of the *APC* tumour-suppressor gene (a pivotal regulator of the wnt/β-catenin proliferation pathway), which initiates chromosomal instability. Constitutive activation of the EGFR-signal transducer *KRAS* (more often than *BRAF*) accompanies adenoma formation. Further progression is associated with altered TGFβ signalling, most frequently due to or *SMAD2/4* inactivation through loss of heterozygosity (LOH) at 18q, and final malignant transformation with inactivation of *TP53*, a critical cell cycle caretaker.

The MSI pathway by contrast originates from defective DNA mismatch repair. The resulting genomic instability affects several critical genes with effects analagous to those of the classical pathway; interruption of wnt signalling, *BRAF* (more than *KRAS*), *CDC4*, *TGFβRII*, *BAX* and *IGF2R* have all been described, bringing about adenocarcinoma by a *TP53*-independent mechanism.

Figure compiled by Richard Matthews and reproduced with full permission; adapted from Knudson (2001); additional data from Walther *et al* (2009).

1.4.3 Colorectal cancer subtypes

CRC is a very heterogeneous disease as well as consisting of multiple molecular and histopathological subtypes. These subtypes can correlate to prognosis and prediction of response to therapy although few are taken into account within clinical diagnosis.

1.4.3.1 Molecular subtypes

Apart from familial and hereditary CRC subtypes there are multiple pathways to malignancy within sporadic disease. Sporadic disease stems from genetic instability which can take multiple forms(68). Although Fearnon and Vogelstein's model is still sound, it is too simplistic to explain all of CRC and in fact plots the somatic evolution of CRC within the predominant genetic instable CRC subtype of the chromosomal instability (CIN) pathway. CRC can also occur through other forms of genetic instability namely: microsatellite instability (MSI) and the CpG-island methylator phenotype (CIMP)(53).

1.4.3.1.1 Chromosomal instability

The CIN pathway is found to be responsible for between 70 and 85% of all CRC(55, 219). The presence of CIN usually confers a worse prognosis than other subtypes and has a higher probability of distant metastasis(53, 55). CIN, as mentioned previously, has the molecular hallmarks of loss of the tumour suppressor genes APC, SMAD4, DCC and TP53 and activation of the oncogene KRAS. Tumours with CIN phenotype also tend to be highly differentiated and rarely mucinous with little lymphocytic infiltration and located in the distal colon (221).

1.4.3.1.2 Microsatellite instability

The MSI pathway is characterised by multiple mutations at microsatellites (short tandem repeats in the DNA) and is correlated to a loss of DNA mismatch repair (MMR) enzymes through mutation of their genes or hypermethylation of their promoters(219, 222). The most common MMR genes lost in the MSI pathway are MLH1, MSH2 and MSH6 (223). MSI CRCs make up approximately 15% of CRC, arise in the proximal colon, are typically mucinous with moderate to poor differentiation and have a high immune infiltrate(222, 224). These cancers also have a

better prognosis than CIN as the patient rarely experiences distant metastasis(53, 219). MSI high patients are typical of the hereditary Lynch syndrome but can also be found in sporadic cancer, in which they tend to have a mutation in BRAF(225).

1.4.3.1.3 CpG Island Methylator Phenotype

CIMP positive pathway overlaps molecularly with the MSI one. The CIMP pathway induces epigenetic silencing through hypermethylation of promoters of MMR genes in particular MLH1, MSH2 and MGMT(226). The hypermethylation of CpG promoter sites of tumour suppressor genes also occurs and CIMP is associated with $BRAF^{V600E}$ mutations (227). CIMP is present in 20-30% of all tumours and is associated with poor differentiation, mucinous CRC, high immune infiltrate, located in the proximal colon and poor prognosis(55, 228), although it has also been shown to confer better prognosis than CIMP negative tumours(229).

The three molecular pathways involved in CRC are not mutually exclusive and CRC tumours may be classified at the molecular level by a combination made up of the three definitions(68). These molecular subtypes have been shown to confer prognostic and predictive information for the personalised clinical treatment of a patient's tumour.

1.4.3.2 Histolopathological subtypes

Although 90% of CRC tumours are adenocarcinomas there are multiple histolopathological and morphological subtypes which may also confer information on the prognosis of the patient. Prognosis is, however, not correlated to histopathological subtype in clinical practice(230). These histopathological subtypes may also be correlated to a certain molecular profile. Aside from classical adenocarcinoma the most prevalent of these subtypes is mucinous carcinoma; which makes up around 10% of CRC adenocarcinomas. Mucinous carcinoma is diagnosed by the presence of secretory mucin in at least 50% of the tumour and is loosely associated with a poor prognosis(231), although it has not been shown to be independently associated with disease specific death(232). Mucinous carcinomas are associated with MSI and CIMP however a more aggressive subtype is associated with microsatellite stability (MSS) CRC(103, 233). Signet cell carcinomas are so called as they have at least 50% of the cells in the tumour where intra-cellular mucin pushes the

nucleus to one side; these CRCs make up around 2-4% of the adenocarcinomas(230). Signet cell carcinomas have a more established link to poor prognosis and feature poor differentiation(234). Other more rare CRC histological subtypes include medullary carcinoma, squamous cell carcinoma and small cell carcinoma(235).

Other heterogenous histopathological features which have correlation to prognosis with CRC adenocarcinomas are: Grade (Differentiation), perineural invasion, vasculature invasion, vasculature density, immune cell infiltrate and the pattern of the invasive margin(102, 236, 237).

1.4.4 Tumour staging of CRC

Although multiple subtypes of CRC exist and while some are correlated with prognosis, routine clinical pathological prognosis and recommendation for adjuvant therapy is still mainly determined by stage and grade of the tumour. Tumours are graded as 'well differentiated' with an epithelial and gland forming phenotype which suggest a more non-invasive tumour and 'poorly differentiated' where greater than 50% of the tumour is gland forming but has non-epithelial, and a more mesenchymal, cell phenotype and can be highly proliferative and invasive(230, 238). However, due to the assessment of grade being very subjective and thus reports high observer variability(233) the decision to administer adjuvant therapy is less focused on tumour grade and more on tumour stage.

1.4.4.1 Tumour Node Metastasis

The Tumour Node Metastasis (TNM) system is universally implemented for the staging of CRC patients and directly impacts on prognosis and adjuvant therapy decision making(239). TNM staging is summarised in Appendix B of this thesis (AJCC Colon and rectum staging, 7th edition). TNM staging for CRC is continuously revised and updated by the International Union against Cancer (UICC) who have published the 7th edition(240), however within the UK, pathologists still report from a standardised pro forma which includes the 5th edition of TNM(102, 241). This is due to a lack of evidence base to support the alterations in the newer editions and no significant improvement on prognosis(239, 241).

The TNM staging is based on gross observation and analysis of histopathological tissue sections under the microscope and revolves around the depth of local invasion (T), presence of cancer within the lymph nodes (N) and if the cancer has metastasised (M). The basics of the TNM 5th edition staging groups are detailed in Table 1.

Stages	Cancer present in inner lining of rectum	Begun growing into muscle wall	Broken through outer layer of muscle	Through outer layer and into nearby structures	Cancer detected in 1-3 lymph nodes	Cancer detected in >4 lymph nodes	Distant metastasis detected
0	✓	x	x	x	x	x	x
1	✓	✓	x	x	x	x	x
2A	✓	✓	✓	x	x	x	x
2B	✓	✓	✓	✓	x	x	x
3A	✓	✓	x	x	✓	x	x
3B	✓	✓	✓	✓ x	✓	x	x
3C	✓	✓	✓ x	✓ x	✓	✓	x
4	✓	✓	✓ x	✓ x	✓ x	✓ x	✓

✓ Cancer is present x Cancer is not present
✓ x Cancer may or may not be present

Table 1. Summary of TNM staging criteria.

TNM staging is excellent at returning prognostic information on a population of patients; however, it is less specialised at predicting prognosis at the personalised level(219). A patient's prognosis is worse the higher the stage they are classified within, however the TNM system does not differentiate between good and poor outcome of patients within the same stage(237). There are defined adjuvant treatment guidelines associated with the various stages of CRC(242). Stage 0 and I cancers will not routinely receive adjuvant chemotherapy and surgical resection is considered curative. Adjuvant therapy is recommended for Stage III and IV patients however there remains ambiguity about whether to treat all, a subset or no stage II patients with adjuvant chemotherapy(243, 244).

1.4.4.1.1 Stage II sub-stratification

Although the majority of stage II patients will receive no adjuvant therapy an average of ~30% will experience disease recurrence and poor outcome(243, 245, 246). The QUASAR clinical trial reported only a 3.6% increase in absolute survival in a stage II patient population which were treated with adjuvant chemotherapy(247). Due to quality of life factors, including increased morbidity and mortality associated with treatment related toxicity and cost-effectiveness, it is recommended that in general stage II patients do not receive chemotherapy(243, 246). Accurate identification and stratification of high-risk stage II patients, some of whom have comparable or worse outcome than stage III patients(248), who could benefit from adjuvant therapy is therefore imperative to increase disease free survival rates.

Lymph node involvement is a key prognostic indicator which correlates with poor outcome and distant disease. Lymph node involvement upgrades a patient from a stage II classification to a stage III one which in turn triggers the decision to administer adjuvant therapy(249). A possible reason for the poor outcome of a subgroup of stage II patients could be due to their understaging(250). Although patients in stage I and II CRC have been classified as pN0 occult lymphatic and nodal involvement may be present, suggesting the cancer has taken on invasive and metastatic capabilities. Occult nodal involvement, whether it is isolated tumour cells or micrometastasis, is also significantly associated with poor prognosis(251, 252). It is essential that at least 12 lymph nodes are harvested and examined for cancer cell involvement(238, 241) while number of nodes examined is a prognostic marker in itself(253).

There are additional histopathological factors which have been correlated with poor prognosis and lymph node metastasis and are listed within the core data sets for the reporting of CRC as dictated by the Royal College of Pathologists (RCPath)(102) (Appendix A). Although some are disregarded in clinical decision making for the management of stage II CRC patients some features, if present, may invoke the decision to treat the patient with thymidine synthase inhibitors in combination with oxaliplatin. These “high-risk” factors include pT4 local spread (where the tumour has directly invaded neighbouring organs or structures (pT4a) and/or perforates the visceral peritoneum (pT4b)), extramural lymphovascular invasion and poor

differentiation(238, 244, 254). However, there are no clinical trials to date which have examined the advantage of adjuvant therapy on stage II patients with additional high risk factors.

Furthermore there exist promising histopathological features listed in the literature which have been significantly correlated with poor prognosis and lymph node metastasis but which are only listed in the non-core data set and rarely feature in final clinical reports(102) (Appendix A). There is growing evidence that immune cell infiltrate(50, 255) and perineural invasion(256, 257) are strongly correlated with poor patient outcome while lymphatic vessel invasion and the invasive growth pattern, including tumour budding, are two of the most promising histopathological features which have been significantly associated with lymph node metastasis and disease specific survival(20, 90, 236, 252, 258-260).

1.4.4.1.1.1 LVI

Cancer cells must invade the lymphatic vasculature locally prior to metastasising to the lymph nodes(4). Lymph node metastasis is highly correlated to poor prognosis and is an essential feature of stage III CRC(238, 241, 261). The robust quantification of lymphatic vessel invasion (LVI) within the primary tumour could therefore be an early and sensitive feature to predict both lymph node metastasis and disease specific survival; in fact several studies have proven this theory and shown a significant correlation(252, 260, 262-264). Although there is mounting evidence of the prognostic value of LVI it is still listed as a non-core data item and the evidence is not thought to be sufficient to be included as a core data item(102). A reason for this could be the difficulty in the accurate observation of lymphatic vessels in H&E stained CRC tissue sections, which in turn is a reason for variable results(265, 266). The use of immunohistochemical labelling with antibodies such as D2-40, which specifically bind to the endothelial cells of the lymphatic vasculature, may aid in the reporting of LVI and decrease observer variability(252, 265).

1.4.4.1.1.2 Invasive growth pattern

The pattern of the cancer's invasive front has been significantly correlated to lymph node metastasis and disease specific death(236, 267, 268). Poor prognostic factors associated with the morhphology and histology of the cancer's invasive edge include

an infiltrating invasive pattern, tumour budding and poorly differentiated clusters(20, 259, 267, 269). Tumour budding is commonly defined as clusters of tumour cells within the stroma at the leading edge of cancer invasion and which are up to 5 cells in size(270). Poorly differentiated clusters are similarly located within the cancer microenvironment but are larger than 5 cells in size but are not gland forming(269, 271). Although there is a strong body of evidence for the prognostic significance of these features, only tumour budding is listed within the RCPath guidelines and then only in the non-core items section(102). This is due to non-standardised quantification methodology and variability in reporting. Variability in observer rates of tumour budding is in part due to inherent patient heterogeneity as well as the feature's obscurity when reporting on H&E stained tissue sections(272); although this may be overcome in part by the use of cytokeratin-based immunohistochemistry(92, 265). Reproducible and reliable studies with large patient cohorts which take into account standardised prognostic factors may allow for tumour budding to be included in the core date set of the UK guidelines.

1.4.4.1.1.3 The role of image analysis in stage II patient stratification

The standardisation and robust quantification of both lymphatic vessel invasion and tumour budding could result in both features being reported routinely within clinical practice. Automated computer-based quantification of these histopathological features would not only allow the standardisation of reporting criteria but also negate observer variability. The proof of a robust quantification method, which reports consistently high significance associated with prognosis in stage II patients, could allow for these features to be included in clinical decision making.

It is important to not only standardise the reporting of promising histopathological features, or identify novel ones through image analysis, but to assess which features are most significant. Meat-analysis reviews attempt to identify the most significant parameters which predict poor outcome(258), however, this is optimally carried out when comparing quantification methodology on the same tissue section. As TNM staging is the internationally recommended system to make a prognosis on CRC(239, 241) it would be prudent to evaluate how novel image based significant histopathological features can augment the classical system instead of replace it. An

integrative pathological signature could prove to be more significant and robust at predicting poor outcome in stage II CRC patients than any one individual method.

1.5 Hypotheses

Image analysis can be utilised to quantify set histopathological features in order to stratify stage II CRC patients into low and high risk of disease specific death.

Image analysis may be employed to capture unbiased multi-parametric signatures from the invasive front of CRC in order to identify novel histopathological features to stratify stage II CRC patients into low and high risk of disease specific death.

1.6 Aims and objectives

1.6.1 Aims

1. To develop an image analysis algorithm to allow standardised quantification of set histopathological features from the invasive front of CRC.
2. To develop an image analysis based pipeline to identify significant parameters from the unbiased multi-parametric data capture of automatically segmented objects within a tissue sample.
3. To integrate image based histopathological features with parameters from the clinical pathology report in order to asses if patient prognosis may be improved.

1.6.2 Objectives

1. Create image analysis algorithms for histopathological feature segmentation and quantification. Employ the image analysis algorithm to quantify tumour budding, vasculature invasion and density across a training and validation set of CRC patients in order to stratify stage II patients into high and low risk of disease
2. Employ an image analysis algorithm to segment and extract multi-parametric data from each object within an immunofluorescence digital image. Employ decision tree models to identify the parameter within the imaging data which are most significant at prediction of disease specific death. Apply the novel parameter to a validation set of stage II CRC patients
3. Identify significant parameters from the clinical pathology report associated to the patient cohorts. Assess statistical methodology to compute the integration of optimal clinical and image-based parameters to be included into novel prognostic signature.

Chapter 2: Materials and Methods

2.1 Patients and specimens

2.1.1 Colorectal cancer training cohort

The training cohort (n = 118). The training cohort contained all the patient tissue and follow up data made available to this study and was taken from part of a larger cohort which was prospectively collected and compiled as previously described (273). CRC patients in the training cohort were under the age of 55 diagnosed between February 1996 and July 2003. Patient follow up comprised date of death, CRC specific death and disease specific survival (months). All patients were initially interviewed soon after diagnosis and gave written consent for their tissue to be used for research purposes. Half the patients were male and half were female. Nineteen percent of whom died of disease.

2.1.2 Colorectal cancer validation cohort

Validation cohort (n=134): The validation cohort was comprised of all sequential cases of stage II CRC treated in NHS Lothian hospitals over 2 concurrent years (years 2002 and 2003), resulting in a cohort of 147 patients. Clinical follow up was up to 11.5 years. Due to insufficient available material 13 patients were excluded leaving a remaining 134 patients within the validation set; 20 of whom died of disease during follow up.

Corresponding clinical pathology data sets for each patient were retrieved from the original pathology report through NHS Lothian's APEX laboratory information system (Table 8). Patient follow up was sourced from the Information Services Division (ISD) which is within NHS Scotland. Patient follow up comprised date of death, CRC specific death and disease specific survival (months). Census was taken on the 31st of March 2014. The resultant validation cohort comprised 56 (42%) patients who survived follow up, 58 (43%) patients who died of other causes and 20 (15%) who died of CRC disease during follow up.

2.1.3 Tissue Microarray (TMA)

H&E stained whole tissue sections for each patient to be included in a TMA were sourced from their archives. Histopathological microscopic evaluation was carried out by a consultant pathologist, alongside either a trained technician or myself. During histopathological examination, regions of interest (ROI) within the whole tissue sections were marked. Tissue cores were extracted from corresponding areas within the paraffin embedded tissue blocks and TMAs were subsequently constructed by a qualified technician (Y. Zhou or In hwa Um) as described in detail by Kononen et al. (274). 3µm thick sections were cut from the completed TMA block and mounted on glass microscope slides for histochemistry or immunohistochemistry analysis.

2.1.3.1 Optimising TMA

Residual diagnostic CRC material was requested for 10 patients from the NHS Lothian NRS BioResource. A tumour rich ROI was selected from each tissue section and a 0.6mm core extracted. This TMA was utilised for optimising histochemical stains and antibodies for immunohistochemistry.

2.1.3.2 Training cohort TMA

The training cohort TMA comprised of cores from all 118 patients within the training cohort. The ROIs in this TMA were from tumour rich areas at the invasive front from where a 0.6mm core was extracted. This TMA was utilised to evaluate if TMAs were a suitable material to report prognostic significance from the quantification of histopathological features.

2.1.3.3 Tumour Bud TMA

50 patients from within the validation cohort were selected who had high tumour budding. Histopathological examination of the corresponding H&E stained tissue sections confirmed the budding status of the sections. High budding ROIs from the invasive front and well differentiated tumour gland ROIs from the tumour centre were marked on the tissue section from where a 1mm core was extracted. Two cores from each ROI for each patient were included in the TMA.

2.1.4 Whole tissue sections

3µm thick whole tissue sections were cut from paraffin embedded tumour blocks and mounted on glass slides for histochemistry or immunohistochemistry based analysis.

2.1.4.1 Control whole tissue sections

Tissue blocks containing lymph nodes associated with patients in the training cohort were utilised as positive controls for lymphatic vessel visualisation.

A positive and negative control patient sample was selected from the training cohort. Histopathological analysis of H&E stained tissue sections was undertaken by a consultant pathologist and myself. A tissue section which contained a high level of lymphovascular invasion was termed as the positive control and a tissue section which contained no lymphovascular invasion was termed as the negative control. The positive and negative controls were utilised in assay and image analysis development.

2.1.4.2 Training set whole tissue section

A 50 patient subset was taken from the patient training cohort on which to perform whole tissue section image analysis. This patient number corresponded to all whole tissue blocks which were available for this study. The patients had CRC diagnoses from Stage I through to Stage III. The Stage II patients (n=29) comprised of good prognosis Stage II CRC patients (n=16; survived follow up) and poor prognosis patients (n=13; died of CRC during follow up). Stage I patients (n= 13) and Stage III patients (n=8) were also included to assess if the good or poor prognosis Stage II patients respectively responded similarly.

Patient follow up comprised date of death, CRC specific death and disease specific survival (months). Of the 50 patients selected for whole slide imaging, 40% died specifically of CRC and one patient died of other causes during the follow up period. Census was taken on the 1st of July 2012. Patient data is listed in Table 7.

2.1.4.3 ECCS Whole tissue section

All 134 Stage II patients selected for the validation cohort were analysed by whole tissue section. In this manner the validation cohort was handled as a prospectively

collected retrospective trial and there were no exclusion criteria, making it a clinically relevant cohort.

2.1.5 Ethical approval

The provision of this material and the subsequent research was conducted under the approval held by the NHS Lothian NRS BioResource, which is a REC-approved Research Tissue Bank (REC approval ref: 13/ES/0126). This approval was granted by East of Scotland Research Ethics Service, which is part of the National Research Ethics service and NHS Health Research Authority. This provides the necessary ethical approval for the BioResource, and associated researchers to collect, store and use patient samples and associated clinical data for research. In accordance with the approval held, all samples were anonymised when released by the BioResource to the research group.

2.2 Histochemistry and Immunohistochemistry

2.2.1 Tissue section preparation

Formalin fixed paraffin embedded tissue blocks, containing either full tissue or TMAs were cut in 3µm sections and mounted on positively charged microscope slides prior to incubation at 37°C overnight. The sections were then dewaxed in three 5 minute washes of xylene and rehydrated in decreasing grades of ethanol (100% x2, 80% and 50%) and finally running water for 2 minute washes each. Post staining (apart from immunofluorescence staining) tissue is dehydrated through increasing graded alcohol washes (50% and 80% for 30 seconds and 100% two x 2 minutes), next the slides are washed for three 5 minute washes in xylene before mounting using pyrex and a coverslip.

2.2.2 Haematoxylin and Eosin (H&E) staining

The following staining protocol was applied to all H&E stained sections after a reagent optimisation experiment.

Post tissue preparation slides are incubated in Haematoxylin solution for 5 minutes, washed in water, dipped in 1% acid alcohol for 3 seconds, washed in water, dipped in

Scott's tap water solution for 15 seconds, incubated in Eosin aqueous solution for 5 minutes before a final wash in water. The tissue is next air dried, dehydrated, mounted, as described in section 2.2.1, prior to microscopic analysis.

2.2.3 Elastic Verhoeff-Van Geison (EVG) staining

The following staining protocol was applied to all EVG stained sections after a reagent optimisation experiment.

Post tissue section preparation slides were stained in Verhoeff solution (alcoholic haematoxylin, ferric chloride and Lugol's iodine solution; 20ml, 8ml, 8ml respectively) for 30 minutes, rinsed in water and differentiated in Ferric chloride solution (20ml ferric chloride and 80ml water) for 3 minutes before transfer into 95% alcohol for 1 minute, rinsed in water and counterstained in Van Gieson solution for 1 minute before a final rinse in water. Tissue is dehydrated and mounted as described in section 2.2.1, prior to microscopic analysis.

2.2.4 Immunohistochemistry

Post tissue section preparation heat induced antigen retrieval is performed in a pressure cooker containing either Tris EDTA, pH9 buffer or 0.15mM Sodium Citrate, pH6 buffer. The solution is pre-boiled for 10 minutes in a microwave prior to the addition of tissue slides whereupon the solution is further heated for 5 minutes. Slides are left to cool for 20 minutes in the heated buffer after cold water is added. Slides are next washed in 0.1% PBST (Phosphate saline solution with 0.1%Tween) two times for 5 minutes each. Endogenous hydrogen peroxidase is blocked with incubation of the slides in 3% hydrogen peroxide solution for 10 minutes. Two further 5 minute washes in 0.1% PBST are performed prior to 10 minute incubation in Dako serum-free block (Dako, #X0909) in order to prevent the binding of primary antibody to non-specific antigens. Sections are next incubated in a primary antibody solution diluted in Dako antibody diluent (Dako, #S0809) at either room temperature for 1 hour or overnight at 4ºC. If dual staining is performed a further three 5 minute PBST wash steps are carried out between primary antibody incubations and once again prior to visualisation. A list of all primary antibodies utilised and their conditions is located in Table A.

Antibody	Supplier	Species	Dilution	QC
PanCK	Dako, Z0622	Rabbit	1:150	Specific
PanCK	Dako, M3515	Mouse	1:300	Specific
CD31	Dako, M0823	mouse	1:1000	Specific
D2-40	Dako, M3619	Mouse	1:2000	Specific
Beta catenin	BD Biociences, 610153	Mouse	1:500	Specific
E-Cadherin	BD Biociences, 610181	Mouse	1:1000	Specific
CK7	Dako, M7018	Mouse	1:250	Specific
CK20	Sigma, SAB4502249	Rabbit	1:250	Specific
CK5/6/8/18	Leica, CK5/6/8/18	Mouse	1:100	Specific
CD44	CST, 3570S	Mouse	1:100	Specific
EpCAM	CST, 2929S	Mouse	1:200	Specific
Vimentin	Sigma, V6630	Mouse	1:400	Specific
Snail	Abcam, ab180714	Rabbit	1:800	Specific
MMP9	Dako, A0150	Rabbit	1:250	Specific
CD133	Mitlenyi biotech, 130090422	Mouse	1:500	Specific
Ki67	Dako, M7240	Mouse	1:50	Specific
EGFR	Invitrogen, 28005	Mouse	1:50	No stain
Src	CST, 2110S	Mouse	various	No Stain
Lgr5	Abgent, AP2745d	Rabbit	various	No stain
MMP7	CST, 38015	Rabbit	various	No stain
UPAR	Dako, M7294	Mouse	1:25	No stain
TGFB1	R&D Systems, MAB240	Mouse	1:25	No stain
PARD3	Sigma, HPA030443	Rabbit	Various	Non specific
Scrib	Thermo, PA5-2862	Rabbit	various	Non specific
MET	CST, 4560S	Rabbit	various	No stain
MEK1/2	CST, 4694S	Mouse	1:50	No stain
YAP	CST, 4912	Rabbit	1:200	No stain
p-YAP	Abcam, ab76252	Rabbit	1:100	No stain
Nanog	CST, 4903	Rabbit	1:400	No stain
Oct4	CST, 2840	Rabbit	1:100	No stain
Sox2	CST, 3579	Rabbit	1:100	No stain

Table A. Primary antibodies utilised throughout the study and their experimental conditions.

2.2.4.1 Chromogenic visualisation

Single antibody visualisation was carried out by incubating slides in DAKO Envision antibody labelled with horse radish peroxidase (HRP) (Dako, anti-mouse: #K4001 or anti-rabbit: #K4003) for 30 minutes. Slides were next washed three times for 5 minutes in PBST whereupon the tissue is incubated in 3, 3 -diaminobenzidine (DAB) visualisation solution.

The initial step in dual antibody staining was as above; however, with the addition of goat anti-mouse bound Alkaline Phosphatase (Sigma, #A3562, 1:50) to the anti-rabbit HRP. Visualisation was performed using the Vector Black Alkaline Phosphatase Substrate Kit (Vector laboratories, #SK-5200) and Vector NovaRed Peroxidase Substrate Kit (Vector laboratories, #SK-4800) as per manufacturer's protocol.

The slides were washed in water for 2 minutes after visualisation steps and incubated in Haematoxylin for 1 minute prior to tissue dehydration and mounting, as described in section 2.2.1, before microscopic visualisation.

2.2.4.2 Immunofluorescence visualisation

Dual antibody visualisation was performed by incubating slides in a secondary antibody solution of 1:25 dilution of goat anti-rabbit or goat anti-mouse Alexa555 Ab (Invitrogen, anti-rabbit; #A21428, anti-mouse; #A21422) in Dako Envision goat-mouse HRP antibody for 1.5 hours in the dark at room temperature. Slides were washed for three x 5 minutes in PBST. Cy5 Tyramide was diluted 1:50 in target signal amplification diluent (Perkin Elmer, #SAT705A001EA, 1:100) and used to incubate the tissue for 10 minutes at room temperature in the dark. A final wash of PBST was performed prior to tissue dehydration using 80% alcohol for 1 minute and air drying for 2 hours in the dark. Once the tissue was dry slides were mounted by adding Prolong Gold anti-fade reagent containing DAPI (Invitrogen, P36931) to a coverslip which was placed over the tissue. Slides were air-dried to cure overnight in the dark.

2.3 Microscopy

2.3.1 Brightfield

Brightfield microscopic images of tissue sections or TMA cores were captured and digitised on an Olympus DotSlide (Olympus, Southend- on-Sea) microscope or a Leica SCN400 whole slide scanner (Leica Microsystems UK Ltd, Milton Keynes, UK).

2.3.2 Fluorescence

Whole slide and TMA immunofluorescence images were captured and digitised on an Olympus AX-51 epifluorescence microscope (Olympus, Southend-on-Sea, UK) or a Carl Zeiss AxioScan.Z1whole slide scanner (Carl Zeiss, Göttingen, Germany). Both microscopes were fitted with filter blocks for DAPI, Cy3 and Cy5 visualisation. The set exposure times on the Olympus AX-51 epifluorescence microscope were as follows: DAPI (200ms exposure for nuclei), Cy3 (35ms exposure for panCK) and Cy5 (200ms exposure for D2-40). The set exposure times on the AxioScan.Z1whole slide scanner were as follows: DAPI (50ms exposure for nuclei), Cy3 (10ms exposure for panCK) and Cy 5 (50ms exposure for the various biomarkers)

The Olympus AX-51 epifluorescence microscope was linked to HistoRX's AQUAsition image capture software. This allowed an overview scan of the whole slide at 4x objective to be captured. ROIs within the whole slide image were then selected through the AQUAsition software and were captured with a 20x prior to exporting for image analysis as .TIFF files.

2.4 Image Analysis

All image analysis algorithms were developed and executed using Definiens image analysis solutions (Definiens AG, Munich, Germany). The two software packages from Definiens which were used were Definiens Tissue Studio® and Definiens Developer XD. Tissue Studio® utilises pre-installed algorithms to build image analysis solutions for the detection, segmentation and quantification of tissue morphometrics and associated biomarkers. Developer XD, although more user

intensive and complex to programme, allows the creation of bespoke image analysis solutions which results in a higher flexibility of image manipulation. Both software packages are capable of brightfield and fluorescence image analysis. Initial image analysis solutions from Tissue Studio® may be imported into Developer XD for further algorithm development and optimisation.

Images were imported into the Definiens software as 8bit .TIFF files when captured on the Olympus AX-51 epifluorescence microscope coupled to the HistoRX's AQUA image capture software. A customised import algorithm was created in order to perform this action. Images captured by the other three whole slide scanners were imported directly into Definiens in their native file formats; the 10bit Olympus dot-slide (.vsi), the 12bit Leica SCN400 (.scn) and the 16bit Carl Zeiss AxioScan.Z1 (.czi), through Definiens pre-installed image importers.

Multiple iterative image analysis algorithms and solutions were created in Definiens Tissue Studio® brightfield and immunofluorescence software environments to optimise the segmentation of tumour from stroma and tumour gland lumen/necrosis and to quantify set histopathological features. Initial tissue detection and the segmentation of images was consistently performed within Tissue Studio®, however due to constraints within the software package, tissue artefact and tissue heterogeneity the Tissue Studio® segmented images were imported into Developer XD for further processing. An iterative process of algorithm programming within Developer XD allowed for more sophisticated image analysis development. Further details of the image analysis algorithms are provided in the Results chapters and specific settings for each algorithm are detailed in the appendices.

2.5 Installation of a Digital Pathology Pipeline

The digital pathology pipeline consists of components which allow the capture of high resolution digital pathology images from microscope slides, their storage, the remote viewing of stored digital pathology slides and their analysis by computer-based image analysis algorithms (Figure A).

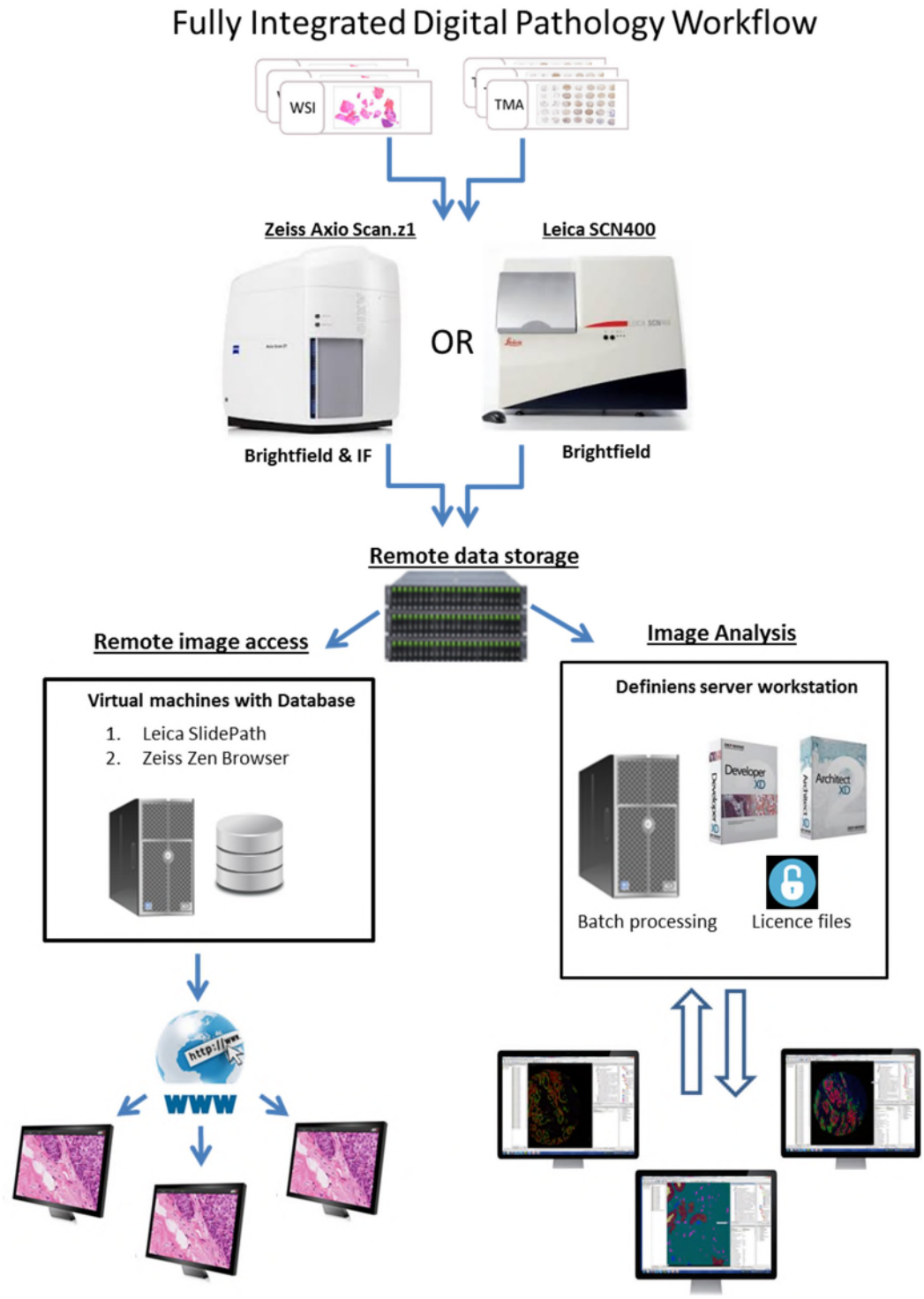

Figure A. Fully integrated digital pathology pipeline. Glass tissue sections were digitised by either the Leica SCN400 or the Zeiss AxioScan.z1 whole slide imagers. Whole slide images (WSI) were saved and backed-up to a remote storage location. Remote viewing software (SlidePath or Zen Browser) can access the remote storage and allow access to WSI through the internet. Definiens image analysis software accessed images within the remote image repository for automated image analysis. Image analysis processing and software licences were stored centrally and accessed remotely by users.

2.5.1 Leica SCN400

A Leica SCN400 brightfield whole slide scanner was installed in the Royal Infirmary of Edinburgh's pathology department laboratories. The scanner has the capability of capturing high resolution brightfield images of whole tissue sections and TMAs at 20x or 40x magnification using a single 20x objective. The scanner can automatically scan 4 slides in each run. This scanner was introduced to the pipeline to digitise small batches of routine clinical and research chromogen stained slides.

2.5.2 Carl Zeiss Axio Scan.Z1

The Carl Zeiss Axio Scan.Z1was also installed in the Royal Infirmary of Edinburgh's pathology department laboratories. The scanner has the capability to digitise either brightfield and fluorescence whole tissue sections or TMAs mounted on microscope slides with 5x, 20x and 40x objectives. The scanner contains 2 separate cameras for brightfield or fluorescence and has two separate illumination sources: an HXP bulb illumination and LED illumination alongside 9 separate fluorescence filter blocks for multiplexing. The scanner can hold a magazine of 100 slides in each run. This scanner was introduced to the pipeline for complex multiplexed immunofluorescence based pathology and for large batches of chromogen stained slides.

2.5.3 Image Storage

Images captured with the whole slide scanners are uploaded to and stored on a remote file storage system within the University of Edinburgh's IT infrastructure (ECDF NAS, University of Edinburgh). The file storage system is NTFS formatted with SAMBA file sharing capabilities. The storage system also has an associated UNC path to make the files accessible for the remote viewing software. The data storage contains a 1TB hard drive and is managed and fully backed up by the University of Edinburgh.

2.5.4 Remote viewing

Two virtual machines with associated MS SQL server databases (Microsoft Corporation, Redmond, USA) were installed within the digital pathology pipeline to facilitate the remote viewing of digital slides. Each machine requires a quad core CPU, 4GB of RAM a 1GB NIC card and 64-bit windows server 2008 to be installed. One

machine hosts Leica's Slidepath remote viewing and file indexing system while the other hosts a similar system from Zeiss called Zen Browser.

Both SlidePath and Zen Browser allow users to store and view their images remotely with no client software needed on the end user's computer or device. Images can be accessed, annotated and shared or saved locally from any compatible device with an internet connection and access to the World Wide Web (www). Both systems are password protected and users only have access to images they are authorised to view.

2.5.5 Image Analysis

The digitized images which are stored on the remote storage file system can be directly imported from this location into Definiens image analysis software. A central workstation computer holds both the Definiens software licences and the engine licensce. The central image analysis workstation has the recommended system requirements of: Windows 7 64-bit operating system installed, an Intel Quad Core CPU, a NVIDIA graphics card, 8GB RAM and a 1TB hard disk. The Definiens software is downloaded onto an end-user's computer and the end-user utilises the remote software license, which sits on the central workstation, in order to activate the software. The images are imported directly into the software in their native format (Leica; .scn files and Carl Zeiss; .czi files) using Definiens pre-installed image importers. The end user configures the image analysis solution locally. Once the image analysis solution is ready to be run across all images within a project workspace the end user sends the workspace for batch processing to the analysis engine located on the remote central workstation server. Once the image analysis is complete the end user can view the results on their local machine. Multiple image analysis workspaces can be queued for analysis on the analysis engine and from multiple users.

2.6 Statistics

Where multiple images were captured across a patient tissue sample the resultant export parameters were either summed or averaged to create a single row of data per sample. Optimal cut-offs, based on disease specific survival, were calculated for each

histopathological parameter reported in the thesis. Parameter values were loaded into X-Tile (University of Yale) (275) software along with patient outcome information and significant cut-offs for each parameter were calculated from Kaplan-Meier analysis. To avoid over-fitting and multiple cut-point selection, corrected *P*-values for the cut-offs were calculated using cross-validation within Monte Carlo simulations (n=1000). Monte Carlo simulations are a problem solving technique used to approximate the probability of certain outcomes by running multiple trial runs, called simulations, using random variables.

Patient survival data and binary parameter data, according to cut-offs, were uploaded into SPSS software (IBM, New York, USA) for univariate and multivariable Cox-regression analysis. Pearson's Correlation between set histopathological features was calculated using the SPSS software and *P*-values for the correlation were adjusted by Bonferoni correction for multiple testing. Principle Component Analysis was also executed within the SPSS software. TMA navigator (http://www.tmanavigator.org/)(276) was used to calculate and plot Kaplan-Meier survival curves and the significance of the separation was calculated via the log-rank (Mantel-Cox) test while the *P*-values are false discovery rate (FDR) corrected using the Benjamini-Hochberg procedure to account for multiple hypothesis testing.

From the 123 parameter phenotypic fingerprint the most significant features which differentiate between good and poor outcome were identified using Random Forest and associated Gini score while a decision tree mathematical model to identify novel histopathological features was constructed using a classification and regression tree approach (CART) (Salford Predictive Miner, Salford Systems, San Diego, USA). Random Forest results were validated by 2/3rds out-of-the bag validation. To avoid over-fitting in the CART model, 10-fold cross-validation was carried out as part of the binary recursive partitioning.

PCA was utilised in this study to reduce the dimensions of the large multi-parametric phenotypic fingerprint and enable its visualisation and clustering of patients in a 2D scatter plot. PCA was therefore output as 2 dimensions. PCA identifies the principal components within the data which differentiate the patient samples ie which

parameters contain the most variance. PCA converts the data into linearly uncorrelated principal components where the 1st component accounts for the most amount of variability and the second the most variance after the 1st. 72% of the variance was captured within the 2 components in this study.

Random forest was utilised to identify the significant parameters within the phenotypic fingerprint. The random forest model created 5000 decision trees to model 2/3rds of the original data. The remaining 1/3rd of the data was used for out of the bag validation of the model. Random forest examined every branch of every tree in deciding the overall model and the importance of each parameter via majority ensemble voting and outputs the parameters which are the most statistically relevant in making the binary decision of risk of disease specific death. Random forest assigns a Gini score to each parameter which directly correlates to the variable importance and the extent to which each variable contributes to optimal separation of the outcome patients (disease specific death during follow up). This model was used to reduce the phenotypic fingerprint to only its significant parameters and to delete redundant ones.

Unlike random forest, CART produces a single decision tree which acts as a flow chart, where each node or branch point is a test on a parameter. CART identifies the optimal combination of parameters and calculates their cut-off from these tests. CART is therefore applicable to a clinical test as it identifies the single optimal combinations of parameters within a multi-parametric data set and informs on a patient's cut-off for that test from their continuous data set of that parameter.

Chapter 3: Quantifying the lymphatic vasculature through image analysis

1.1 Introduction

The lymphatic and blood vasculatures are vital components of the tumour's microenvironment. They are not only responsible for delivering the host's immune reaction to the neoplastic growth but also for providing the oxygen and nutrients needed for the tumour's expansion, while ultimately providing routes of invasion from the primary tumour allowing systemic and metastatic spread of the disease (277).

A wealth of original studies, systematic and meta-analysis reviews have been published on the subject of lymphatic vessel invasion (LVI) (252, 256, 260, 264, 278), blood vessel invasion (BVI) (256, 278-280) and vessel density (281-283). A number of these have concentrated on early stage disease and the ability to utilise histopathological features to predict lymph node metastasis, distant metastasis or to stratify patients at high risk of disease recurrence and poor outcome (47, 252, 262-264, 283, 284). Although LVI and BVI have been shown to be significantly prognostic in the majority of these studies, only extramural lymphovascular invasion (EMLVI), not intra-tumoural, is stated historically as being a parameter to be recorded routinely as part of the core data set compiled by the RCPath (261). In reality the parameter which is predominantly reported is extramural venous invasion, because LVI itself is difficult to recognise confidently in H&E stained CRC tissue sections. The parameter of EMLVI has been replaced, by RCPath in 2014, with venous invasion to acknowledge this fact and due to the possibility that intra-tumoural invasion may also be prognostic(102). The pathologist is encouraged to distinguish between the two classifications of vasculature invasion, although only venous invasion and not lymphatic invasion is recorded within the core data set (102). LVI can be difficult to observe within H&E stained tissue sections. LVI's obscurity is due to the lack of a surrounding rim of muscle and the absence of blood cells in lymphatic vessels, such as is found with blood vessels(285), and confusion of lymphatic vessels with retraction artefact(286, 287). Retraction artefact is a product of the fixation process and the result

is that of retraction of the stromal tissue from a neoplastic gland or nest of tumour cells, leaving white space surrounding the tumour cells, which can be misrepresented as an invaded lymphatic vessel (Figure 5).

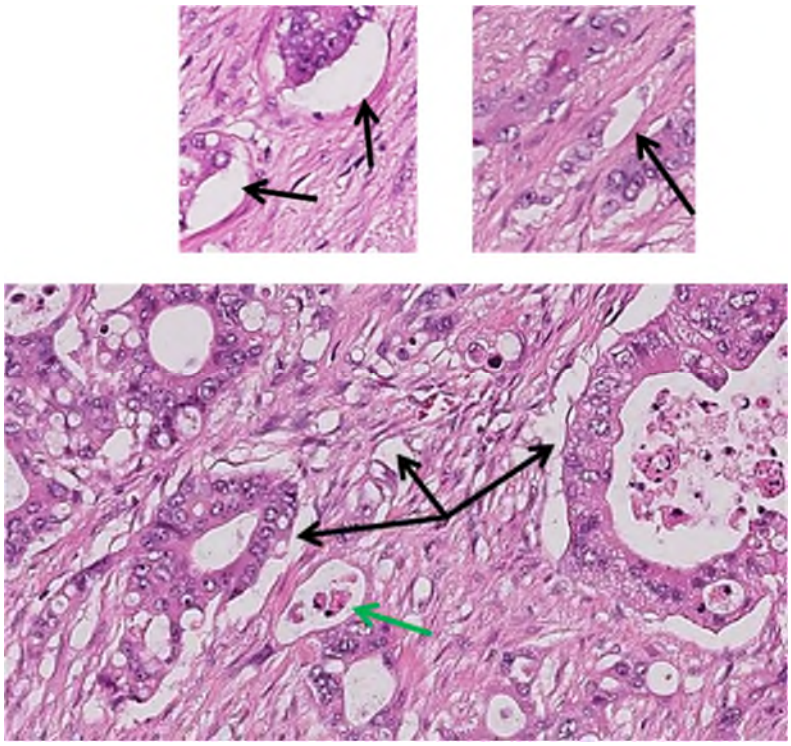

Figure 5. Examples of retraction artefact in H&E stained CRC tissue. Black arrows show retraction artefact around cancer cells or neoplastic glands. Green arrow shows cancer cells within white space which may be a lymphatic vessel or may be retraction artefact. Images captured with a x 20 objective.

The phenomenon of ‘occult LVI’ or unobserved isolated tumour cells is even more pronounced when involving microvessels within an H&E stained tissue section; in this case a single or small number of tumour cells have invaded such a microvessel, which easily goes unreported due to its obscurity.

Although blood vessels are simpler to identify in H&E stained tissue sections both BVI and LVI are routinely under-recognised under observation (266, 279), affecting the variability of reporting within these studies. There are a number of reasons for this: inter and intra-observer variability (92, 93, 278, 283), multiple quantification and sampling methodologies resulting in no agreed or standardised reporting system (20,

272, 288, 289) and the difficulty in observing occult and rare phenomena in routine H&E stained tissue sections (265, 266, 279). Thus the manual, semi-quantitative scoring employed in these studies is subjective, open to variability and is time consuming.

Specific stains are more frequently being employed (136, 252, 260, 265, 279, 283) in order to increase reporting rate and decrease observer variability but there is no consensus yet on what is best. The use of specific histochemical markers, such as Elastin staining, CD31and CD34, have been employed to highlight blood vessels and increase reporting rates of invasion events (279, 286, 290). Roxburgh(279) and Kirsch R et al(291) have both recently and independently shown a 3-fold and a 2-fold increase respectively in events of BVI in CRC when employing Elastin staining compared to H&E staining. Studies also showed a decrease in observer variability when an elastin based stain is employed(291). To overcome the problem of identifying LVI and differentiating blood vessels from lymphatic vessels, studies have employed immunohistochemical staining with a D2-40 antibody which specifically binds to lymphatic vessel endothelial cells (252, 265). The Royal College of Pathologists now recommends the use of D2-40 to verify LVI when it is suspected, although they do not insist on the routine application of the stain(102). Although there are rarely blood cells within the lymphatic vessels, multiple immune cell types may be present. Invading CRC epithelial cells can take on a more mesenchymal or rounded phenotype which may be confused with such immune cell types. These morphological transitions may be another source of LVI reporter variability adding to the reasons it has not provided enough proof to be included in the core data set. Dual staining of epithelium and vessels allows easier recognition and reporting of LVI events (265) within the complex tumour microenvironment which should decrease observer variability.

Whether BVD and LVD are predictors of poor outcome and disease recurrence is somewhat more controversial. Studies published in the literature have shown both significance and non-significance in a correlation of LVD and prognosis(43, 283, 284, 292). Due to this reason vessel density is not mentioned in the UKs institutional guidelines(102). There is even greater scope for observer variability when manually reporting vessel densities in a semi-quantitate manner in H&E stained slides and

vasculature stains are routinely adopted to allow such quantification(43, 284). Vasculature density assessment is, however, not standardised and most researchers employ various magnifications and numbers of vessel “hot-spots” utilised to create a mean vessel density. Observer variability has been shown to be strong in reporting vessel density (283).

Although specific histochemical and immunological stains may increase the observer rate of rare and obscure histopathological events there is still scope for variability and human error. The utilisation of computer aided quantification of digital images brings additional robustness with the ability to standardise the quantification of histopathological features while minimising observer variability(293, 294). Modern and sophisticated image analysis solutions allow the robust quantification of such features across TMAs as well as whole slide images while simultaneously correcting erroneous object segmentation of tissue artefacts such as non-specific staining and autofluorescence. Accurate and standardised reporting of histopathological features, such as vasculature invasion, through image analysis could allow the more robust analysis of their prognostic value, as the same algorithm may be tested on multiple validation cohorts from international institutes.

This chapter lays out the optimisation of specific histochemical stains to visualise the vasculature within the CRC microenvironment and details the development of novel associated computer based algorithms created for the quantification of lymphatic vessel invasion and lymphatic vessel density. Occult LVI, isolated tumour cells or small tumour clusters within microvessels, are especially difficult to observe in H&E stained tissue sections, and therefore remain unquantified in the clinical setting. The hypothesis for this study is that occult LVI is a poor prognostic factor and the quantification of this event could sub-stratify stage II CRC patients. The finalised quantification algorithm is therefore designed to quantify occult LVI, larger invasion events and LVD across a CRC training set and from where optimal prognostic cut-offs are calculated. These cut-offs are then applied to larger and clinically relevant validation set to assess their prognostic relevance. The standardised quantification of the histopathological features, if proven prognostically significant after further large validation studies, is amenable to being applied to clinical practice.

1.2 Optimisation of vasculature histochemical stains

Specific histochemical stains were employed to evaluate the visualisation of the blood and lymphatic vasculature and its quantification in a reproducible manner. These stains were first assessed for specificity, before being optimised, in colorectal tissue sections. Two methodologies were tested for specificity of staining blood vessels and one for the staining of lymphatic vessels.

1.2.1 Elastic Verhoeff-Van Geison (EVG) histochemical stain

Elastic Verhoeff-Van Geison (EVG) stain specifically binds to and stains the elastin fibres present in tissue, such as in the adventitia of veins and associated arteries, a black colour while lymphatic vessels remain unstained. The stain can therefore be used to visualise and differentiate blood vessels from lymphatic vessels and aids in the reporting of venous invasion. Serial sections were cut from the control CRC whole tissue sections and stained with H&E or EVG (at 2 minutes and 3 minutes differentiation with Ferric Chloride) for comparison. The slides were scanned using the Olympus Dot-slide. The EVG methodology successfully stained the elastin within the walls of arteries and larger blood vessels black, although not always encompassing the entire vessel. This was the case when the tissue was differentiated for both 2 and 3 minutes in Ferric Chloride, although the black elastin fibres were more pronounced after only 2 minutes of differentiation (Figure 6 A, B, D & E). EVG allowed blood vessels to be visualised with greater ease than in H&E stained serial sections (Figure 6 C & F). Although EVG was specific for staining larger blood vessels, the majority of microvessels and capillaries remained unstained (Figure 6 G, H & I). As microvessel invasion is more difficult to observe and report than larger arterial invasion in classical H&E stained tissue sections, and as they remained unstained by the EVG, this stain was not taken forward for the final vasculature quantification assay.

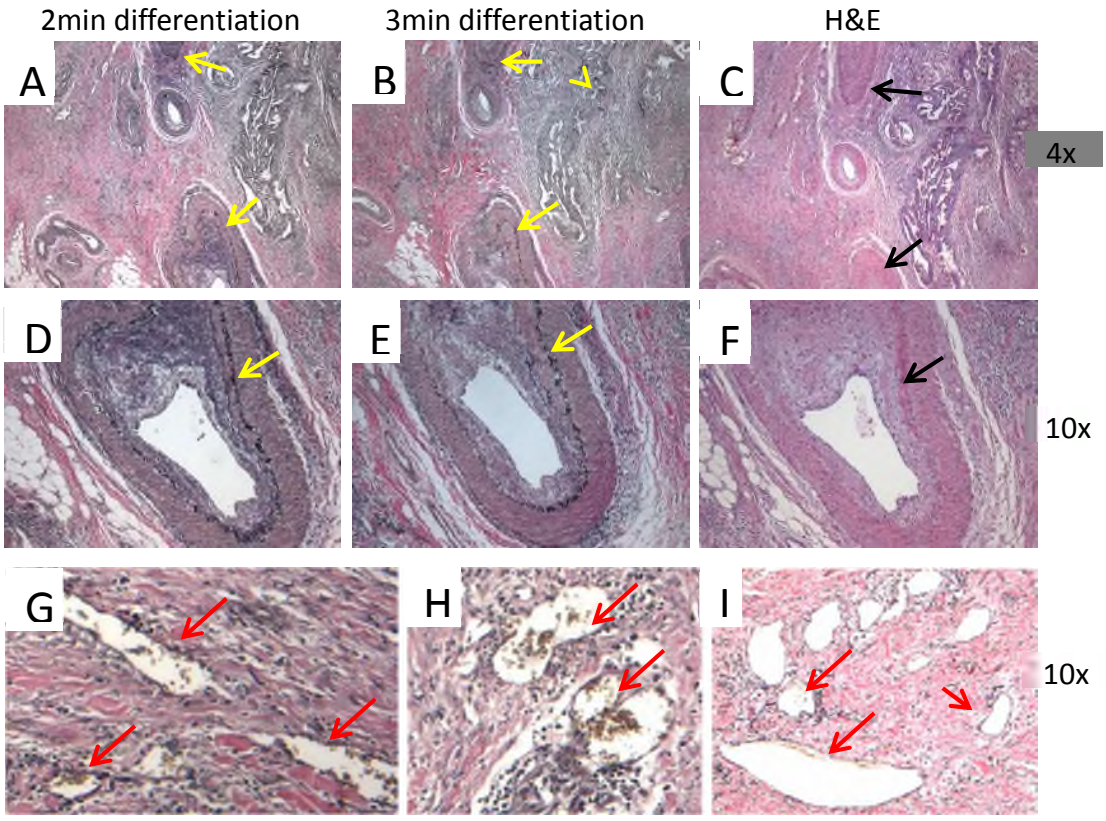

Figure 6. Optimisation of EVG labelling of blood vessels. Yellow arrows show positively labelled blood vessels by EVG. Red arrows show non labelling of blood vessels after EVG. Black arrows show elastin fibres in H&E stained tissue. A) EVG stain with 2 minutes differentiation in Ferric Chloride, B) EVG stain with 3 minutes differentiation in Ferric Chloride and C) H&E stain show serial sections of a CRC tumour block captured with a 4x objective; arrows show elastin fibres surrounding blood vessels. D, E and F show the serial sections captured with a 10x objective which correspond to A, B and C respectively. G, H and I show small blood vessels which remain unstained after EVG labelling. Image captured with a x 10 objective.

1.2.2 CD31 immunohistochemistry

In an attempt to obtain a more complete contrasting stain for blood vessels, IHC, using the antibody CD31 (Platelet endothelial cell adhesion molecule; PECAM-1), was performed. CD31 is an endothelial cell marker which is specific to blood vessels and does not bind to the endothelial cells of the lymphatic channels. Antibody dilution was optimised on the CRC optimising TMA (Figure 7) and visualised through DAB staining while nuclei are counterstained with haematoxylin. The slides were digitised

using the Olympus Dot-slide. At a dilution of 1:1000 the antibody was found to be specific to blood vessels within the CRC tissue samples. More concentrated dilutions of antibody resulted in non-specific binding within the tumour microenvironment.

1.2.3 D2-40 immunohistochemistry

In order to visualise the lymphatic vessels, and differentiate them from retraction artefact and from smaller blood vessels, IHC using the antibody D2-40 (Podoplanin) was tested. D2-40 binds specifically to the antigen Podoplanin which is present in lymphatic vessel endothelial cells but absent from blood vasculature. The dilution of antibody was optimised using the CRC optimising TMA (Figure 7) and visualised through DAB staining, while nuclei were counterstained with haematoxylin. The slides were digitised using the Olympus Dot-slide. A dilution of D2-40 antibody at 1:1000 was found to specifically bind to lymphatic vessels and not stromal components of the tumour microenvironment as was the case at more concentrated dilutions.

1.2.4 Immunohistochemistry specificity and robustness

To further investigate the specificity of the antibodies to solely stain the intended vessel type, either blood or lymphatic, further IHC was performed for each antibody on serial sections of the control whole CRC tissue block and in parallel with H&E stained sections. On the serial sections the same area containing blood and lymphatic vessels was identified and the specificity assessed visually. The slides were digitised using the Olympus Dot-slide. In Figure 8, two areas where D2-40 and CD31 have accurately labelled lymphatic or blood vessels respectively can be seen. In the H&E stained section, the larger blood vessels are easy to identify, however some lymphatic channels are difficult to differentiate from white space and retraction artefact.

This adds strength to the argument that specific stains are needed to observe lymphatic channels and quantify occult lymphatic vessel invasion within smaller vessels. The D2-40 label’s contrast to background is strong and complete lymphatic vessels are stained compared to partial or weak labelling of blood vessels by CD31.

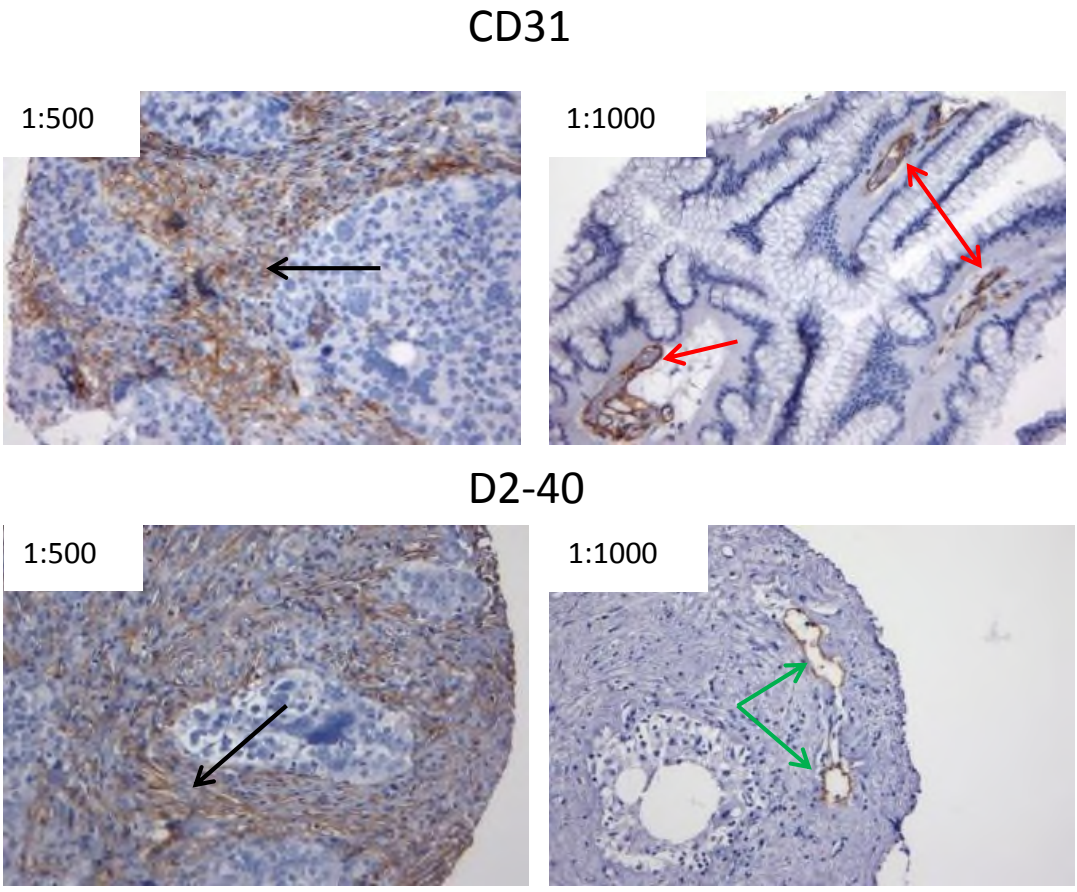

Figure 7. CD31 and D2-40 antibody optimisation. At 1:500 dilution both CD31 and D2-40 antibodies showed non-specific stromal labelling (black arrows). CD31 (blood vessels; red arrows) and D2-40 (lymphatic vessels; green arrows) showed specific labelling at 1:1000 dilution. Image captured with a x 10 objective.

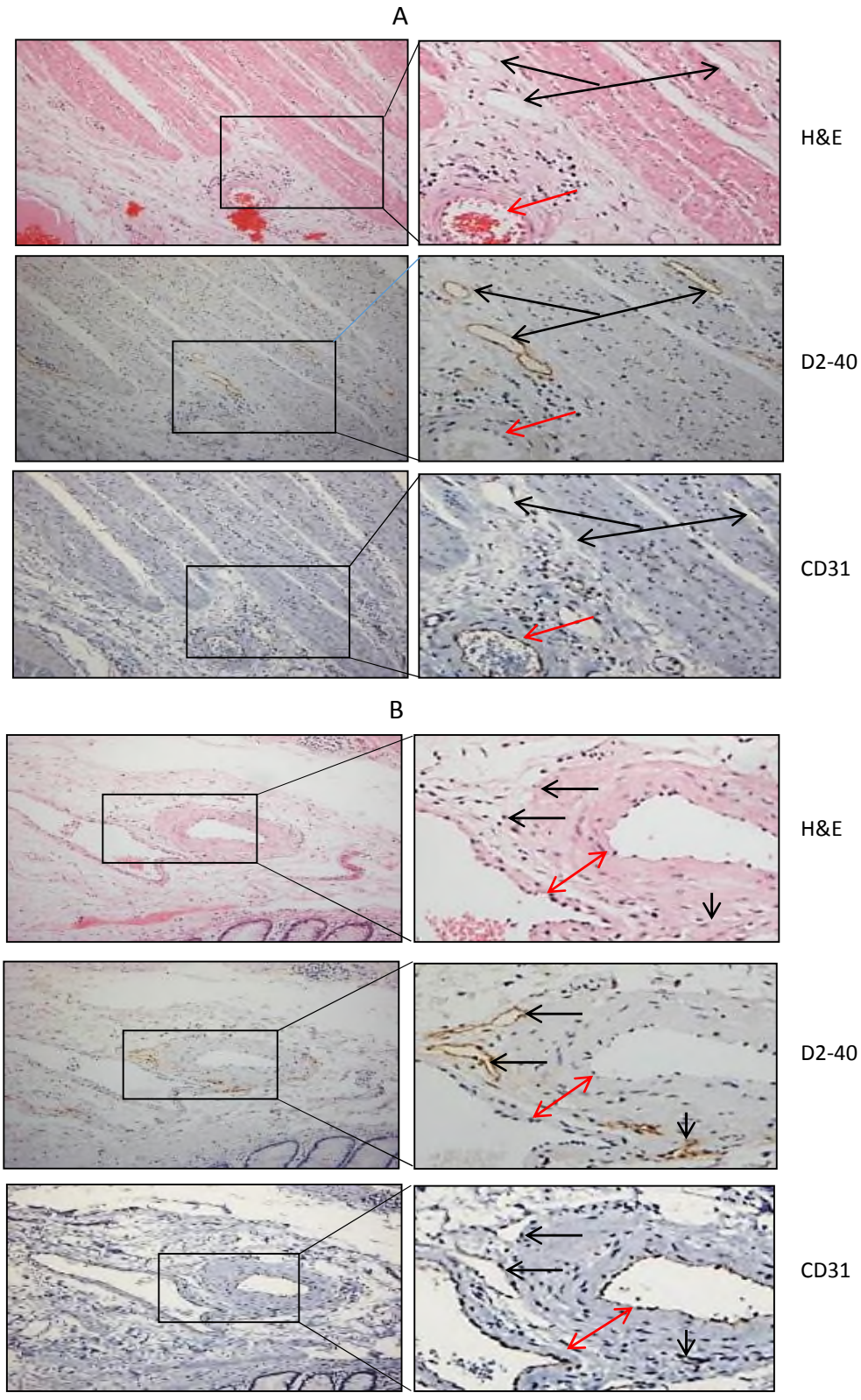

Figure 8. Accuracy of CD31 and D2-40 vasculature labelling. A and B show 2 areas containing blood and lymphatic vessels. Serial sections were cut and labelled with either H&E, D2-40 or CD31. Black arrows indicate lymphatic vessels and red arrows indicate blood vessels. Left panel was captured with a x 5 objective and the right panel was captured with a x 10 objective.

This inconsistency in labelling of blood vessels by the antibody CD31 is further demonstrated in Figure 9. Not all blood vessels are completely labelled by CD31 and weak DAB visualisation may be further masked by the haematoxylin counterstain, whereas some remain completely unlabelled.

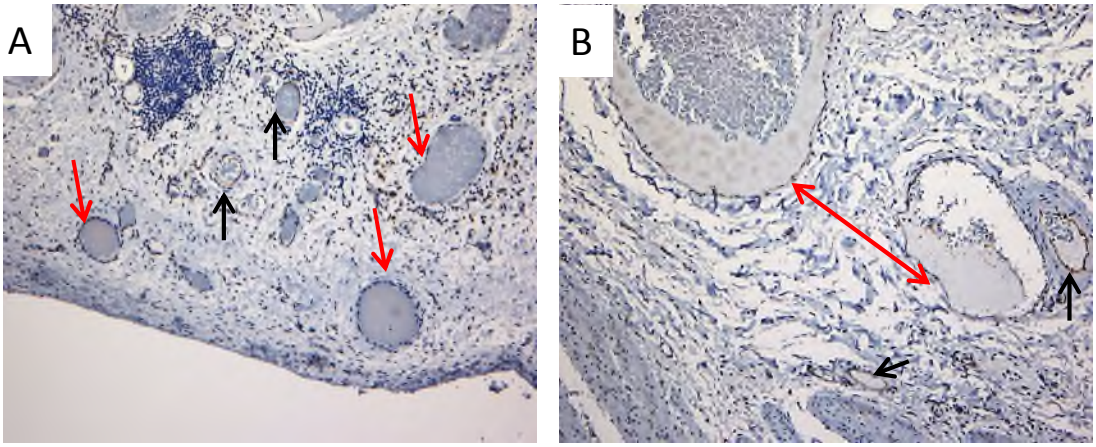

Figure 9. Incomplete labelling of blood vessels by CD31. A and B show two areas of a tissue section labelled with CD31 immunohistochemistry. These areas contain large and small blood vessels. Red arrows show blood vessels which remain unlabelled. Black arrows show blood vessels with partial or weak labelling. Left panel was captured with a x 5 objective and the right panel was captured with a x 10 objective.

For this reason, and due to CD31 also reacting to certain T-Cells, leukocytes and neutrophils, its use was not continued to label blood vessels. In contrast the D2-40 antibody robustly labelled the lymphatic vasculature and therefore the study progressed to computer based analysis of only the lymphatics within the CRC tumour microenvironment and assessed their prognostic significance in CRC. To add further proof of specificity and to act as a positive control for the D2-40 antibody to label lymphatic vessels, IHC with D2-40 was performed on lymph nodes from CRC patients. Lymphatic vessels within the lymph node and surrounding fatty tissue are labelled strongly and completely with D2-40 while lymphocytes and blood vessels remain unstained (Figure 10). Table 2 summarises the labelling protocols and their specificity.

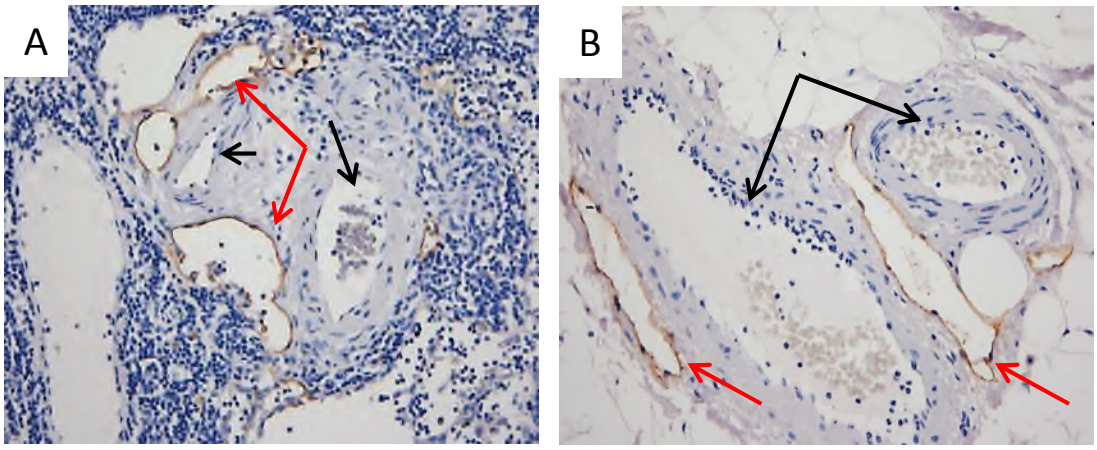

Figure 10. Positive control lymph nodes labelled with D2-40 Immunohistochemistry. Red arrows show lymphatic vessels in the lymph nodes labelled with D2-40. Black arrows demonstrate blood vessels which remain unlabelled by the D2-40 antibody. Images captured with a x 10 objective

Histochemical label	optimisation	vasculature stained	specificity	utilised in final assay
EVG	2 min differentation	venous only	incomplete staining	No
CD31	1:1000 dilution	venous only	incomplete staining	No
D2-40	1:1000 diltuon	lymphatic only	complete staining	Yes

Table 2. Summary of the optimisation of histochemical vasculature labelling.

1.3 Brightfield image analysis

To quantify the D2-40 labelled lymphatic vessels through image analysis the tissue section must first be digitised. Sections were taken from the control CRC blocks and D2-40 based IHC performed with DAB visualisation and haematoxylin counterstain. The tissue sections were digitised on the Leica SCN400 and imported into Definiens Tissue Studio®, using the Definiens pre-installed Leica image import algorithm.

1.3.1 Automated quantification of lymphatic vessels

Post image import the chromogen optimised Vessel Detect algorithm was selected from the list of pre-installed Tissue Studio® algorithms and used to detect lymphatic

vessels within the digitised tissue section. DAB stain thresholds and vessel area metrics were selected to allow the segmentation and quantification of lymphatic vessels **(**Figure 11, Vessel Detection**).** Once segmented the vessels are classified by size and if they contain a lumen (Figure 11, Vessel classification). The cut-offs for small, medium and large vessels were performed manually and under the supervision of a consultant pathologist. Full algorithm settings are listed in Appendix 1.

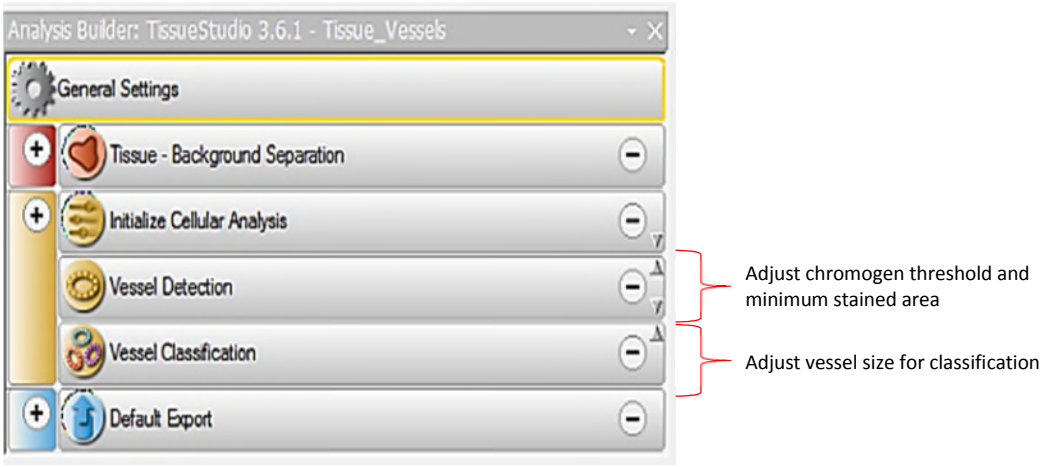

Figure 11. Tissue Studio's Vessel Detect algorithm. Algorithm detects vessels through chromogen and area thresholds before classifying them by size. Vessel detection section allows the adjustment of the DAB chromogen threshold which relates to quantifying the positive labelling of vessels. The Vessel classification section allows the thresholding of vessels dependent on size. Arbitrary figures may be selected to identify small, medium or large vessels.

The algorithm successfully segmented and quantified vessels accurately (Figure 12). Algorithm export parameters are listed in appendix 2 and include; number of vessels, area of vessels and vessel density.

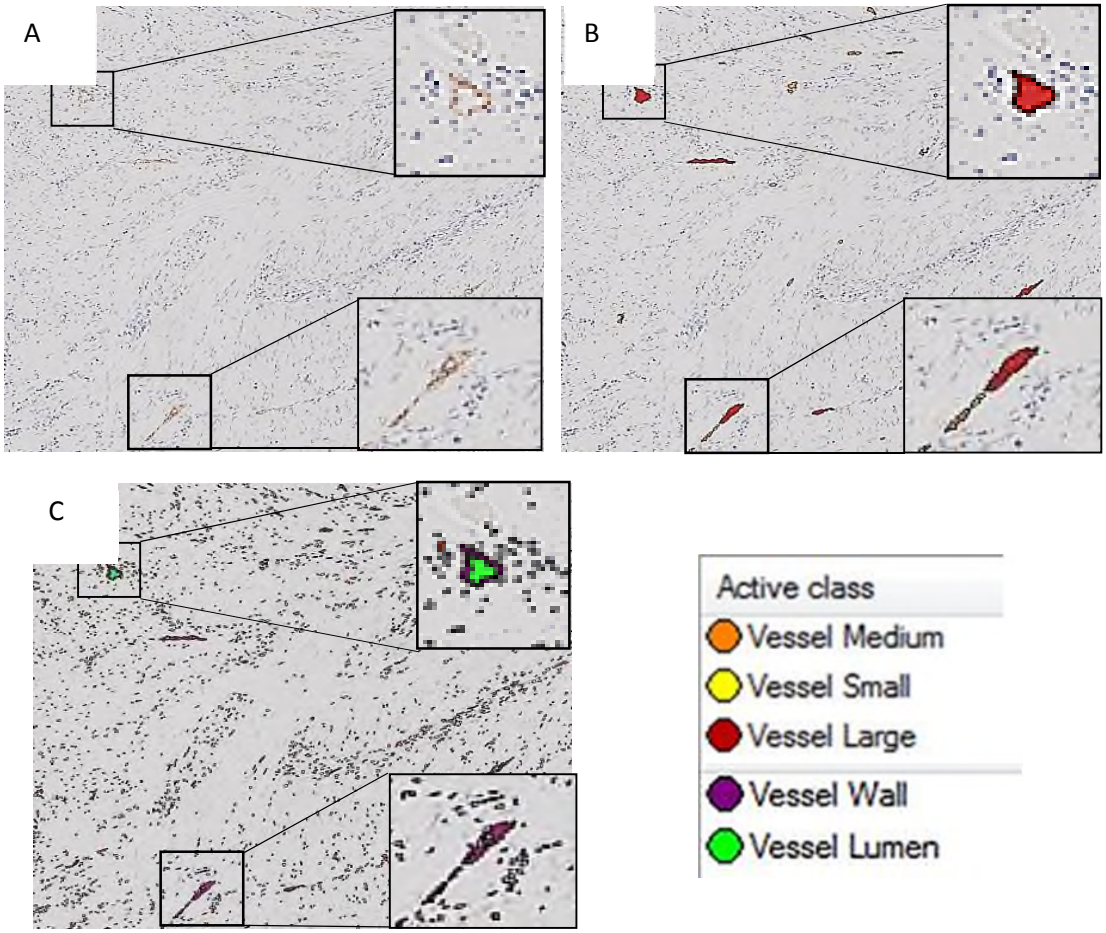

Figure 12. Segmentation of D2-40 DAB labelled lymphatic vessels through image analysis. A) Original digitised image of lymphatic vessels labelled with DAB after IHC with D2-40. B) Definiens image analysis mask classifying vessel by size. C) Definiens image analysis mask segmenting vessel walls and lumen. Images captured with a x 5 objective.

1.3.2 Automated quantification of lymphatic vessel invasion

After manual assessment of digitised whole tissue sections stained with D2-40, some lymphatic vessels containing cells within the lumen were observed (Figure 13). Although the majority of the cells within the lymphatic vessel lumen seemed non-epithelial containing small and round nuclei akin to lymphocytes, it proved difficult to be certain of distinguishing host from epithelial cancer cells. A reason for this is the heterogeneous morphology of host immune cell nuclei. Invading CRC epithelial cells may also take on a more mesenchymal phenotype which adds to their confusion with host cells.

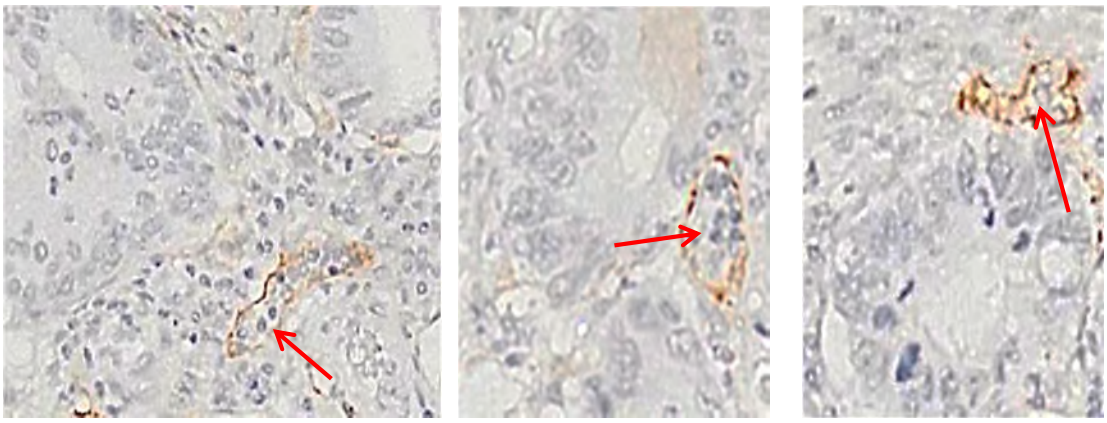

Figure 13. Cells observed within lymphatic vessel lumen. Immunohistochemsitry with D2-40 visualised with DAB shows lymphatic vessels containing haematoxylin stained nuclei within their lumen. Images captured with a x 20 objective.

To be able to quantify LVI accurately through image analysis, the software must be able to detect if the cells within the vessel are epithelial cancer cells and not host immune cells. An initial attempt was made to utilise Tissue Studio®'s nuclear detection and morphometry algorithm, in concert with the previously optimised vessel detect algorithm, to train the software to recognise only epithelial cancer cells using nuclear morphology and exclusion parameters (Figure 14). The algorithm detects all nuclei based on haematoxylin and size thresholds. Nuclei are excluded depending on length/width, haematoxylin stain and area parameters. Using these parameters an attempt was made to exclude host immune cell nuclei which were round, small and dark haematoxylin stained. The non-round, large and lighter haematoxylin stained nuclei which were more typical of epithelial cancer cells remain quantified. Nuclei which pass the parameter exclusion criteria were then classified as small, medium or large. Full algorithm settings are listed in Appendix 3.

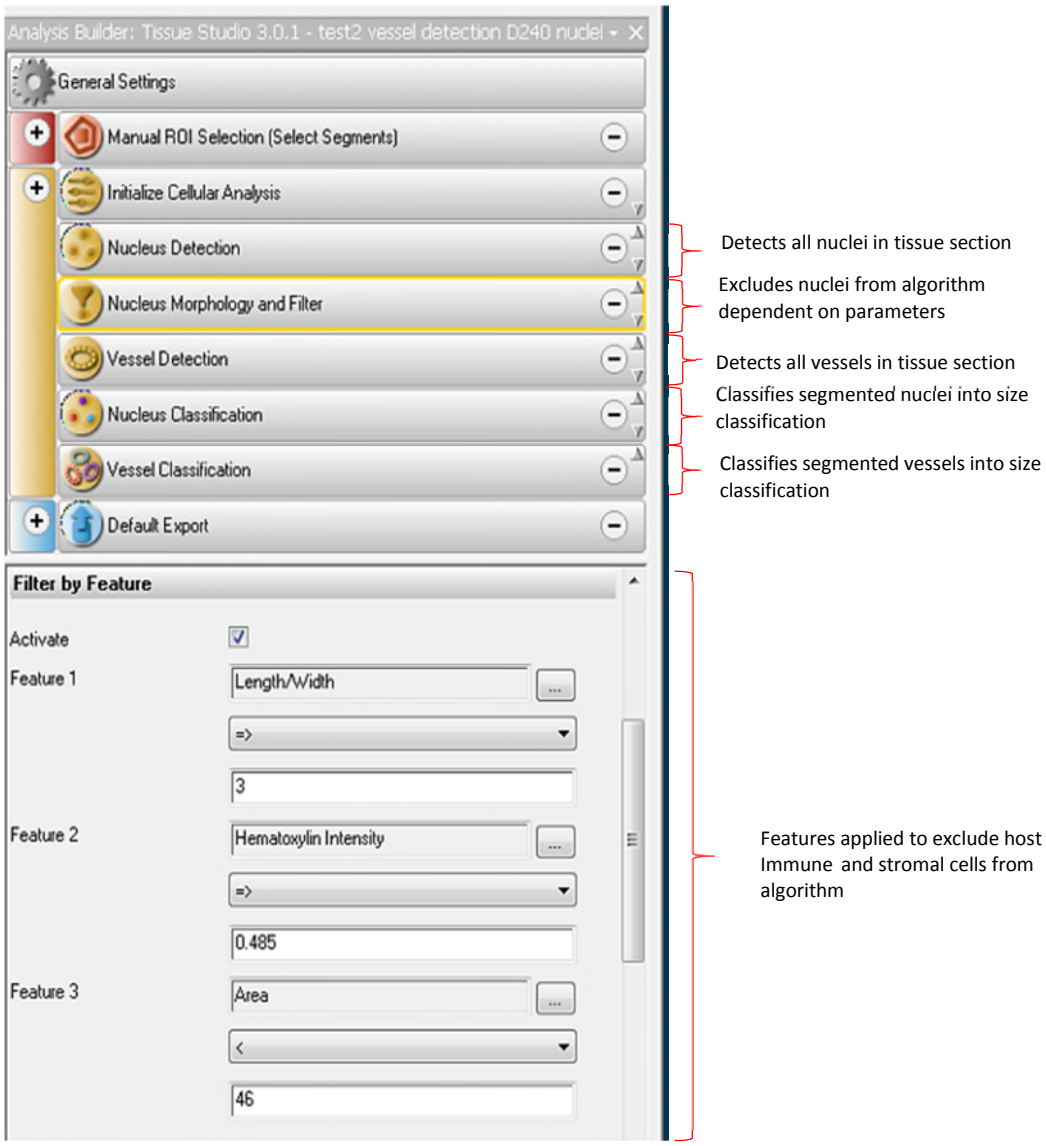

Figure 14.Tissue Studio Vessel Detect algorithm utilising exclusion parameters to differentiate host immune cells from cancer epithelial cells. All Nuclei are segemented by haematoxylin but the nuclear morphology and filter settings are utilised to attempt to exclude small and round host cells. Post vessel detection nuclei are classified dependent on their size.

Limitations within the Tissue Studio® software only allow a maximum of 3 exclusion nuclei parameters and are unable to perform logic gating on the parameters. This coupled with the heterogeneity of epithelial, mesenchymal and immune cell populations resulted in this algorithm not being robust enough to ensure only epithelial cells were quantified. This resulted in host cells being retained for quantification and epithelial cells being excluded from the algorithm. (Figure 15).

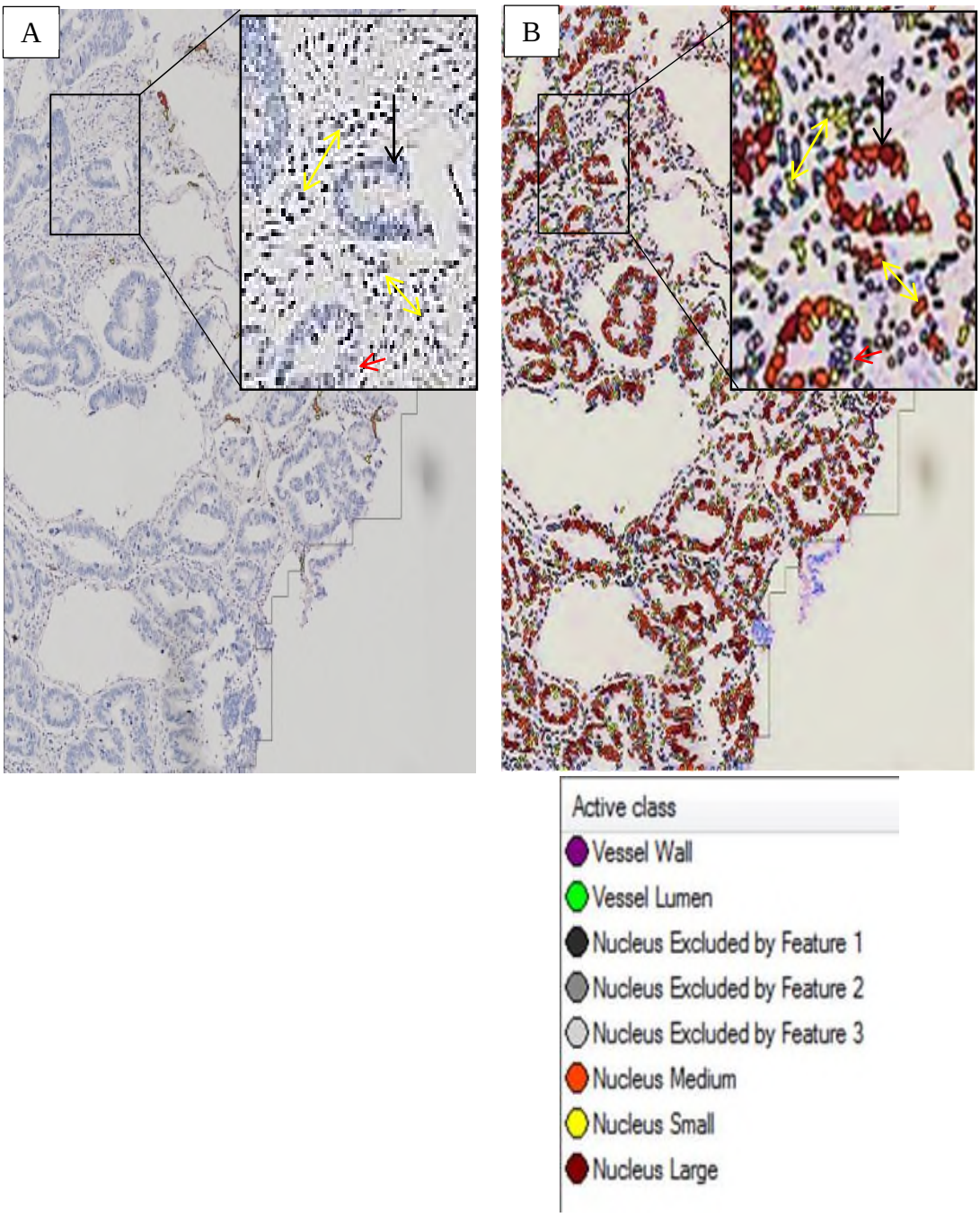

Figure 15. Vessel Detect algorithm's incorrect classification of host and cancer cells. Image A) shows cells within neoplastic glands as well as host stromal cells counterstained with haematoxylin. Image B) displays Tissue Studio's nuclear classification image analysis mask. Epithelial cells should be classified as small (yellow), medium (orange) or large (red) while stromal host cells should be excuded (grey). Green arrow shows correctly identified cancer cells, red arrow shows cancer cells excluded as host cells and yellow arrow shows stromal cells included and classified as tumour cells. Images captured with a x 5 objective and digitally magnified.

1.4 Dual immunohistochemistry

Cancer epithelial cells were not able to be detected and differentiated from host cells through nuclear morphometry and haematoxylin alone. In order to quantify epithelial cancer cells robustly though digital pathology and automated image analysis a specific epithelial stain was utilised. Cytokeratins are exclusively expressed in epithelial cells and an antibody recognising a broad number of cytokeratins, named as a pan-cytokeratin antibody (panCK), can be used to visualize adenocarcinoma cells. A panCK antibody ensures the visualization of all epithelial cells which may be expressing heterogeneous cytokeratins due to mutations in the cancer cell's genome. Dual IHC would allow the visualisation of both lymphatic vessels and epithelial cells within the same tissue section and therefore allow a more robust analysis of lymphatic invading cancer cells.

1.4.1 Pan-cytokeratin immunohistochemistry

The ability of the panCK antibody to specifically label epithelial cells was first assessed in a single antibody assay with DAB chromogen visualisation. Control whole tissue sections were utilised for this experiment. All epithelial cells within neoplastic glands or existing as smaller invasive subpopulations were contrasted against tissue stroma and identified with greater confidence than with H&E alone (Figure 16).

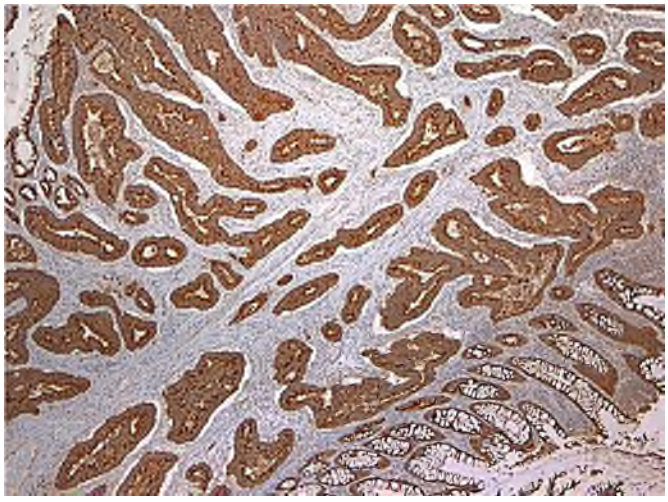

Figure 16. Immunohistochemistry with panCK DAB (brown stain) visualisation of colorectal cancer epithelial cells. Tissue section was counter stained with haematoxylin. Image captured with a x10 objective.

1.4.2 Multi-colour chromogen visualisation

In order to differentiate and visualise antibodies against panCK and D2-40, on a single tissue section, contrasting coloured chromogens must be used. The antibodies against panCK and D2-40 were combined in a multiplexed IHC which implemented NovaRed and Vector Black respectively for antibody visualisation and haematoxylin as counterstain. The resultant combination of colours on the single tissue section would be red (D2-40), black (panCK) and blue (nuclei). Prior to multi-plexing, the two chromogenic visualisation reagents were tested individually using the D2-40 antibody and were compared to DAB labelling of lymphatic vessels. Serial sections of the optimising TMA were cut and D2-40 IHC performed with DAB, NovaRed or Vector Black visualisation reagents. Both NovaRed and Vector Black reagents caused non-specific stromal staining and the contrast of vessel from stromal and tumour background, for both new reagents, was worse than that of using DAB (Figure 17).

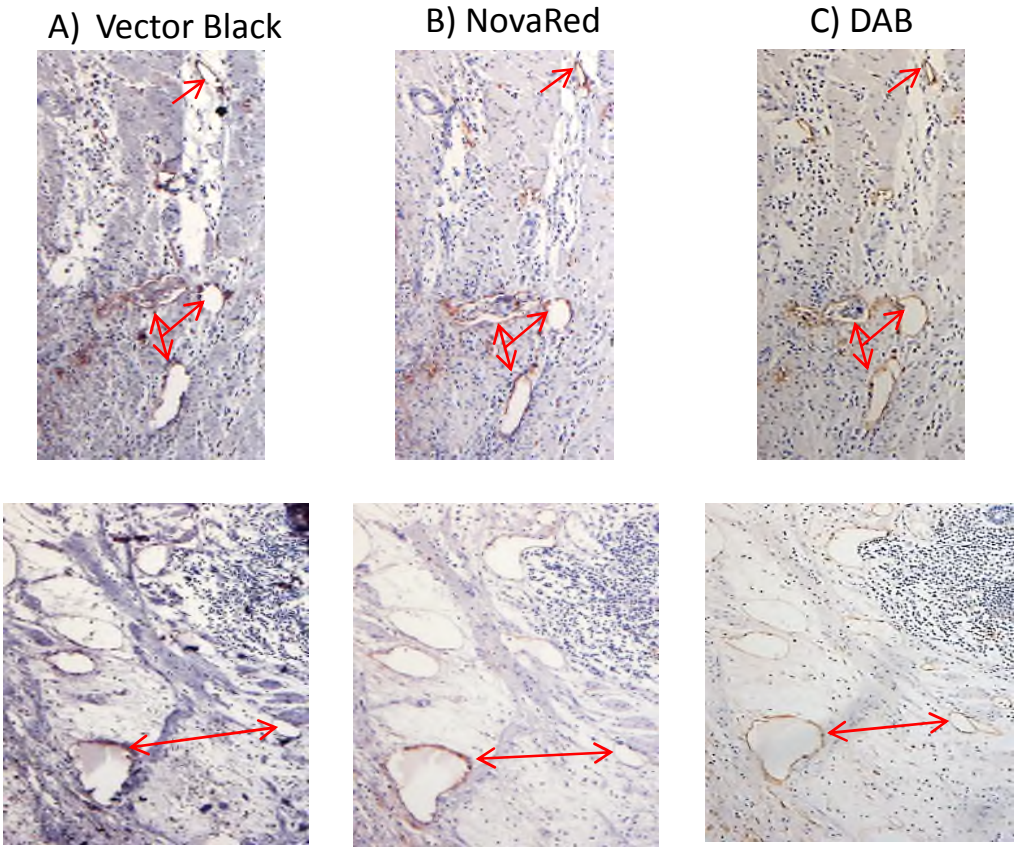

Figure17. Immunohistochemistry of serial tissue sections with D2-40. D2-40 visualised with A) Vector Black, B) NovaRed and C) DAB. Red arrows show lymphatic vessels positive for D2-40. Images captured with x5 objective.

Upon performing the triple multiplex IHC on single tissue sections taken from the Optimising TMA, it proved difficult to differentiate the red from black chromogen and the NovaRed reagent additionally created artefacts within the epithelium (Figure 18). Vessels were also poorly contrasted when compared to the original DAB experiment. Due to their poor labelling, the introduction of artefacts and the inability to differentiate the two stains, without spectral unmixing, these images were not imported into Definiens for image analysis and the methodology was abandoned.

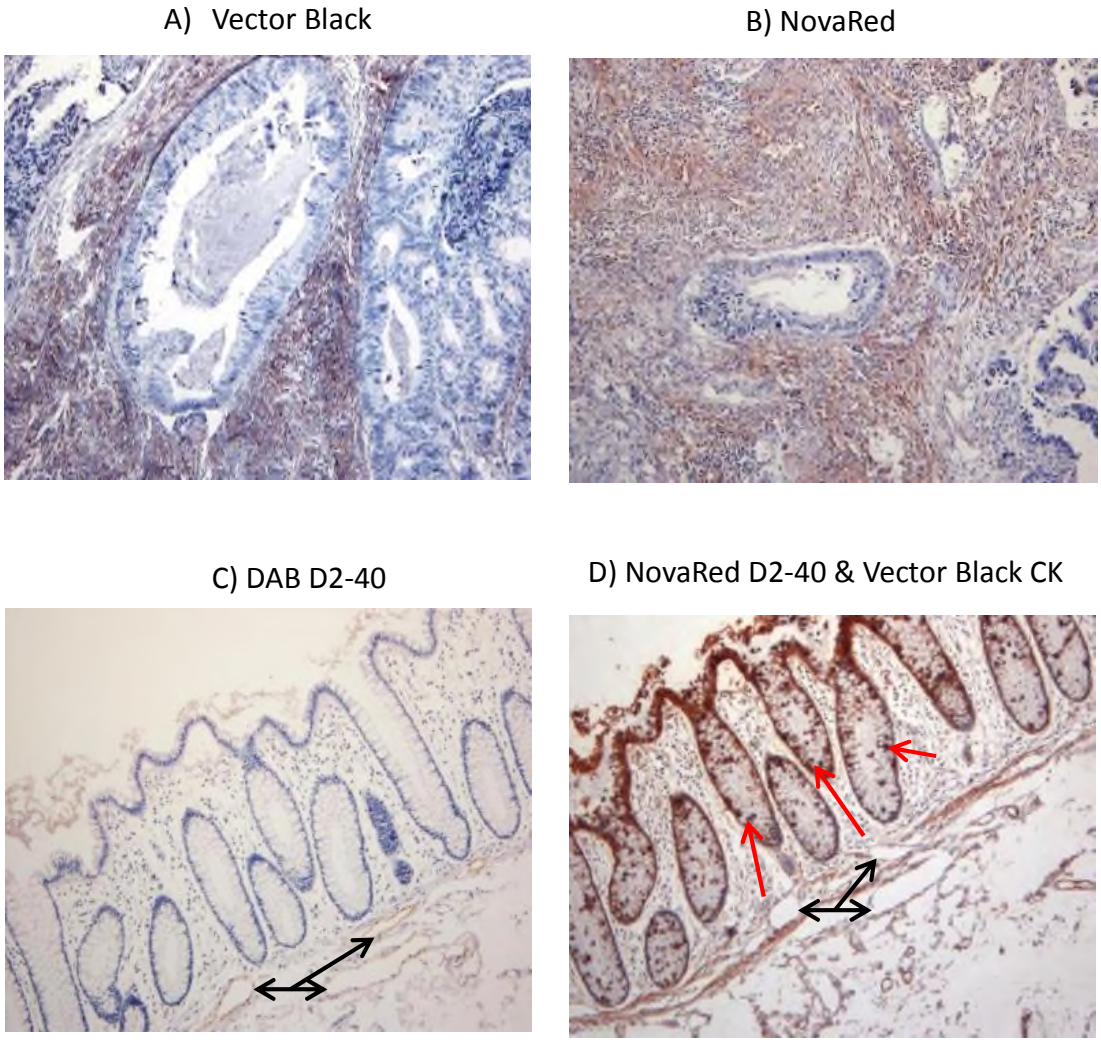

Figure 18. Brightfield based IHC dual labelling of epithelial cells (panCK) and lymphatic vessels (D2-40). Both Vector black and NovaRed visualisation reagents created non-specific staining of the stromal tissue (A & B). C) DAB visualised D2-40 highlights lymphatic vessels (black arrows). D) Dual labelling of panCK and D2-40 created similar chromogenic colours and Vector Black created staining artefact in the epithelium (red arrows).

1.5 Immunofluorescence

Immunofluorescence allows the clear visualisation and separation of the three histopathological features of interest within the multiplexed antibody IHC described above. Each antibody as well as nuclear DNA is labelled with a distinct fluorophore and fluorescence is captured on a fluorescence microscope at distinct wavelengths ensuring no bleed through of emission spectra. This results in three separate and individual grey-scale images containing the visualisation of either panCK (epithelium), D2-40 (lymphatic vessels) or DAPI (all nuclei). These three images are combined into a composite image where all three histopathological features can be visualised distinctly in a single image (Figure 19). The multiplexed immunofluorescence assay allows the clear identification of tumour cells within the lymphatic vessels with no confusion with host cells. Immunofluorescence images were captured on the Olympus AX-51 microscope as monochromatic high definition image layers for the panCK (epithelium), D2-40 (lymphatic vessel) and DAPI (nuclei) wavelengths prior to being imported into Definiens Tissue Studio® image analysis software to create composite images and for image analysis.

1.5.1 Immunofluorescence Image analysis

1.5.1.1 Tissue Studio algorithm Development

Tissue Studio®'s immunofluorescence analysis builder creates algorithms based around pre-installed image analysis solutions and which are made up of three stages of analysis. The 1st stage is "ROI detection" where the tissue is initially segmented dependent on histologically relevant regions of interest (ROI). The 2nd stage is "Cellular analysis" where objects such as nuclei and cells are segmented and classified within the previously segmented ROIs. The 3rd stage is "Data Export" from both ROIs and segmented objects.

Fluorescence image analysis algorithm development was performed on the control whole tissue sections. These positive and negative control tissue sections were utilised to test the algorithms accuracy in quantifying LVI events and to identify LVI positive

patients. 35 images were randomly captured at x20 magnification across the two tissue sections for image analysis. Two separate image analysis algorithm approaches were created around the backbone of two pre-installed Tissue Studio algorithms and executed to quantify LVI and LVD. The two pre-installed algorithms were Tissue Studio®'s immunofluorescence 'Vessel Detect and 'Marker Area' algorithms. The results from both image analysis approaches were compared against manual scoring, and sensitivity and specificity to detect LVI was assessed.

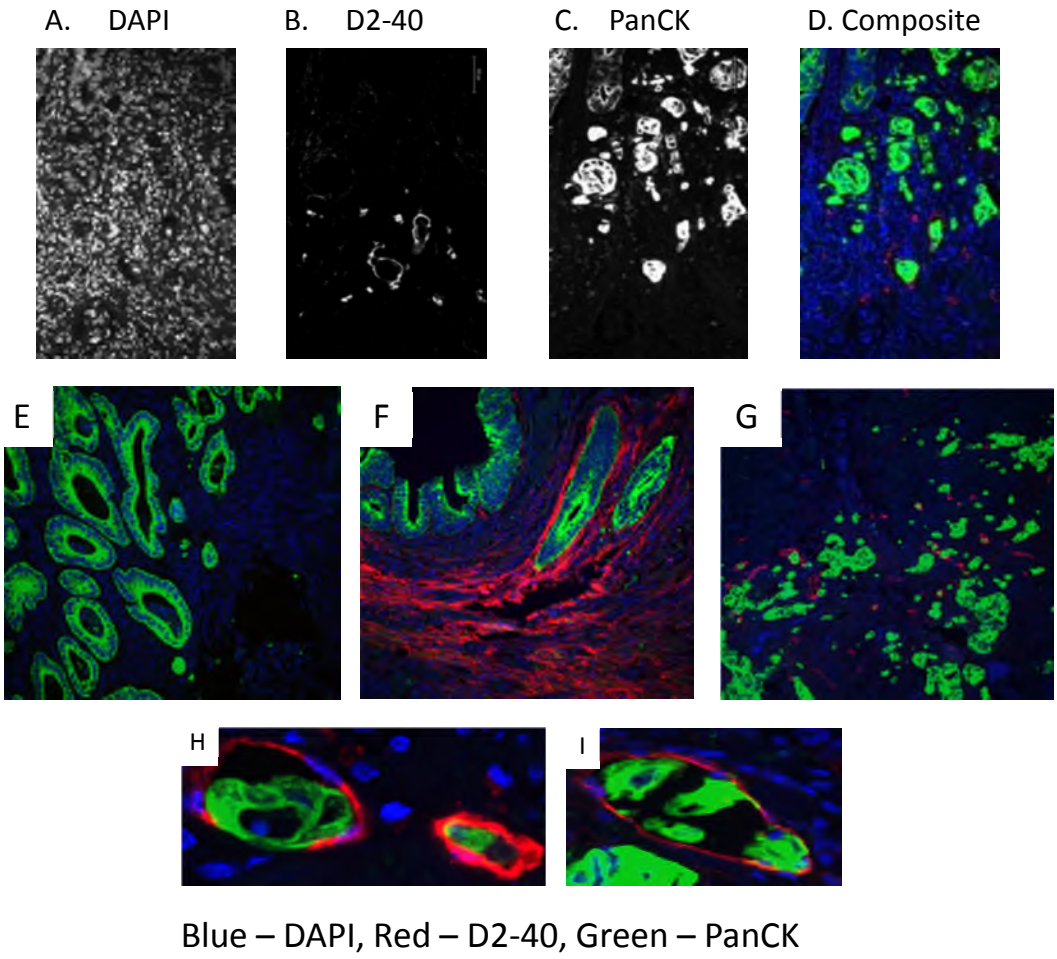

Figure 19. Immunofluorescence visualisation of panCK, D2-40 and nuclei multi-plexed on a single tissue section. Grey scale image layers captured at each wavelength; A) DAPI (nuclei), B) D2-40 (lymphatic vessels) and C) panCK (epithelial cells). D) Composite image showing all three image layers. Composite images showing: well differentiated neoplastic glands (E), high lymphatic vessel density and large neoplastic gland within a vessel (F) and high tumour budding with occult lymphatic vessel invasion (G). H) & I) show micro vessel invasion of occult LVI at higher magnification. Images captured with a x 20 objective.

1.5.1.2 Tissue segmentation

Both initial 'Vessel Detect' and 'Marker Area' algorithms executed the same ROI tissue segmentation method which initially segmented the image into three distinct ROIs: 'tumour', 'stroma' or 'lumen/necrosis'. This initial segmentation was performed using Definiens machine learning Composer technology™ which trains the computer algorithms to segment and quantify the regions of interest (ROI) in the tissue section. This is performed by manually selecting or "painting" representative areas of tumour, stroma or tumour gland lumen/necrosis. The algorithm 'learns' the intensity and morphometric parameters associated with these areas and automatically segments the rest of the tissue section accordingly. (Figure 20). Figure 21 displays the image analysis algorithm settings.

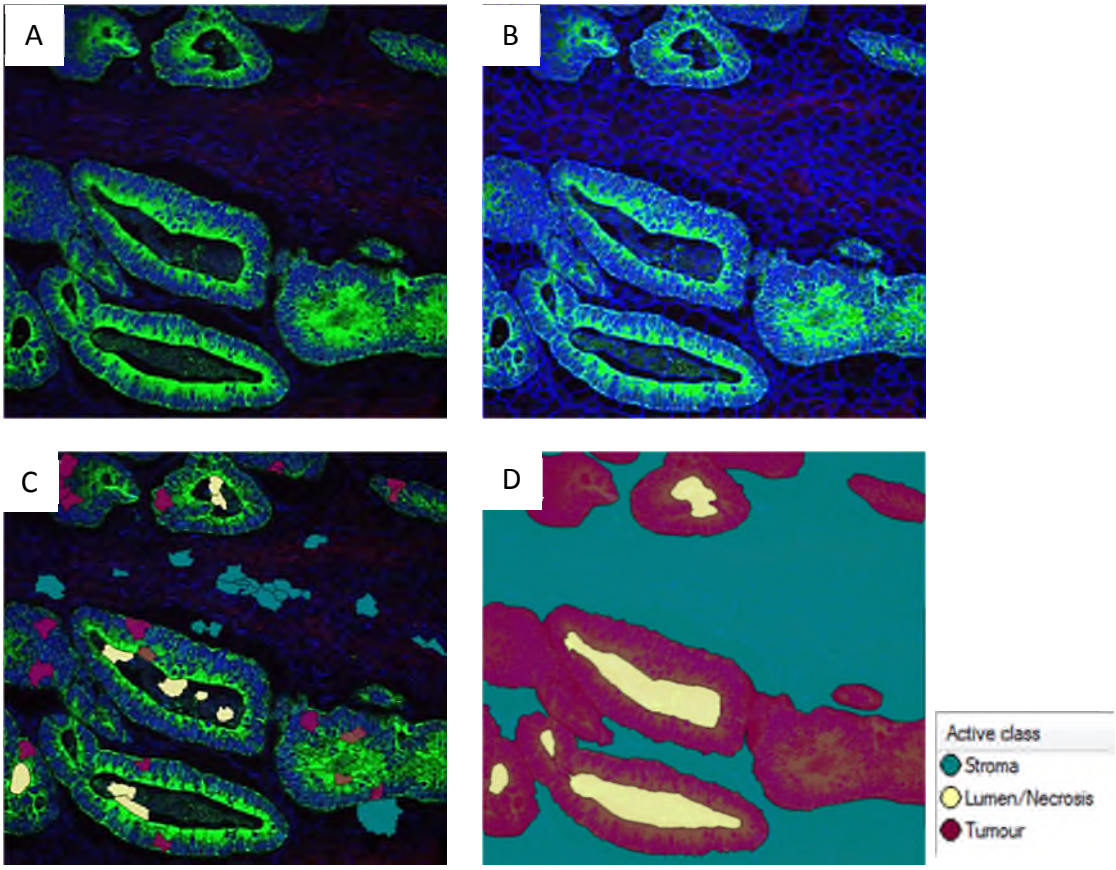

Figure 20. Composer Technology™ machine learning for automated tissue segmentation. A) Composite image of panCK (green), D2-40 (Red) and DAPI (blue). B) Tissue studio auto-image segmentation. C) Sections of stroma (turquoise), tumour (purple) and lumen/necrosis (yellow) are labelled by the user. D) Composer Technology™ learns the spectral properties of each ROI and segments images automatically. Images captured with a x 20 objective.

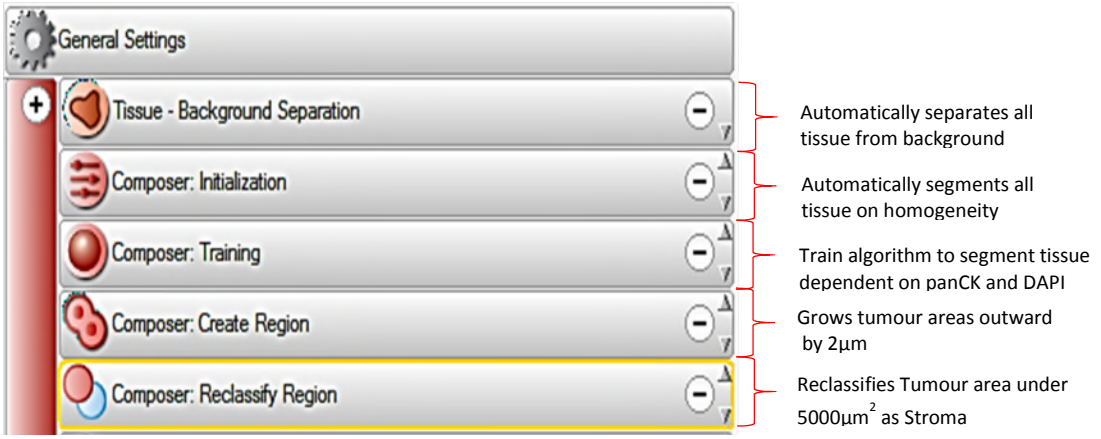

Figure 21. Tissue ROI Segmentation algorithm. The algorithm automatically separates tissue from background dependent on user specified settings. Next it automatically segments the image into regions of similar homogeneity prior to the user training the algorithm to recognise ROIs (Composer training). The algorithm next grows all tumour ROI out by 2µm in each direction as specified by the user. Finally any ROI classified as tumour which is below 5000µm^2 is automatically reclassified as Stroma. Once the algorithm is taught it automatically segments and classifies all subsequent images within the Definiens workspace. Within each section of the algorithm shown above are further settings which the user can apply to uniquely programme the software to perform the listed tasks.

Lymphatic vessels are located within the stroma area only and the algorithm is programmed only to quantify D2-40 positive objects exclusively within the stroma ROI, however panCk invasive subpopulations may be classified as tumour by the Composer technology™. The panCk subpopulations and the vessels which they invade may therefore be classified within the tumour ROI and remain unquantified. Therefore the next step of the tissue segmentation is to reclassify any region of segmented tumour ROI which is below 5000µm^2 into stroma ROI. This allows any invading panCK positive cancer cells to be quantified within the stromal area (Figure 22). Full algorithm settings for the Tissue Segmentation algorithm is listed in Appendix 4.

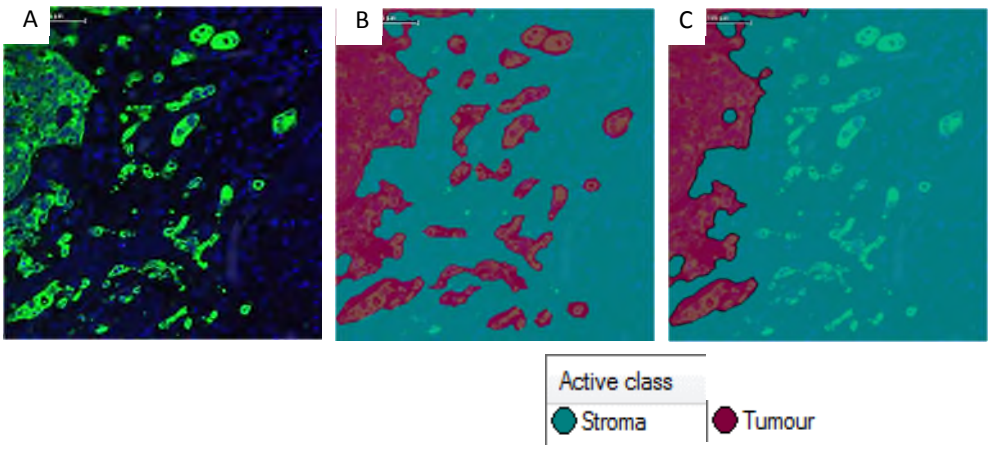

Figure 22. Automatic reclassification of small Tumour ROI into Stroma. A) Composite raw image. B) Epithelial cells are classified as Tumour. C) Algorithm automatically reclassifies any Tumour below 5000µm^2 as stroma in order to quantify occult LVI. Images captured with a x 20 objective.

1.5.1.3 Vessel detect algorithm.

The initial image IF analysis algorithm to be tested was based around Tissue Studio®'s pre-installed 'Vessel Detect' module.

Post ROI segmentation, iterative steps of intensity and size thresholding were performed to ascertain the optimal settings for nuclei segmentation and vessel detection. Nuclei are segmented from DAPI positive objects based on intensity and size thresholding. Post nuclei segmentation all nuclei are discarded apart from those which are above a 50au threshold of panCK intensity and are above 5µm^2 in area. The nuclei which are kept are deemed to be epithelial and the panCK threshold is set high due to the observation that invasive tumour cells had increased panCK intensity over the cells within the neoplastic glands. Smaller DAPI positive objects are discarded as stromal, debris or artefact and not quantified. Vessels are next segmented based on D2-40 threshold intensity. As vessel staining is occasionally incomplete, any gap of 4µms between D2-40 positive objects is automatically linked and segmented as one vessel. The remaining nuclei are then classified as LVI 'nucleus high' if they contain a D2-40 intensity of above 18au; essentially quantifying nuclei which have an area of D2-40 and panCK colocalised above set thresholds equating to an epithelial cell within a vessel. Vessels are then classified as small, medium or large and if they contain a

lumen or not (Figure 23). Full algorithm threshold settings listed in appendix 5. An overview of the algorithm set-up is displayed in Figure 24.

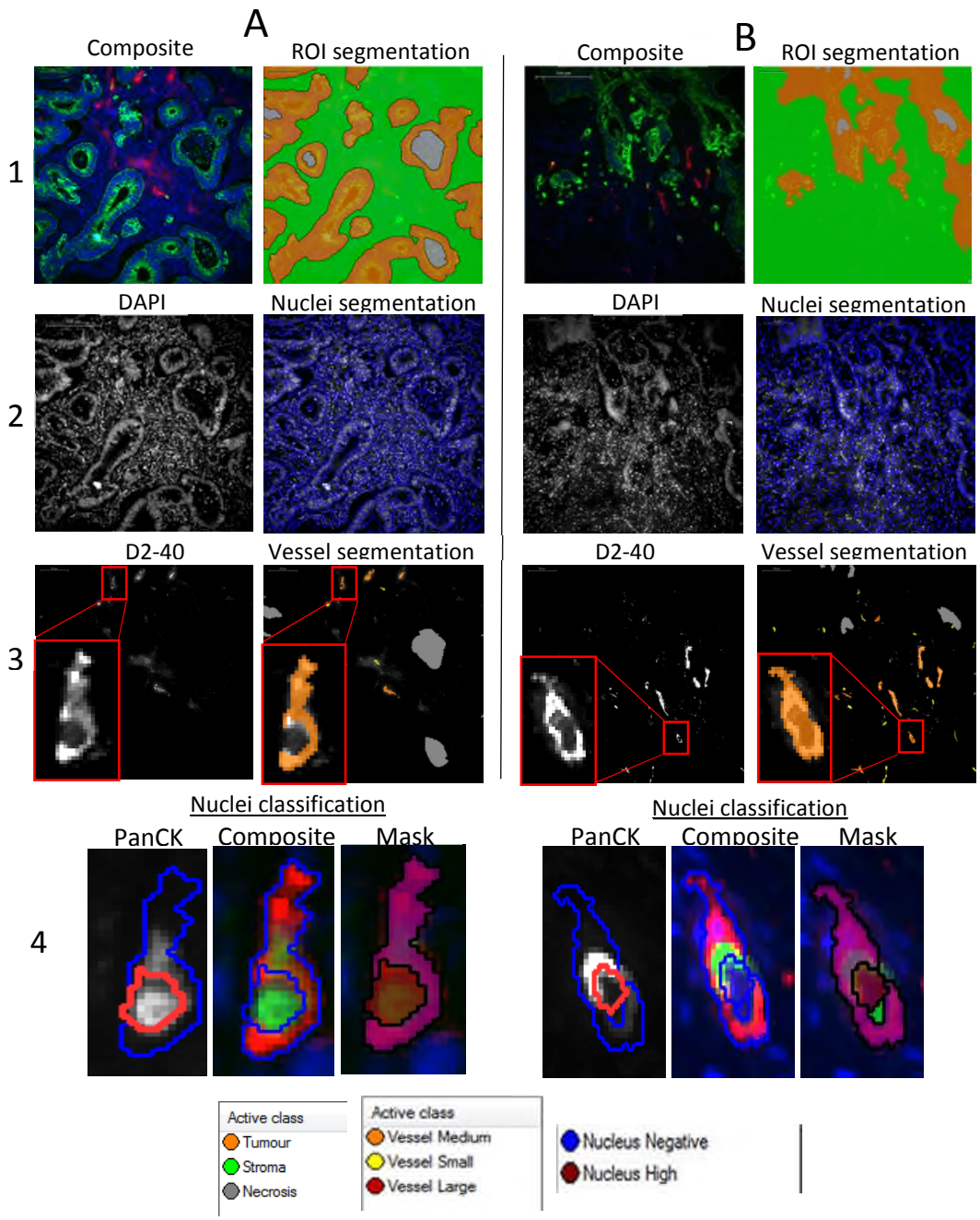

Figure 23A. Immunofluorescence vessel detect algorithm. A) & B) display 2 separate tissue sections which were analysed by the algorithm. 1) The raw composite image (panCK: green D2-40: red, DAPI: blue) is segmented into ROIs (tumour: orange, stroma: green, lumen: grey). 2) All nuclei (greyscale DAPI) are segmented automatically (blue image analysis outline). 3) D2-40 positive lymphatic vessels (greyscale D2-40 labelling) are segmented and classified dependent on size (orange mask shown equates to a medium sized vessel. Images were captured with a x 20 objective. 4) panCK positive nucleus (greyscale PanCK) within a D2-40 positive vessel (Composite; green: panCK, red: D2-40, blue: DAPI) are classified as "Nucleus High" (dark red nuclear mask) within a positive vessel (purple vessel mask) and quantified as an occult LVI event.

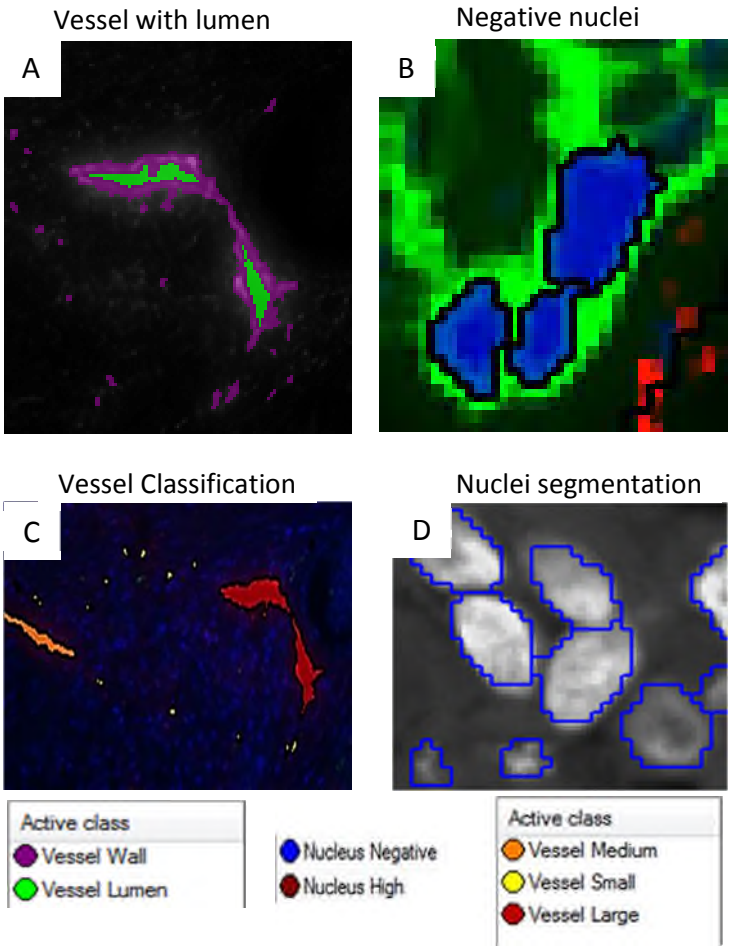

Figure 23 B. Digital zoom of: A) segmented vessel with vessel wall (purple) and vessel lumen (green) classified. B) Epithelial nuclei not within a vessel (blue; Nucleus Negative). C)lymphatic vessels classified as small (yellow), medium (orange) and large (red). D) automatic segmentation of nuclei.

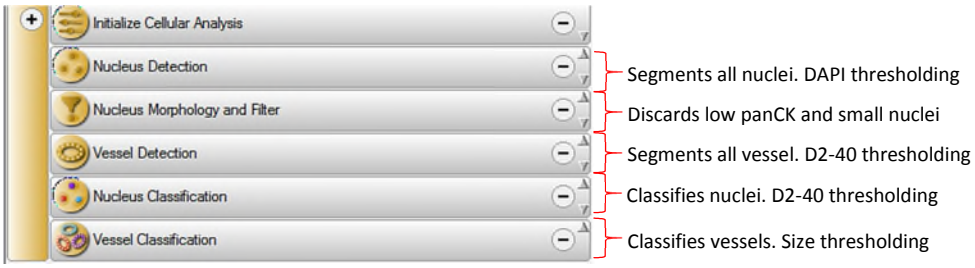

Figure 24. Immunofluorescence vessel detect algorithm settings. Post Tissue segmentation the vessel detect algorithm segments all nuclei through user specified DAPI thresholding. Discards small and low intensity panCK nuclei through user specified panCK and object area thresholding. Segments vessels, classifies nuclei as positive or negative dependent on user specified D2-40 intensity thresholding and finally classifies vessels dependent on area.

Post analysis it was discovered that false positives were created when quantifying positive nuclei in the stromal ROI due to areas of high background intensity of fluorophores. Positive LVI hits were therefore re-classified as “Nucleus high” which bordered a vessel wall. False positive nuclei were also located within the Tumour ROI due to artefact staining of D2-40 antibody. A final positive LVI nucleus count was classified as positive cells bordering a vessel within the stromal ROI only. Tissue Studio® allows customisable data exports. The algorithm was set to export the number of “Nucleus high” within the stroma and which bordered a vessel. The number of these positive events were quantified for each tissue section and classified as the number of LVI events per sample.

The results compare the LVI positive and negative control tissue sections from both the image analysis results and from manual visual quantification of the fluorescence images (Figure 25). Eight images within the positive LVI control were manually identified as containing LVI events and of those five were correctly quantified by the algorithm as positive for LVI. The algorithm correctly quantified zero LVI events in the negative control section. Manually identified positives, in the positive control section, in image 18 and 24 are excluded by image analysis due to being falsely classified within the tumour ROI and thus not quantified.

Microvessel density is reported for each image and this parameter is automatically exported from the algorithm. The negative control section contained LVD hotspots (large areas of dense vasculature) while the positive control did not. Initial results

suggest that increased LVD does not correlate with LVI, albeit after analysing only two cases (Figure 26). The full results are summarised in Table 3.

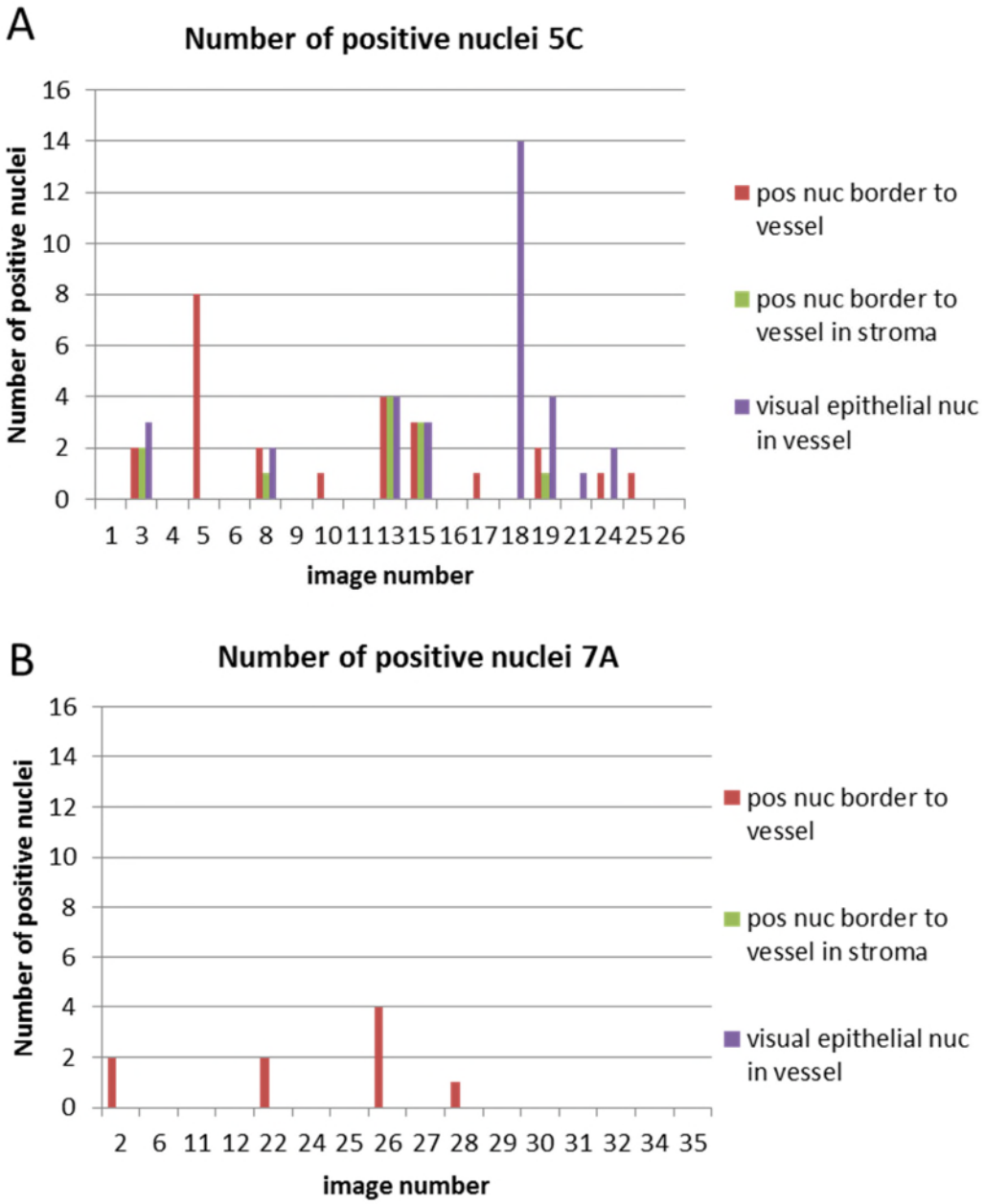

Figure 25. Immunofluorescence Vessel Detect image analysis results. Quantifying only positive nuclei which were bordered to a vessel (red) gave false positive LVI events due to tumour gland cells being quantified as positive nuclei. Final automated LVI count was therefore reported as positive nuclei which were bordered to a vessel within the Stroma (green). This was compared to LVI quantified by manually assessing the IF images (purple).

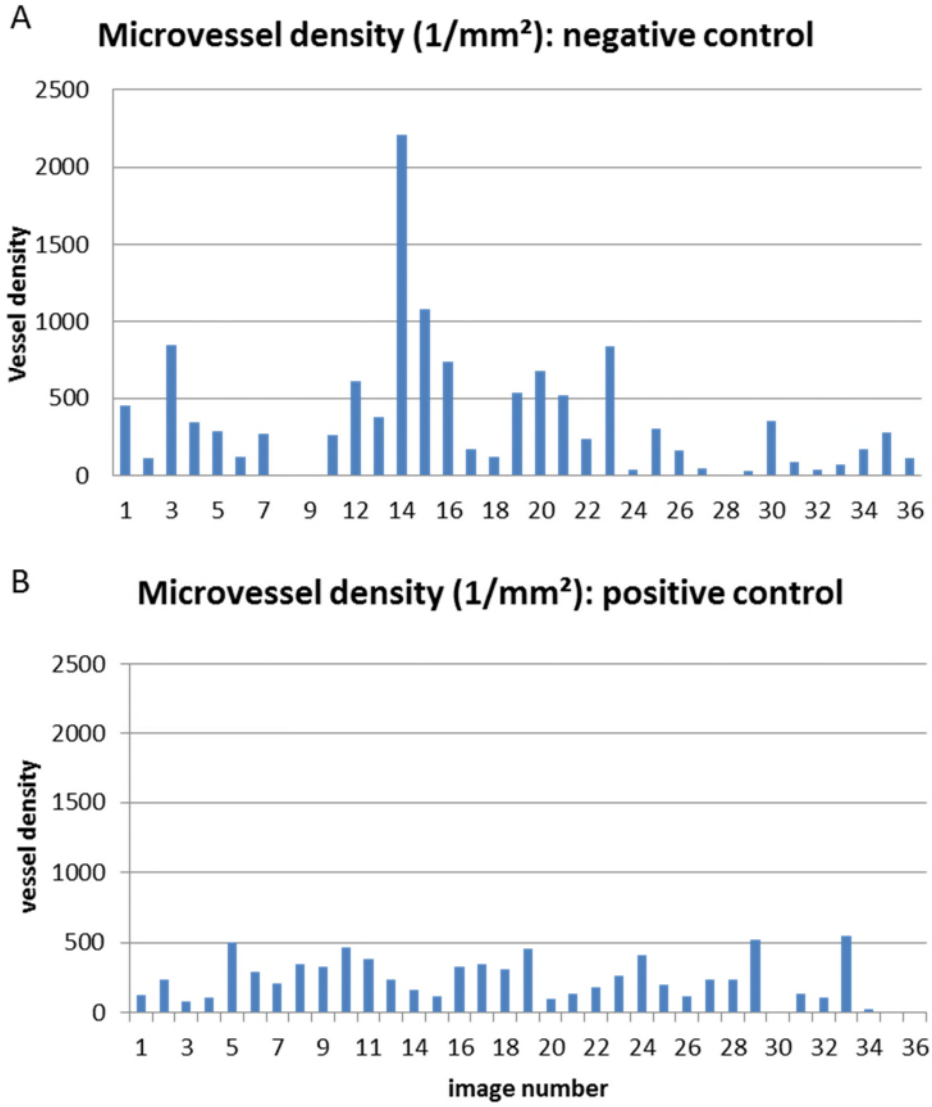

Figure 26. Quantification of microvessel density across the separate A) negative control and B) positive control whole tissue sections through the immunofluorescence Vessel Detect algorithm. Vessel density is reported across each image captured across each section

	Positive control	Negative control
No. Manual assessed LVI	8	0
No. Image analysis LVI	5	0
specificity	100%	
sensitivity	62.50%	

Table 3. Summary of the exported Vessel Detect algorithm LVI results.

1.5.1.4 Marker Area algorithm

Post ROI segmentation the algorithm is programmed only to quantify objects of interest within the stromal region. Nuclei are not segmented or quantified in this algorithm. The algorithm segments objects within the stromal region which are above a set intensity threshold for panCK and D2-40 which were established per tissue section due to inter-section heterogeneity (Figure 27). Positive objects must also be above a minimum stained area of 11µm^2 as below this an object was not considered big enough to be a cell or vessel. The algorithm classifies panCK positive objects as "marker 1", positive D2-40 objects as "marker 2" and colocalised panCK and D2-40 objects as "marker 1 & 2" (Figure 28). A full list of algorithm settings can be found in appendix 6. Co-localised markers classified as "marker 1 & 2" are deemed to represent LVI. To calculate LVD the area (µm^2) of marker 2 (D2-40) objects per image within the stroma is divided by the total stromal area (µm^2). An advantage of this algorithm over the 'Vessel Detect' algorithm is that it does not rely on the panCK intensities measured within the nucleus, which will naturally be lower than within the cytoplasm. The 'Marker Area' algorithm simply quantifies the area of co-localisation and so picks up cytoplasmic expression of panCK as well as nuclear intensity. This results in the algorithm accurately identifying more true positives.

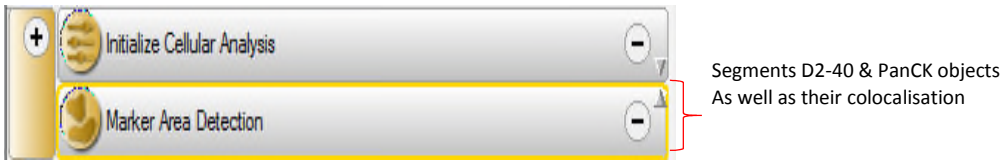

Figure 27. Cellular analysis section for Marker Area Algorithm. Algorithm segments positive panCK and D2-40 fluorescence objects above a set threshold. Algorithm next classifies any colocalised objects.

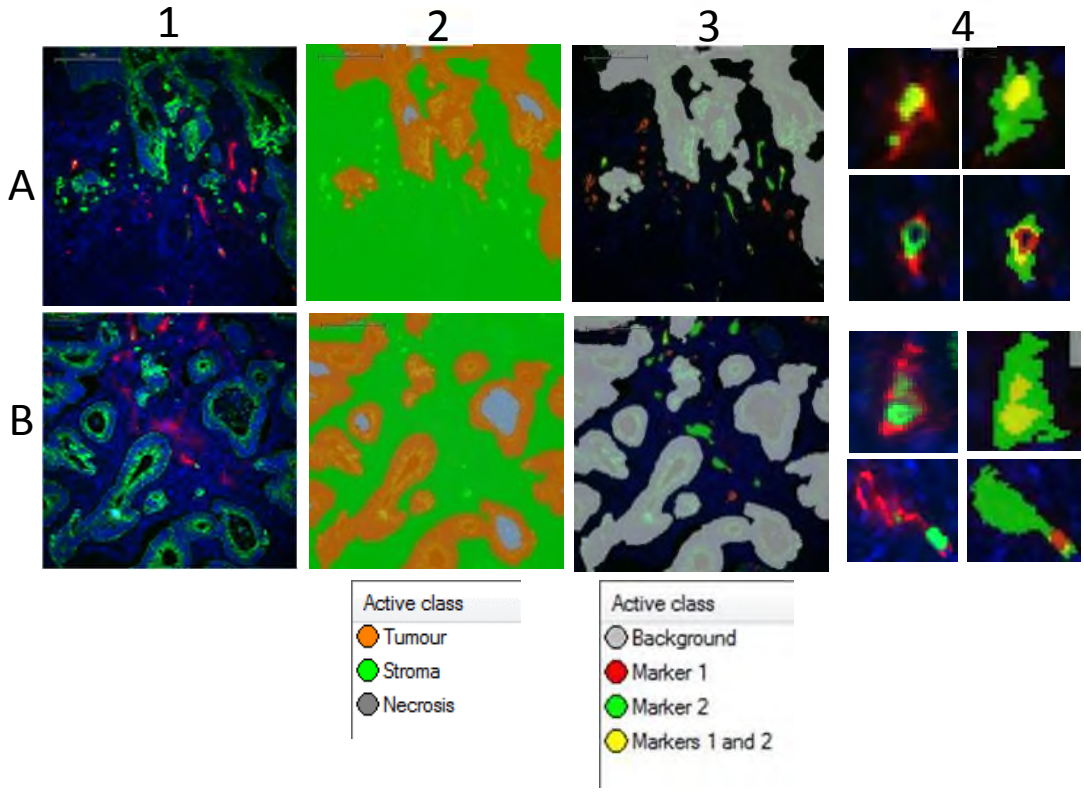

Figure 28. Immunofluorescence Marker Area algorithm. A) & B) display two tissue sections which were quantified by the Marker Area algorithm. 1) composite raw image of panCK (green), D2-40 (red) and DAPI (blue). 2) Tissue Studio automatically segmented Tumour (orange) from Stroma (green). 3) Algorithm segmented positive D2-40 (green mask) or panCK (red mask) objects within the Stromal ROI only. 4) Occult LVI is quantified as colocalisation of D2-40 and panCK (yellow mask).

In the positive LVI control 6 out of 8 images were correctly quantified as containing LVI events whereas the negative control reported no LVI events quantified (Figure 29). As with the Vessel Detect algorithm, two images were visually identified as containing LVI but were not quantified within the algorithm, due to a mis-classification of stromal ROI and tumour ROI.

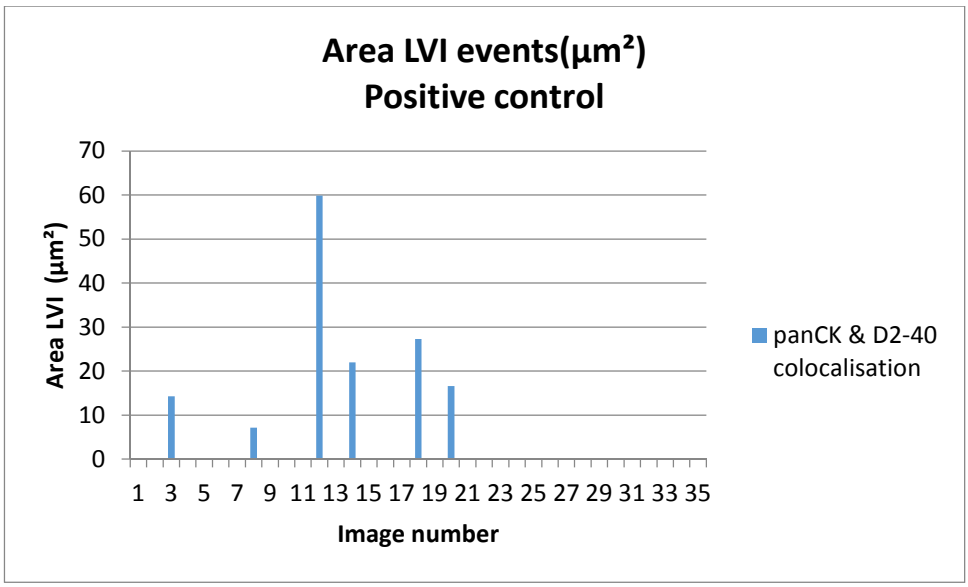

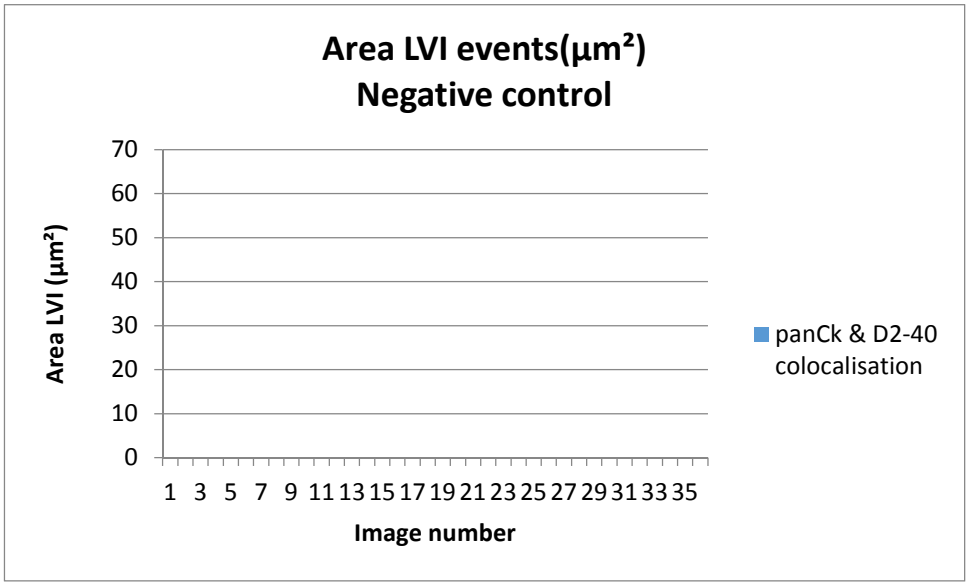

Figure 29. Immunofluorescence Marker Area image analysis results. Positive control reports 6 images within the section which contain positive D2-40 and panCk co-localisation. The negative control reports no LVI events within any images taken across this section

Similar to the vessel detect algorithm, it was observed that the positive control tissue section contained a lower LVD than the negative control (Figure 30).

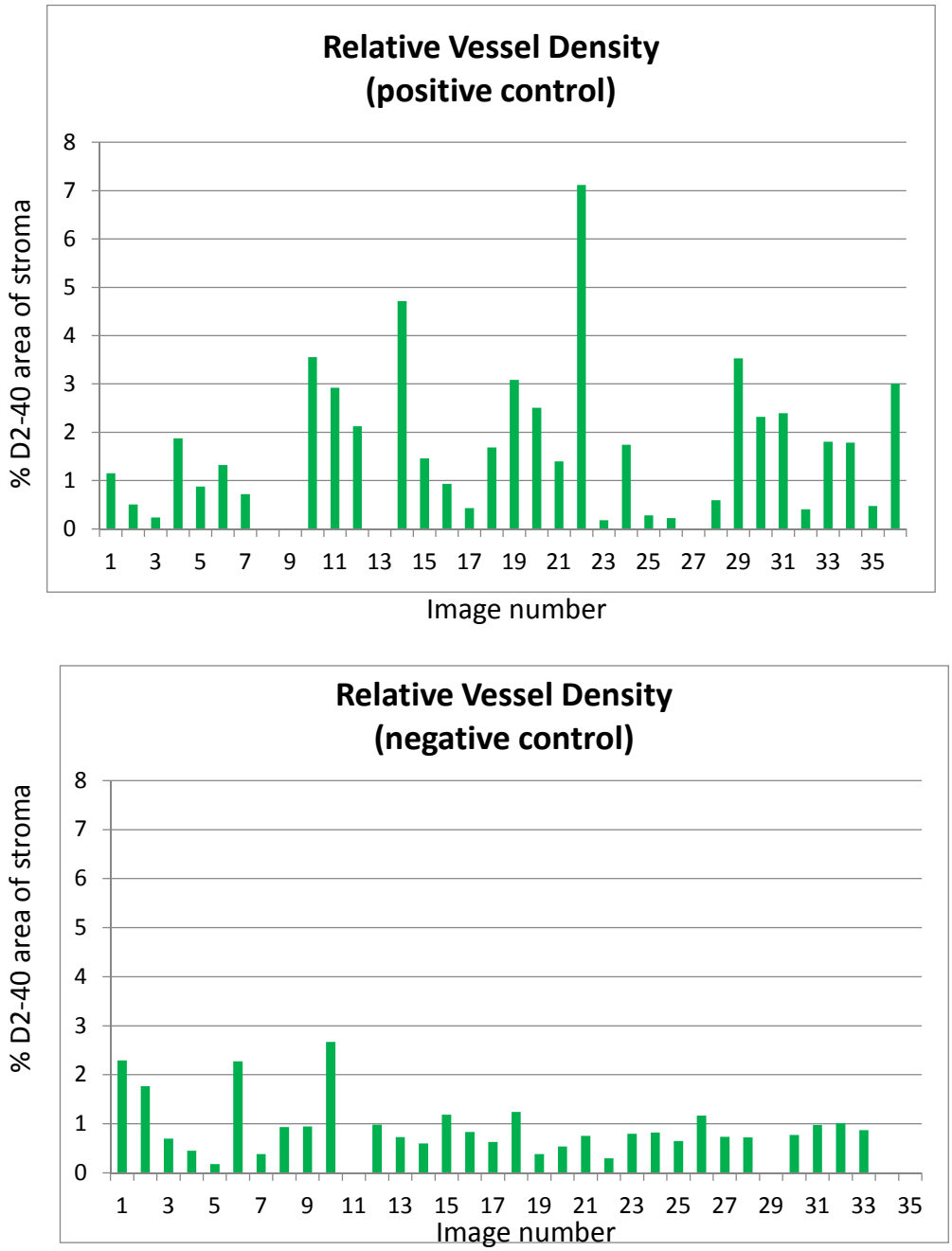

Figure 30. Immunofluorescence Marker Area algorithm microvessel density export across images captured within the positive control or negative control. The parameter is calculated by dividing the percentage D2-40 by the percentage of stroma.

The results for LVI quantification reported by the 'Marker Area' algorithm are summarised in Table 4.

	Positive control	Negative control
No. visual LVI	8	0
No. quantified LVI	6	0
specificity	100%	
sensitivity	75.00%	

Table 4. Summary of Marker Area results.

1.5.2 Tissue Microarray LVI & LVD quantification

Both 'Vessel Detect' and 'Marker Area' algorithms reported no LVI events in the negative control and successfully identified the majority of LVI events within the positive control. The 35 images which were randomly captured across each whole tissue section required analysis resulting in a processor heavy assay. An advantage of using TMAs is that patient numbers can be scaled up with only one image to analyse per patient sample and hundreds of patients may be analysed on a single microscope slide. The training cohort TMA was employed in this experiment to evaluate the accuracy and robustness of the image analysis algorithms to automatically quantify LVI and LVD across a large heterogeneous TMA mounted patient cohort in a batch process manner with no manual intervention.

After immunofluorescence and image capture on the Olympus Ax-51 microscope system the images were imported into Definiens immunofluorescence Tissue Studio® for analysis with both the 'Vessel Detect' and 'Marker Area' algorithms. Seven tissue cores were manually identified as containing LVI events and classified as 'visual positives'. Extensive iterative optimisation was required to convert the algorithms to be TMA amenable. The main source of error within the algorithms when run across a TMA was due to tissue, biomarker and nuclear inter-patient heterogeneity, both in intensity and morphology, as well as artefacts introduced by the TMA creation such as tissue folding and edge effect.

1.5.2.1 Tissue Segmentation

Due to inter-core heterogeneity the algorithm could no longer robustly quantify necrosis. The tissue was segmented into tumour, stroma and 'no tissue'. The 'no tissue' trained ROI was introduced to overcome edge effect, where non-specific staining is prevalent (Figure 31). Classifying background as 'no tissue' allows the exportation of the distance of a biomarker to 'no tissue'. If the biomarker is within 30µm of 'no tissue' it is discarded as a false positive in post processing. Post processing consisted of manually analysing of output data and removing objects within the 30µm distance to 'no tissue' exclusion zone. An area of high panCK intensity may overlap the segmented border of a neoplastic gland and be segmented within the stroma which result in a false positive LVI event occurring if a vessel is close to this border. To overcome this, the algorithm automatically grows out all tumour areas into stromal space by 2µm in all directions. The algorithm only quantifies biomarker intensity within stromal areas. TMA ROI segmentation algorithm settings are listed in Appendix 7.

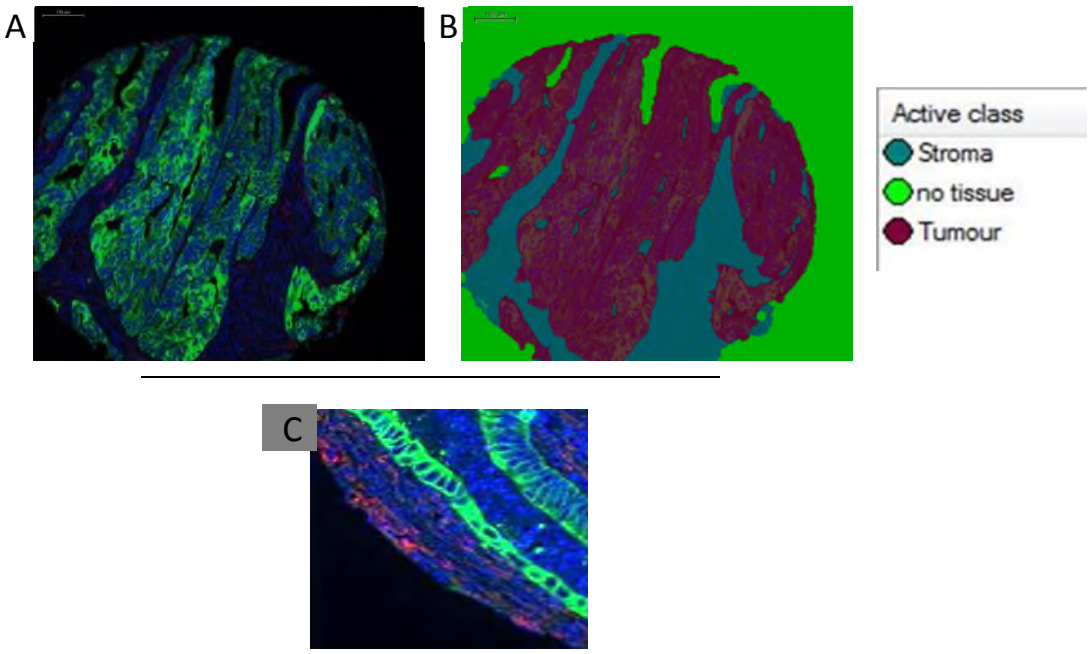

Figure 31. TMA tissue ROI segmentation algorithm. A) Composite image of TMA core (green: panCK, blue: DAPI). B) Tissue Studio automatically segmented Tumour (purple), Stroma (turquoise) and no tissue (green) after composer training. C) Example of edge effect non-specific antibody fluorescence from the D2-40 antibody.

1.5.2.2 Vessel Detect algorithm results

The ‘Cellular analysis’ section of the algorithm, which quantifies ‘Nuclei high’ as LVI, is identical to the whole tissue algorithm detailed in section 3.5.1.3. Table 5 summarises the results from the TMA analysis with the ‘Vessel Detect’ algorithm. Five cores of the seven manually identified LVI positive cores were identified by the algorithm as containing LVI events; however the nuclei within TMA core 51 and 104 which were identified as LVI were false positives while the true positives within these images were missed. Due to false positive nuclei being detected in core 51 and 104 only three of the seven LVI positive cores were identified correctly. Only TMA core 30 and 66 identified all LVI nuclei within each image correctly. Image 65 was not quantified as LVI positive due to stroma being incorrectly classified as ‘no tissue’. Other reasons for positive LVI nuclei not being quantified were due to a below-threshold nuclear panCK intensity or poor nuclear segmentation due to inter-core DAPI intensity heterogeneity. Twenty nince false LVI positive cores were identified across the TMA. Manual post-processing and quality control of the images and the data discarded the majority of false positives, which were due to TMA effect (folded, torn and overlapping tissue) and edge effect, leaving 8 images containing false positive nuclei. Post processing is a manual and labour intensive step which involves the deletion of cores from the quantification which contain TMA artefact or the exclusion of objects due to edge-effect. The export of parameters ‘distance to no tissue’ and ‘Stromal intensity’ allows such post processing to occur. The remainder of the false positives were due to incorrect tissue or nuclear segmentation and non-specific panCK staining (Table 5). Microvessel density was also quantified and automatically reported by the algorithm (Figure 32).

Visual positives	Algorithm quantified positives	Algorithm reported false positives	Remaining false positives after manual post-processing
10 (5)	10 (1)	8 (6)	16 (3)
30 (3)	30 (3)	12 (1)	26 (2)
51 (1)	51 **(1)**	16 (4)	48(1)
66 (1)	66 (1)	23 (4)	55 (1)
65 (>10)	65 (0)	25 (3)	73 (2)
82 (1)	82 (0)	26 (2)	84 (1)
104 (9)	104 **(2)**	43 (2)	106 (1)
		45 (2)	110 (1)
		47 (2)	
		48 (8)	
		49 (9)	
		50 (3)	
		53 (1)	
		55(1)	
		57 (2)	
		59 (1)	
		73 (2)	
		74 (3)	
		75 (1)	
		80 (29)	
		81 (3)	
		84 (2)	
		85 (1)	
		87 (1)	
		93 (2)	
		103 (1)	
		106 (2)	
		109 (21)	

Table 5. Summary of Vessel Detect TMA algorithm results. Positive LVI cores are entered under each heading and the number of LVI events within each core is reported within brackets. Visual positives were identified manually from the IF images. Quantified positives were reported by the analysis algorithm. False positives were also reported by the algorithm. LVI events in bold type were within LVI positive cores, however the algorithm reported on false positive events within these. Positive LVI Cores in red type were not quantified by the algorithm.

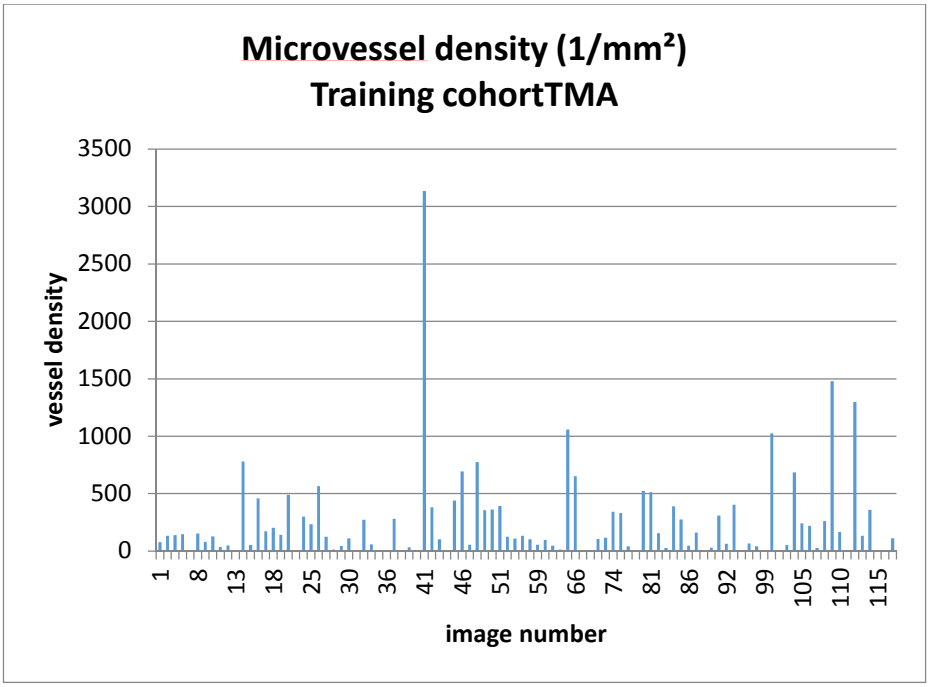

Figure 32. Microvessel density results reported by the Vessel Detect TMA. Vessel density is reported per TMA core.

1.5.2.3 Marker Area algorithm results

Post ROI tissue segmentation the 'cellular analysis' section of the algorithm, which quantifies colocalisation of "Marker 1" (panCK) and "Marker 2" (D2-40) as LVI, is identical to the whole tissue algorithm in section 3.5.1.4. All 7 cores visually identified as LVI were correctly quantified by the algorithm while 23 false positives were reported. After manual post-processing of the false positives, there remained 5 cores reporting false positive LVI (Table 6). Manual post-processing steps were similar to the vessel detect algorithm with a few additional exclusion parameters added. If a panCK positive object was deemed to be too small to be a cell (under 22µm) or if there was a high background D2-40 staining in the stroma (mean stromal intensity threshold of 17au across the TMA core) the positive object was removed. These results reported a specificity of 91.82% and sensitivity of 100% for the number of correctly identified LVI positive cores. Microvessel density was also exported from the algorithm (Figure 33).

Algorithm quantified positives	Algorithm reported false positives	Remaining false positives after manual post-processing
10	1	16
30	3	32
51	4	40
66	5	48
65	6	53
82	8	
104	11	
	16	
	23	
	26	
	28	
	29	
	32	
	35	
	40	
	41	
	48	
	49	
	50	
	53	
	57	
	59	
	114	

Table 6. Summary of Marker Area TMA algorithm results. The TMA core number quantified by the algorithm is entered under each heading. Algorithm reports total area of LVI and so individual events are not listed.

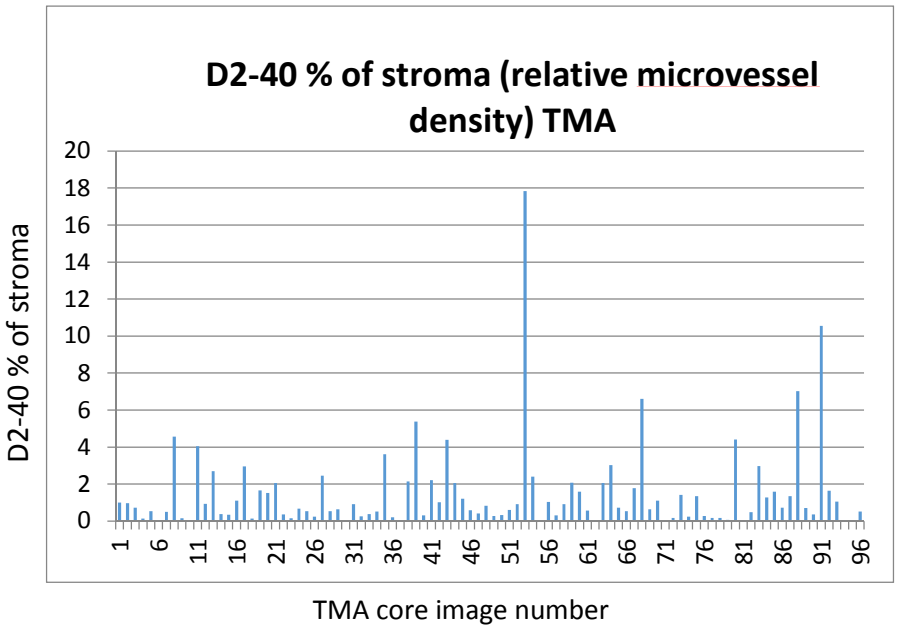

Figure 33. Microvessel density results reported by the Marker Area TMA algorithm.

1.5.3 Tissue Studio® algorithm constraints

Although manual post processing decreases the number of false positives reported in both TMA optimised algorithms there still remains multiple sources of false positives and negatives. Manual post processing is not amenable to automatic image analysis. Nuclei are not used for LVI quantification in the 'Marker Area' algorithm due to Definiens' hierarchical image analysis layers. Definiens image analysis algorithms produce multiple layers of tissue segmentation which allow objects to belong to other objects located on above or below layers. Therefore objects in a layer below other objects, such as marker 1 and marker 2 objects within but below the Stroma ROI layer, will always be connected to and belong to the Stroma ROI (Figure 34). This object relationship means that objects in a layer below retain the segmentation from the object in the layer above.

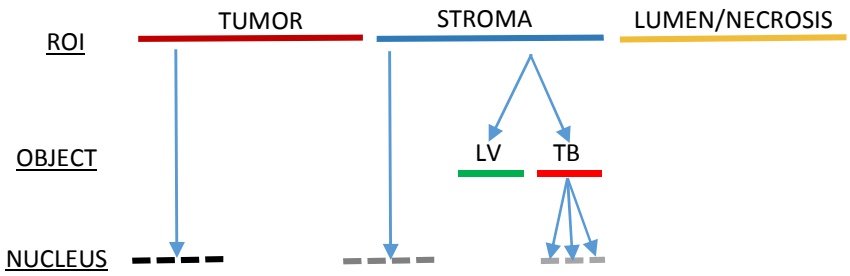

Figure 34. Definiens hierarchical image object relationships. Objects within image levels are connected in a hierarchical fashion. An object in an image level below another object will belong to that object and retain its' segmentation. E.g. LV = lymphatic vessel & TB = tumour bud both belong exclusively to the stroma ROI.

Object layer hierarchy cannot be altered in Tissue Studio®. In the Marker Area algorithm nuclei must always be in the hierarchical layer above 'markers' (panCK or D2-40). Therefore the nuclei segmentation dissects the objects in the layer below (Figure 35). This results in nuclei segmenting the objects below into multiple smaller objects and creating a false increase in numbers of positive tumour cell, vessel and LVI objects. This also results in the algorithm not being able to quantify nuclei within a marker object, making it impossible to report on the number of nuclei or cells which have invaded a vessel.

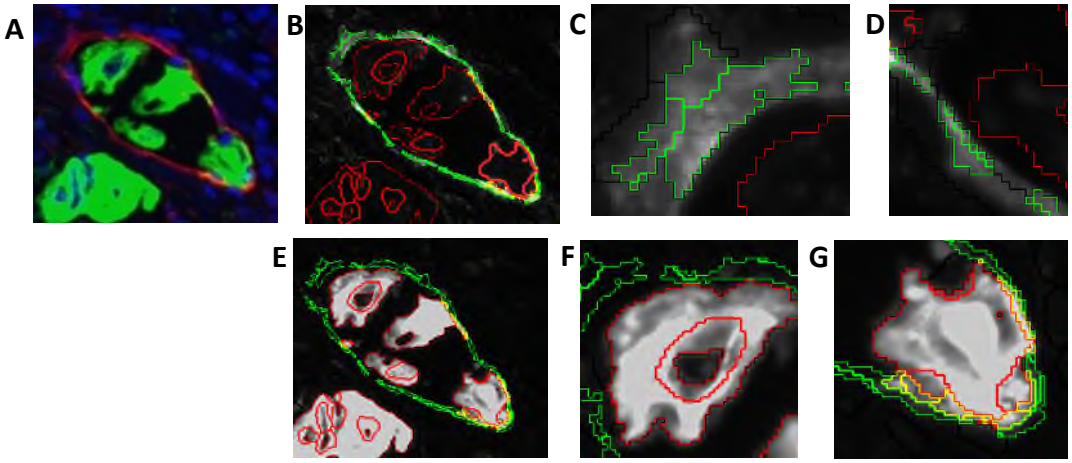

Figure 35. Marker 1 and marker 2 objects segmented by hierarchical objects within the layer above. A) composite raw image displaying occult LVI (green: panCK, red: D2-40, blue: nuclei). B) D2-40 image layer displaying panCK (red outline) and D2-40 (green outline) objects segmented by the image analysis algorithm. C) & D) Digital zoom of examples where the D2-40 positive lymphatic vessels have been segmented into multiple objects due to hierarchical image segmentation. E) panCK image layer displaying panCK and D2-40 objects segmented by the image analysis algorithm. F) & G) Digital zoom of examples where the panCK positive cancer cells have been segmented into multiple objects due to hierarchical image segmentation. Image captured with a x20 objective.

In the 'Marker Area' algorithm only basic intensities are measured and not complete cells or nuclei, therefore the algorithm can be prone to creating false positive objects due to staining artefacts. Quantification of LVI relies on the colocalisation of panCK and D2-40 markers. Only a small area, or sometimes none, of an invading cell's cytoplasm and membrane may colocalise with the D2-40 positive vessel wall, creating further challenges to accurately quantify the positive result.

Within the 'Vessel Detect' algorithm many true positives remain unquantified while false positives are detected. The main reason for this is stain intensity heterogeneity. Low DAPI intensity can result in nuclei being undetected while a high DAPI background can result in false nuclei being segmented. Similarly high and low background intensities for panCK and D2-40 may cause erroneous results. PanCK is primarily a membrane marker, however the algorithm relies on quantification of panCK intensity within the nuclei which may be low even in positive epithelial cancer cells. D2-40 is also measured within the nuclei and if a LVI positive cell is within the

lumen of a large vessel there may be very low D2-40 staining present in the segmented nuclear compartment resulting in an invading cell remaining unquantified.

There was too much scope for erroneous results to take the ‘Vessel Detect’ algorithm forward for a prognostic assay and so this algorithm was discarded. Although the ‘Marker Area’ algorithm quantified all correct LVI cores, it was felt that due to the constraints mentioned above true LVI and LVD could not be accurately quantified in a large heterogeneous patient cohort without further algorithm optimisation.

1.6 Image analysis development in Developer XD

Due to the constraints of the Tissue Studio® software the ‘Marker Area’ algorithm was imported into Definiens’ Developer XD image analysis software for further development. Developer XD is a much more flexible and powerful image analysis software, however it does not include pre-installed analysis algorithms and so image analysis solutions must be created through programming by the user. Pre-segmented images from Tissue Studio® can be imported into Developer XD and further developed. The images which had been segmented by the ‘Marker Area’ Tissue Studio® algorithm were imported into Developer XD in order to programme solutions to the constraints listed above. One addition in Tissue Studio® to the ‘Marker Area’ algorithm is the quantification of all nuclei through the DAPI channel. This was done in the same manner as detailed in section 3.5.1.3 for the ‘Vessel Detect’ IF algorithm.

Post import of the ‘Marker Area’ segmented images, the initial step within the Developer XD software is to split the analysis into two separate unconnected scenes. One scene contains only segmented marker 1 objects (panCK) and the other contains only marker 2 objects (D2-40). The nucleus level and all associated nuclear segmentation is deleted from both scenes at the marker 1 or 2 level. The algorithm next merges all neighbouring markers in each scene, and fills in any gaps enclosed by the newly formed object. Marker 2 objects are also expanded into any neighbouring area above 40au D2-40 intensity to capture more complete vessels and their lumen. This creates a more accurately segmented area of epithelial cell invasive bodies as well as vessels and their lumen (Figure 36).

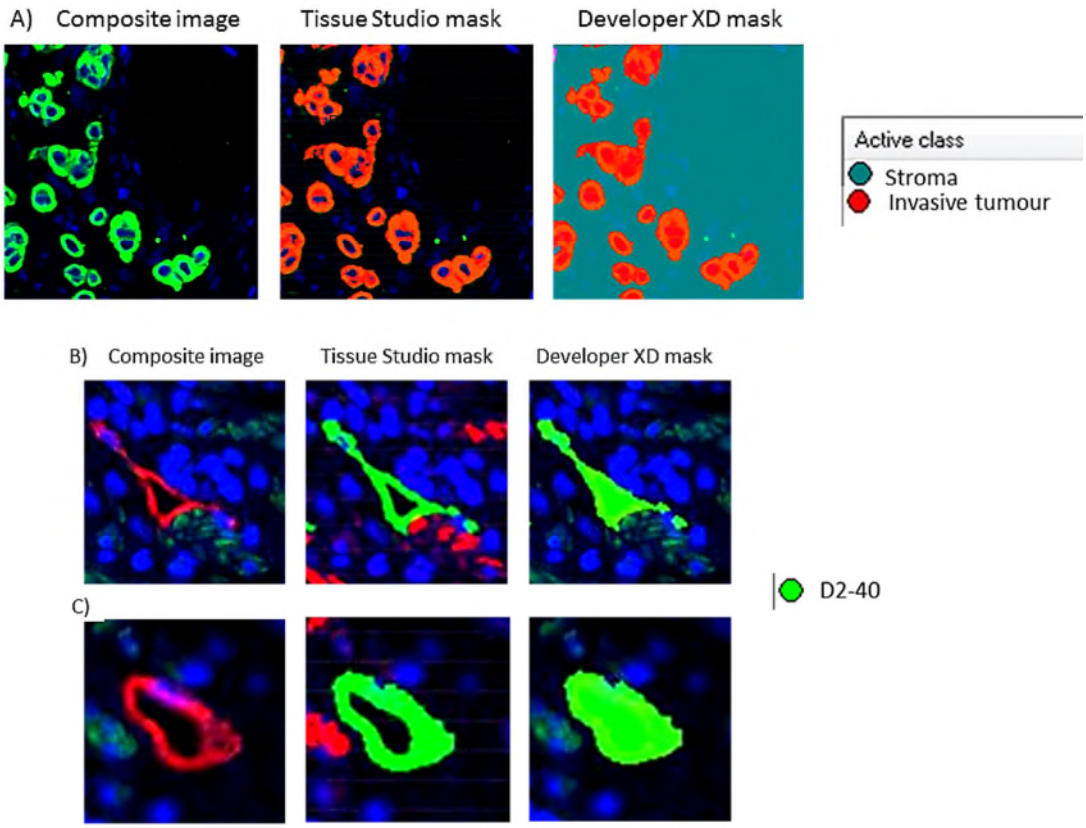

Figure 36. Developer XD optimisation of Marker object areas. A) Invasive tumour cells (green) with Tissue Studio and Developer XD image analysis mask (red). B) & C) Lymphatic vessels (red) with Tissue Studio and Developer XD mask (green). Images captured with a x 20 objective.

The DAPI channel along with its segmented nuclei is then reinstated as an image layer below the marker layer. This results in no false segmentation of markers by the nuclear segmentation while simultaneously allowing the number of nuclei within an invading cancer cluster to be quantified. A distance calculation of all marker 1 or 2 objects to 'no tissue' is programmed and a marker object within 50µm is automatically reclassified as 'edge effect' (Figure 37).

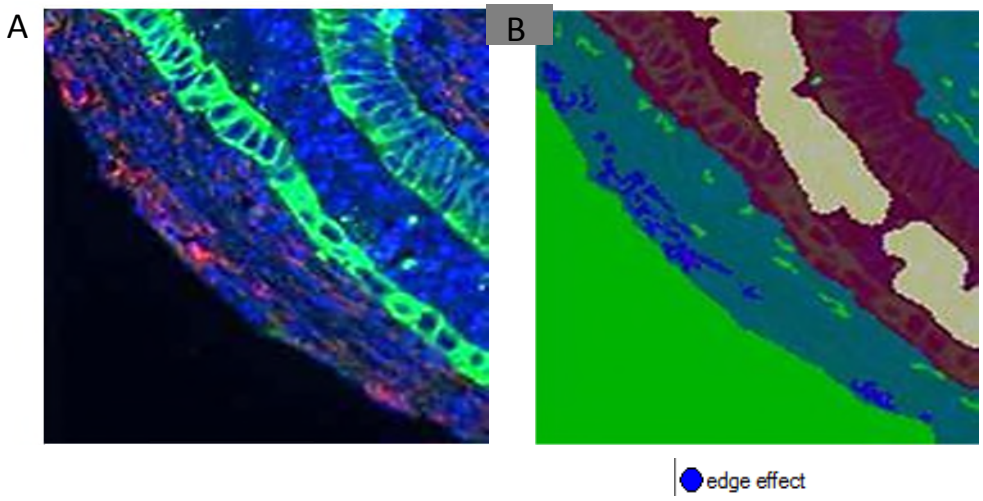

Figure 37. Automatic classification of edge-effect artefact by image analysis algorithm. A) non-specific labelling of D2-40 antibody at the edge of tissue. Algorithm classifies this as edge effect (blue mask). Images captured with a x 20 objective.

Any marker 1 (panCK) object below 55µm^2 was deemed to be too small to be a cell and therefore reclassified as 'debris'.

Due to heterogeneous levels of DAPI staining across cores, as well as varying levels of background DAPI intensities, some false nuclei are segmented. These are automatically 'cleaned up' and reclassified as 'false nucleus' within Developer XD programming (Figure 38). Similarly autofluorescence of muscle in the cy3 (panCK) channel as well as non-specific staining of panCK is reclassified as 'Non-specific CK' (Figure 39). Both 'false nuclei' and 'Non-specific CK' are excluded through area, intensity and texture parameters.

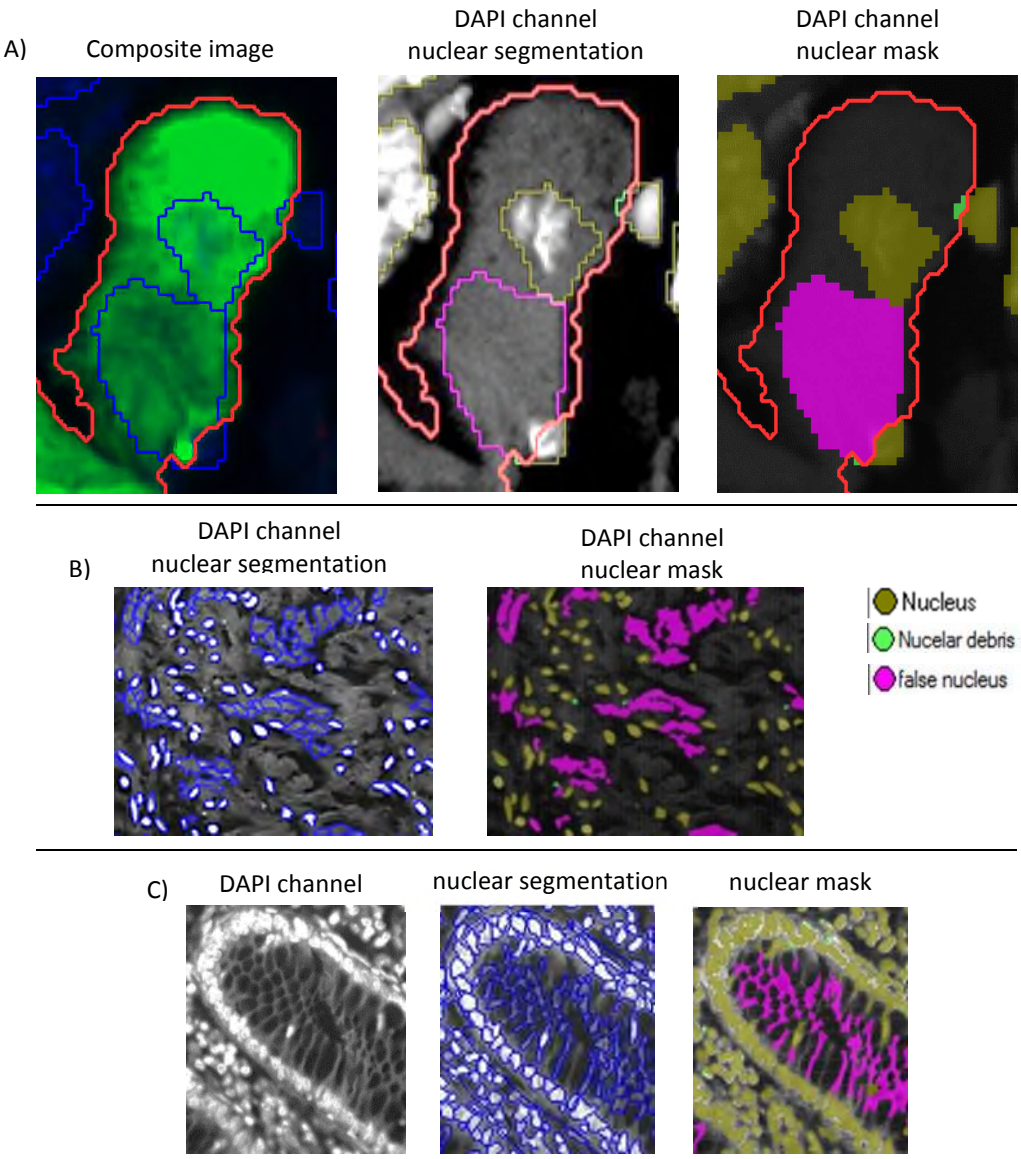

Figure 38. Automatic image analysis false nuclei re-classification. A) Composite image with nuclear segmentation overlay; DAPI channel only displaying high background intensity within cancer cells with classified nuclear segmentation; Developer XD mask classifying the false nucleus (pink) and the genuine nucleus (khaki). B) High stromal DAPI intensity results in multiple false nuclei which the image analysis algorithm corrects. C) High autofluorescence in DAPI channel within colonic glands; nuclear segmentation and algorithm mask correcting for the false nuclei. Images captured with a x 20 objective.

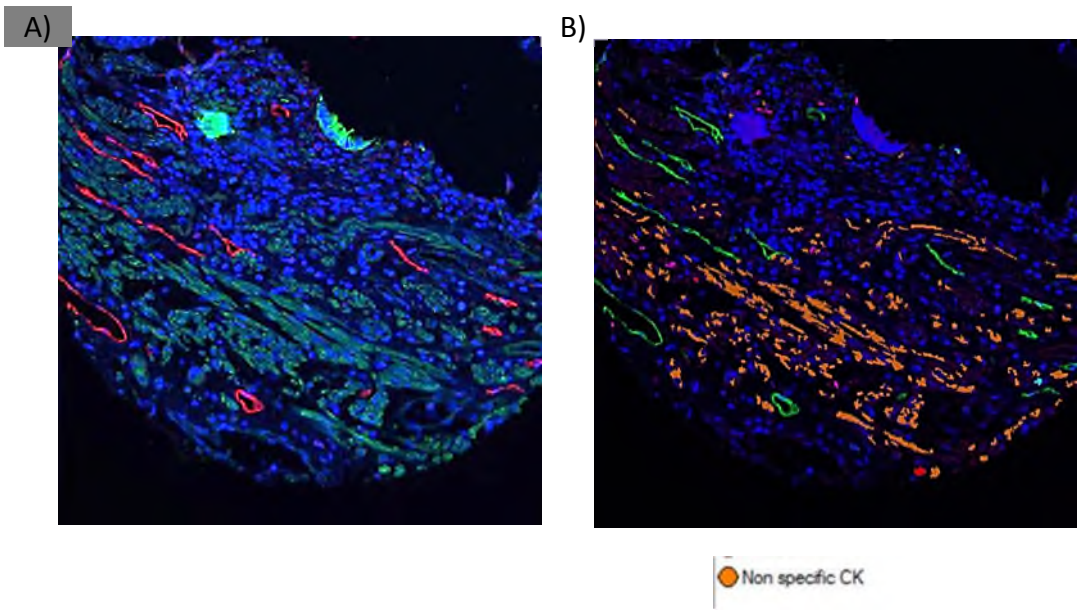

Figure 39. Automatic image analysis autofluorescence re-classification. A) Composite image (blue: DAPI, red: D2-40) where considerable autofluorescence (green) is captured within the panCK channel. B) Image analysis algorithm is programmed to identify autofluorescence and re-classify as Non-specific CK (orange). Images captured with a x 20 objective.

Once vessels (marker 2) and epithelial invasive clusters (marker 1) are accurately classified within their own image analysis scenes the two scenes are merged together and colocalisation of the optimised marker 1 and 2 is classified as 'marker 1&2' (Figure 40). Figure 40 also shows that the area of colocalisation captured in Tissue Studio® between a vessel's wall and invading cancer cells can be small and incomplete. Tissue Studio® analysis also does not always capture the entire vessel wall. Developer XD optimisation, as detailed above, allows not only the complete vessel wall to be segmented as one object, but also the vessel's lumen. Upon colocalisation, in Developer XD, whole invading cells with an accurate area of colocalisation are quantified. Marker 1&2 positive areas are further classified depending on the number of nuclei within the marker 1 object. The algorithm quantifies and exports cancer cell clusters with ≤5 associated nuclei within a vessel as 'occult LVI' and larger invading clusters (>5 associated nuclei) as LVI. LVD is also exported as a calculation of the marker 2 (vessels) area percentage of stroma (μm^2).

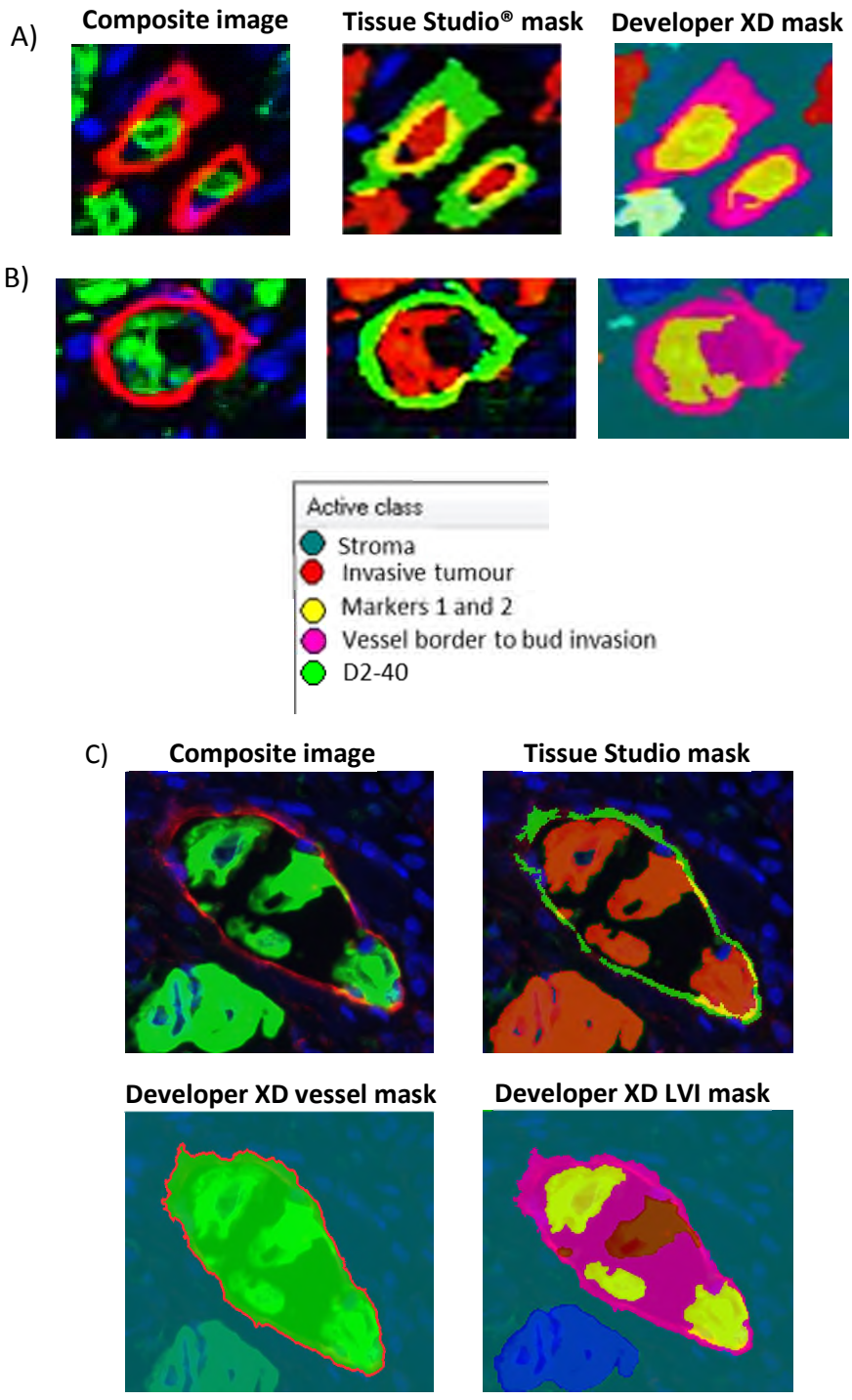

Figure 40. Developer XD algorithm's quantification of LVI. Composite image (red: D2-40, green: panCK, blue: DAPI). A) & B). Single cancer cell invasion of microvessels with Tissue Studio mask and Developer XD mask of colocalisation of marker 1 and 2 (yellow mask). Developer XD captures an accurate representation of the invading cancer cell. C) Only a very small area of colocalisation of four cancer cells within a vessel wall is quantified by the Tissue Studio algorithm (yellow mask). The Developer XD algorithm quantifies the entire vessel and thereby captures an accurate representation of all four invading cancer cells (yellow mask). Images captured with a x 20 objective.

The final Developer XD algorithm outlined above and optimised from the Tissue Studio® 'Marker Area' algorithm was used for all future results to quantify LVI and LVD. This algorithm was subsequently named the Lymphatic Vasculature Analyser (LVA).

1.7 Prognostic evaluation of Lymphatic Vasculature Analyser (LVA) quantified Occult LVI & LVD

1.7.1 Quantification of CRC training cohort TMA

The LVA allows a higher accuracy of quantifying lymphatic vessels and lymphatic vessel invasion. The training set TMA of 118 patient cores was labelled with the triple multiplexed immunofluorescence for panCK, D2-40 and DAPI. The algorithm was executed across the training set TMA images and the exported results of the number of occult LVI events and the LVD per patient were assessed for prognostic significance. The image analysis algorithm was completely automated with no manual interference. Results along with survival data were loaded into TMA Navigator for prognostic survival analysis. TMA navigator automatically splits the patients into up to three evenly sized groups according to each reported parameter from the analysis algorithms. Survival for each parameter is plotted as a Kaplan-Meier curve. Neither of the two parameters (occult LVI and LVD) was able to predict significantly poor prognosis or stratify patients into high or low risk groups (Figure 41).

Occult LVI events can be rare and often located at the invasive front of the CRC tumour. A single TMA core may be too low a sampling area to capture occult LVI events if they do occur within a patient's tumour. Similarly, manual quantification methodology for LVD usually requires the observer to locate LVD hotspots. These hotspots may not be captured by a single TMA core.

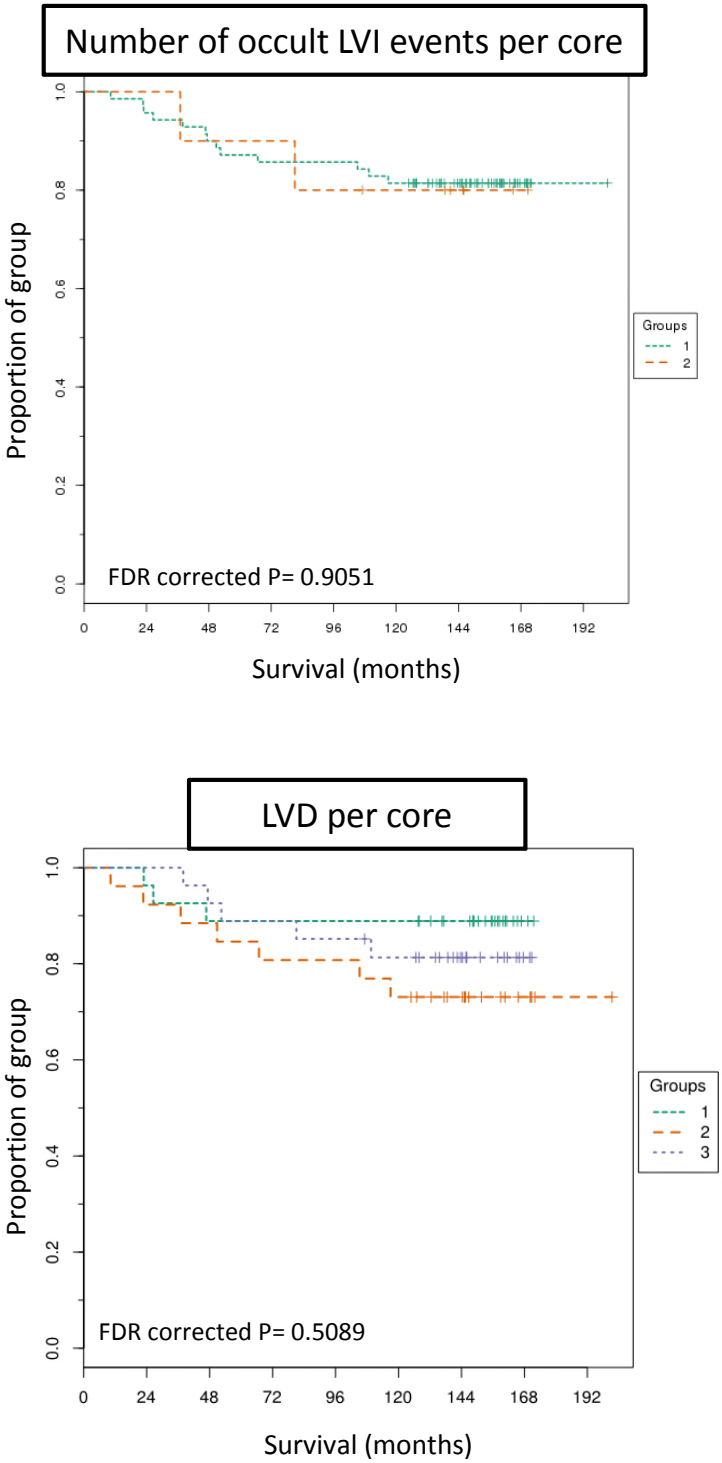

Figure 41. Kaplan-Meier curves for patients within the training set TMA (n=118) post quantification by LVA. Patients were not significantly stratified into high and low risk groups from quantification of occult LVI or LVD.

1.7.2 Quantification of CRC whole slide imaging

1.7.2.1 Training Cohort

To assess if a single TMA core was too low a sampling area to accurately report if a patient's tumour had invaded the lymphatic vasculature, a whole slide imaging approach was performed. The whole tissue section training set was utilized to assess the algorithm's export parameters' ability to stratify high and low risk patients of CRC specific death. All tissue sections were labelled with the triple immunofluorescence multi-plex assay of panCK, D2-40 and DAPI.

A low resolution 4x objective was emplyed to image the whole tissue section in the panCK channel on the HistoRX imaging platform. From this image the invasive front is manually located and highlighted for automatic imaging at high definition using the 20x objective (Figure 42).

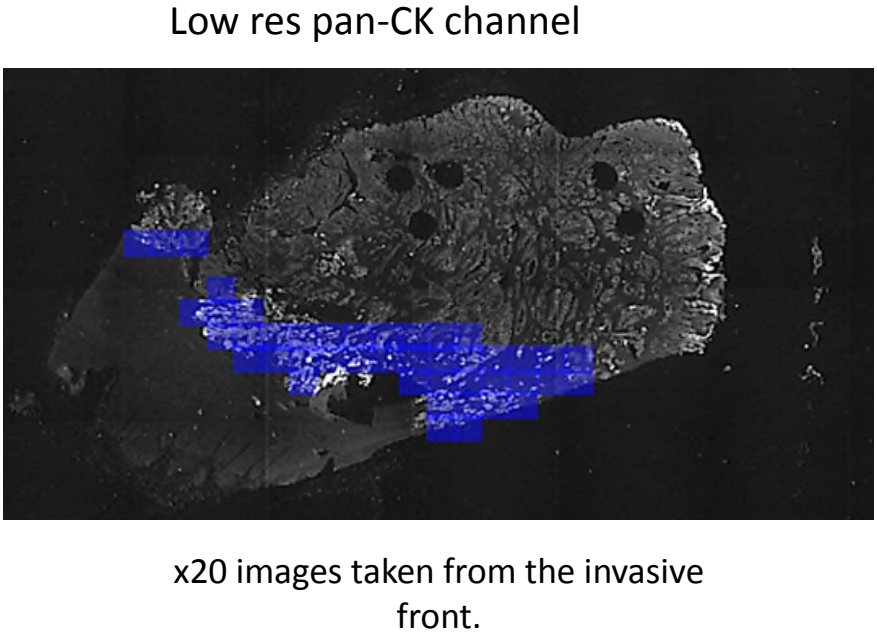

Figure 42. Locating the invasive front of CRC from whole slide imaging. Whole tissue section was digitised with a 4 x objective in the panCK channel. Invasive front is manually located and labelled for capture (blue squares) at high resolution through a 20x objective.

All 20x images are imported into Definiens Developer XD and LVA was executed across them. Due to inter-patient heterogeneity in labelled fluorophore intensities the initial algorithm thresholds in Tissue Studio® are set for each tissue section. Automated tissue segmentation is taught through the Composer Technology™ for each set of images from each tissue section. An ROI correction step was added to the Tissue Studio® tissue segmentation. This allows the end user to manually correct any erroneously automatically segmented tissue. After the initial intensity thresholds were set for each tissue section the algorithm is run automatically. Occult LVI and LVD results were exported from the LVA. The invasive front of the smallest tissue section was captured in its entirety by 15 images. Therefore only 15 images from the invasive front of subsequent tissue sections were used to quantify the histopathological features. The 15 images containing the highest number of occult LVI events were selected from each patient. The sum of all occult LVI events and the mean of LVD are calculated across the 15 images per patient for the final exported prognostic parameters.

1.7.2.1.1 Clinicopathological and Cox-regression analysis

Significant cut-offs for each parameter were calculated from the full Stage I-III training cohort for high and low sub-groups and their significance established by Monte Carlo simulations for occult LVI (cut-off = 16 LVI events across 15 images, p <0.0001), LVD (cut-off = 0.7 vessel percentage of stroma averaged across 15 images, p = 0.002). The cut-offs established in this manner were then applied to stratify the Stage II subpopulation. Clinicopathological data, from the corresponding pathology report, the quantified occult LVI and LVD parameters and regression analysis are summarised in Table 7. Univariate analysis showed occult LVI (HR =9.9; 95% CI, 3.57-27.98) and LVD (HR =5.1; 95% CI, 2.04-12.99) to be significant predictors of survival within the cohort. In multivariable cox-regression analysis the predictive model was adjusted for T stage, N stage, Dukes stage, occult LVI and LVD, these being the four parameters which reported significance in univariate analysis, and the results showed that only depth of local invasion (T stage, HR = 5.22; 95% CI,1.77-15.44) and occult LVI (HR =6.08; 95% CI, 1.17-31.41) were independent predictors of survival. To assess if LVD and occult LVI were associated Pearson's correlation

was performed and found them to be significantly correlated (r=0.71, p <0.0003) (Figure 43).

Clinicopathological parameters	patient number (n)	Univariate				Multivariable			
		HR	95% CI		P value	HR	95% CI		P value
			lower	upper			lower	upper	
Stage		**3.34**	**1.61**	**7.01**	**0.001**	0.33	0.08	1.36	0.12
I	13								
II	29								
III	8								
Gender		1.77	0.73	4.31	0.26	N/A			
M	24								
F	26								
Age at diagnosis		0.99	0.92	1.05	0.773	N/A			
30s	5								
40s	27								
50s	18								
T stage		**3.04**	**1.53**	**6.03**	**0.001**	**5.22**	**1.77**	**15.44**	**0.03**
pT1	7								
PT2	7								
pT3	27								
pT4	9								
N Stage		**2.62**	**1.54**	**4.46**	**<0.001**	1.62	0.69	3.81	0.27
N0	40								
N1	8								
N2	1								
N3	1								
Differentiation		1.14	0.37	3.54	0.83	N/A			
Well	5								
Moderate	39								
Poor	6								
Histology		0.49	0.11	2.11	0.34	N/A			
Standard	42								
Mucinous	8								
Site		0.77	0.45	1.31	0.33	N/A			
Rectal	17								
Right side	17								
Left side	16								
Occult LVI		**9.99**	**3.57**	**27.98**	**0.0001**	**6.08**	**1.17**	**31.41**	**0.03**
High	17								
Low	33								
LVD		**5.15**	**2.04**	**12.99**	**0.0001**	1.3	0.3	5.59	0.72
High	19								
Low	31								

Table 7. Clinicopathological data with associated univariate and multivariable analysis for disease specific survival within the CRC training cohort.

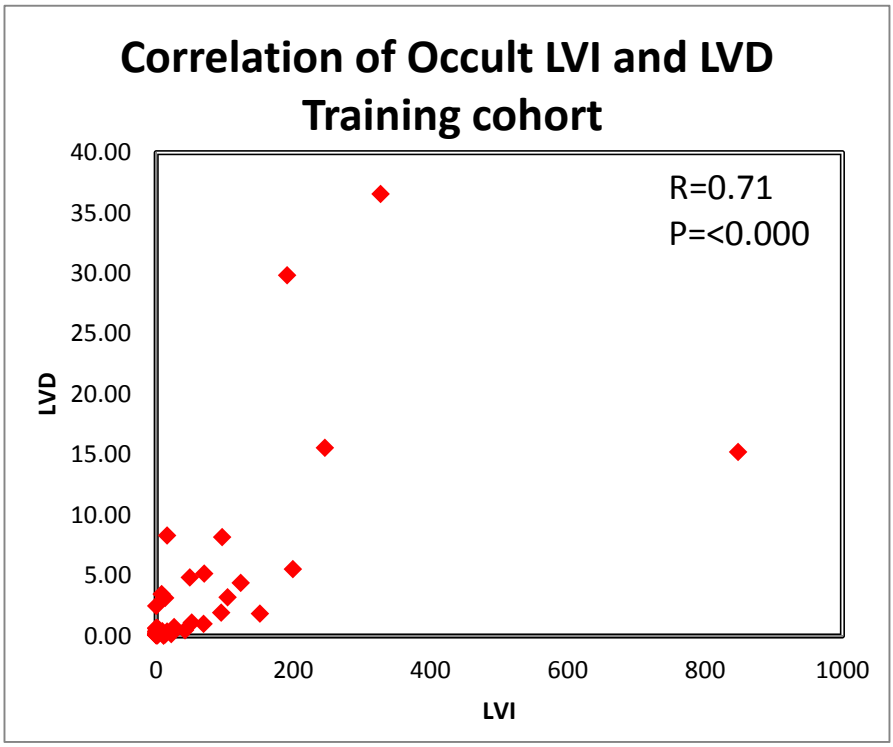

Figure 43. Pearsons' correlation of LVD and Occult LVI within the training cohort.

1.7.2.1.2 Kaplan-Meier survival curves

Kaplan-Meier plots were computed to assess the ability and significance of LVD and occult LVI in stratifying high and low risk CRC patients and particularly the stratification of Stage II patients.

1.7.2.1.2.1 Lymphatic vessel density

High LVD was significantly associated with poor outcome and shorter disease specific survival in the full training cohort (p = 0.0001) and the Stage II subpopulation (p = 0.0001). Only 26% of patients within the full training cohort and 11% within the Stage II subpopulation, who were within the above-cut-off LVD (> 0.7% vessel density) group, survived full follow up. All 8 Stage III patients were within the high LVD subgroup (Figure 44).

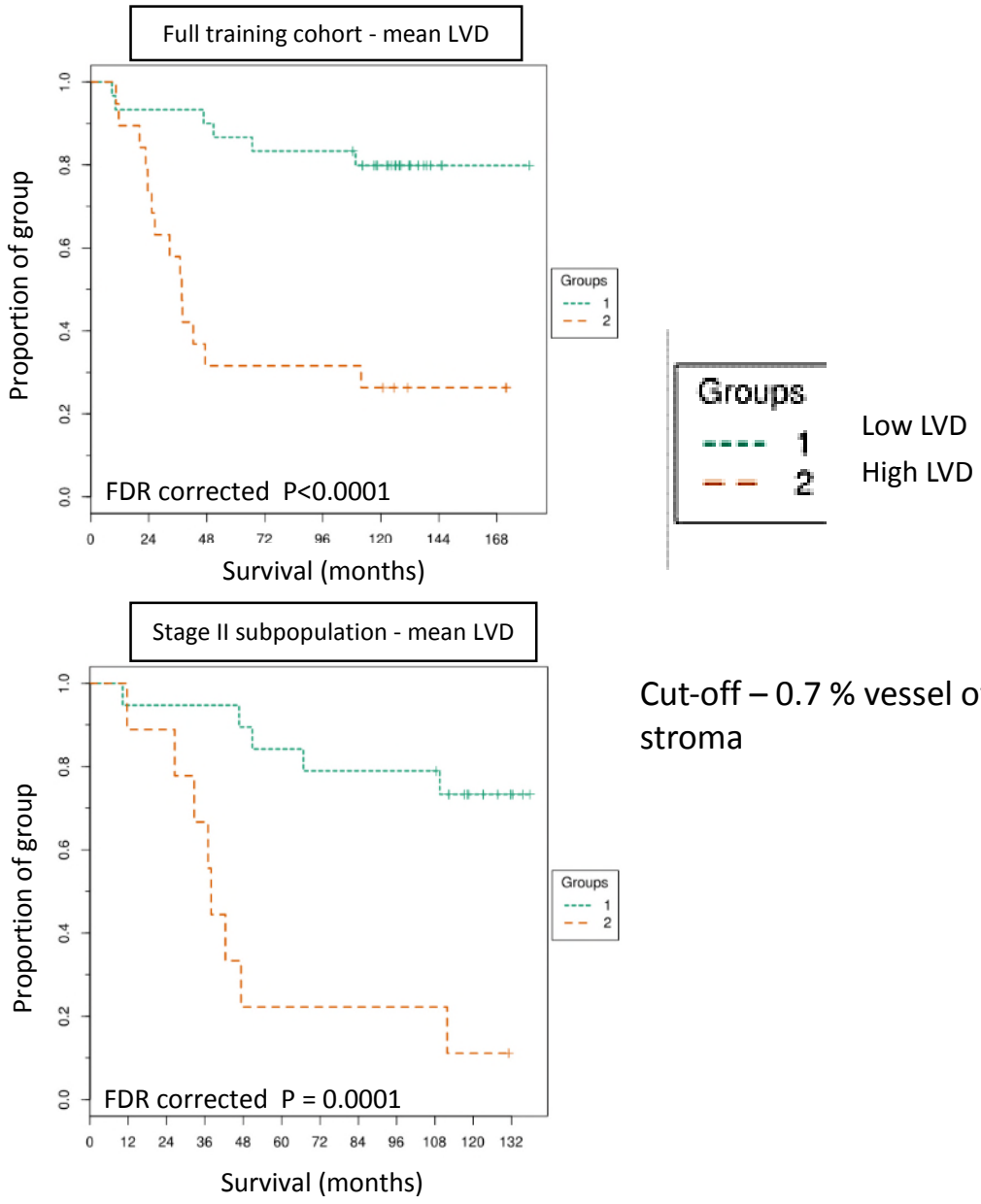

Figure 44. Kaplan-Meier curves for LVD; training cohort whole slide imaging. Patients within the full cohort (n=50) and the stage II subpopulations (n=29) were significantly stratified into high and low risk of disease specific death through the quantification of LVD.

1.7.2.1.2.2 Occult lymphatic vessel invasion

KM analysis was performed and occult LVI was shown to be the most significantly prognostic parameter associated with shorter survival times in both the full training cohort (p <0.0001) and the Stage II subpopulation (p <0.0001) (Figure 45). No patients survived full follow up within the above cut-off occult LVI group (>16 occult LVI events) in the Stage II patient subpopulation and only 11% survived follow up within the full cohort.

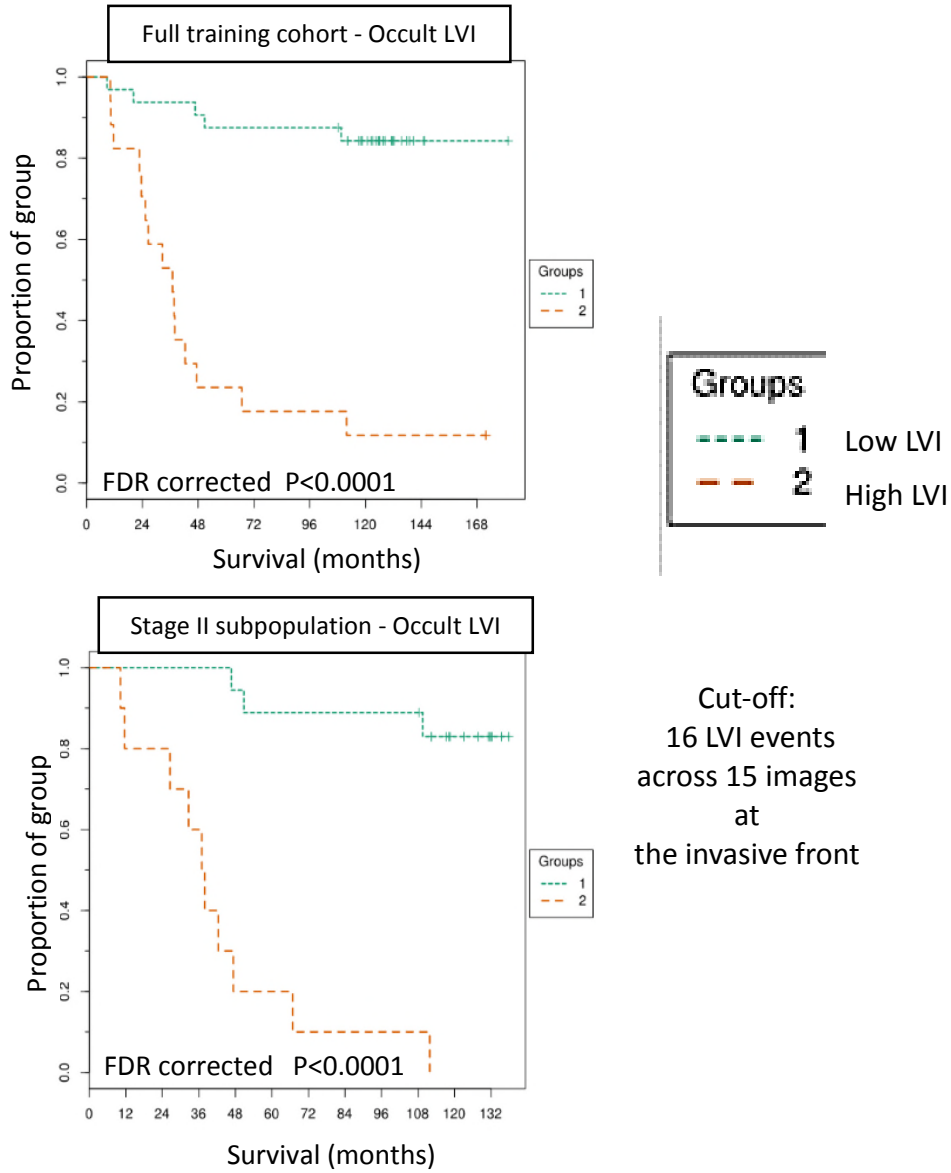

Figure 45. Kaplan-Meier curves for Occult LVI; training cohort whole slide imaging. Patients within the full cohort and the stage II subpopulations were significantly stratified into high and low risk of disease specific death through the quantification of Occult LVI.

1.7.2.2 Validation cohort

Both LVD and occult LVI are predictors of disease specific death within the 50 patient training cohort and the stage II subpopulation (n=29). The main objective of this chapter was to determine if the quantification of LVD and occult LVI allowed the stratification of high risk Stage II patients. To validate the results from the training set a clinically relevant and larger validation cohort, consisting of 134 Stage II patients, was analysed by the LVA algorithm across WSI captured images.

The immunofluorescence and image acquisition methodology as well as image analysis was identical to section 3.7.2.1.

1.7.2.2.1 Clinicopathological and Cox-regression analysis

Training set LVD and occult LVI parameter cut-offs were applied to the validation set results and the corresponding data assessed for significance in survival prediction by cox-regression analysis.

Clinicopathological data and regression analysis is summarised in Table 8. Univariate analysis showed high occult LVI (HR =2.46; 95% CI, 1 - 6.05) but not high LVD (HR =1.39; 95% CI, 0.46 - 4.16) to be significant predictors of survival within the validation cohort. The hazard ratio and significance of the occult LVI parameter was however greatly reduced within the validation set, compared to the training set.

From the clinicopathological core data set parameters only T-stage and differentiation were also significant predictors of disease specific death. Pearson's Correlation showed that Occult LVI and LVD were correlated within the validation cohort (R = 0.64, $P<0.0001$) (Figure 46).

Clinicopathological parameters	patient number (n)	Univariate			
		HR	95% CI		P value
			lower	upper	
Stage					
II	134				
Gender		0.933	0.601	1.45	0.759
M	69				
F	65				
Age at diagnosis		1.4	0.82	2.41	0.22
<=70	52				
71-79	39				
>=80	43				
T stage		**4.26**	**1.76**	**10.33**	**0.001**
pT3	102				
pT4	32				
Differentiation		**2.17**	**1.14**	**4.13**	**0.018**
Well	3				
Moderate	109				
Poor	22				
Histology		0.82	0.27	2.49	0.72
AC	121				
MC	7				
AC/MC	6				
Site		0.87	0.5	1.51	0.61
Rectal	42				
Right side	47				
Left side	45				
Tumour Diameter*		1.7	0.66	4.42	0.27
<5cm	68				
≥5cm	48				
Total Node examined		0.6	0.24	1.5	0.27
<12	35				
≥12	99				
EM LVI		0.359	0.14	0.94	0.04
Yes	20				
No	114				
Occult LVI		**2.46**	**1**	**6.05**	**0.05**
High	35				
Low	99				
LVD		1.39	0.46	4.16	0.56
High	25				
Low	109				

Table 8. Clinicopathological data with univariate cox-regression analysis for disease specific survival within the validation cohort.

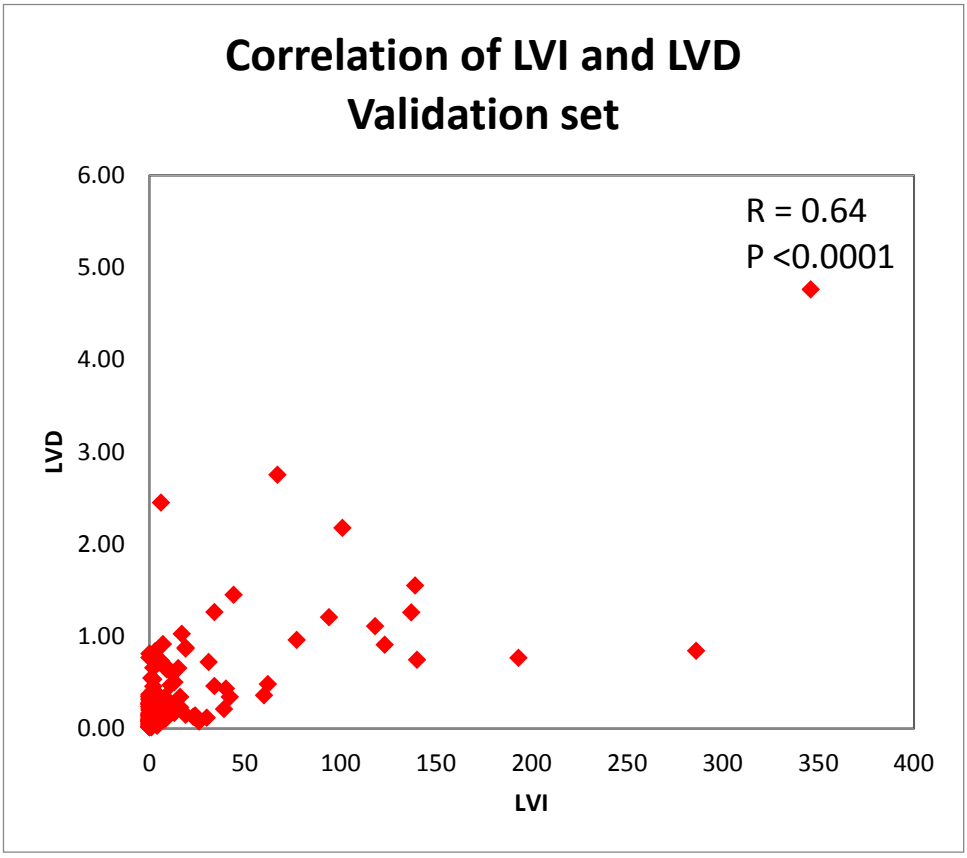

Figure 46. Pearsons' correlation of LVD and Occult LVI within the validation cohort.

1.7.2.2.2 Kaplan-Meier survival curves

Survival over time was calculated and plotted on KM curves for both LVD and occult LVI

1.7.2.2.2.1 Lymphatic vessel density

LVD was not associated with poor outcome and shorter disease specific survival in the Stage II validation cohort (p = 0.56). High and low LVD cut off groups could not be stratified into high or low risk patient groups across overall disease specific survival (Figure 47).

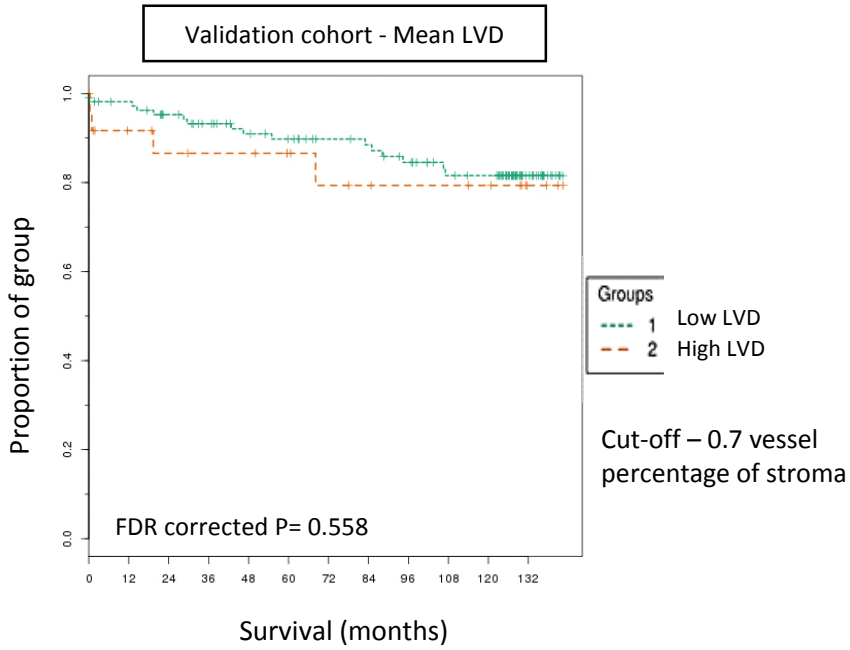

Figure 47. Kaplan-Meier curves for LVD within the validation cohort (n=134). Patients within the validation cohort were not significantly stratified into high and low risk of disease specific death through the quantification of LVD.

1.7.2.2.2.2 Occult lymphatic vessel invasion

KM analysis was performed for occult LVI on the Stage II validation cohort. Occult LVI was shown to be a significantly prognostic parameter associated with shorter overall survival times (p = 0.05). The results reflect the Cox-regression analysis and occult LVI is much less significant at high risk patient stratification than in the training cohort results (Figure 48).

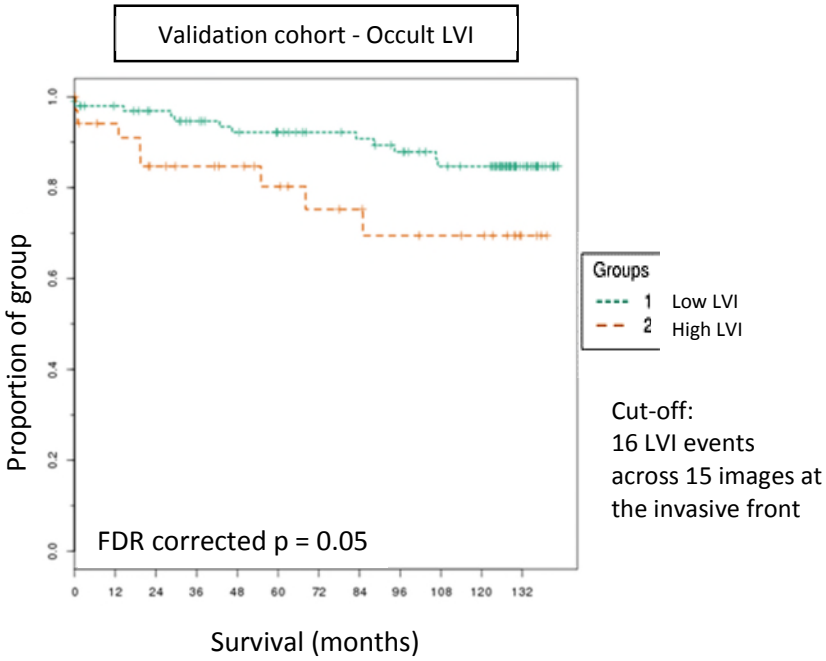

Figure 48. Kaplan-Meier curves for occult LVI within the validation cohort (n=134). Patients within the validation cohort were significantly stratified into high and low risk of disease specific death through the quantification of occult LVI.

1.7.2.3 Total Lymphatic vessel invasion

In the previous studies within this chapter occult LVI was quantified and reported by the image analysis algorithm. Occult LVI was defined as small islands of tumour cells, of 1-5cells in size, which had invaded a lymphatic vessel. Although a highly significant prognostic parameter within the training set, occult LVI was only marginally significant in the validation set. In order to attempt to stratify high risk stage II patients more effectively and significantly a parameter named 'Total LVI' was exported from the analysis algorithm. The LVA already quantifies LVI involving tumour clusters which are larger than 5 cells, although this parameter was not yet used in this study. The number of 'LVI' was subsequently added to 'occult LVI' to create a new parameter of 'Total LVI'. An optimal cut-off of 43 'Total LVI' events (p <0.0001) was calculated for the training set by Monte Carlo simulations within X-tile software. This cut-off was then applied to the Stage II patient validation set and KM curves were

plotted for both the stage II populations of the training cohort and validation cohort (Figure 49).

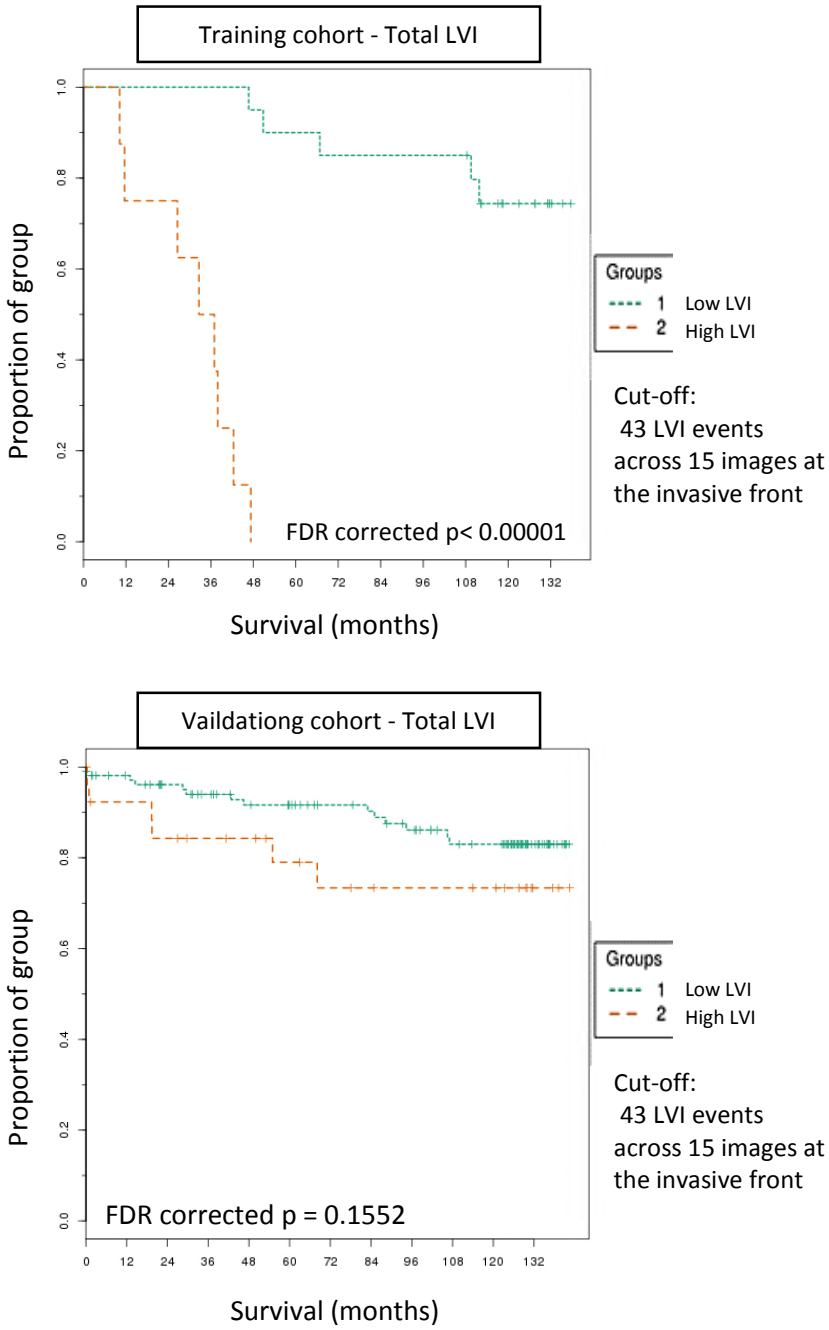

Figure 49. Kaplan-Meier curves for Total LVI within the training (n=50) and validation cohort (n=134). Total LVI was highly significant in stratifying patients within the training cohort into high and low risk of disease specific death; however this parameter was not significant within the validation cohort.

Compared to occult LVI, 'Total LVI' increased patient stratification for the training cohort where no patients in the high cut-off group survived for over 4 years (p <0.00001), however it decreased the significance of patient stratification within the validation cohort to below a significant threshold (p = 0.15).

1.7.2.4 Optimal Validation set cut-offs

Optimal training cohort cut-offs were calculated by performing 1000 iterations of Monte Carlo simulations and identifying the optimal p value from KM curves. Upon plotting p values for each possible cut-off of the training cohort it was observed that large ranges of cut-offs were highly significant for Occult LVI and Total LVI (Figure 50A, 51A). The computationally selected training cohort cut-off, which was one of many possibilities, may therefore not be the optimal cut-off for the validation cohort. Other significant cut-offs from the training cohort may be more significant for the validation cohort. In order to identify a cut-off which is significant for both the training cohort and the validation cohort all possible p values for both cohorts were plotted on the same graph. This was performed for Occult LVI, Total LVI and LVD (Figure 50A, 51A, 52). A cut-off was then selected which was highly significant, in relation to KM curve p values, for both the training cohort and the validation cohort.

1.7.2.4.1 Kaplan-Meier survival curves

This new optimal cut-off was utilised to sub-stratify the Stage II patients within the validation cohort into high and low risk of disease specific death by plotting the survival times as a KM curve. The new optimal cut-off for Occult LVI was 19 events and this reported a p value of <0.0001 for the training cohort and 0.018 for the validation cohort. The significance in the training cohort was not altered, however the significance increased from a p value of 0.05 to 0.018 in the validation cohort upon plotting when utilising the new cut-off (Figure 50 B).

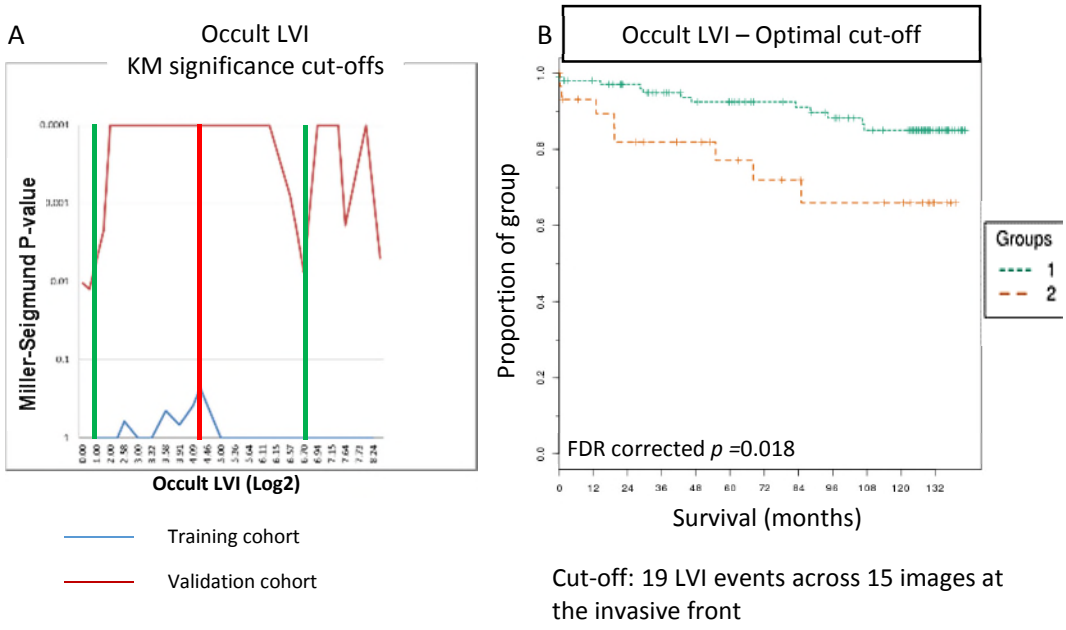

Figure 50. Assessment of optimal cut-offs within the training and validation cohorts for occult LVI. A) *P* values for all possible cut-offs within the training cohort and validation cohort were plotted on the same graph. An optimal cut-off of 19 occult LVI events was selected which reported significant values for both cohorts (red line). The green lines mark the area containing 80% of the training cohort. B) The optimal cut-off of 19 occult LVI was utilised to plot Kaplan-Meier curves which significantly stratified the validation cohort (n=134) into high and low risk of disease specific death.

The new optimal cut-off for Total LVI was 37 events and this reported a *p* value of <0.0001 for the training cohort and 0.01 for the validation cohort. The significance in the training cohort was not altered, however the significance increased from a *p* value of 0.15 to 0.018 in the validation cohort (Figure 51B).

Occult LVI and Total LVI yielded identical significance and stratification of high- risk stage II patients within the validation cohort.

There was no significant LVD cut-off for the validation cohort at any data-point and therefore LVD was deemed to be non-significant in a larger clinically relevant stage II patient cohort (Figure 52).

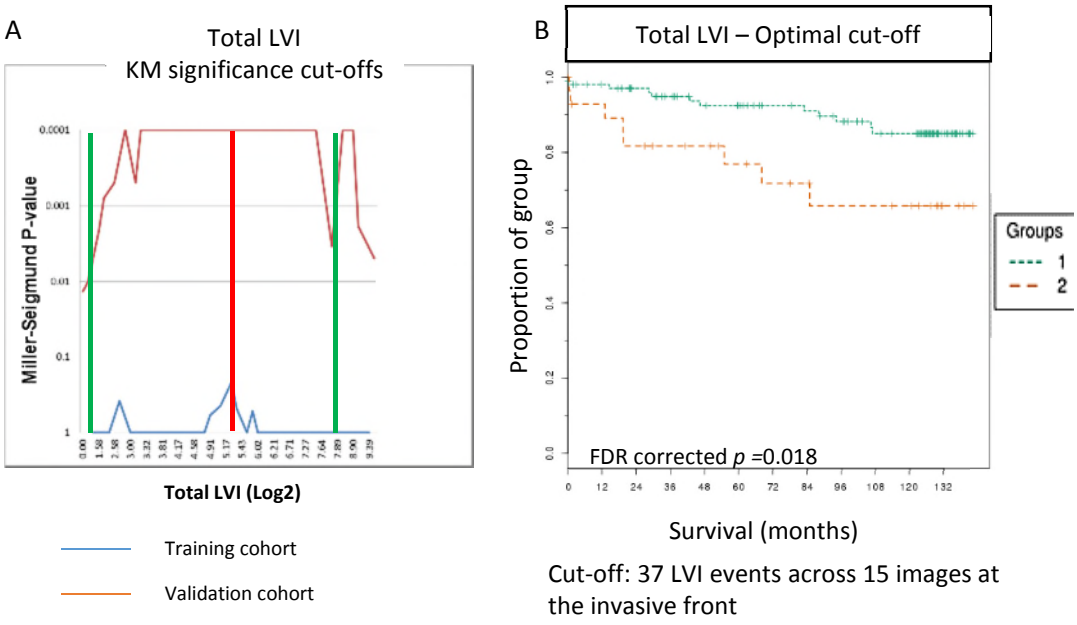

Figure 51. Assessment of optimal cut-offs within the training and validation cohorts for Total LVI. A) *P* values for all possible cut-offs within the training cohort and validation cohort were plotted on the same graph. An optimal cut-off of 37 Total LVI events was selected which reported significant values for both cohorts (red line). The green lines mark the area containing 80% of the training cohort. B) The optimal cut-off of 37 Total LVI was utilised to plot Kaplan-Meier curves which significantly stratified the validation cohort (n=134) into high and low risk of disease specific death.

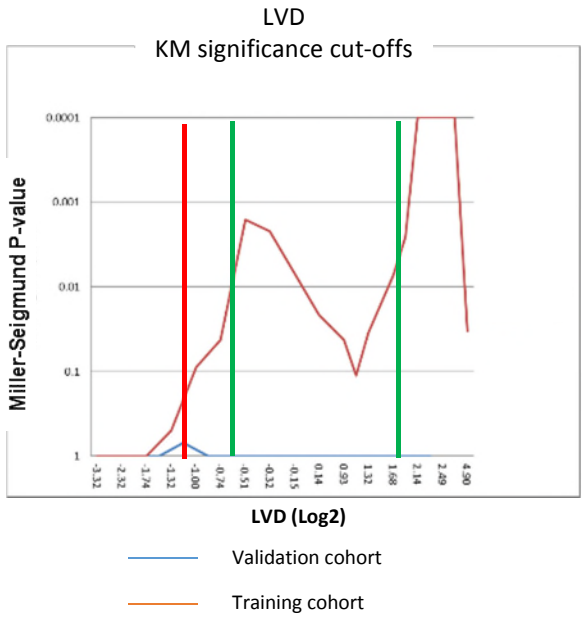

Figure 52. Assessment of optimal cut-offs within the training and validation cohorts for LVD. A) *P* values for all possible cut-offs within the training cohort and validation cohort were plotted on the same graph. There was no significant cut-off associated with the validation cohort which was optimal for the training cohort.

1.7.2.4.2 Cox-regression analysis

Univariate cox-regression analysis was performed on the categorical sub-grouped Stage II validation cohort, after applying the new optimal cut-off, for both occult LVI and total LVI. Both of the LVI parameters were significant predictors of disease specific death with identical hazard ratios (HR= 2.9) and *p* value significance (p =0.02) (Table 9), which reflected the KM curve results.

Clinicopathological parameters	patient number (n)	Univariate			
		HR	95% CI		P value
			lower	upper	
Occult LVI		2.9	1.2	7	0.02
High	30				
Low	104				
Total LVI		2.9	1.2	7.1	0.02
High	29				
Low	105				

Table 9. Univariate Cox regression of occult LVI and Total LVI utilising optimal cut-offs on the Validation cohort.

1.8 Discussion

Venous invasion is widely under-reported in the clinic with large observer variability when observing under H&E stained tissue sections alone(266, 291, 295). To overcome this problem pathologists are employing the use of specific stains such as CD31(286) and, more commonly in the clinic, elastic based labelling(279, 291, 295). These studies show an increase in observer concordance as well as an increase in the number of events reported. The increase in the reporting of blood vessel invasion was shown to have a prognostic impact correlated to poor outcome or prediction of metastasis(47, 279, 296).

In this study it was found that Elastica staining and CD31 did not label all blood vessels and it displayed incomplete staining of the venous vasculature, which could allow for some venous invasion to go unreported. Although it clearly has the potential to be utilised to aid the reporting of venous invasion by manual quantification(279), it would be unsuitable for computer-based quantification. The disadvantage of computer-based quantification is the lack of extra histological knowledge which can be gleaned from manual observation even with feint and incomplete venous labelling. Due to this fact image analysis contrasts must have a high signal to noise ratio and allow robust staining of vessels in order to quantify them accurately under computer-based analysis. Blood vessel invasion was therefore not included in the automated vasculature quantification within this study.

Unlike CD31 and Elastica based staining, D2-40 immunohistochemistry demonstrated strong staining of lymphatic vessels. The study therefore concentrated efforts on quantifying LVI and LVD through automated image analysis. LVI is not included in the clinical core data set as described by RcPath(102) due to insufficient evidence of significance in prognosis. A reason for lack of evidence is that pathologists do not routinely quantify LVI due to its obscurity in H&E stained sections. This, alongside no standardised reporting methodology, are contributing factors for the absence of lymphatic vascular based prognostic features from the clinical core data set and so standard practice is not to routinely report LVI or LVD in the clinic. Automated quantification, however, adds robustness and standardisation to histopathological feature reporting while minimising observer variability. LVI alone has been associated with lymph node metastasis (LNM) and poor outcome (252, 260). The under-recognition of LVI may therefore be a contributing factor for the under-staging of CRC patients (252, 266) and disease recurrence in ~30% of the Stage II population (245, 297).

Definiens Tissue Studio is an “out of the box” image analysis solution which comes with multiple pre-installed image analysis algorithms. Although the software is user-friendly and powerful it is not flexible. The study attempted to quantify LVI and LVD through two of the pre-installed algortihms. Although LVD could be quantified accurately through the ‘Vessel Detect’, algorithm LVI could not. Due to patient

heterogeneity and tissue artefact many false positives were associated with LVI quantification. Manual post processing of the data can correct most false positives but this negates the advantage of automated image analysis. Although studies do perform image analysis to quantify histopathological features through pre-installed manufacturer software algorithms, they do not address how they overcome image-based problems such as biomarker intensity heterogeneity and tissue artefacts without manual intervention(298, 299). To overcome the complexity of accurately quantifying tumour cells within vessels, Tissue Studio® was purely utilised to segment the tissue. Developer XD is a much more programmer-intensive software package but allows for much greater flexibility. By importing the Tissue Studio® segmentation into Developer XD the constraints of the algorithm can be overcome allowing the accurate quantification of entire vessels and invasive tumour, as well as quantifying the number of cells within the cancer clusters. Developer XD also allowed the automated exclusion of false positives due to heterogeneity and tissue artefacts.

Our methodology quantifies tumour cell clusters of either under or over 5 cells in size which have invaded lymphatic vessels; which were termed as ‘occult LVI’ or ‘LVI’ respectively. The sum of the two parameters was termed ‘total LVI’. The results show that occult LVI and total LVI are significantly prognostic in the training cohort. Occult LVI is also significantly associated with disease specific death in the validation cohort when the training set cut-off is applied; however Total LVI is not. KM analysis shows that no stage II patients with above cut-off LVI survived follow up within the training cohort. Occult LVI was also the only image based quantified parameter to be associated independently with an adverse effect on disease specific survival in the training cohort and it was also significant at predicting poor outcome in univariate analysis in the validation cohort when the training cohort cut-off was applied.

Some studies have shown LVD to be prognostic and associated with poor outcome or LNM (292, 300), however others show that no correlation exists (283, 301). LVD assessment is, however, not standardised and most researchers employ various magnifications and numbers of LVD “hot-spots” utilised to create a mean LVD while observer variability has been shown to be poor (283). Bias is therefore introduced in these studies which can be negated by WSI and automated image analysis of the

invasive front or entire tissue sections. In the methodology, which was demonstrated here, the stroma is automatically segmented from the tumour and by doing so it was possible to calculate the LVD only within the stromal compartment. The methodology does not rely on the manual locating of LVD hot-spots, rather it quantifies LVD across 15 images taken from the invasive front and which contained the highest occult LVI events. By adopting this LVD calculation and minimising sampling bias, it was shown that LVD is significantly associated with poor outcome ($p = 0.0001$) in a small training cohort, however it is not significant when quantified across a large and clinically relevant validation cohort (p= 0.56). All stage III patients within the training set were within the high category of LVD which suggests that lymphangiogenesis may occur as the disease progresses. It is unknown whether lymphangiogenesis occurs due to a host reaction attacking the tumour or by tumour cell signalling; however the results show that LVI is correlated to LVD (r=0.71, p<0.0003) which is in accord with separate studies (281, 302).

The training cohort in this study was specifically selected for similar numbers of stage II patients who survived or died specifically of CRC during follow up. Although this is a relevant cohort to test if image analysis quantification of occult LVI and LVD can stratify the two groups, it is not a clinically representative cohort and therefore the cut-offs calculated within the training cohort may not be optimal when applied to a larger validation set. The training cohort had multiple highly significant cut-offs and the X-tile software, used to identify significant cut-offs in data sets, selected one of these automatically. Upon applying the LVI based training cohort cut-offs to the validation cohort occult LVI was just significant prognostically, but Total LVI was not. Identifying an optimal cut-off for the validation cohort alone would defeat the purpose of including a training cohort and therefore an “optimal” cut-off was identified which was highly significant for both CRC cohorts and utilised to stratify the validation cohort. Upon applying the optimised cut-off to the training cohort no decrease in significance was observed in occult LVI ($p < 0.0001$). When applying the optimised cut-off to the validation cohort the prognostic significance of both occult LVI and Total LVI increased to $p = 0.018$ for KM patient stratification and a hazard ratio of 2.9 with associated significance of $p = 0.02$ in cox regression prediction of disease specific death. Interestingly occult LVI and Total LVI yielded identical prognostic results. This

suggests that small clusters of cancer cells invading into microvessels are an indicator of poor prognosis and a risk of disease specific death, presumably via distant metastasis through the lymphatic vasculature. Isolated tumour cells within lymph nodes have shown to be predictors of disease relapse(251) however an automated image analysis algorithm requiring only a single tissue section per patient would save considerable time over the manual quantification of multiple tissue sections from multiple lymph nodes per patient.

In summary this study reports a novel computer based methodology to identify and quantify the prognostic histopathological features of LVI and LVD across the invasive front of colorectal carcinoma. The features are captured and exported from a single tissue section using one continuous image analysis algorithm: LVA. This saves considerable resource, compared to serial sectioning and staining across multiple tissue blocks per patient, prior to manual semi-quantification of each histopathological feature. The LVA negates observer variability or bias and allows the standardised quantification of LVI thus making the approach amenable to a time-dependent clinical setting.

Chapter 4: Quantifying Tumour Budding through Image Analysis

1.1 Introduction

Although TNM classification is the gold standard in CRC prognosis(239, 241), there have been multiple attempts to improve on its ability to stratify high risk CRC patients. Tumour morphology(68) and differentiation(303, 304) are two histological features which have been investigated in an attempt to identify a more invasive or aggressive cancer. Jass *et al* proposed a novel way to grade CRC which was based on differentiation, lymphocytic infiltration and the morphology of the invasive margin (an expanding and pushing border or an infiltrative one) (Figure 54)(236).

Initial results proved promising, however, they were unable to be reproduced independently(305) and, although observer variability was good for infiltrative border, it was poor for lymphocytic infiltration(267). The concept of prognostic value being attached to tumour morphology at the invasive front of CRC was re-investigated predominantly by a group of Japanese researchers who investigated clusters of tumour cells unattached to tumour glands at the invasive front. Morodomi(306) in 1989 was the first to term this phenomenon "Tumour Budding" (TB). Hase, in 1993, further defined TB as 'Microscopic clusters of undifferentiated cells just ahead of the invasive front' (307). In order to overcome observer variability this definition was further refined by Ueno in 2002 who stated that tumour buds were individual cancer cells or clusters of cancer cells consisting of up to five cells in size located in the stroma at the invasive margin(270). Although Ueno's definition of a tumour bud has become widely accepted, the research community has not come to a consensus on a standardised quantification methodology and there exists high inter-observer variability and associated reproducibility issues(93, 308). Two reported quantification methods have shown a decrease in observer variability, but these have not been widely adopted(92, 309). Further reason for observer variability in TB is its obscurity in H&E stained tissue sections, especially when isolated cancer cells are concerned and where there is a high immune cell infiltrate(272). Recent reports state that poorly differentiated

clusters of cancer cells which are larger than 5 cells, but have no glandular morphology, are more significantly associated with lymph node metastasis and poor patient outcome than TB(269, 271). Inter-observer variability when counting poorly differentiated clusters was also shown to be less than with TB which the researchers attributed to easier visualisation of the larger tumour clusters(90, 269). Immunohistochemistry with Cytokeratins has also been employed in order to increase the accuracy of TB counts and decrease observer variability by differentiating them from stromal cells(136, 288).

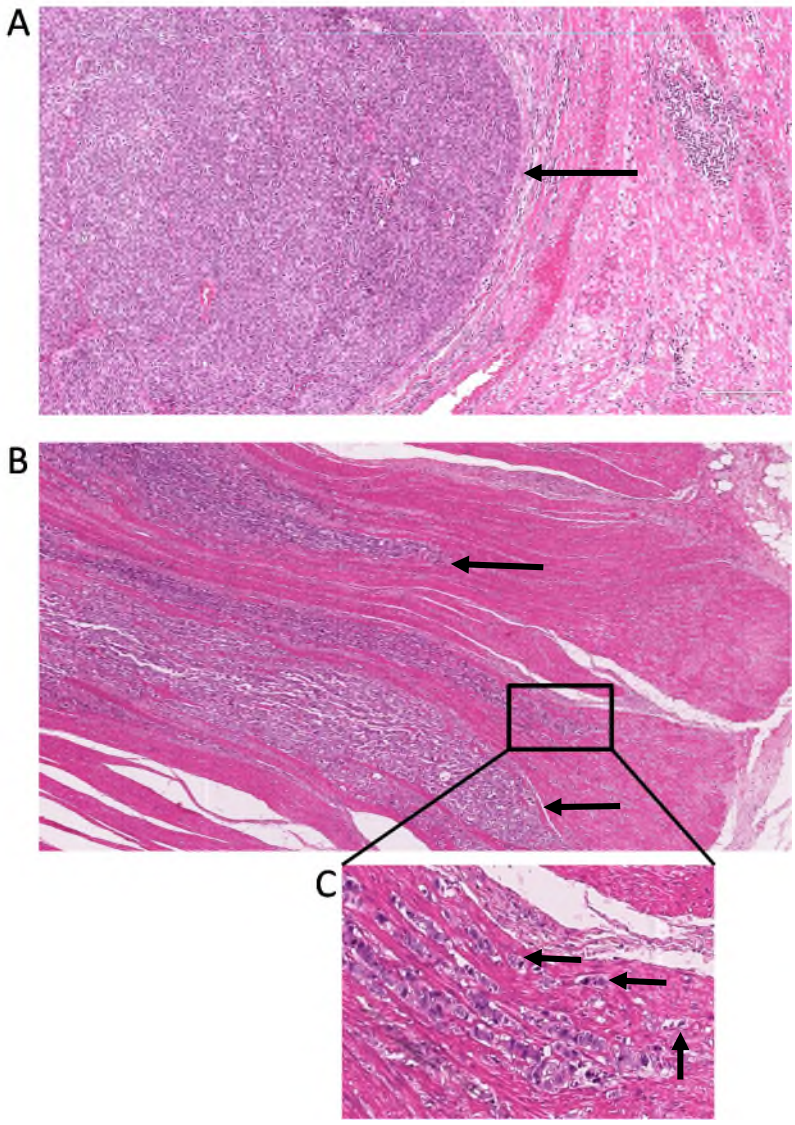

Figure 54. Invasive pattern of stage II CRC. A) H&E stained CRC tissue section demonstrating a pushing invasive border (arrow). B) H&E stained CRC tissue section demonstrating an infiltrative pattern invasive border (arrow). C) Digital zoom of section B) demonstrating tumour budding (arrows) at the tip of the invasive infiltrate. Image captured at x 10 objective.

Although there exist multiple scoring methods, cut-offs and sampling areas in the TB literature, a large body of evidence shows that TB is a significant predictor of poor prognosis and is correlated to lymph node metastasis(20, 91, 135, 136, 265, 272, 307), however a recent paper showed no association of TB and lymph node metastasis(271). TB is not, however, included as a core data item in RcPath guidelines and is still only listed as a non-core data item due to insufficient evidence and a lack of a standardised quantification methodology(102). Although tumour bud count has been shown to hold prognostic power, there is still a debate over whether these buds have disseminated from the invasive front or if they are in fact a 2D mechanical artefact which has been cut from a larger tumour gland (272). When serial sections are cut and examined it was shown that almost all tumour buds were in fact attached to spindle-like outgrowths from tumour glands(205, 310).

TB may be a significant parameter to stratify Stage I and II CRC patients into high and low risk of disease recurrence(136, 311-313). In fact, it has been reported that Stage II patients with a high degree of TB show similar or worse outcome to Stage III patients(307).

It is widely accepted in the literature that tumour buds, no matter their 3D structure, have undergone a certain level of EMT. EMT is the loss of a polarised cell's epithelial phenotype, which involves attachment to the basement membrane and neighbouring epithelial cells, and the gain of a more invasive and mesenchymal one(17). The loss of E-cadherin is one of the first steps of EMT which is closely related to the loss of membranous β-catenin, both of which play a major role in cell-cell junction complexes(18). A loss of cell membrane connections allow the cells to disseminate and migrate away from an epithelial sheet of cells. Tumour buds have been shown to have a decrease in E-Cadherin, an increase in the mesenchymal marker Snail as well as an increase in nuclear β-Catenin whereupon it acts as an oncogenic transcription factor and is involved in aberrant WNT signalling(314-316). Tumour buds have also shown a loss in other epithelial markers such as CD44 and EpCam and a decreased proliferation rate marked by a decrease in Ki67 expression(317-319). Mesenchymal-like cells may also display a loss of polarity through aberrant expression of Pard3 or

Scrib3(320, 321) which allows their dissemination from the polarised epithelial layers from which they originated. The mesenchymal phenotype also involves the upregulation of proteins involved in ECM remodelling such as MMP and uPA/R in order to invade through the stroma and muscle(26). Tumour buds have been reported to show an increase in ECM remodelling protein expression(322, 323). Cancer stem cell-like phenotypes are advantageous for a metastasising cell to display. This phenotype may allow the cell to survive outwith homeostatic control but also undergo MET and the colonisation of a metastatic site in order to form a secondary tumour mass. Tumour buds have been associated with higher expression levels of Colonic stem cell markers such as CD133 and ABCG5(314, 324).

All previous TB scoring methodology and associated proteomic evaluation has relied on manual semi-quantitative reporting where, no matter which cut-off and scoring method is utilised, it will be open to observer variability. The era of quantitative digital pathology allows the reporting of biomarker expression and histopathological features in a fully quantifiable and robust manner (187, 298, 299). Computer-based quantification is also amenable to the standardisation of bud scoring where an identical image analysis algorithm can be executed across remote institutes with the minimisation of observer variability. The study reported here will detail the development of a computer based analysis algorithm to automatically quantify TB across the invasive front of digitised CRC tissue sections. The algorithm is executed across a training and validation cohort in order to assess the prognostic power of quantifying tumour buds. A further algorithm, detailed within this study, will allow the segmentation of the tumour into distinct subpopulations and investigate their proteomic expression profile across the invasive front and the tumour centre.

1.2 Brightfield image analysis

Brightfield image analysis solutions were performed on either H&E stained or panCK immunohistochemistry labelled CRC tissue sections to assess their ability and accuracy in segmenting and quantifying tumour buds within the tumour to stroma invasive margin. The mainstream methodology for visualising tissue within medical

laboratories is through brightfield microscopy. Therefore the quantification of tumour buds by image analysis through brightfield microscopy was attempted in the first instance.

1.2.1 Automated quantification of tumour bud nuclei in H&E stained tissue sections

Tissue sections were cut from optimizing CRC tissue blocks, stained with H&E and digitized on the Leica SCN400. Images were imported directly from remote storage utilizing the Digital Pathology Pipeline into Definiens Tissue Studio®. Tissue Studio®'s "Nuclei" algorithm was employed to segment tumour bud nuclei within the stroma for a TB count. This was undertaken in an attempt to classify tumour cells, through their nuclear morphology, as either belonging to tumour buds or tumour glands and to differentiate them from stromal cells. Initial nuclear segmentation in H&E stained sections was inaccurate and could not be used to differentiate cells within tumour buds from those within tumour glands or stromal host cells through nuclear morphometry alone (Figure 55). Image based automatic quantification of H&E stained sections was therefore abandoned.

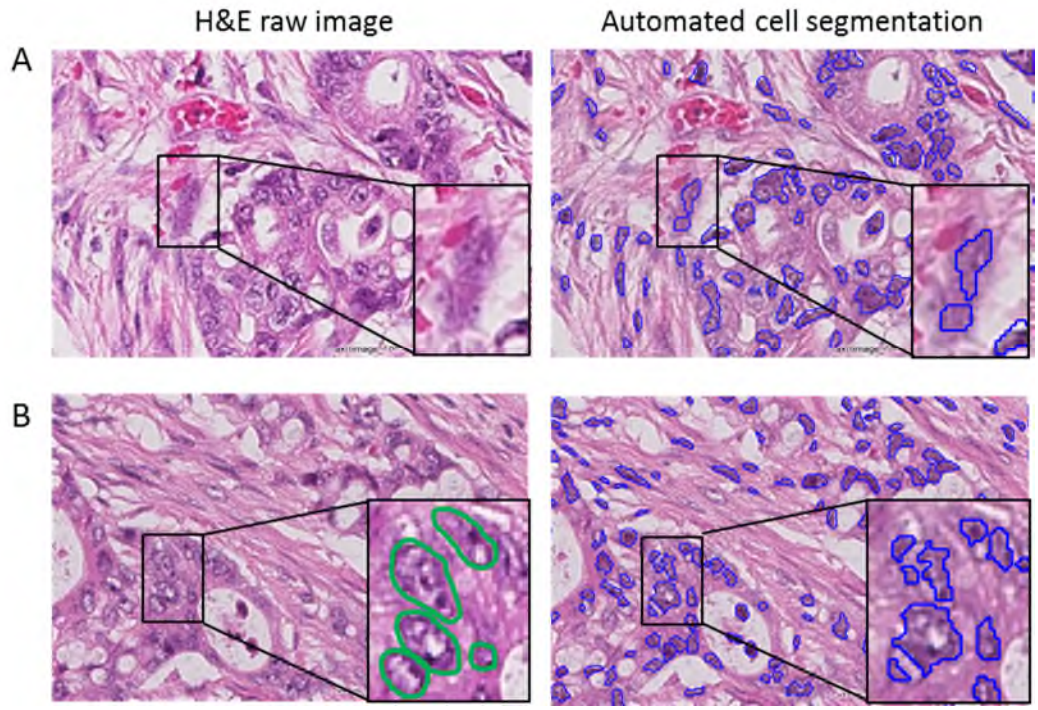

Figure 55. Nuclear segmentation of H&E stained digital tissue sections. CRC tissue sections were stained with H&E and digitized prior to image analysis to segment nuclei. Nuclei were incorrectly segmented and therefore H&E was not able to be used for accurate differentiation of tumour buds and stromal cells. Image A highlights an area where there are no nuclei although the algorithm has segmented two false nuclei (blue outline). Image B highlights an area containing 5 nuclei (correct segmentation in green) although the algorithm has segmented them incorrectly (blue outline).

1.2.2 Automated quantification of tumour bud nuclei in panCK immunohistochemistry labelled tissue sections

Cytokeratins are expressed in epithelial cells but not in stromal cells. PanCK immunohistochemistry was performed on CRC tissue sections in order to visualise epithelial cells within tumour buds, tumour glands and to differentiate them from the stroma. Whole tissue sections from control CRC tissue blocks were cut and panCK immunohistochemistry performed. The panCK antibody was visualised with DAB and the nuclei were counterstained with haematoxylin. Tissue sections were digitised on the Leica SCN400 and images imported into Definiens Tissue Studio® for image analysis. The image analysis algorithm, which was built around the brightfield "Nuclei & Marker Area" pre-installed algorithm, was developed to segment tumour from stroma ROIs and to attempt to quantify tumour buds automatically within the stroma (Figure 56).

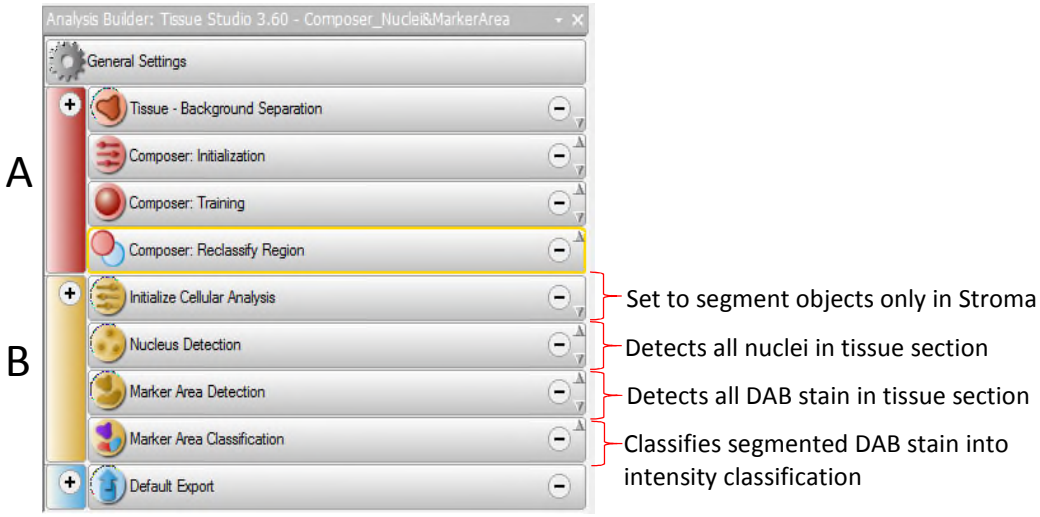

Figure 56. Algorithm for quantification of tumour buds through DAB immunohistochemistry and automated image analysis. A) ROIs are automatically segmented across tissue sections by training the Tissue Studio Composer technology and reclassifies areas of Tumour into stroma which are below 5000µm^2. B) Cellular Analysis module of the algorithm detects nuclei based on haematoxylin thresholds prior to segmenting DAB positive areas above a set size threshold and classifying them dependent on intensity.

Tissue is initially segmented into ROIs using Tissue Studio's Composer™ as previously described in chapter 3. Briefly areas of panCK, lumen/necrosis and stroma are used to teach the technology to automatically segment the tissue into ROIs. (Figure 56 A) Figure 57A-C). The algorithm's 'Cellular Analysis' section (Figure 56 B) first segments nuclei dependent on haematoxylin settings on size and stain threshold (Figure 57 D). PanCK positive DAB areas above a set threshold and a minimum stained area are segmented and classified as marker 1. Marker 1 objects are classified as low, medium or high for marker intensity (Figure 57 F, I & L). Marker 1 objects within the stroma were assessed for their ability to report TB. Full algorithm settings are listed in Appendix 9.

The algorithm was not further developed nor taken forward for tumour bud quantification as the software could not accurately segment nuclei or tumour buds. Dark areas of DAB were falsely segmented and classified as nuclei thereby obscuring true tumour bud area and cell number (Figure 57 G-L).

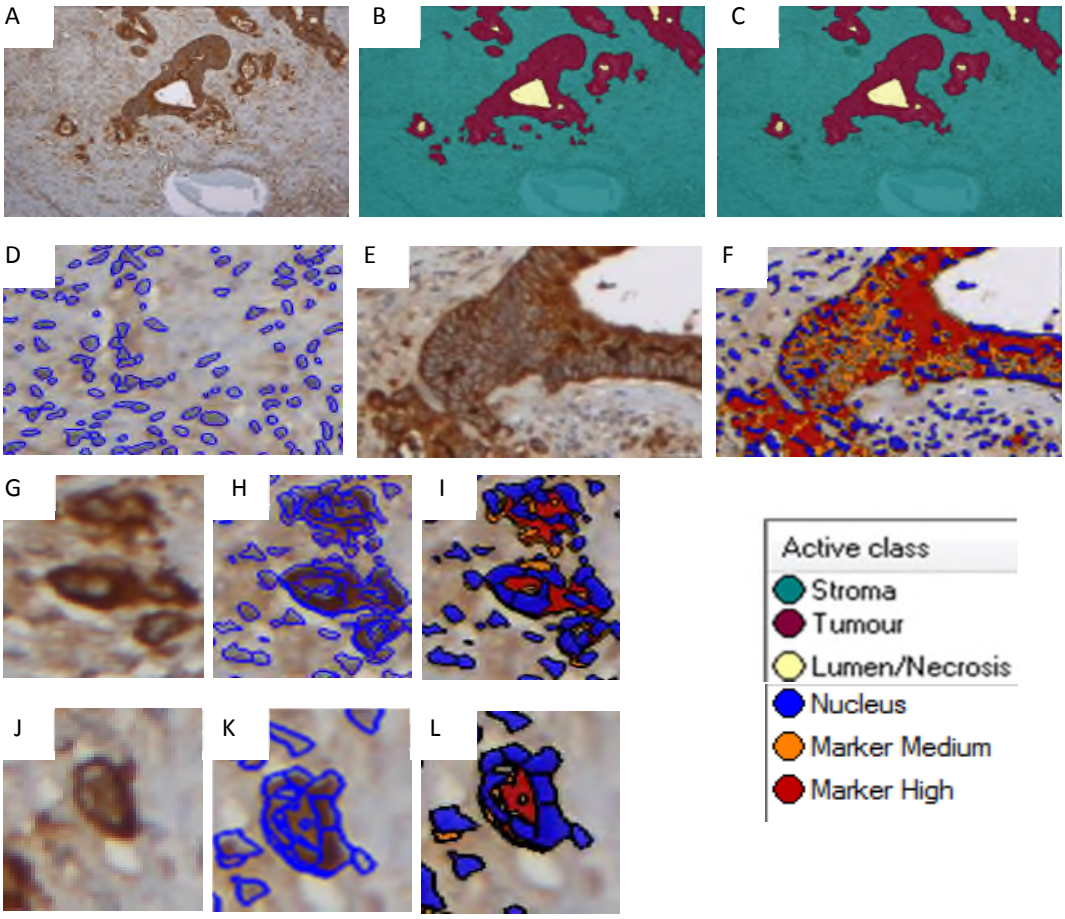

Figure 57. Quantification of tumour buds through DAB immunohistochemistry and automated image analysis. A) Invasive front of a CRC tissue section labelled for panCK. B) Composer technology automatically segments tumour (purple), stroma (turquoise) and Lumen/Necrosis (yellow). C) Tumour areas under 5000µm^2 are reclassified as stroma. D) All nuclei are segmented. E) Digital zoom of DAB positive neoplastic gland with Tissue Studio mask overlay (F) displaying nuclei and medium (orange) or high (red) DAB intensity areas of tumour. G) & J) DAB positive tumour buds, H) & K) Tissue Studio segmentation of DAB and nuclei. I) & L) Erroneous nuclear segmentation in tumour buds (blue). Images taken with a 10x objective.

1.3 Immunofluorescence image analysis

To quantify nuclei and panCK positive tumour cells more accurately an immunofluorescence approach was implemented with an antibody against panCK and DAPI as nuclear counterstain. This was to ensure the DAPI (nuclei) and panCK

(epithelial cells) were captured at different wavelengths and in different channels so that there was no bleed through of fluorescence. Nuclei could then be segmented purely on DAPI with no interference from the panCK. For algorithm development whole tissue sections were cut from the optimising CRC TMA block and labelled with panCK and DAPI. Tissue sections were imaged on the AQUA HistoRX imaging platform and imported into the Definiens software suite through a customised image importer.

1.3.1 Tissue Studio quantification of tumour buds

"Marker Area" was selected from the pre-installed Tissue Studio® immunofluorescence algorithms. The immunofluorescence algorithm ROI segmentation was constructed in the same manner as in Chapter 3.5.1.2. Post ROI segmentation only the "marker area detection" algorithm was utilised for panCK (Marker 1) object segmentation (Figure 58). Algorithm set up and thresholds were identical to those stated for panCK segmentation and Marker 1 classification in Chapter 3.5.1.4. Only quantification of Marker 1 areas within the stroma are utilised and exported from the algorithm.

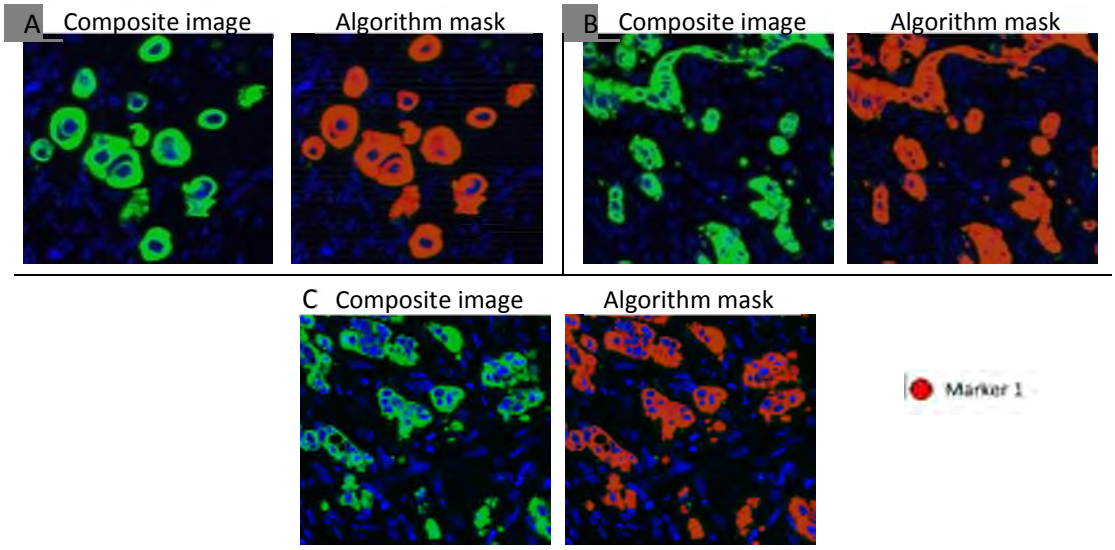

Figure 58. Immunofluorescence panCK object segmentation in Tissue Studio. A), B) and C) display examples of tumour budding visualised through IF with panCK (green) and the Tissue Studio image analysis mask (red). Image taken with x 20 objective.

Manual post processing of the data from Marker 1 (panCK) objects allows the estimated quantification of tumour buds. After extensive manual evaluation of multiple tissue sections the majority of tumour buds fell between an area of 22 and 270µm^2. If the exported area data of Marker 1 objects fall within these area margins they are manually classified as tumour buds. If a Marker 1 object falls above 270µm^2 or below 22µm^2 they were deleted from the dataset as debris or tumour clusters larger than 5 cells.

1.3.1.1 Whole slide image analysis

The IF algorithm was initially tested for tumour bud quantification on whole tissue sections cut from the positive and negative control tissue blocks as detailed in Chapter 3.5.1.1

Images were randomly taken from across each control tissue section on the HistoRX imaging platform, imported and analysed with the Tissue Studio® 'Marker Area' algorithm as detailed above. The number of tumour buds was quantified for each image across the tissue sections. It was noted that the LVI positive control contained a larger total number of TB than the LVI negative control. TB heterogeneity was also observed across the tissue section with some areas containing high TB and some low for both sections (Figure 59).

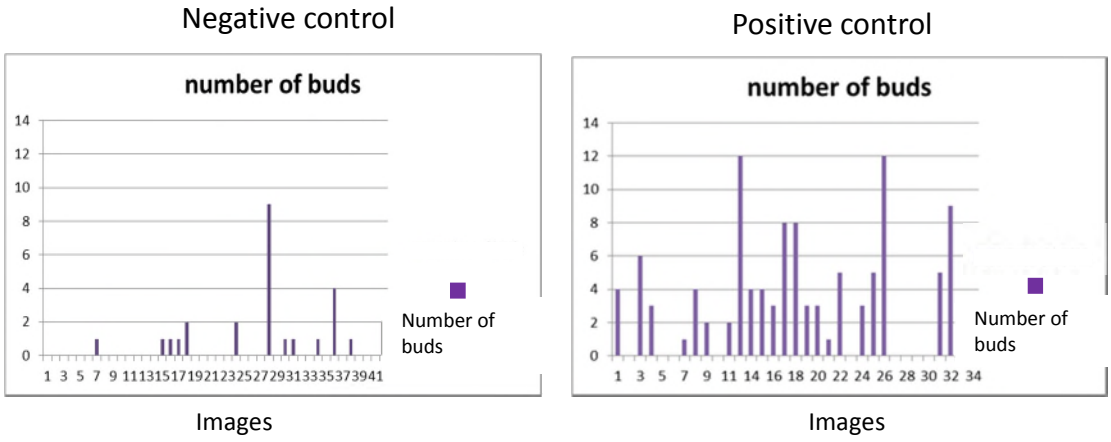

Figure 59. Results of immunofluorescence whole slide image quantification of tumour buds in Tissue Studio®. Tumour buds are quantified within each image taken across the whole tissue sections. Negative control tissue section contains fewer TB than the positive control.

1.3.1.2 TMA analysis

Tissue Studio® 'Marker Area' algorithm's capability to automatically quantify tumour buds across a heterogeneous patient cohort, mounted as a TMA, was assessed. The TMA, immunofluorescence and image import was the same as detailed in Chapter 3.5.2, apart from no D2-40 being incorporated. The number of tumour buds was automatically quantified as panCK objects within the stroma and manual post processing excluded objects below 22µm^2 and above 270µm^2 (Figure 60).

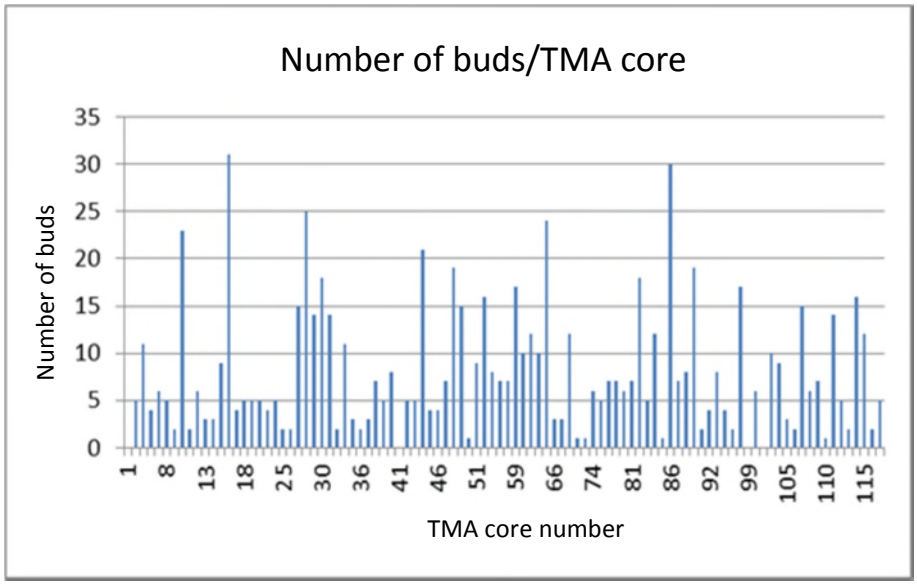

Figure 60. Results of immunofluorescence TMA image quantification of tumour budding in Tissue Studio®. Cores (n=118) across the TMA show inter-patient heterogeneity in the number of buds/core.

Due to heterogeneity of panCK fluorescence, resulting in poor segmentation, whole buds were on occasion incorrectly segmented into several, resulting in an over- scoring of buds per image.

1.3.1.3 Tissue Studio® algorithm constraints

The cells which make up tumour buds are heterogeneous in size, both within a TMA core and between patient cores. This in turn makes tumour bud size heterogeneous across a section and between patient samples. The average tumour bud fell between 22µm^2 and above 270µm^2 however some were indeed outwith this range leading to a false tumour bud count. Epithelial cell debris may also be picked up as a tumour bud and false positives can be reported. To quantify a tumour bud as it is defined in the literature, the cluster of cells must be 1-5 cells in size. Therefore a panCK object must contain 1-5 nuclei for it to be classified as a tumour bud regardless of its area. As stated in Chapter 3.5.3, if nuclei are segmented within the Tissue Studio® algorithm they will create false segmentation of the panCK object in the image layer below, which will in turn create a false number of buds within each image (Figure 61).

Due to the constraints presented within Tissue Studio® the algorithm was deemed not to be suitable for tumour bud quantification without further development.

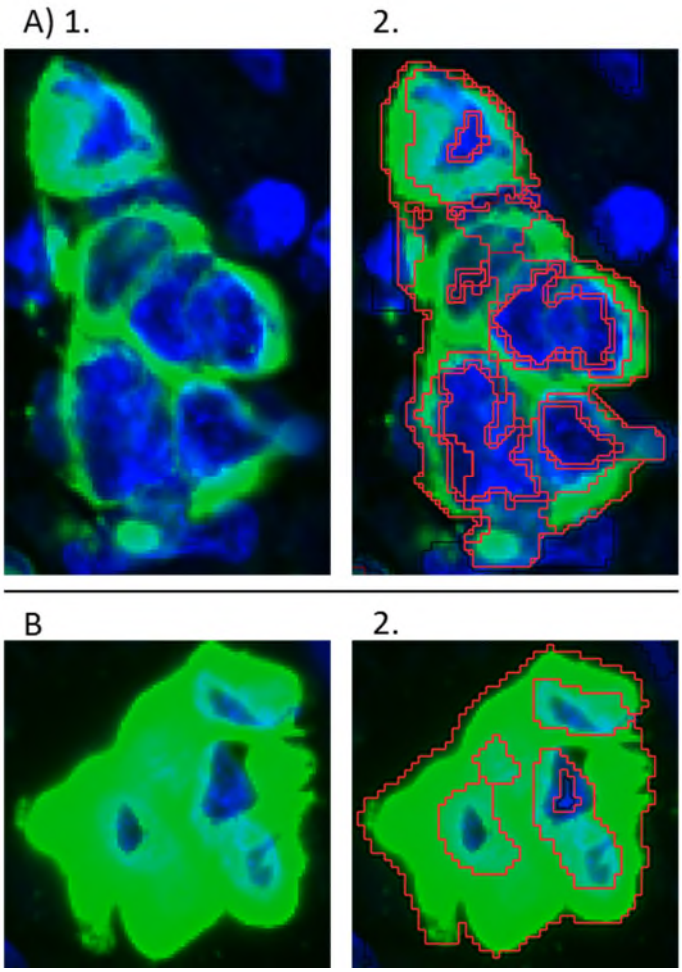

Figure 61. A) & B) The false segmentation of two tumour buds by image analysis of nuclei. 1. show examples of two tumour buds (green: panCK, blue: DAPI). 2. Tissue studio nuclei segmentation (red line) in the image layer above is retained in the marker 1 layer and falsely segments the tumour buds into multiple smaller areas creating a false TB count. Image was taken with a x 20 objective.

1.3.2 Quantification of tumour buds using Definiens Developer XD™.

The Tissue Studio® segmented image, as detailed above, was imported into Definiens Developer XD software for further optimization.

Identical marker 1 (panCK) object optimisation was carried out as described in Chapter 3.6; neighbouring objects were merged, holes within panCK objects are filled and the segmented nuclei were relocated in an image layer below the marker 1 object layer.

This allows for accurate epithelial panCK object area segmentation within the stroma ROI and the quantification of nuclei per object (Figure 62). Non-specific panCK and false nuclei are similarly excluded as in Chapter 3.6.

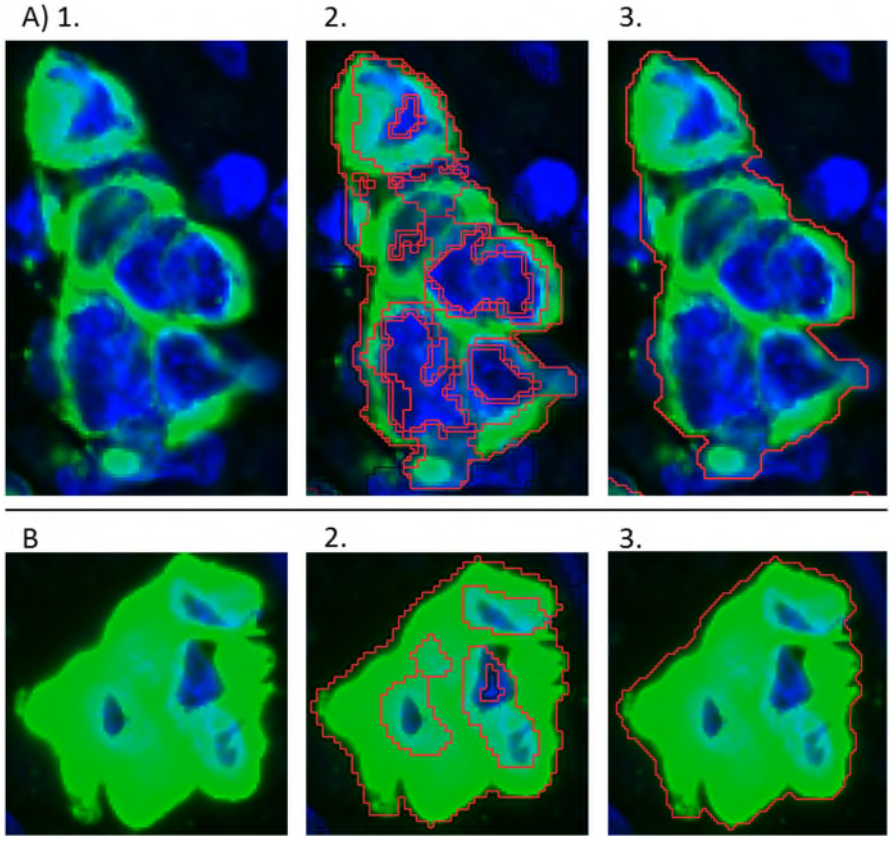

Figure 62. Accurate segmentation of tumour buds through Developer XD algorithm development. A) & B) 1 show examples of two tumour buds. 2. Tissue studio nuclei segmentation in the image layer above is retained in the marker 1 layer and falsely segments the tumour buds into multiple smaller areas creating a false TB count. 3. Developer XD tumour bud segementation creates an accurate otline of the tumour buds. Image taken with a x 20 objective.

After optimising the segmentation of epithelial objects within the stroma they were further classified depending on their associated nuclei: 'irrelevant marker' (no associated nuclei), 'bud with debris marker' (only debris nuclei associated with marker), 'tumour bud' (1-5 associated nuclei) and 'Large tumour bud' (over 5 nuclei associated and below 5000µm^2) (Figure 63).

The final algorithm as set out was utilised for all subsequent tumour bud quantification in this study and was named the Tumour Bud Analyser (TBA).

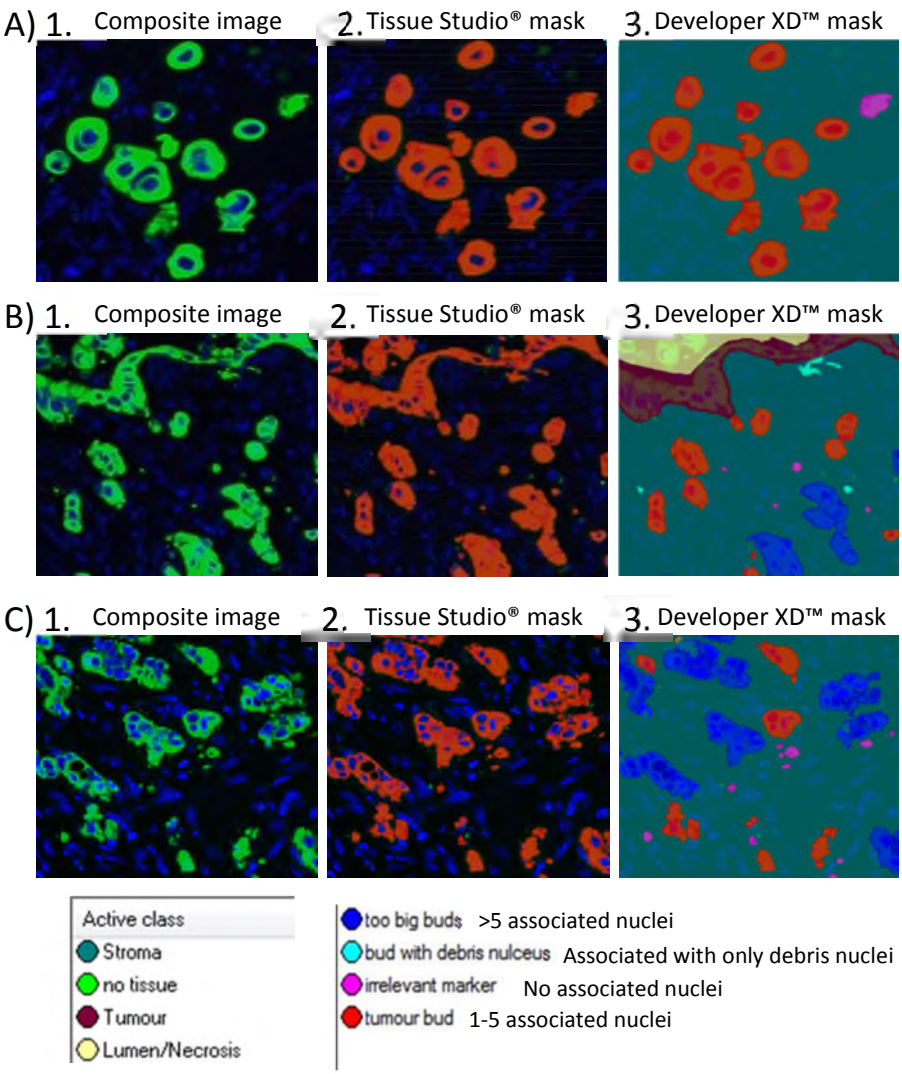

Figure 63. Classification of panCK objects into tumour bud categories. A), B) & C) 1. Raw composite images of tumour bud examples. 2. Tissue Studio classifies all panCK positive objects as 'marker 1'. 3. Developer XD image analysis algorithm classifies panCK objects dependent on the associated nuclei. Image taken with a x 20 objective.

1.4 Prognostic evaluation of Tumour Bud Analyser quantified Tumour Budding

1.4.1 Quantification of TMA – training set

A higher accuracy of TB quantification and a classification in line with the TB community is possible through the application of algorithm development within the Developer XD software.

The algorithm was applied to the training cohort TMA and the number of tumour buds was exported by the TBA for each core. The TBA was fully automated and no manual intervention took place thereby excluding any observer variability. Patient stratification was assessed by KM curves which were plotted in TMA Navigator software. The quantification of tumour buds across a single core from a TMA was unable to stratify a cohort of early stage CRC patients into high and low risk of disease specific death (Figure 64).

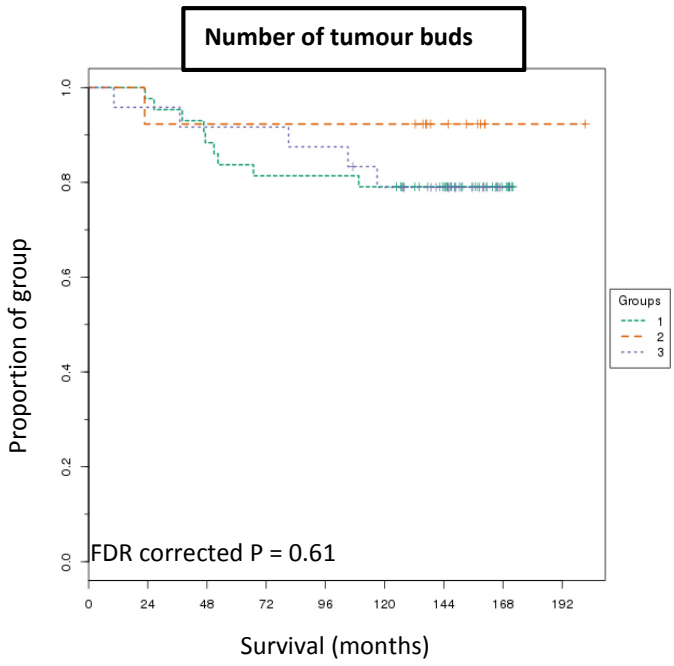

Figure 64. Kaplan-Meier curves for patients within the training set TMA (n=118) post quantification by TBA. Patients were not significantly stratified into high and low risk groups from quantification of tumour budding.

1.4.2 Quantification of CRC whole slide imaging

1.4.2.1 Training cohort

Reports in the literature quantify TB from the invasive front and usually over multiple fields of view, although some researchers employ only a single field of view(20). In order to assess if a single core was too low a sampling area for prognostic quantification of TB, whole slide analysis was performed on the whole tissue section training cohort involving 50 patients, as in Chapter 3.7.1. Whole tissue sections underwent immunofluorescence with panCK and DAPI. Image capture and import into Definiens Developer XD was similar to that set out in Chapter 3.7.1. The number of tumour buds per image was exported from the TBA. The 15 images from each patient containing the highest number of tumour buds were retained for analysis and the number of buds totalled across these 15 images. The total number of tumour buds across the 15 images was the final parameter assessed for prognostic significance.

1.4.2.1.1 Cox-regression survival analysis

Monte Carlo simulations, within X-tile software, were again utilised to establish significant high and low tumour bud patient sub-group cut-offs from the training cohort (cut-off = 287 tumour buds across 15 images, $p = 0.0001$). The cut-off of 287 tumour buds was then applied to the stage II subpopulation for the assessment of stratification of high risk patients. Cox-regression analysis is summarised in Table 10. TB was a significant predictor of disease specific death in univariate analysis (HR =5.7; 95% CI, 2.38-13.8), but was insignificant when a multivariable model was adjusted for T, N and Dukes staging as well as the image analysis quantified LVI and LVD results from Chapter 3.7.2.1 (HR =2.56; 95% CI, 0.9-7.27). To assess if TB was correlated to LVI, Pearson's correlation was performed. TB and LVI are significantly correlated within the training cohort ($r = 0.69$, $p < 0.0003$) (Figure 65).

Clinicopathological parameter	patient number (n)	Univariate				Multivariable			
		HR	95% CI		P value	HR	95% CI		P value
			lower	upper			lower	upper	
Tumour Budding		**5.76**	**2.38**	**13.8**	**0.0005**	2.56	0.9	7.27	0.08
High	13								
Low	37								

Table 10. Univariate and multivariable Cox regression analysis on disease specific survival for tumour budding within the training cohort.

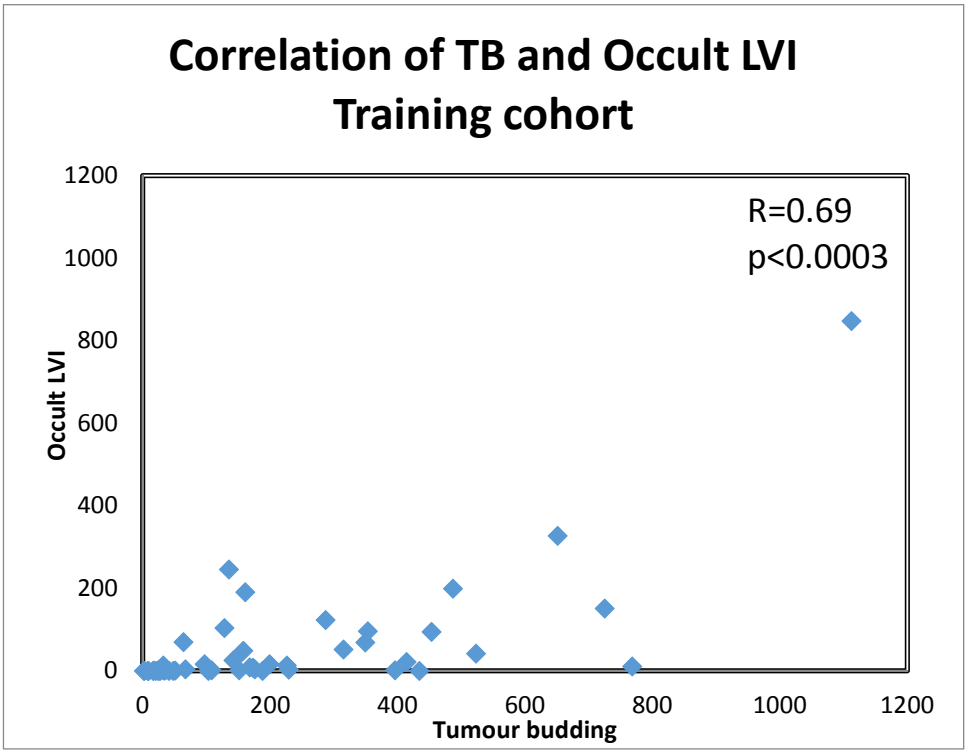

Figure 65. Pearson's correlation of tumour budding and occult LVI in the training cohort.

1.4.2.1.2 Kaplan-Meier survival curves

KM curves were plotted using TMA Navigator to assess the prognostic relevance of TB in the full training cohort as well as across the stage II subpopulation (Figure 66A). TB was significantly prognostic for poor outcome and shorter disease specific survival times in both the full training cohort (p <0.0001) and within the stage II subpopulation (p = 0.0005). The percentage of patients still alive at the end of the study and in the

above cut-off subgroup (> than 287 buds) was 7.7% compared to 76% in the low budding subgroup for the training cohort and 10% compared to 73% in the stage II subpopulation. Automated analysis allows the quick comparison of the size of the tumour bud to the significance of prognosis. The TBA was further programmed to segment, quantify and export the number of panCK positive objects within the stroma which contained only 1-2 nuclei (small tumour buds) and also those which contained over 5 nuclei (large tumour buds). Interestingly, the results reported identical survival curves when quantifying buds with up to 2 nuclei and buds with 1-5 nuclei within the training cohort. The quantification of large tumour buds (islands of tumour cells larger than 5 cells but below 5000μm^2) showed slightly less significant separation of survival between high and low risk groups than when quantifying tumour buds (Figure 66B). When examining the results from the stage II subpopulation identical results are shown when comparing classical tumour buds with small tumour buds, however large tumour buds report a slight improvement by identifying an additional poor prognosis patient correctly stratified into the high budding group (Figure 66C).

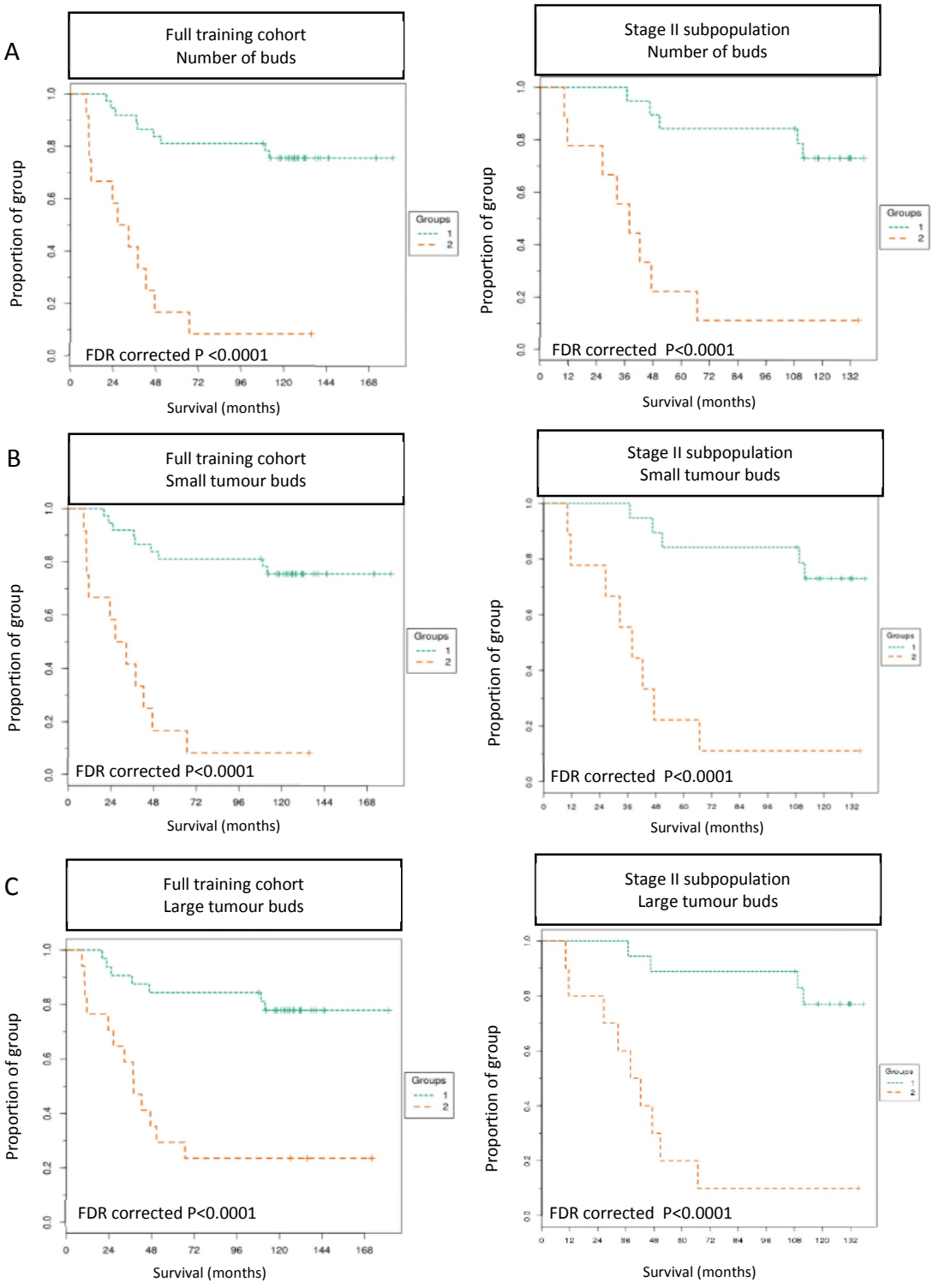

Figure 66. Kaplan-Meier curves for tumour budding across WSI; training cohort. A) Patients within the full cohort (n=50) and the stage II (n=29) subpopulations were significantly stratified into high and low risk of disease specific death through the quantification of classical TB. Both the quantification of small tumour buds B) and large tumour buds C) were able to stratify CRC patients into high and low risk of disease specific death.

1.4.2.2 Validation cohort

TB is a highly significant prognostic factor with the ability to significantly stratify the training cohort into high and low risk of disease specific death. In order to validate whether TB can stratify a larger stage II population of patients into high and low risk of disease specific death we applied this methodology to the validation cohort. The immunofluorescence, image acquisition methodology and image analysis was identical to the training cohort study for WSI (section 4.4.2.1).

1.4.2.2.1 Cox-regression survival analysis

The training cohort cut-offs were applied to the exported automated image analysis results from the 15 images per patient within the validation cohort. The corresponding groups of patients were assessed for significance of prediction of survival by univariate Cox-regression analysis. TB was a significant predictor of disease specific death in the validation cohort (HR=2.49; 95% CI, 1.03-5.99) (Table 11). Similar to the occult LVI results in chapter 3.7.3.1, both hazard ratio and significance are substantially reduced from training cohort results. TB and Occult LVI were found to be significantly correlated (r = 0.64, p<0.0001) within the validation cohort after a Pearson's correlation was calculated (Figure 67).

Clinicopathological parameter	patient number (n)	Univariate			
		HR	95% CI		P value
			lower	upper	
Budding		2.49	1.03	5.99	0.04
High	44				
Low	90				

Table 11.Tumour budding univariate Cox-regression analysis for disease specific survival within the validation set.

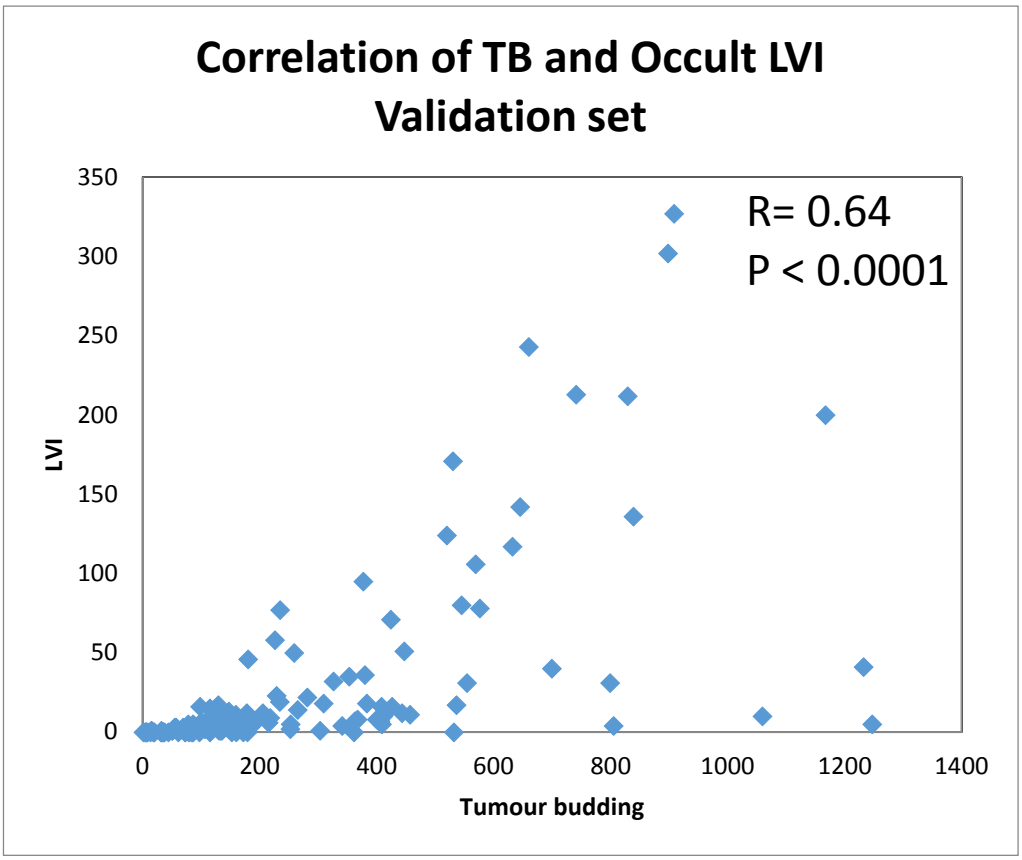

Figure 67. Pearsons' correlation of Tumour budding and Occult LVI within the validation cohort.

1.4.2.2.2 Kaplan-Meier survival curves

KM curves were plotted to assess survival times across low and high TB subgroups after the training cohort cut-offs were applied to the validation cohort. TB was significantly prognostic for poor outcome and shorter disease specific survival time in the validation set (p = 0.04), albeit considerably less so than in the training cohort (Figure 68).

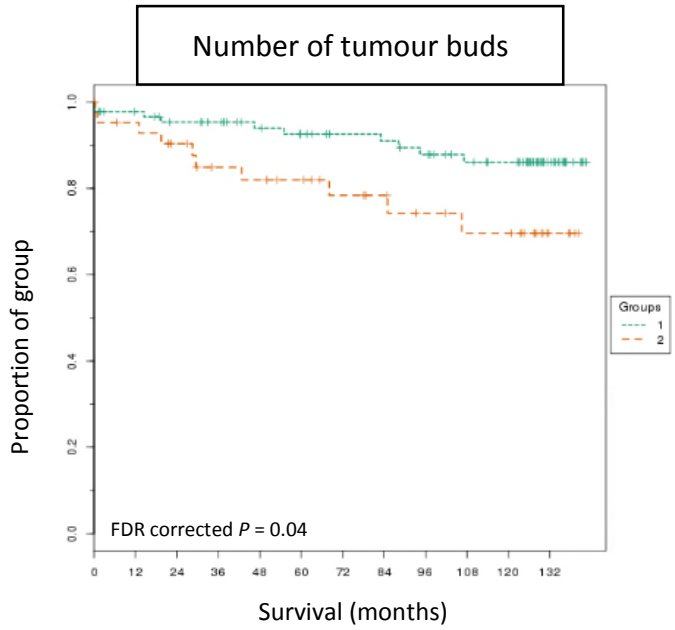

Figure 68. Kaplan-Meier curves for tumour budding within the validation cohort. Patients within the validation cohort were significantly stratified into high and low risk of disease specific death through the quantification of tumour budding.

1.4.2.3 Total Tumour Budding

The TBA was programmed to quantify TB as stated in the literature and the RCPath guidelines; that is, tumour islands of 1-5 cells in size which are separated from tumour glands at the invasive front. Although this parameter was successful at stratifying high and low risk patients within the training cohort with high significance, its ability to stratify stage II patients in a larger sequentially selected validation cohort was less significant. Large tumour buds were also shown to hold prognostic significance in the training cohort. A new combined parameter of the number of tumour buds and large tumour buds across the 15 analysed images per patient was created which was termed "Total budding". This was exported from the TBA in an attempt to stratify high and low risk stage II patients in the validation cohort at a higher significance. Monte Carlo simulations reported the optimal cut-off for Total budding within the training cohort to be 640 events across 15 images and to have a significance of $p = 0.003$. The training cohort cut-off was applied to the validation cohort and survival analysis was performed through Kaplan-Meier curves for both the training and validation cohorts (Figure 69). No patients survived past 5.5 years in the high cut-off Total budding group in either

the full training cohort or its Stage II subpopulation. However, when the cut-off of 640 events was applied to the validation cohort there was no significant separation of risk and this was therefore a poorer parameter for stage II patient stratification than tumour buds alone.

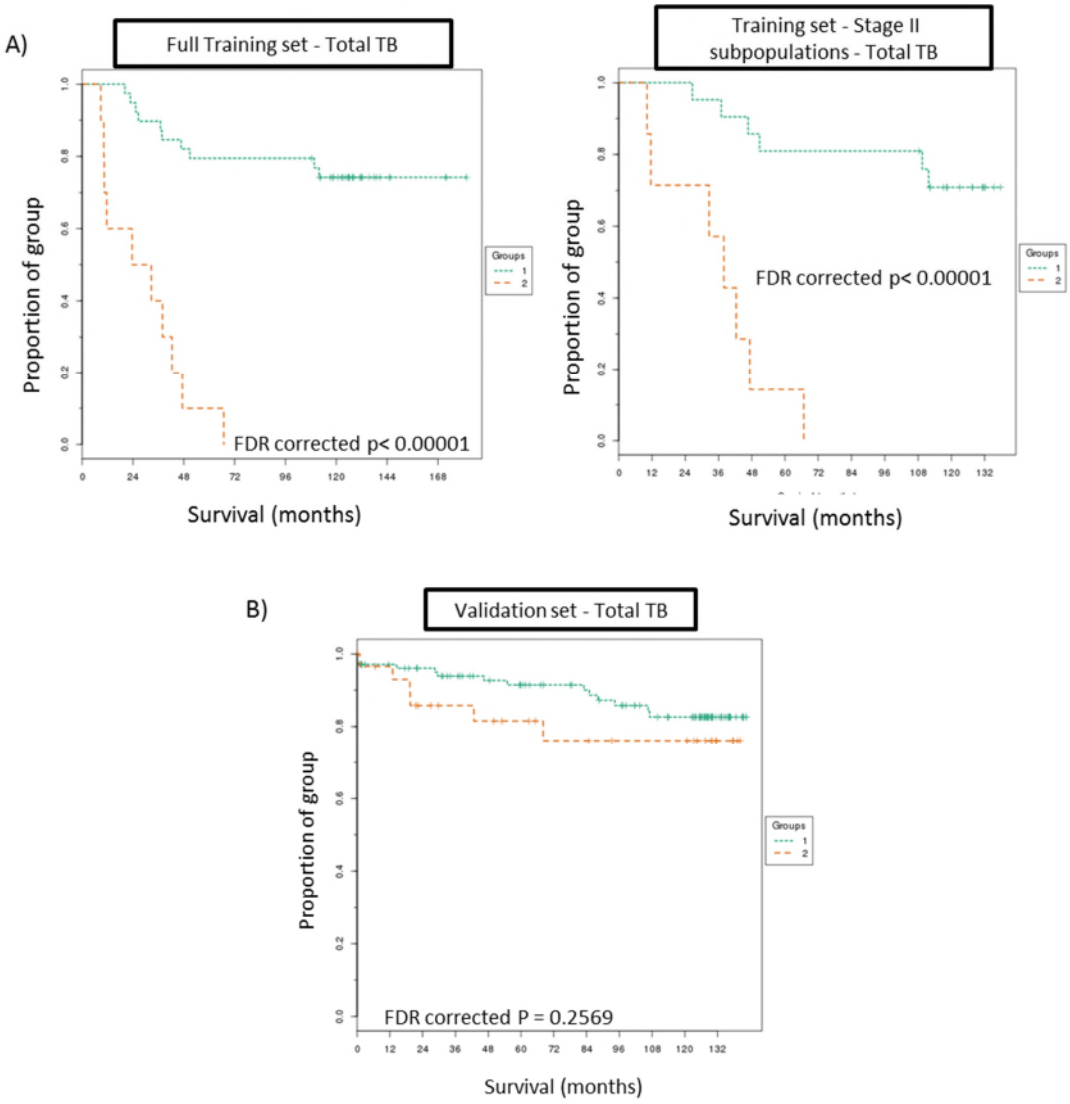

Figure 69. Kaplan-Meier curves for total tumour budding (Total TB) within the training (n=50) A) and validation cohort (n=134) B). Total TB was highly significant in stratifying patients within the training cohort into high and low risk of disease specific death; however this parameter was not significant within the validation cohort.

1.4.3 Optimal Validation cohort cut-offs

As in Chapter 3.7.2.4, when plotting all possible cut-offs of the data against significance there were large ranges of highly significant cut-offs for the exported TB parameters; in this study those parameters were tumour buds and total budding. The single optimal cut-off, selected from multiple significant cut-offs, and validated for the training cohort by the X-tile software, may not in fact be the optimal cut-off for subsequent validation cohorts representing the greater stage II CRC patient population. This study assesses if one of the other highly significant tumour bud cut-offs from the training cohort allowed more significant stratification of the validation cohort into high and low risk of disease specific death. In order to do so all training cohort and validation cohort TB and total budding cut-offs with associated *p*-values, determined by KM curves, were plotted on the same graph (Figure 70A & 71A). A cut-off for each parameter was selected which held mutual high significance within each cohort. This new mutually significant cut-off was then utilised to stratify the validation set into high and low risk groups. The new cut-off of 253 tumour buds and 341 total budding events created highly significant separation of high and low risk patient survival over time of $p = 0.0009$ and 0.001 respectively in the validation cohort (Figure 70B & 71B). The training cohort significance remained high at $p < 0.0001$ and 0.003 for tumour buds and total buds respectively.

Univariate Cox-regression of Tumour buds (HR = 4.5; 95% CI, 1.8-11.2) and Total buds (HR = 4.5; 95% CI, 1.7-11.9) show that both are strong, significant and near identical predictors of disease specific death within the validation cohort (Table 12).

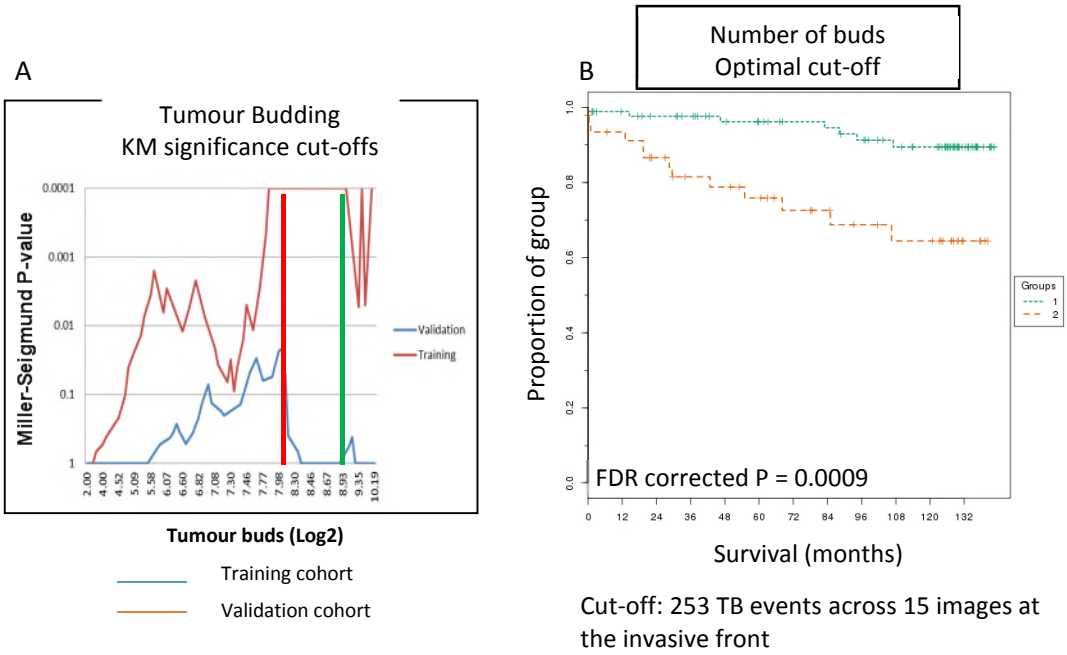

Figure 70. Assessment of optimal cut-offs within the training and validation cohorts for tumour budding. A) *P* values for all possible cut-offs within the training cohort and validation cohort were plotted on the same graph. An optimal cut-off of 253 tumour buds was selected which reported significant values for both cohorts (red line). The green lines mark the area containing 80% of the training cohort. B) The optimal cut-off of 253 tumour buds was utilised to plot Kaplan-Meier curves which significantly stratified the validation cohort into high and low risk of disease specific death.

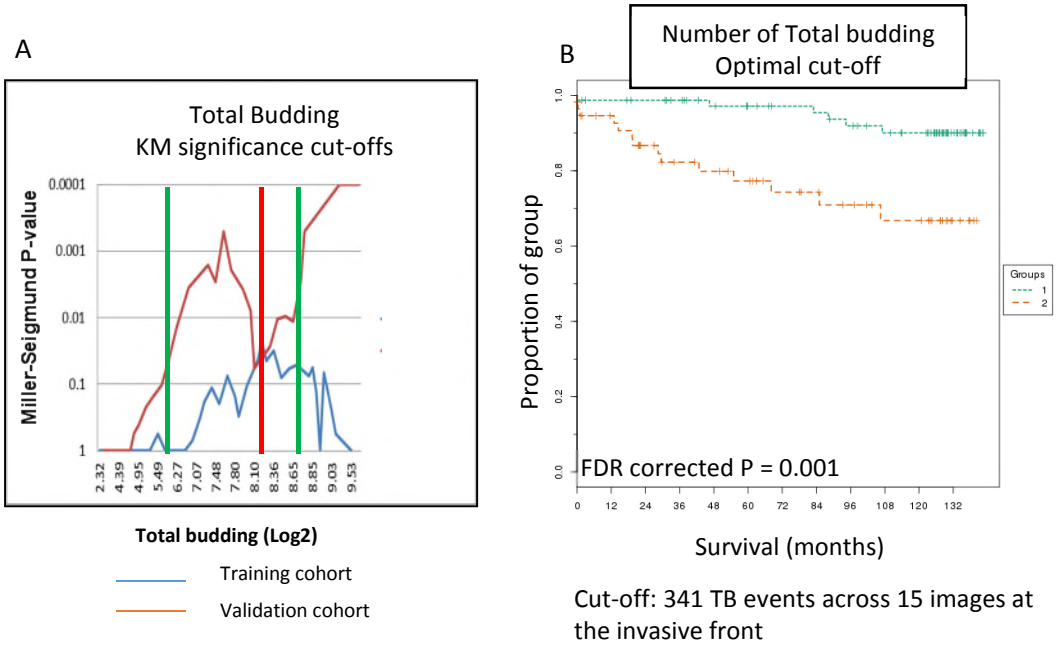

Figure 71. Assessment of optimal cut-offs within the training and validation cohorts for total budding. A) *P* values for all possible cut-offs within the training cohort and validation cohort were plotted on the same graph. An optimal cut-off of 341 total buds was selected which reported significant values for both cohorts (red line). The green lines mark the area containing 80% of the training cohort. B) The optimal cut-off of 341 total buds was utilised to plot Kaplan-Meier curves which significantly stratified the validation cohort into high and low risk of disease specific death.

Clinicopathological parameters	patient number (n)	Univariate			
		HR	95% CI		P value
			lower	upper	
Optimal Tumour Bud		4.5	1.8	11.2	0.002
High	47				
Low	87				
Optimal Total Budding		4.5	1.7	11.9	0.002
High	57				
Low	77				

Table 12. . Univariate Cox regression of TB and Total TB utilising optimal cut-offs on the Validation cohort.

1.5 LVA & TBA combined image analysis algorithm

Both the LVA and TBA Developer XD algorithms utilise similar programming to optimise the segmentation of panCK objects. Therefore it was possible to add the additional coding from the TBA to the LVA and combine the two. The additional coding which was merged from the TBA involved the quantification and assignment of the number of nuclei within panCK objects as tumour bud classifications, as detailed above in section 4.2.2. After panCK objects were classified as a tumour bud category they were merged with the vessel analysis from the LVA allowing colocalising of the tumour bud object classifications with vessels. This then allows the classification of the epithelial objects invading the lymphatic vessels as “Tumour bud invasion” or “Non-bud invasion”.

Non-bud invasion includes panCK objects which are classified as “bud with debris nuclei” or “large tumour buds” and which colocalise within a vessel. “Tumour bud invasion” refers to tumour buds which colocalise with D2-40 positive vessels.

The merged single image analysis algorithm has the capability to segment and quantify multiple tumour bud categories, multiple LVI categories as well as LVD from a single immunofluorescence labelled tissue section.

Full algorithm specifications and output parameters are listed in Appendix 9.

1.6 Analysing heterogeneous subpopulations through image analysis

Tumour subpopulations with differential nuclear morphometry and expression of panCK were observed in the digitised pathology slides of both the training and validation set. The majority of tumour buds and large tumour buds expressed high intensity levels of panCK and large round nuclei with a low spatial density (Figure 72A). On the contrary, tumour glands prevalently contained lower panCK intensity and smaller oval or columnar nuclei which were in extremely close proximity to each other (Figure 72B). Specific tumour glands at the invasive front and in close proximity to tumour buds were observed to have similar panCK intensities and nuclear properties to tumour buds (Figure 72C). A hypothesis was formed that the tumour buds had disassociated from these "bud like" glands and that both had picked up driver aberrations making them more adaptable to invasion through the stromal ECM. These glands were termed "budding stations".

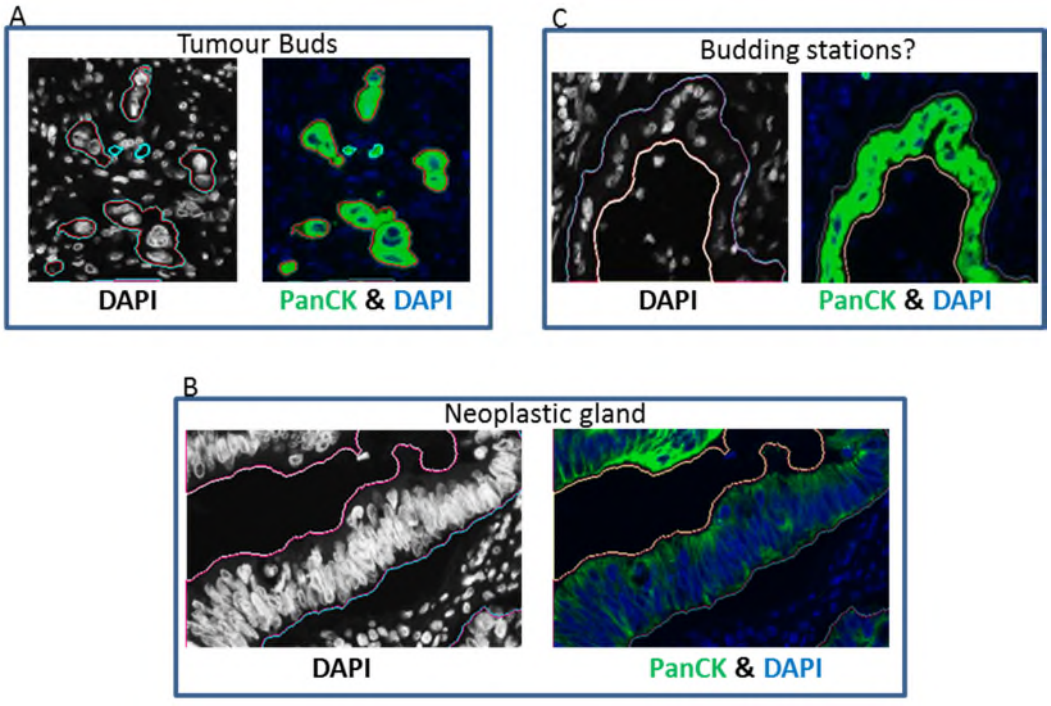

Figure 72. Heterogeneity of panCK intensity (green) and nuclear morphometry (Gray scale and blue) within tumour subpopulations. Images from within the same tumour section show: A) tumour buds containing large and round nuclei and expressing a high panCK intensity, B) neoplastic glands containing columnar densely packed nuclei and expressing low panCK and C) neoplastic glands with similar nuclear morphometry and panCK intensity as tumour buds. Images taken with a x 20 objective.

1.6.1 Segmenting tumour buds and tumour glands for heterogeneity analysis

Image analysis was employed across the training cohort in order to quantify the visual observations detailed above. The TBA was adapted to quantify panCK intensity and nuclear morphometry within set subpopulations. The algorithm is already pre-programmed to quantify these subpopulations; ‘tumour gland’, ‘tumour bud’ and ‘large tumour bud’. Multiple nuclear morphometries and intensities were calculated at single nucleus resolution and exported within the algorithm (Appendix 10). Each nucleus associated parameter was meaned within one of the three pre-segmented subpopulations: tumour gland, tumour bud or large tumour bud, and again across the same 15 images captured at the invasive front as in section 4.3.2. This gave the mean of the mean of each nuclear parameter within three distinct tumour subpopulations and across 15 images per tissue section. The whole tissue section training cohort was analysed using this image analysis methodology. Although there is considerable inter-patient heterogeneity of panCK intensities across the training cohort, intensity was consistently higher within the tumour buds and the large tumour buds than within the tumour glands. This was the case for every patient tissue section analysed (Figure 73). Only one out of seven patients with a mean tumour gland intensity above 80au survived follow-up, suggesting that high panCK intensity is a poor prognostic factor and associated with an more invasive phenotype.

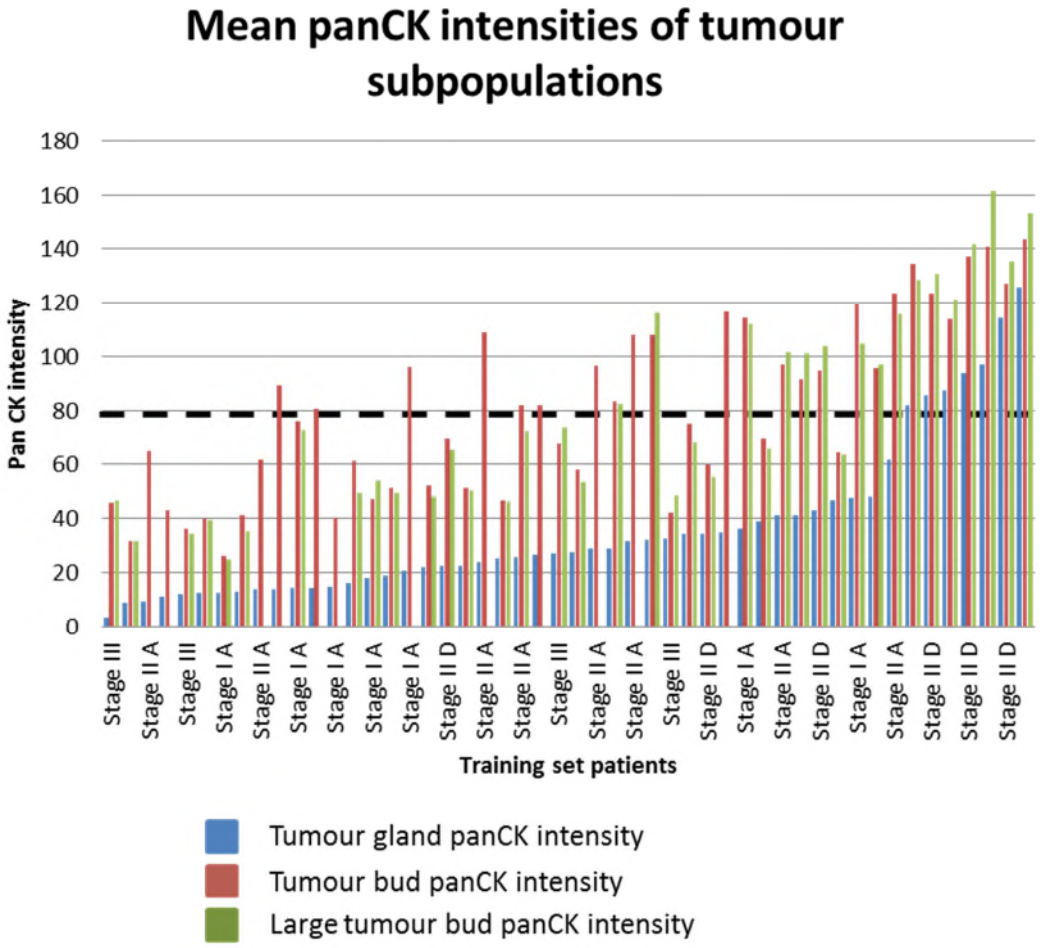

Figure 73. Mean panCK intensities within tumour subpopulations of patients within the training cohort. Tumour gland panCK intensity (blue) was consistently lower than the intensity within either tumour buds (red) or large tumour buds (green). Patients with a panCK intensity of above 80 au (dotted line) had a poor prognosis.

The thirteen nuclear morphometric parameters, as detailed in Appendix 10, were exported for each nucleus and averaged separately within either their tumour bud or tumour gland subpopulations. Each parameter showed a trend of differential nuclear morphometry between the glands and the buds. Nuclear area, roundness, border length and width displayed the largest difference between the two subpopulations across the tissue sections (Figure 74).

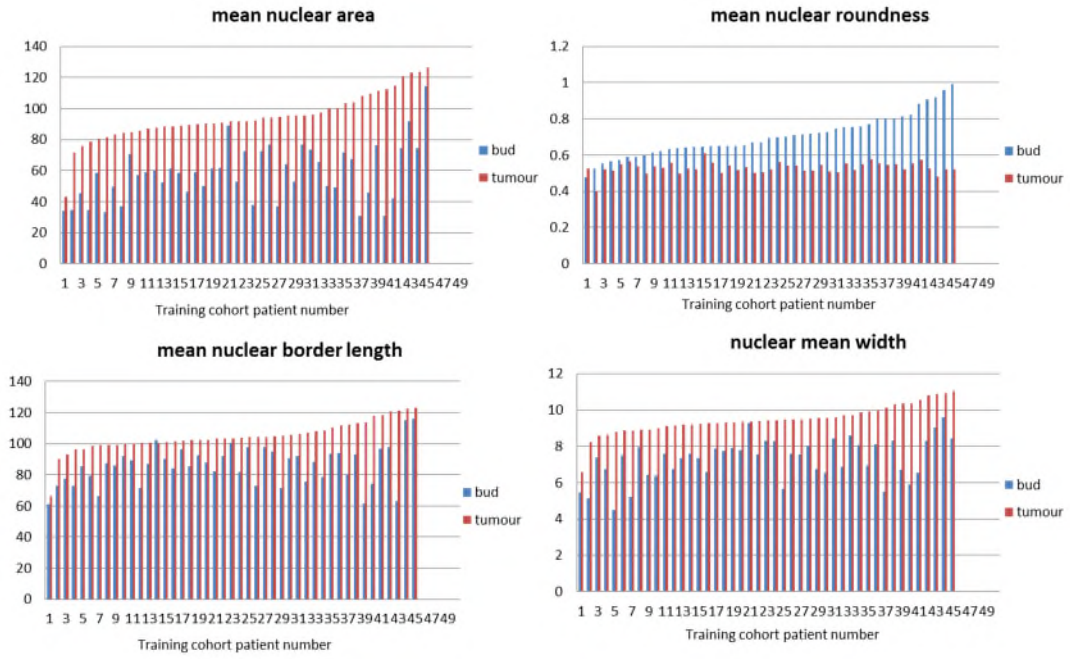

Figure 74. Differential nuclear morphometric parameters within tumour glands (red) or tumour buds (blue) of the training cohort.

Single parameters showed differential morphometry between the two subpopulations, however by performing principal component analysis (PCA) on all the parameters within each subpopulation it was possible to create a nuclear morphometric fingerprint for each patient sample. Three components were exported from the PCA and plotted in 3D to allow the visualisation of the nuclear morphometric fingerprint. This was performed in order to analyse the differential nuclear signatures between tumour buds and tumour glands.

Figure 75 shows that there is very little inter-patient heterogeneity in tumour gland nuclear morphometry. The multi-parametric nuclear phenotypic fingerprint of each tissue section's tumour gland cluster tightly in statistical space thus representing little variation across patients. In contrast, not only do the tumour bud nuclear morphometrics clearly cluster away from those of the tumour glands, there is also substantial inter-patient heterogeneity. There is no significant separation of tumour bud or tumour gland nuclear morphometry across the TNM stages.

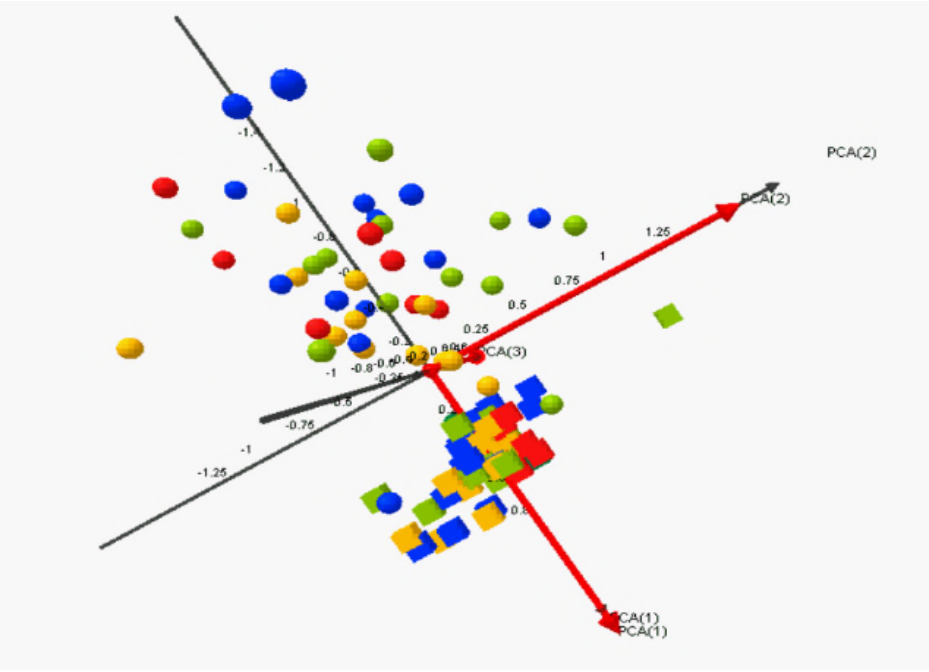

Figure 75. PCA of nuclear phenotypic fingerprint for tumour buds vs tumour glands within the training cohort (n=50). Stage I (blue), stage II alive (green), stage II dead (red) and stage III (orange) patient nuclear morphometric phenotypic fingerprint for tumour buds (circle) and tumour buds (square) are plotted.

1.6.2 Assessing mechanistic proteomic signatures across heterogeneous subpopulations through image analysis.

Tumour buds, large tumour buds and tumour glands display differential panCK intensities within the same tissue section. Tumour buds and tumour glands also show differential nuclear morphometrics and nuclear spatial densities. This led to the hypothesis that tumour subpopulations within the same tissue section express differential proteomic signatures. These proteomic signatures may identify driver mutations which confer on the tumour buds a more invasive phenotype or allow them to disassociate from the tumour glands. Previous image analysis algorithms detailed in this thesis segment nuclei within set subpopulations but do not allow the segmentation of the cell. As certain proteins of interest are expressed in the membrane or cytoplasm of tumour cells a new image analysis approach must be undertaken.

1.6.2.1 Subcellular segmentation through Tissue Studio

As with all of the immunofluorescence image analysis algorithms detailed so far within this thesis the first step in analysis is to utilize Tissue Studio's Composer machine learning technology to teach the algorithm to segment the tissue into 'Tumour', 'Stroma' and 'no tissue' before optimising the segmentation. The second step is to segment the nuclei across each image. Both of these steps are identical to those explained in Chapter 3.

Post nuclear segmentation the algorithm next simulates the cell's cytoplasm by growing out from the nucleus, in all directions, into an area of panCK above a set threshold until it meets the border of a neighbouring cell's cytoplasm. Due to low panCK background staining this threshold is also set low in order to capture cells expressing low intensities of the cell marker. A typical cell size is set at 200μm^2 to aid the algorithm in cell segmentation. The algorithm now assigns a nuclear and cytoplasmic compartment for each segmented cell. The final step of the Tissue studio cell segmentation algorithm is to assign each cell to a classification of high, medium or low panCK intensity. As a subpopulation of tumour glands expressed similar high panCK intensities to tumour buds these were segmented within the image analysis algorithm by assigning these cells to a high panCK intensity dependent classification (Figure 76).

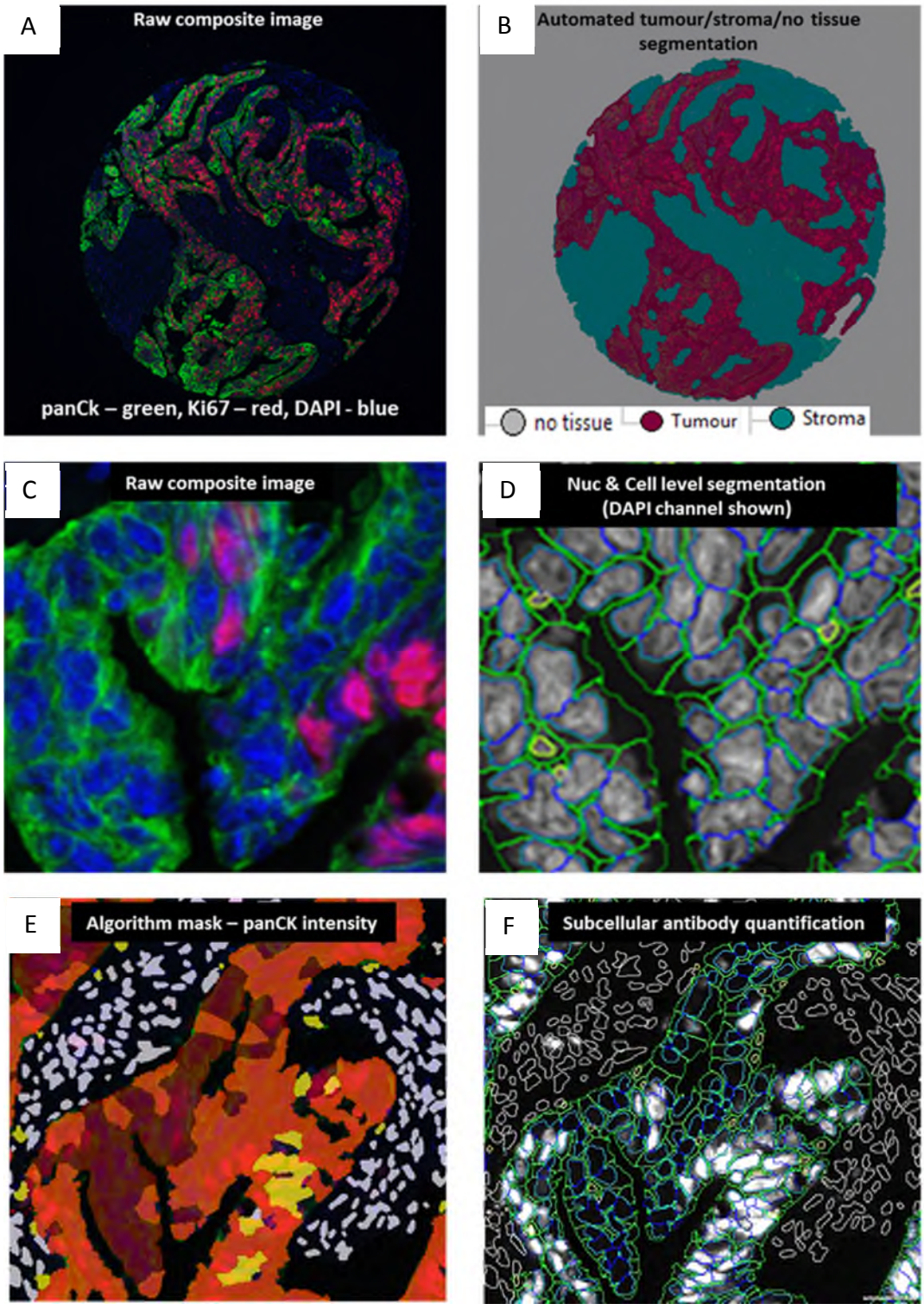

Figure 76. Automated image segmentation of tumour subpopulations and associated biomarker quantification. A) Raw composite image of a TMA core post immunofluorescence with DAPI (blue), panCK (green) and the proliferation marker Ki67 (red). B) Automated tissue segmentation with Composer technology. C) Digital zoom of raw composite image. D) Cellular (green line) and nuclear (blue line) segmentation of tissue. E) Segmented cells are classified as high (maroon), medium (orange) or low (yellow) for panCK intensity. F) Biomarker (Ki67) is quantified within either the nuclear or cytoplasmic compartment of each cell within the image. Images taken with a x 10 objective.

1.6.2.2 Segmentation of subpopulations and biomarker quantification through Developer XD.

The segmented and classified image from Tissue Studio® was imported into Developer XD™ for optimization, creation of subpopulations and for proteomic quantification. The first step of the algorithm is to optimize cellular segmentation by growing each cell into neighbouring unclassified pixels which are above a panCK threshold of 35au resulting in a more accurate tumour cell outline. False panCK positive stromal cells were next excluded from tumour cell classifications. The false classification occurs when a stromal cell neighbours a tumour gland or tumour bud. Both cancer subpopulations contain positive panCK fluorescence, and this fluorescence may become incorrectly segmented within the stromal cell's cytoplasm, resulting in the stromal cell being classified as a tumour cell (Figure 77 A).

Exclusion criteria for falsely classified stromal cells are composed of combinations of cytoplasmic and nuclear morphometric, 'border to' neighbouring objects and panCK intensity parameters (Figure 77 B). False nuclei and debris nuclei are excluded as in Chapter 3. Tumour gland subpopulations were created by merging neighbouring tumour cells, within the tumour ROI, of similar panCK intensity classification: "Cell High", "Cell Medium" or "Cell Low". These merged regions within the Tumour ROI were then classified as subpopulations: "Tumour High", "Tumour Medium" and "Tumour Low". Within the stromal ROI all neighbouring tumour cells, irrespective of panCk intensity classification, were also merged to create subpopulations. If these stromal subpopulations of tumour cells contained 1-5 nuclei they were classified as a tumour bud and if they contained more than 5 nuclei it was classified as a large tumour bud. Enclosed spaces within each merged classified subpopulation were assigned to that classification so that all tumour cell subpopulations were complete and segmented correctly (Figure 78). Areas of adjacent TMA cores may be present within the image due to capturing the image at 10x magnification. The algorithm ignored these on area of tissue thresholding. Full algorithm settings are listed in Appendix 11.

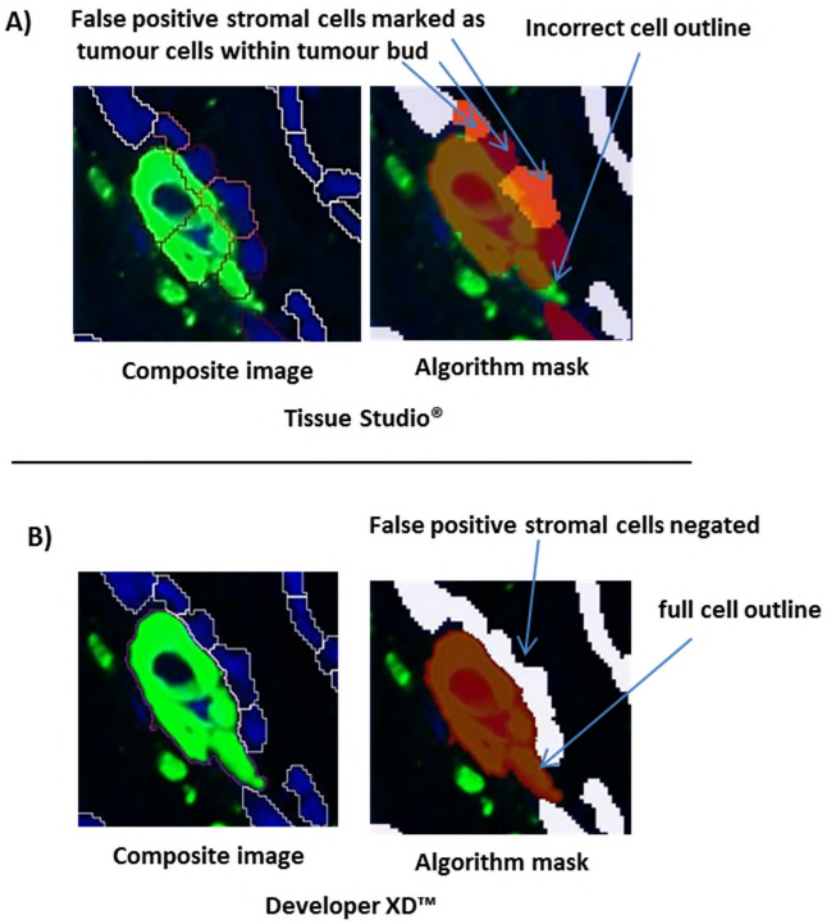

Figure 77. Automated correction of falsely classified stromal cells. A) & B) show a tumour bud with neighbouring stromal cells (panCK: green, DAPI: blue). A) Inaccurate cellular and nuclear segmentation within the Tissue Studio algorithm results in incorrectly classified stromal cells as containing high (maroon) or medium (orange) panCK intensity B) Accurate tumour bud and stromal cell segmentation correctly classifies the stromal cells and being negative for panCK. Images taken with a x 20 objective.

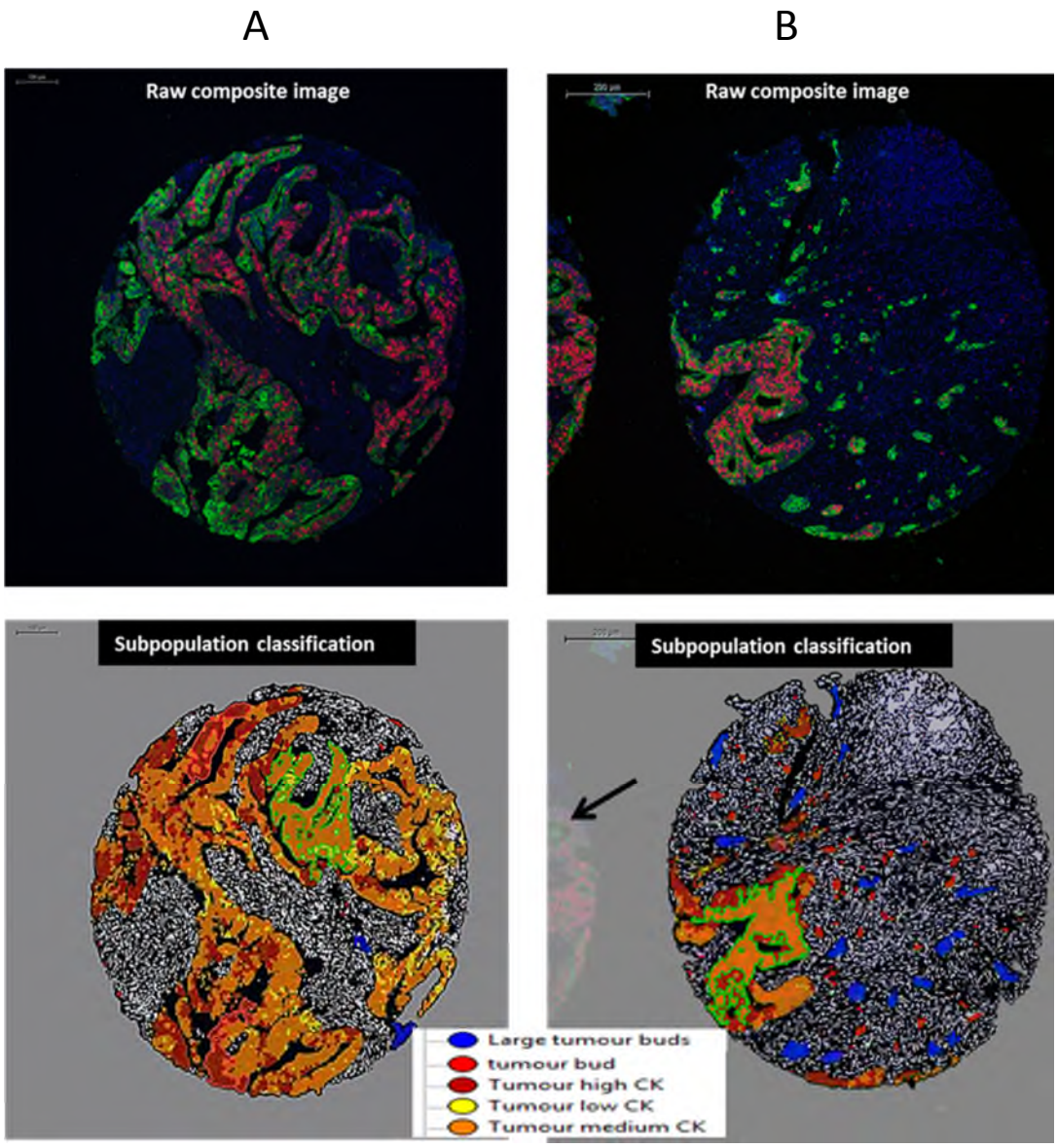

Figure 78. Tumour subpopulation creation and classification within the Tumour bud TMA. A) and B) show two separate cores from the TMA. Top images show the raw composite image with DAPI (blue), panCK (green) and Ki67 (red). The bottom images show the Developer algorithm mask where tumour gland subpopulations have been classified dependent on their panCK intensity. Tumour buds and large tumour buds were classified within the stroma. Arrow in B shows a section of neighbouring TMA core being automatically excluded by the algorithm. Images taken with a x 10 objective

1.6.2.3 Quantification of protein expression within segmented subpopulations

The subcellular mean intensity of a biomarker protein of interest within the cells of distinct subpopulations of: Tumour high, Tumour medium, Tumour low, tumour bud or large tumour bud, is exported by the algortihm. This allows the investigation of heterogeneously expressed protein signatures across the tumour subpopulations within the CRC invasive margin.

Two areas of high TB were identified, after image analysis, in each of 50 patient tissue sections from the validation set. These areas, as well as two areas of high tumour gland density, were marked onto H&E stained tissue sections which consequently were used to mark the areas onto the original tissue blocks. A TMA was created containing cores taken from high TB areas and high tumour gland areas. A panel of proteins was selected with which to interrogate the TMA. This study was carried out to investigate if TB subpopulations expressed differential protein signatures from tumour glands and whether high panCK tumour subpopulations (representing our hypothetical budding stations) expressed a bud-like protein signature or a tumour gland-like one.

This study was also carried out to identify the tumour bud's mechanistic drivers and to see if they expressed invasion like protein signatures. β-Catenin was selected to identify whether Wnt signaling was differentially activated in the subpopulations as well as aberrant epithelial cell status. Ki67 was selected to identify if the subpopulations underwent differing proliferation rates. Nanog, Sox2, Oct4, CD44 and CD133 were selected to identify if the subpopulations contained stem-like cancer cells. E-Cadherin, pan-Cadherin, Src, snail, EpCam, Vimentin and a panel of cytokeratins were selected to identify whether the subpopulations underwent EMT. MMPs were selected to identify if the subpopulations remodeled the ECM, whereas Scrib3 and Pard3 were selected to identify if subpopulations exhibited a loss of polarity. The antibodies utilised and their optimised dilutions are listed in Table 2 in Materials and Methods. Although all antibodies had been previously validated through western blot and IF in either the University of Edinburgh or the University of St Andrews laboratories all underwent a further optimisation experiment to identify the optimal dilution to be used. Optimisation experiments were carried out at three dilutions on a

CRC optimisation TMA. A number of the antibodies failed this further validation step and were not carried forward to be tested on the tumour bud TMA for subpopulation expression evaluation. The mean intensity of each subpopulation was again averaged across the four cores taken per patient sample (two cores from a high budding area and two from a high tumour gland area).The value for each subpopulation within a patient sample was then averaged across the subpopulations of each patient sample. This was calculated to inform on patterns of differential protein expression common across the patient cohort. A high level of inter-patient heterogeneity was found across all proteins.

1.6.2.3.1 Proliferation rates within tumour subpopulations – Ki67

The nuclear expression of Ki67 was automatically quantified across the tumour subpopulations within each TMA core prior to data collation as described above. Although there was a large amount of inter-patient heterogeneity of nuclear Ki67 intensities there was a trend for tumour buds to contain less proliferation cells than the tumour gland subpopulations (Figure 79 A) suggesting that tumour buds have, on average across all patient samples, a lower proliferation rate than tumour glands.

Figure 79 B shows the intensity profiles of cores taken from two different patient samples. The expression levels of Ki67 differ greatly between the patient samples across each subpopulation, demonstrating the high inter-patient heterogeneity. In both patient samples the tumour buds and large tumour buds express less Ki67 than the tumour subpopulations demonstrating intra-patient heterogeneity. This intra-patient differential expression pattern suggests tumour bud subpopulations have a lower rate of proliferation than tumour gland subpopulations.

A)

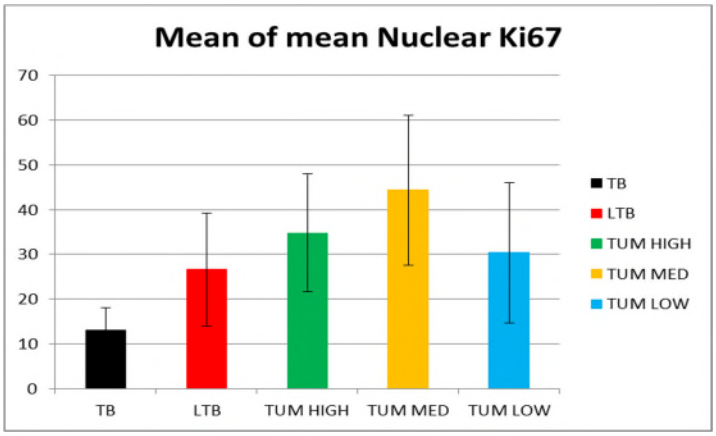

B)

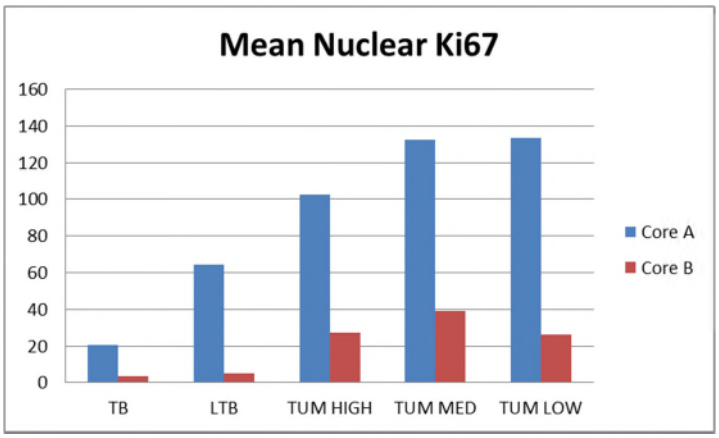

Figure 79. Mean intensity of Ki67 within distinct tumour subpopulations: tumour buds (TB), large tumour buds (LTB), neoplastic gland subpopulations with high panCK intensity (TUM HIGH), neoplastic gland subpopulations with medium panCK intensity (TUM MED) and neoplastic gland subpopulations with low panCK intensity (TUM LOW). A) Mean intensity of Ki67within tumour subpopulations averaged across 50 patients. Standard deviation error bars represent the inter-patient heterogeneity. B) Mean intensity of Ki67 within tumour subpopulations of 2 individual patients: Core A and B.

1.6.2.3.2 Mesenchymal signature within tumour subpopulations – Vimentin & Snail

Cytoplasmic expression of Vimentin was quantified across the tumour subpopulations within each TMA core. The mesenchymal marker Vimentin's expression was on average increased within the tumour bud and large tumour bud subpopulations compared to the tumour gland subpopulations upon assessing all subpopulations across 50 patient samples (Figure 80 A).

Figure 80 B shows the Vimentin intensity profiles of the subpopulations taken from two different patient samples. The expression levels of Vimentin demonstrate high inter-patient heterogeneity. In both patient samples the tumour buds and large tumour buds express more Vimentin than the tumour gland subpopulations. This intra-patient differential expression pattern suggests tumour buds may have taken on a more mesenchymal cellular phenotype than the cells within the tumour glands.

Although Vimentin expression was increased in the tumour bud subpopulations a second mesenchymal marker's intensity, Snail, was on average slightly decreased in the tumour buds and increased in panCk high tumour subpopulations (Figure 81 A). There was, however, very high inter-patient heterogeneity for Snail expression. The inter-patient heterogeneity is demonstrated in Figure 81 B and, although both patient samples express differential Snail, it seems that the panCK high tumour subpopulations express the highest level of Snail in both tissue sections.

1.6.2.3.3 ECM remodeling within tumour subpopulations – MMP9

The cytoplasmic expression of MMP9 was quantified across all subpopulations. There was no expression of MMP9 within any subpopulations and intensity of MMP9 was at baseline levels (Figure 82). The antibody was specific and stromal cell expression of MMP9 and was observed across patient cores but not within tumour subpopulations.

A)

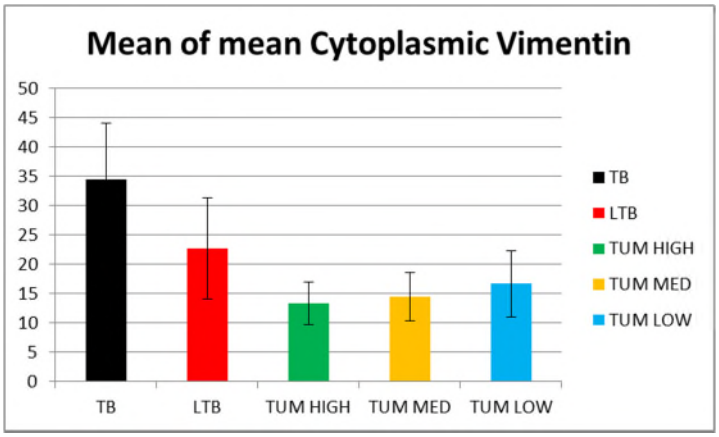

B)

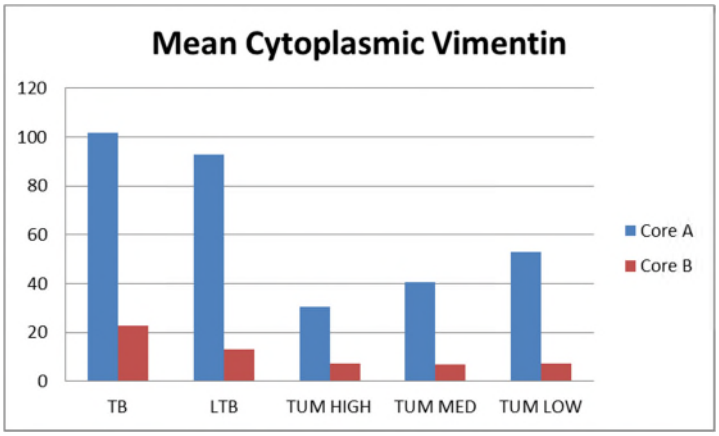

Figure 80. Mean intensity of Vimentin within distinct tumour subpopulations: tumour buds (TB), large tumour buds (LTB), neoplastic gland subpopulations with high panCK intensity (TUM HIGH), neoplastic gland subpopulations with medium panCK intensity (TUM MED) and neoplastic gland subpopulations with low panCK intensity (TUM LOW). A) Mean intensity of Vimentin within tumour subpopulations averaged across 50 patients. Standard deviation error bars represent the inter-patient heterogeneity. B) Mean intensity of Vimentin within tumour subpopulations of 2 individual patients: Core A and B.

A)

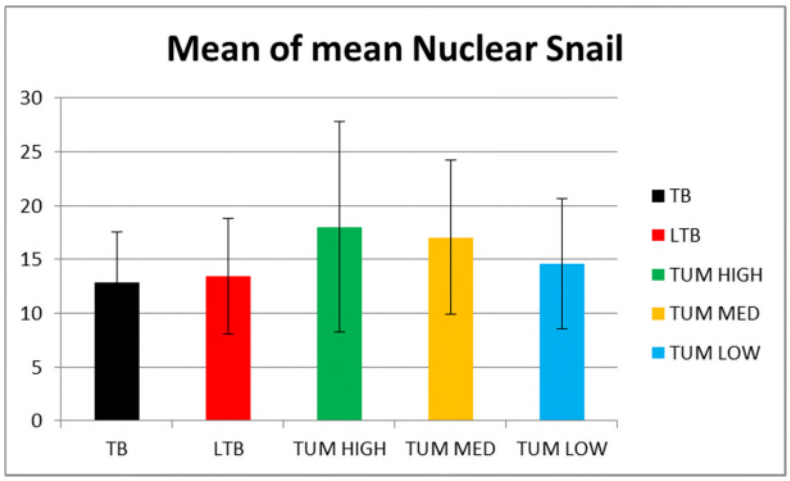

B)

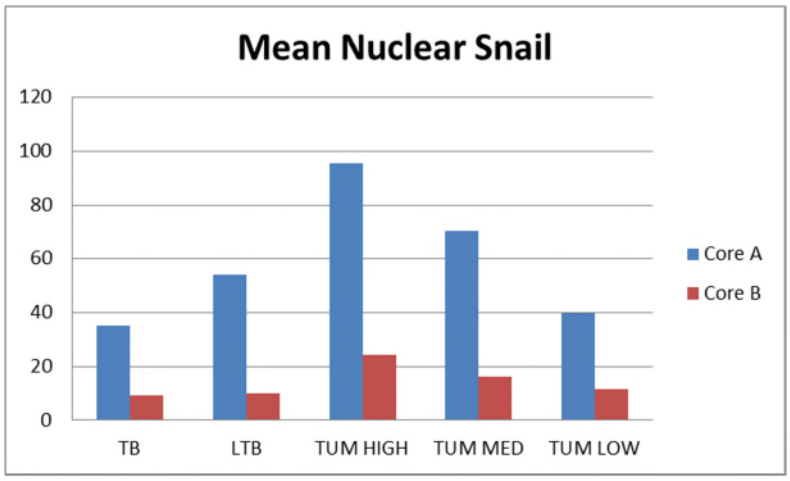

Figure 81. Mean intensity of Snail within distinct tumour subpopulations: tumour buds (TB), large tumour buds (LTB), neoplastic gland subpopulations with high panCK intensity (TUM HIGH), neoplastic gland subpopulations with medium panCK intensity (TUM MED) and neoplastic gland subpopulations with low panCK intensity (TUM LOW). A) Mean intensity of Snail within tumour subpopulations averaged across 50 patients. Standard deviation error bars represent the inter-patient heterogeneity. B) Mean intensity of Snail within tumour subpopulations of 2 individual patients: Core A and B.

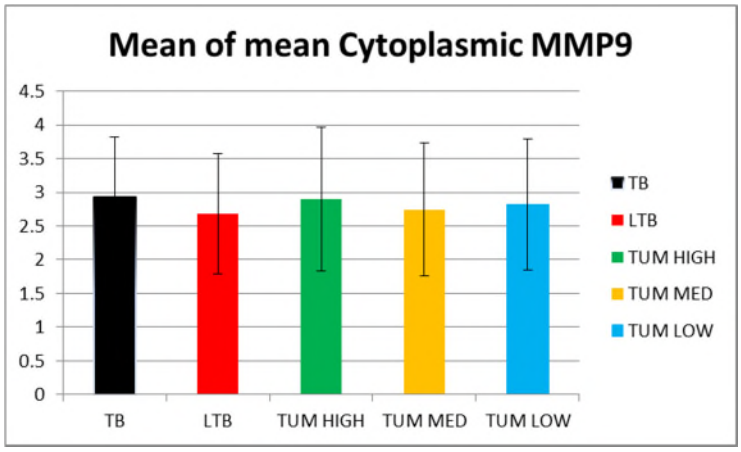

Figure 82. Mean intensity of MMP9 within tumour subpopulations meaned across 50 patients: tumour buds (TB), large tumour buds (LTB), neoplastic gland subpopulations with high panCK intensity (TUM HIGH), neoplastic gland subpopulations with medium panCK intensity (TUM MED) and neoplastic gland subpopulations with low panCK intensity (TUM LOW). Mean intensity of MMP9 within tumour subpopulations averaged across 50 patients. Standard deviation error bars represent the inter-patient heterogeneity.

1.6.2.3.4 Epithelial signature within tumour subpopulations – EpCam, E-Cadherin, CK5/6/8/18, CK7 & CK20

Cytoplasmic expression of all epithelial markers was quantified across the tumour subpopulations of all patient samples. Cytokeratin 7 expression was either present for all tumour subpopulations or absent within the patient samples (Figure 2). There was therefore inter-patient heterogeneity (Figure 83) but no intra-patient heterogeneity. Tumour buds and large tumour buds, on average, expressed lower epithelial markers than the tumour glands. This was true for antibodies against EpCam (Figure 84), E-Cadherin (figure 85), CK20 (Figure 86) and the combined CK5/6/8/18 antibody (Figure 87). In some patient cores, for all antibodies except for E-Cadherin and CK 7, the high panCK tumour subpopulations had similar low expression levels as the tumour bud subpopulations, but this was however not the case for all patient samples.

Subpopulation heterogeneity therefore differs across patient samples. A pattern of lower expression of epithelial markers within the budding areas than the well differentiated neoplastic glands suggests that tumour bud subpopulations partially lose their epithelial phenotype. This, along with average increased Vimentin, may be interpreted as an EMT by a more invasive tumour bud which has adapted to disseminate from glands and migrate within the ECM.

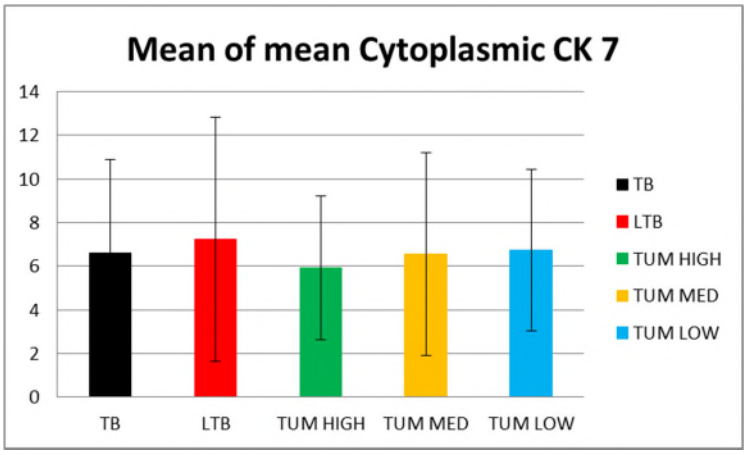

Figure 83. Mean intensity of CK7 within tumour subpopulations averaged across 50 patients: tumour buds (TB), large tumour buds (LTB), neoplastic gland subpopulations with high panCK intensity (TUM HIGH), neoplastic gland subpopulations with medium panCK intensity (TUM MED) and neoplastic gland subpopulations with low panCK intensity (TUM LOW). Mean intensity of CK7within tumour subpopulations averaged across 50 patients. Standard deviation error bars represent the inter-patient heterogeneity.

A)

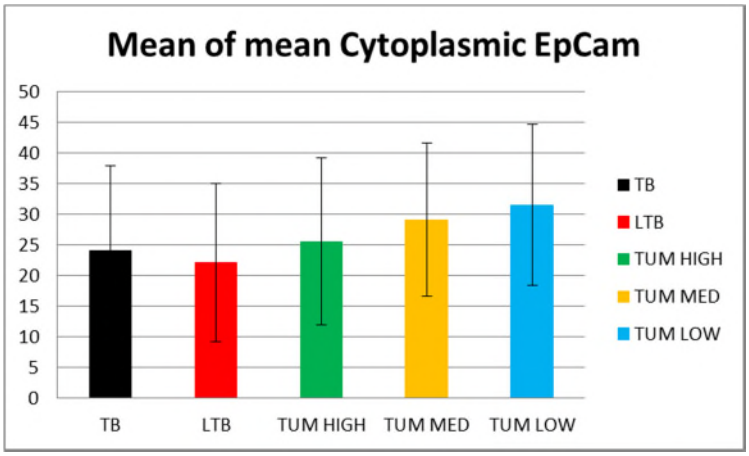

B)

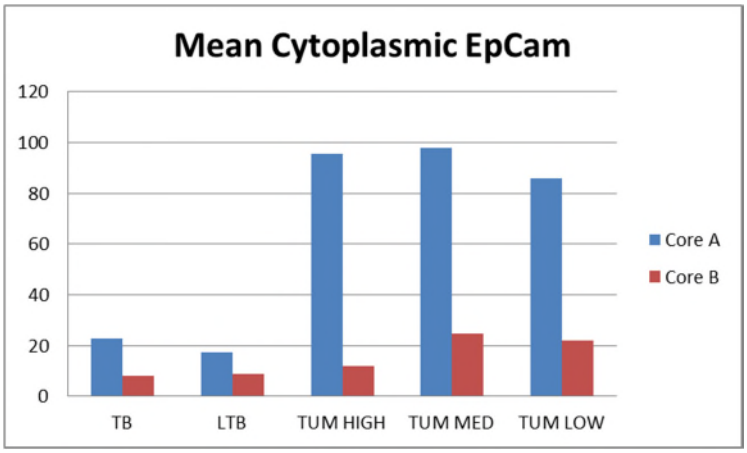

Figure 84. Mean intensity of EpCam within distinct tumour subpopulations: tumour buds (TB), large tumour buds (LTB), neoplastic gland subpopulations with high panCK intensity (TUM HIGH), neoplastic gland subpopulations with medium panCK intensity (TUM MED) and neoplastic gland subpopulations with low panCK intensity (TUM LOW. A) Mean intensity of EpCAM within tumour subpopulations averaged across 50 patients. Standard deviation error bars represent the inter-patient heterogeneity. B) Mean intensity of EpCAM within tumour subpopulations of 2 individual patients: Core A and B.

A)

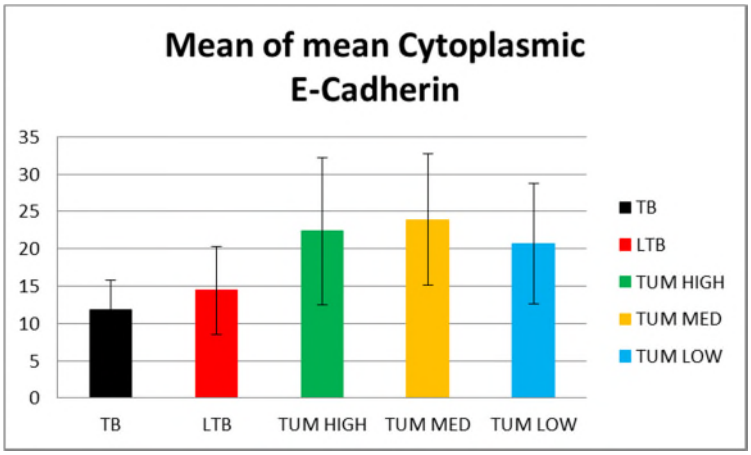

B)

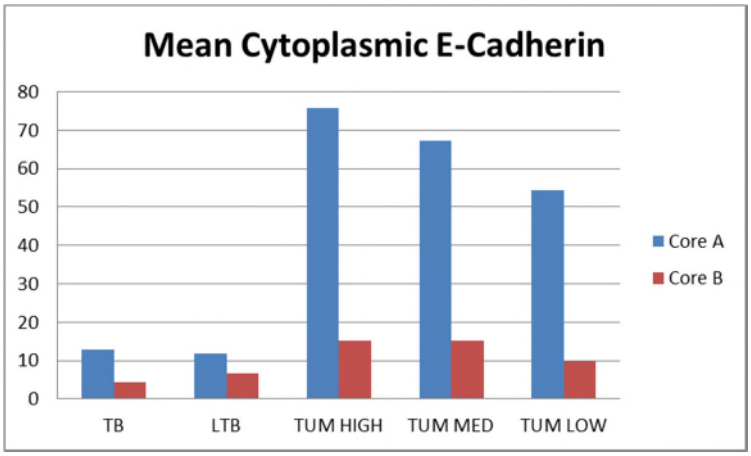

Figure 85. Mean intensity of E-Cadherin within distinct tumour subpopulations: tumour buds (TB), large tumour buds (LTB), neoplastic gland subpopulations with high panCK intensity (TUM HIGH), neoplastic gland subpopulations with medium panCK intensity (TUM MED) and neoplastic gland subpopulations with low panCK intensity (TUM LOW. A) Mean intensity of E-Cadherin within tumour subpopulations averaged across 50 patients. Standard deviation error bars represent the inter-patient heterogeneity. B) Mean intensity of E-Cadherin within tumour subpopulations of 2 individual patients: Core A and B.

A)

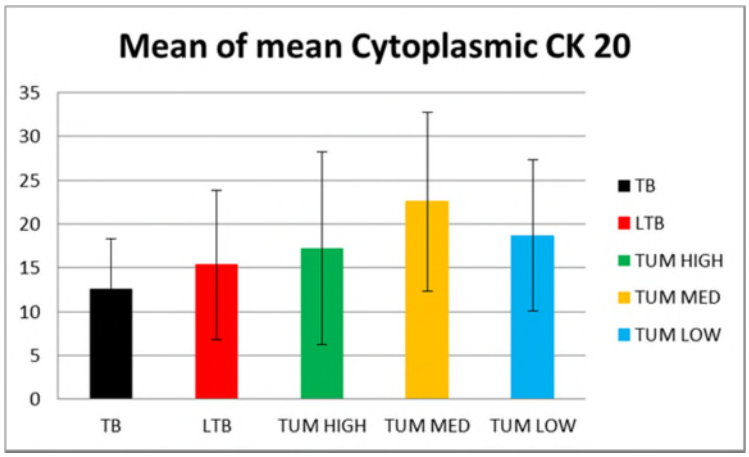

B)

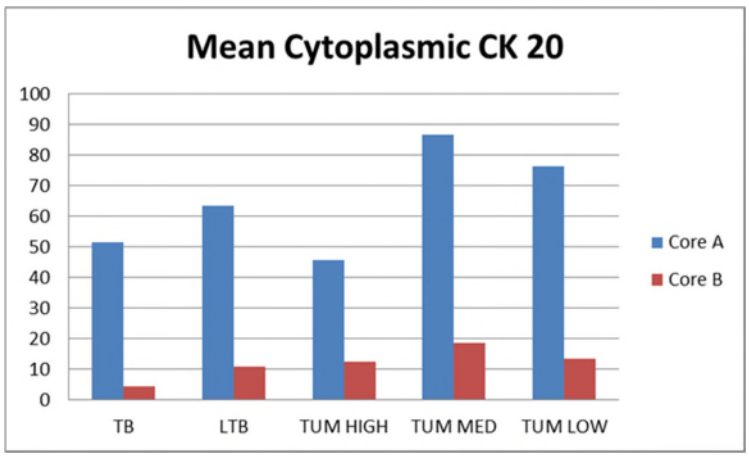

Figure 86. Mean intensity of CK20 within distinct tumour subpopulations: tumour buds (TB), large tumour buds (LTB), neoplastic gland subpopulations with high panCK intensity (TUM HIGH), neoplastic gland subpopulations with medium panCK intensity (TUM MED) and neoplastic gland subpopulations with low panCK intensity (TUM LOW. A) Mean intensity of CK20 within tumour subpopulations averaged across 50 patients. Standard deviation error bars represent the inter-patient heterogeneity. B) Mean intensity of CK20 within tumour subpopulations of 2 individual patients: Core A and B.

A)

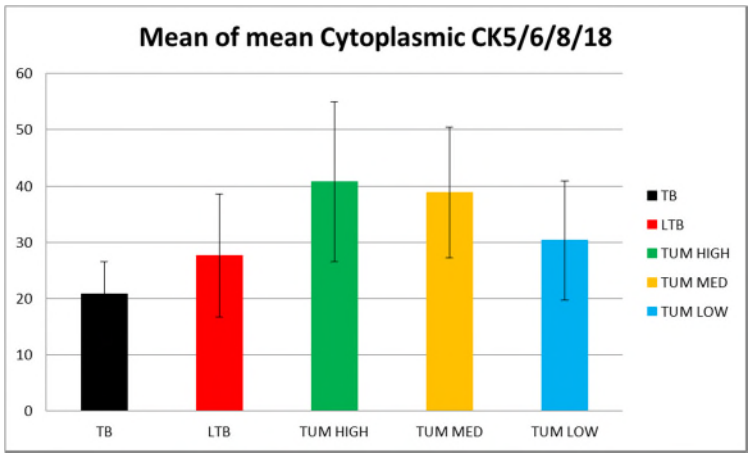

B)

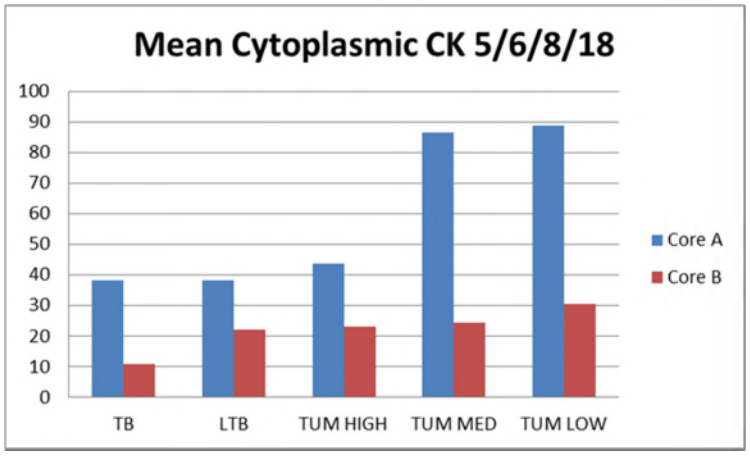

Figure 87. Mean intensity of CK5/6/8/18 within distinct tumour subpopulations: tumour buds (TB), large tumour buds (LTB), neoplastic gland subpopulations with high panCK intensity (TUM HIGH), neoplastic gland subpopulations with medium panCK intensity (TUM MED) and neoplastic gland subpopulations with low panCK intensity (TUM LOW). A) Mean intensity of CK5/6/8/18 within tumour subpopulations averaged across 50 patients. Standard deviation error bars represent the inter-patient heterogeneity. B) Mean intensity of CK5/6/8/18 within tumour subpopulations of 2 individual patients: Core A and B.

1.6.2.3.5 Wnt signalling signature within tumour subpopulations– β-Catenin

An increase in the nuclear to cytoplasmic ratio of β-Catenin is representative of its oncogenic role in CRC and aberrant Wnt signalling. Therefore β-Catenin was quantified within both the cytoplasm and the nucleus of each cell within all tumour subpopulations. The mean nuclear to cytoplasmic ratio was then calculated for each subpopulation within each core. Finally the mean nuclear to cytoplasmic ratio for each subpopulation was calculated across each patient sample. There was high inter-patient heterogeneity present across the cores. On average, there was a higher nuclear than cytoplasmic sublocalisation of β-Catenin in all tumour subpopulations apart from the panCK low and well differentiated tumour glands (Figure 88 A). In some cores the low panCK tumour subpopulations expressed higher cytoplasmic than nuclear β-Catenin (Figure 88 B). This would indicate a loss of β-Catenin's cell adhesion function and an increase in its oncogenic role in subpopulations containing higher panCK intensity.

1.6.2.3.6 Stem-like cell marker expression within tumour subpopulations – CD133 & CD44

Cytoplasmic expression of CD133 and CD44 was quantified within the subpopulations across each patient core.

CD133 was either present in a tumour or absent and showed no intra-patient heterogeneity. Only 3 patient samples expressed CD133 across their subpopulations. A positive and negative sample is plotted in Figure 89.

There was inter- and intra-patient heterogeneous expression of CD44 within the cohort. On average there was a slight increase of CD44 tumour bud expression than in other subpopulations across the whole cohort (Figure 90 A). This was not the case for all patient samples, as some showed an increased expression profile of CD44 in tumour glands than tumour buds and some showed the opposite (figure 90 B).

A) Mean nuclear to cytoplasmic ratio of β-Catenin intensity within tumour subpopulations meaned across 50 patients.

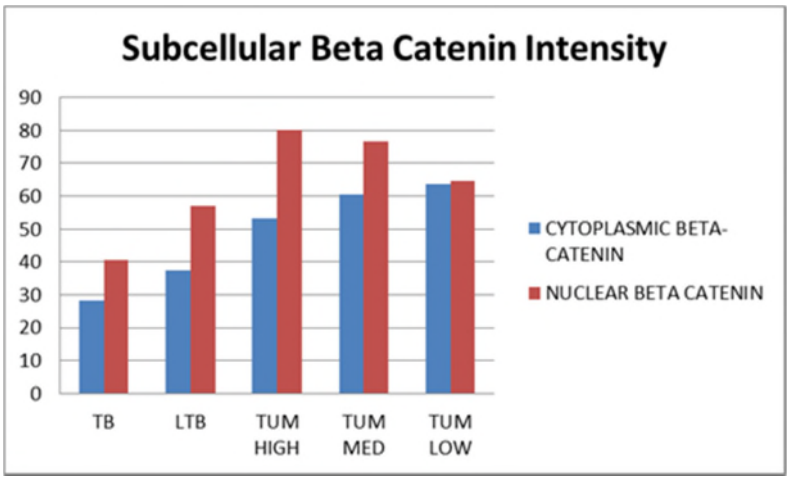

Subpopulation	Mean Nuc/Cyt ratio
TB	1.44
LTB	1.53
TUM HIGH	1.51
TUM MED	1.27
TUM LOW	1.02

B) Nuclear to cytoplasmic ratio of β-Catenin intensity within tumour subpopulations of 2 individual patients.

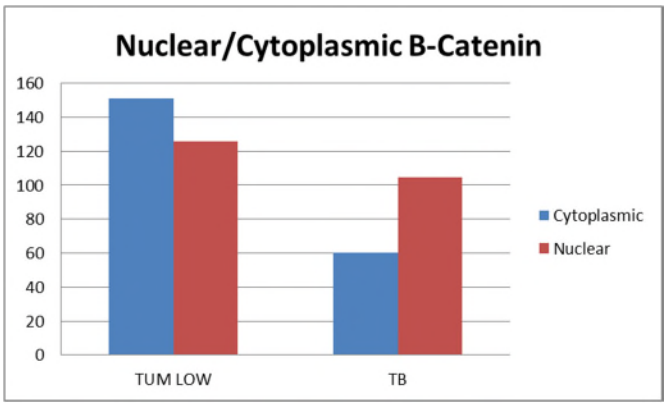

Figure 88. A) Mean intensity of nuclear or cytoplasmic β-Catenin within tumour subpopulations averaged across 50 patients. Nuclear to cytoplasmic ratio of β-Catenin intensity within distinct tumour subpopulations: tumour buds (TB), large tumour buds (LTB), neoplastic gland subpopulations with high panCK intensity (TUM HIGH), neoplastic gland subpopulations with medium panCK intensity (TUM MED) and neoplastic gland subpopulations with low panCK intensity (TUM LOW). The Mean nuclear to cytoplasmic ratio across the 50 patient cohort is tabulated. B) Mean intensity of nuclear or cytoplasmic β-Catenin within tumour subpopulations of an individual patient.

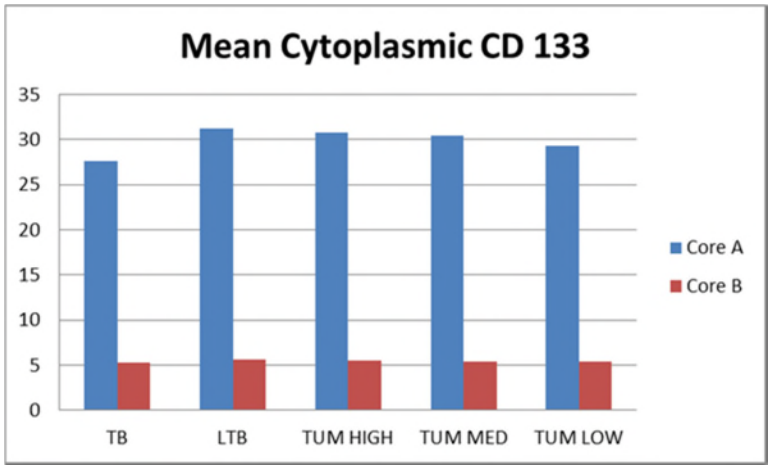

Figure 89. Mean intensity of CD133 within tumour subpopulations: tumour buds (TB), large tumour buds (LTB), neoplastic gland subpopulations with high panCK intensity (TUM HIGH), neoplastic gland subpopulations with medium panCK intensity (TUM MED) and neoplastic gland subpopulations with low panCK intensity (TUM LOW). Two individual patients' data are shown: core A and core B.

A)

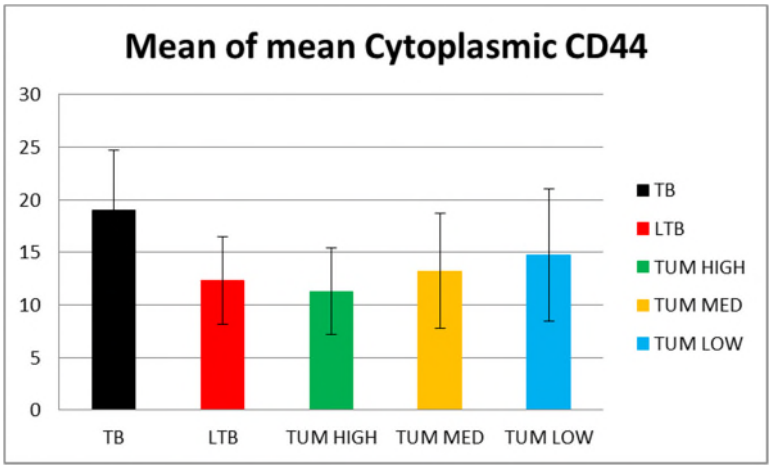

B)

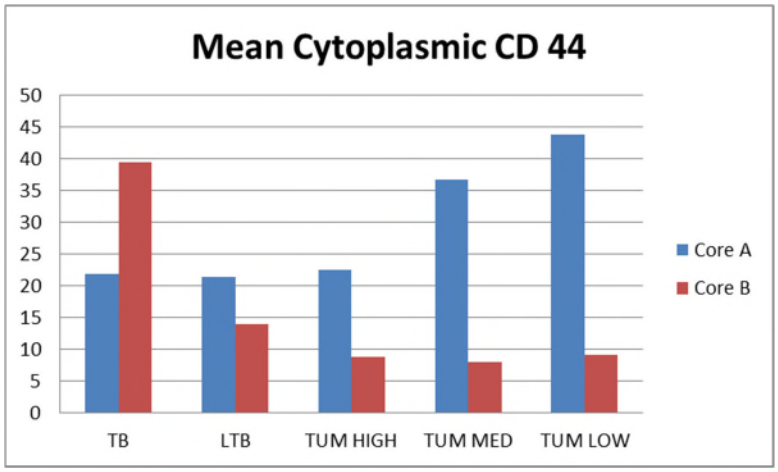

Figure 90. Mean intensity of CD44 within distinct tumour subpopulations: tumour buds (TB), large tumour buds (LTB), neoplastic gland subpopulations with high panCK intensity (TUM HIGH), neoplastic gland subpopulations with medium panCK intensity (TUM MED) and neoplastic gland subpopulations with low panCK intensity (TUM LOW). A) Mean intensity of CD44 within tumour subpopulations averaged across 50 patients. Standard deviation error bars represent the inter-patient heterogeneity. B) Mean intensity of CD44 within tumour subpopulations of 2 individual patients: Core A and B.

1.7 Discussion

The initial aim of this study was to evaluate whether TB can be automatically quantified through image analysis in a robust and reproducible manner. The image analysis algorithm produced to quantify tumour buds was executed across a 50- patient training set and a 134-patient validation set to assess the prognostic power of TB and its ability to stratify stage II patients into high and low risk of CRC specific death. When applying an optimal cut-off, which was highly significant over both cohorts, to the clinically relevant Stage II CRC patient validation set, the hazard ratio for disease specific death, with regard to TB, was 4.5 (95%CI;1.8-11.2). The result reported here reflects multiple other studies which have shown TB to be associated with poor survival, disease recurrence and lymph node metastasis in Stage II patients (91, 92, 265, 272, 307, 309, 312). Although there is a large body of evidence to support TB to be a significant and independent prognostic parameter it is still not included in the RCPath guidelines as a core data item(102). The main reason for this is a lack of standardisation, both in quantification methodology as well as the cut-offs for high and low risk patient stratification and variability of results across studies.

Although most researchers now define tumour buds as clusters of cells within the stroma containing 5 or less cancer cells, as defined by Ueno(270), there is no general consensus as to a standardised quantification methodology. Many studies adopt their own magnification, sample area and cut-offs of what constitutes high grade budding. Cut-offs have varied greatly and have been reported as 5 buds in a 20x field (272, 311) through to 5 buds in a 40 x field (267, 272), however only a few have shown statistically sound evidence for their cut-offs (20, 268, 310). Lugli's laboratory has recently proposed an average bud count across 10 fields at 40x objective which they also compared to 7 other quantification methods and found their method to be the most reproducible and the only one significant for stage II CRC patient outcome(92, 288). Tumour bud counts have either been carried out in H&E(267, 270, 307) or cytokeratin immunohistochemistry(92, 136, 311) studies which produce variable results concerning the proportion of patients with high budding. A reason for these discrepancies could be that tumour buds are easier to identify and therefore are more accurately counted in cytokeratin labelled tissue sections. However observer

variability has been shown, in some cases, to be similar in H&E based studies to those who implement IHC(272).

Although some studies do show good observer concordance in TB count, all previous studies have been undertaken in a semi-quantitative and manual way which can lead to observer variability in reporting of TB. In spite of observer variability and a lack of standardisation TB shows strong prognostic potential due to the majority of studies showing high TB to be associated with a higher risk of CRC specific death or lymph node metastasis(20, 136, 272). This study was carried out to provide methodology which allows the standardisation of TB quantification through an image analysis algorithm while negating observer variability. The image analysis algorithm developed in this study quantified tumour buds and classified them as clusters of up to 5 cells within the stromal region of the invasive margin as defined by Ueno(270). Unlike manual quantification studies in the literature, which quantify TB under brightfield illumination, an IF approach was adopted with panCK and nuclear counterstaining with DAPI. An IF approach allows a separate digital image to be acquired for each fluorophore captured at a specific wavelength: panCK or DAPI. Upon importing the separate images into the Definiens software, panCK positive epithelial objects and DAPI positive nuclei can be segmented within their own image layer resulting in no interference from each other. This was to ensure that nuclei were not obscured by the panCK antibody, as was the case when image analysis was performed on IHC with DAB visualisation. Merging of the two image layers allows the image analysis algorithm to quantify the number of nuclei within each epithelial panCk positive object within the stroma and consequently allows the classification of a tumour bud as containing 1-5 cells.

Although most studies, as was done here, adopt Ueno's definition of a tumour bud being up to 5 cells in size, there is no proof of how this original cut-off was established. Ueno has more recently proposed a novel grading system which quantifies the number of poorly differentiated clusters (PDC) within the stroma with more than 5 nuclei(269) and which he demonstrates has a higher significance on survival outcome than TB. The image analysis algorithm developed in this study therefore also classified and automatically quantified panCK objects within the stroma which fall outwith the 1-5

cell TB classification. PanCK positive objects beneath 5000µm^2 but with more than 5 associated nuclei were classified as “Large Tumour Buds” and their number quantified, as were buds which only contained 1-2 nuclei. An area of 5000µm^2 was manually selected after observing the invasive front of tissue sections within the training cohort. Above this area tumour clusters generally formed gland-like structures. Patients from the training cohort were stratified by the classical TB, TB with only 1-2 associated nuclei and Large Tumour Bud counts. KM curves were plotted to assess CRC specific death over time between high and low budding cut-offs in each bud category. The results from all categories in the Stage II subpopulation were near identical. The sum of TB and LTB categories was classified as “Total Budding” which was created to assess if this resulted in a more prognostic parameter than TB alone. Although Total Budding (HR = 8.1; 95% CI, 3.3-19.8) was a more significant prognostic parameter than TB (HR = 5.76; 95% CI, 2.38-13.8) in the training set it reported near identical results to TB when the optimal cut-off for Total Budding was applied to the clinically relevant Stage II validation set (HR = 4.5, p = 0.002). TB in the training set was not an independent significant prognostic parameter when pT, pN, Dukes, LVI, LVD were included in the model, however Total Budding is an independent predictor of CRC specific death (HR = 4.5; 95% CI, 1.4-14.2). Further large clinical trials will need to be performed to assess if Total Budding is a more significant prognostic parameter than the classical TB classification. TB was also correlated to LVI in both the training set (r = 0.69, p<0.0003) and the validation set (r = 0.64, p< 0.0001), which mirrors similar results by Ohtsuki(265).

TB, as with all histopathological features, is a tissue sectioning artefact. In this study we quantified tumour buds from 3µm thick tissue sections. In the 2D tissue section TB is counted as clusters of 1-5 cells within the stroma of the invasive margin which appear to be dissociated from the tumour glands. There is some proof that tumour buds are in fact connected to neoplastic glands as spindle-like collective invasion when serial sections are reconstructed in 3D(205, 310). If there is little single cell invasion in reality, the size of the tumour bud may be based purely on the area the section is taken from and may therefore be less important as a cut-off than, for example, the morphometry and phenotype of the invading cells within the protrusions. Tumour buds irrespective of their original 3D morphology take on a differential phenotypic and

morphometric change from well-differentiated tumour glands. This study was able to quantify these changes through automated image analysis. The tumour bud nuclear morphometric fingerprint clustered apart from the tumour gland fingerprint within each patient sample from the training set. Tumour gland morphometrics showed relatively little inter-patient heterogeneity however tumour bud inter-patient heterogeneity was pronounced. Tumour buds within each patient sample were larger and rounder than those within the tumour glands. Although this is the first study to show tumour bud morphometry to be differential to tumour gland morphometry, Hamilton showed this to be the case between normal and CRC adenocarcinoma within the same patient(325). Later Deans showed that nuclei in poorly differentiated glands were rounder than those in well differentiated glands and nuclei with a larger diameter were associated with tumours containing an infiltrative growth pattern(326). As tumour buds are associated with a poor outcome these results reflect past studies and have shown nuclear area and shape to be correlated to prognosis(167) as well as a correlation to tumours which have metastasised or contain LVI; which contain larger nuclei(166, 327). Other studies showed no correlation of nuclear morphometry to patient outcome (165, 326).

Nuclear morphometry could act as a surrogate for EMT as it tends to occur at the invasive edge of CRC where poorly differentiated cell clusters are located. TB has also been associated with cancer stem cells and a decreased expression in proliferation(328). These phenotypes would confer an evolutionary advantage for metastasising cancer cells. Although cytokeratin expression is usually associated with epithelial cells(329), TB and LTB showed an increase in panCK intensity compared to the glands from the same patients. This could imply that a full EMT has not occurred in TB and the cells have retained some epithelial characteristics. A decrease in cell adhesion molecules such as E-Cadherin and β-Catenin have, however, been shown to occur in TB(330, 331) which are considered to be essential early markers of EMT(18). An image analysis algorithm was developed to assess if subpopulations of tumour glands (with similar nuclear morphometry and high panCK expression to TB and which were termed ‘budding stations’, TB and LTB had undergone EMT or expressed stem cell-like phenotypes. The algorithm segmented TB, LTB within the stroma and further subpopulations within tumour glands to assess intra-patient heterogeneity. The

gland subpopulations were segmented by panCK intensity. The algorithm then measured biomarker expression within the tumour subpopulations. The quantification of protein expression through image analysis with IF has advantages over semi-quantitative brightfield quantification. These include full continuous data-sets across the dynamic range of the intensity profile (instead of a subjective 1+, 2+. 3+ count), and a decrease in reporter variability.

Similar to other studies of EMT in TB, this study found that, E-Cadherin (331) and EpCam (317) showed a trend of decreased expression in TB and LTB across the patient samples. A further EMT-like phenotype of nuclear β-Catenin expression was seen in TB and LTB which suggests a higher degree of aberrant Wnt signalling and oncogene transcription. Although panCK is increased within the TBs, this is not due to an over-expression of CK7, as previously reported(332, 333), and CK5, 6, 8, 18 and 20 are in fact decreased in TB and LTB which is correlates with the EMT theory. Further proof of an EMT within TB and LTB is the increase in the mesenchymal marker Vimentin(334) although Snail was shown to be decreased in TB and LTB which is in conflict with the EMT theory. Although TB have shown an increase in uPAR(328) and MMP9(322) expression, to allow remodelling of the ECM, the only antibody which showed specificity in this study was MMP9 and no tumour subpopulation expressed this protein, although stromal cells did. The proteins Lgr5, Nanog, Sox2, Oct4, CD133, CD44 and EpCAM have been associated with cancer stem cell and tumour progression(335-337). CD133 showed no intra-patient heterogeneity in the tumour subpopulations when analysed in this study and patient cores either expressed CD133 in all subpopulations or none. CD44 showed a general trend of increased expression in TB but in some patients this was the opposite. There was large inter-patient heterogeneity in the expression of all of the proteins studied which may have masked the trend of subpopulation differential expression when the patient data was accumulated across the samples; however when observing single patient data most followed the trends described above.

Inter-patient heterogeneity in tumour bud morphometrics leads to the hypothesis that there is intra-patient heterogeneity even within the same subpopulations e.g. tumour buds which express a more stem-like or invasive phenotype than others within the

same patient sample. Dawson et al suggested that tumour buds were a heterogeneous population when examining proliferation and apoptosis markers(319) and this is probably also the case in our study. This source of heterogeneity could stem from a mechanistic artefact of the tumour block cutting process where some TB in a tissue section are simply the edge of a cross section of a tumour gland and therefore does not display EMT or invasive phenotypes. The inclusion of these tumour bud artefacts in a TB count may decrease the prognostic significance of TB. Some tumour buds within the tissue sample may not have developed invasive driver mutations, although they have undergone EMT. To investigate this further, single cell data coupled with spatial heterogeneity statistics, and not subpopulation mean data, would need to be exported from the image analysis algorithm. Tumour buds which display EMT, stem-like or invasive signatures could subsequently be included in the tumour bud count while the rest are discarded. The counting of more "aggressive" TB could potentially increase TB's significance as a prognostic marker. If these aggressive buds can be further correlated to a nuclear or cellular morphology this morphometric signature could be utilised as a surrogate marker for the aggressive budding. Utilising a morphometric surrogate for aggressive budding would discard the need for multiple serial sectioning and the associated IHC to identify EMT and stem cell protein biomarkers. TB heterogeneity, in this manner, could explain the inter-patient heterogeneity within the nuclear morphometrics described within this study. Future TB proteomic and morphometric studies could therefore serve two purposes: 1) to identify the mechanism of invasion for novel drug targets and 2) to identify a subpopulation of tumour buds which are in fact invasive and are responsible for poor prognosis. The identification of tumour subpopulations through Tissue Phenomics may also allow the purification of the subpopulations for further omics-based studies to elucidate novel drug targets or mechanisms of cancer progression.

In summary, TB has been shown in this study to be a significant prognostic parameter capable of stratifying stage II CRC patients into high and low risk of CRC specific death. Image analysis allows the standardisation of TB count while negating observer variability. Further validation studies utilising the TB image analysis algorithm could overcome the obstacles preventing the parameter from being included in clinical core-data sets.

Chapter 5: Discovering Novel Prognostic Features in Colorectal Cancer through Tissue Phenomics

1.1 Introduction

As discussed in Chapters 3 and 4, digital pathology coupled with image analysis has the ability to quantify histopathological features, segment tumour subpopulations and quantify biomarkers across digitised immunofluorescence labelled tissue sections. This methodology transforms pathological scoring from a traditionally semi-quantitative science into a fully quantifiable one while allowing the standardisation of reporting. Automated quantification may additionally free up a pathologist's valuable time and reduce observer variability. However, it does not perform a task which a pathologist could not do themselves and there still remains scepticism of automated methodologies. Quantitative image analysis within clinical pathology research may only take hold and be widely adopted when the technology has the power to perform tasks and calculations which are outwith the scope of manual quantification.

Histopathology is not solely the compilation of a set of recommended histopathological features into a prognosis based on institutional guidelines. The field of pathology recognises the rich data source which lies within the tissue section (338). The pathologist takes into account the entire heterogeneous and heterotypic microenvironment and its interactions across the tissue section. Through experience they are able to process this complex, sometimes subtle information, and translate it in order to aid their diagnostic or prognostic conclusion. Research pathologists also apply this methodology to evaluate novel or significant prognostic features such as the tumour differentiation or invasive morphology at the invasive front(236, 269, 304) or immune response within the microenvironment(339) (340, 341). Although the tumour's microenvironment is becoming more evidently important in a cancer's progression, where complex immune cell infiltrate and its spatial distribution can be quantified by image analysis(298, 342), a simple measurement such as the percentage of stroma at the invasive front has also been shown to be prognostic(343-345).

The empirical science of pathology can be difficult to standardise and quantify due to the inter- and intra-heterogeneous nature of the tumour microenvironment. Automated image analysis based segmentation of digitised tissue sections has the ability to quantify and standardise complex and subtle morphological features or signatures in a continuous data capture manner. The emerging field of Tissue Phenomics allows us to perform such datafication of the tissue phenome from computationally segmented tissue sections. This image analysis methodology quantifies and profiles the complex phenome of the tumour's microenvironment in an *a priori* "measure-everything big-data" approach. This is performed in an attempt to identify and quantify novel clinically relevant histopathological objects from large exported image based multi-parametric data sets. These objects may represent single or combinations of morphometrically quantifiable histological features, which may be subtle or difficult to reproducibly quantify and therefore go unreported under manual observation, but which could prove prognostic or predictive. Beck *et al* demonstrated this technique in breast cancer and found the stromal microenvironment to be specifically relevant to prognosis (192). This study details the development of a novel methodology allowing the identification of novel histopathological features through the implementation of a Tissue Phenomics pipeline. The Tissue Phenomics pipeline consists of performing unbiased image analysis prior to data export and multi-parametric statistical analysis. Initially a sophisticated image analysis solution is required to allow multi-parametric data export and the quantification and extraction of multiple histological features while also capturing the morphometry of the tumour microenvironment. Here, the methodology is demonstrated through profiling the phenome of the invasive front of the CRC microenvironment on immunofluorescence labelled tissue sections, resulting in a phenotypic fingerprint for each patient; the phenotypic fingerprint is created from the hierarchical multi-parametric data exported post image analysis. As tumour morphometry, the tumour microenvironment and the lymphatic vasculature within the microenvironment have been shown to be prognostic in the literature (20, 259, 260, 267, 295), as well as in previous chapters within this thesis, the phenotypic fingerprint within this study includes morphometric and intensity parameters of all tumour subpopulations, such as neoplastic glands and tumour buds as well as the lymphatic vasculature. Nuclear morphometric and fluorophore intensity parameters across the

digitised images were therefore quantified and nuclei assigned to their appropriate subpopulations to retain their heterogeneity. The image segmentation and image analysis algorithm was based on the combined LVI and Tumour bud quantification algorithm as described in Chapter 4.5. In addition to the parameters exported in previous chapters, over one hundred intensity and morphometric parameters were exported across the microenvironment resulting in a phenotypic fingerprint created from all segmented objects. After post processing of the exported phenotypic fingerprint, multi-parametric ensemble and decision tree learning methods were performed in the Tissue Phenomics pipeline in order to undertake a data mining approach to identify a novel prognostic histopathological feature with the ability to stratify Stage II CRC patients into high and low risk of disease specific death.

The study in this chapter applied the Tissue Phenomics pipeline to the image analysis of the CRC invasive front through the triple immunofluorescence multiplex labelling of panCK, D2-40 and DAPI as implemented in previous chapters. The Tissue Phenomics pipeline developed here is not, however, exclusive to this single multiplexed immunofluorescence assay. The Tissue Phenomics pipeline can be utilised to identify, for example, predictive or prognostic histopathological features, spatial density signatures, intensity and texture profiles, *in situ* biomarker quantification and expression levels from other image analysis segmented digital pathology images. The pipeline may also be utilised, after small additions, to integrate multi-omics data into the multiparametric fingerprint. The decision tree statistics allow the identification of single or combinations of multi-modal multi-omics prognostic or predictive signatures.

1.2 Results

1.2.1 Tumour morphometry

The initial step of every immunofluorescence algorithm within this project is to segment the tumour glands from the stroma. This step is done through machine learning with Definiens Composer™ technology. Previously this step was undertaken to identify histopathological features within the stromal ROI while the tumour ROI was excluded from further quantification. In order to assess whether specific tumour morphometric parameters were prognostic the Tissue Studio image segmentation algorithm was further programmed to quantify and export individual tumour gland morphometrics as well as the percentage area of the image of each ROI (Necrosis/Lumen, Stroma and Tumour). Fifteen tumour ROI morphometric parameters were selected for export within the Tissue Studio® custom export feature (Table 13). The updated tissue segmentation algorithm was run over the 15 images captured across the invasive front of the WSI training cohort and which were utilized in Chapter 3.7.2.1 The export parameters, as listed in Table 13, were collated across the 15 images by calculating the mean of each parameter in order to create a single row of data per tissue section. Each parameter was imported into the X-tile software where optimal cut-offs were calculated and *p* values corrected through Miller-Siegmund false discovery statistics. All percentage ROI parameters were highly significant for stratifying the training cohort patients into high and low risk of disease specific survival over 14 years of follow up (Table 13 and Figure 91). Of the tumour gland morphometry parameters, eight were shown to be significant if no *p* value correction was applied and only 'Relative border to stroma' ($p = 0.004$) and 'Perimeter' ($p = 0.04$) were significant after stringent Miller-Seigmund false discovery rate correction (Table 13).

Parameter	Cut-off	Kaplan-Meier *P* Value: Uncorrected	Kaplan-Meier *P* Value: Miller-Seigmund corrected
% Lumen/Necrosis	**1.9**	**<0.0001**	**0.0005**
% Stroma	**67.2**	**<0.0001**	**0.0008**
% Tumour	**25**	**<0.0001**	**0.0016**
Border Index	1.7	0.002	0.06
Area (μm²)	42539	0.05	0.5
Roundness	N/A		Non-significant
Compactness	N/A		Non-significant
Length/width	N/A		Non-significant
Length (μm)	N/A		Non-significant
Width (μm)	130	0.01	0.24
Border to Stroma (μm)	1072	0.04	0.4
Relative Border to Stroma	**0.8**	**0.0001**	**0.0035**
Perimeter (μm)	**1036**	**0.002**	**0.04**
Circularity	N/A		Non-significant
Ellipticity	N/A		Non-significant
Elliptic Fit	N/A		Non-significant
Rectangular Fit	0.8	0.05	0.5
Asymetry	0.6	0.004	0.08

Table 13. Prognostic significance of percentage ROI and tumour morphometry calculated from the training cohort. Optimal cut-offs for each parameter are calculated from KM curves and uncorrected or Miller-Siegmund false discovery rate corrected *p* values are tabulated. Parameters in **bold** were deemed to be significant (MS corrected <0.05).

TMA Navigator software was utilised to plot the KM curves of the significant parameters to assess their ability to stratify patients on survival over time. Patients are split into above or below cut-off groups prior to plotting the curves (Figure 91).

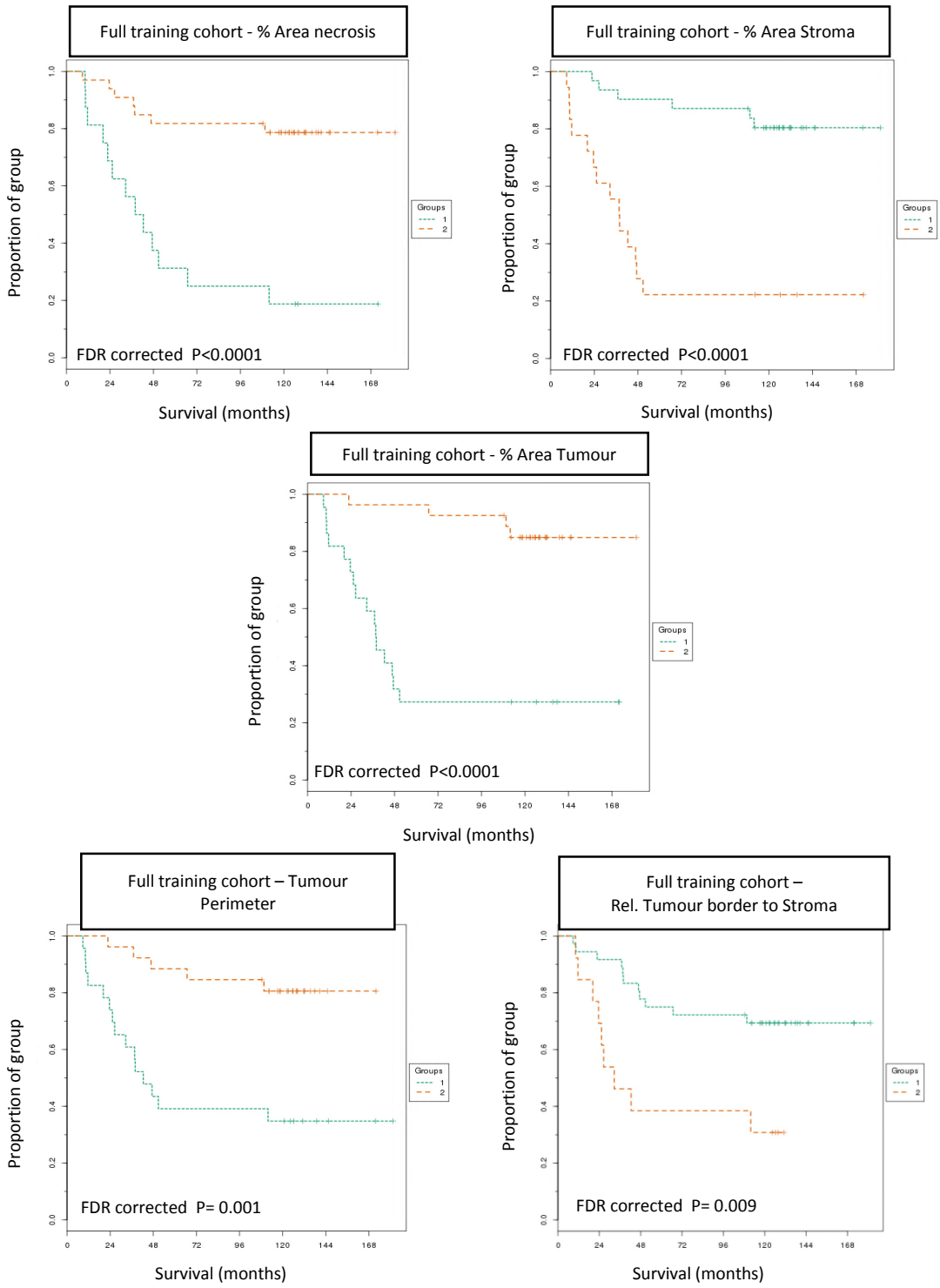

Figure 91. Kaplan-Meier curves for ROI percentage of image and significant tumour morphometrics, Training cohort. Disease specific survival of above and below cut-off categories for each significant percent area ROI and tumour morphometric parameters. Patients categorised in Group 1(green) are below cut-off and Group 2 (orange) above cut-off for each parameter.

A number of the tumour gland morphometrics showed some promise in stratifying patients into high and low risk of disease specific death, although after stringent false discovery rate (FDR) statistics, most fell below significant levels. A combination of these parameters may increase their prognostic significance and therefore the next phase of this study is to create a Tissue Phenomics pipeline to export a multi-parametric phenotypic fingerprint which incorporates a large number of image based analysis parameters, including the tumour gland morphometrics. The fingerprint will be interrogated for significant single or combinations of parameters.

1.2.2 Tissue Phenomics pipeline

The Tissue Phenomics pipeline was constructed to identify novel histopathological features or combinations of features from large multi-parametric image-based data sets (Figure 92). The Tissue Phenomics pipeline was performed on the 50 patient whole tissue section training cohort. The same 15 immunofluorescence labelled (panCK, D2-40, DAPI) images captured across the invasive front of each patient tissue section, as utilised in Chapter 3.7.2.1, were the input for the Tissue Phenomics pipeline. The digital image was segmented through the Definiens XD™ image analysis software suite using the modified Tissue Studio® ROI segmentation ruleset as described in 5.2.1 and the IHA Developer XD™ image analysis algorithm. The algorithm was augmented to allow morphometric, intensity and texture parameters to be calculated and exported for each segmented object to create a Tissue Phenomics Algorithm (TPA). Full algorithm settings for the TPA are listed in appendix 12. The multi-parametric data export was collated across the 15 images to ensure one row of data per tissue section creating a phenotypic fingerprint for each patient. This high dimensional data was analysed through multiple multi-parametric statistical methods. The first of these methods which was applied to the data was Principal Component Analysis (PCA). PCA allowed the graphical visualisation, in 2D, of the phenotypic signature and the evaluation of the fingerprint's ability to stratify high and low risk patients. Regression tree analysis was subsequently applied to the multi-parametric data in order

to identify the significant parameters within the fingerprint. The next step in the pipeline was therefore to perform a Random Forest regression tree model on the phenotypic fingerprint. The parameters were ranked in order of significance through the Random Forest modelling and their associated Gini score. The significant parameters were the input for a Classification and Regression tree analysis (CART) model to identify the optimal significant parameters, within the regression tree, along with associated cut-offs to stratify patients into high and low risk of disease specific death.

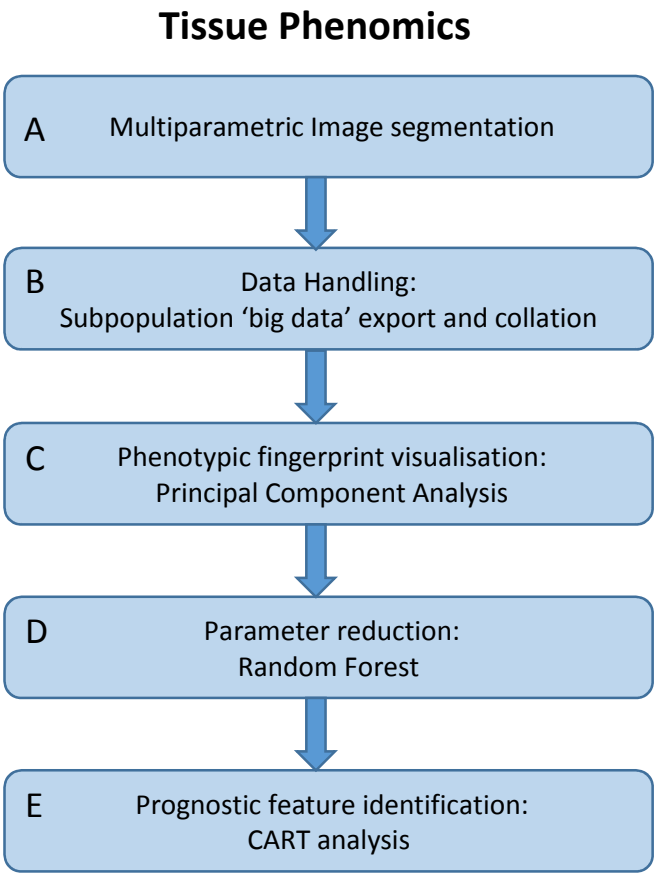

Figure 92. Tissue Phenomics pipeline. A) Digitised images are segmented with image analysis software and resultant objects quantified. B) Associated hierarchical multi-parametric data is exported and collated. C) PCA is performed to visualise the multi-parametric signature and to assess its prognostic value. D) Significant parameters are identified through Random forest. E) The resultant significant parameters act as input to a CART model for prognostic feature identification and cut-off analysis.

1.2.2.1 Image segmentation and data export

The first essential step that a Tissue Phenomics approach requires is to segment the tissue through image analysis (Figure 92A). This quasi-unbiased multi-parametric image feature capture is utilised to discover novel prognostic phenotypic fingerprints and histopathological features. This study aimed to quantify the number of each resultant segmented object as well as multiple morphological, texture and intensity parameters from tumour cell subpopulations as well as the lymphatic vasculature in order to identify novel prognostic features which enable the stratification of stage II CRC patients into high and low risk of disease specific death.

Within this study immunofluorescence was utilised to label epithelial cells, lymphatic endothelial cells and to counterstain the nuclei. The labelling of the tissue enables the TPA to segment every labelled object within the image including tumour glands, smaller invasive tumour bodies within the stroma or within vessels, epithelial debris and lymphatic vessels. Once segmented the TPA allows the quantification and export of morphometric, density and fluorescence intensity and texture measurements (Figure 93).

Spatial information, such as neighbouring and colocalising of objects is further captured and used to further sub-classify objects, such as vessels bordering tumour glands or tumour cells bordering vessels (Figure 94).

Nuclei within the stroma, the tumour glands and the tumour buds contain heterogeneous and differential intensity, morphometric and texture phenotypic features (Figure 95). The algorithm segments nuclei within set subpopulations on a cell by cell basis. An individual nucleus may therefore only belong to a single region of interest; such as a tumour gland or stroma, or an object of interest, such as a tumour bud or vessel invading tumour cell (Figure 93B). This is performed to retain the heterogeneity of nuclei across the tumour microenvironment and within certain histological features. The multi-parametric single object and nucleus by nucleus data

are exported from the TPA and subsequently collated through averaging or summing the parameter data across the 15 images analysed per tissue section. This ensures a single row of data per parameter for each patient sample (Figure 91B). A full list of the 123 parameters exported from the image analysis algorithm and their collation method can be found in appendix 13.

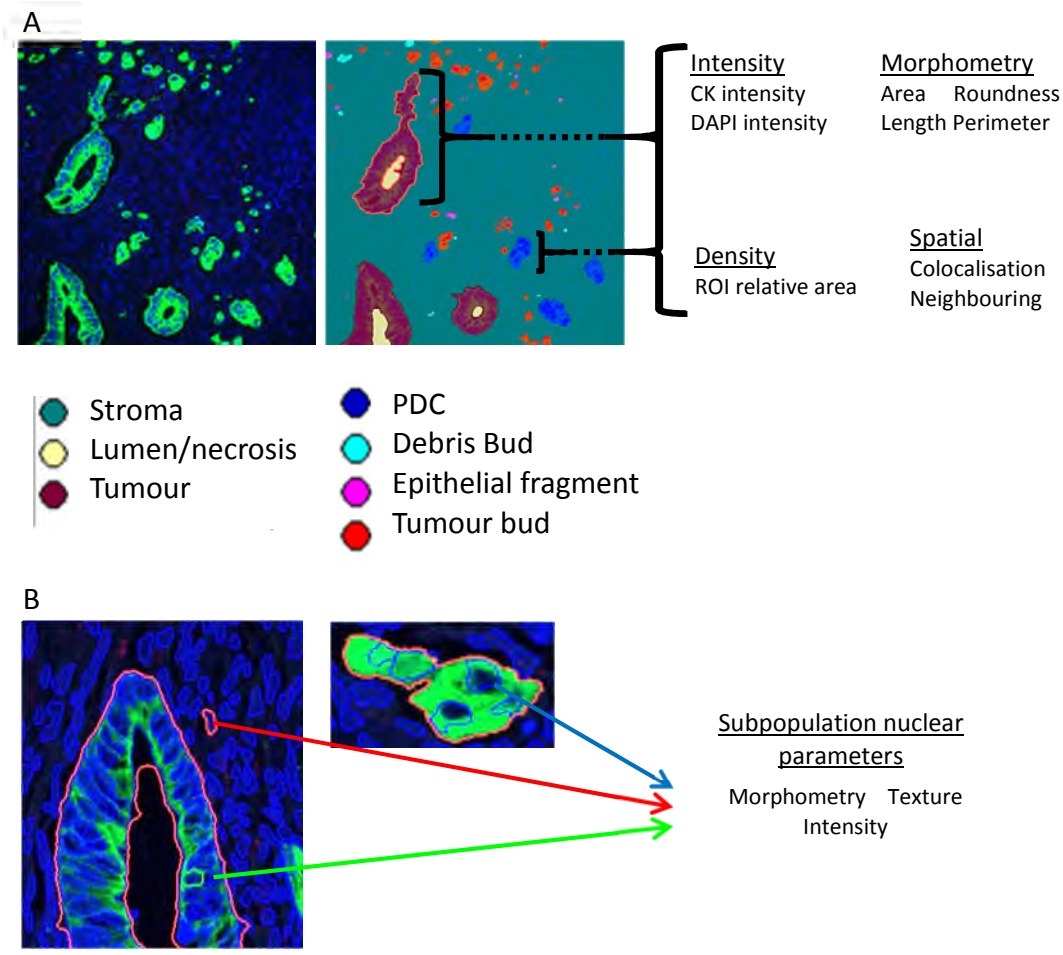

Figure 93. Examples of multi-parametric data export from the Tissue Phenomics Analyser. A) Left panel shows a composite image of panCK:green & DAPI: blue. Right panel shows the algorithm mask which classifies objects within the image. Multiple parameters are exported from each classified object as is the percentage of each ROI within each image. B) Nuclei are subdivided dependent on the hierarchical objects they belong to e.g. within tumour glands (green arrow), stroma (red arrow) or tumour buds (blue arrow). Nuclear morphometric and intensity parameters are exported from within their allocated subpopulations. Images captured with a x 20 objective.

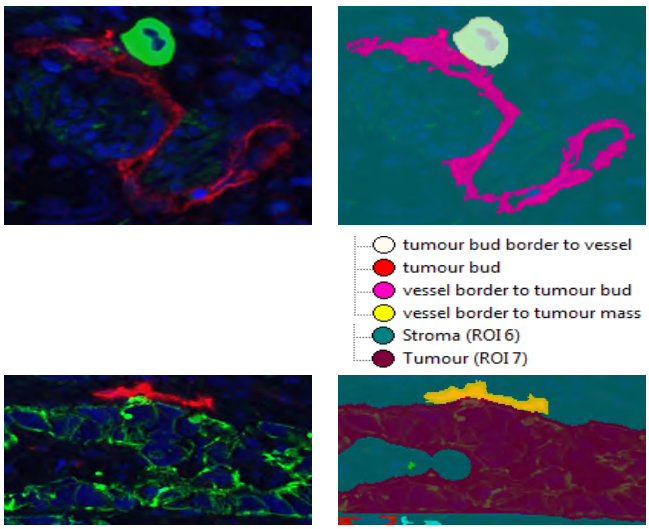

Figure 94. The quantification of spatial relationships of neighbouring objects. Left panel show composite images of PanCK: green, DAPI: blue and D2-40: red. Right panels show corresponding algorithm mask. Further multi-parametric data is exported from the spatial relationships of objects. Colocalised and bordering objects are exported in a hierarchical manner. Top right panel: tumour bud (white mask) which is also bordering to a vessel (pink mask). Bottom right panel: a vessel (yellow mask) which is also bordering to a tumour gland (purple mask).

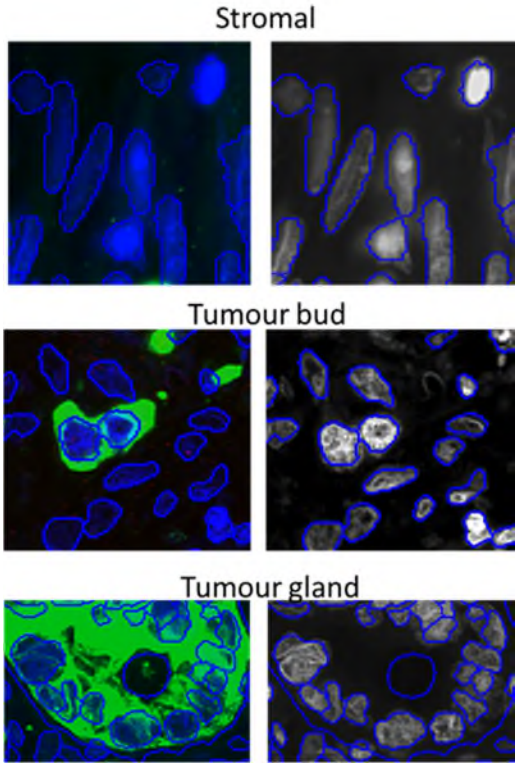

Figure 95. Examples of heterogeneous nuclear morphometry within three microenvironment subpopulations: Stroma, tumour bud and tumour gland.

1.2.2.2 Phenotypic fingerprint analysis

The resultant collated 123 parameters per patient sample make up the patient's multi-parametric phenotypic fingerprint. This raw data is difficult to utilise as a prognostic tool due to its complexity and high dimensionality. To enable the visualisation of the phenotypic fingerprint in a 2D scatter plot a PCA was performed. The data from the first 2 principal components was exported as an x and y coordinate for each patient sample (Figure 96). The 2 principal components capture and explain 72% variance in the data set. Visualising the data by performing PCA allows us to evaluate the effectiveness of the phenotypic fingerprint to stratify all patients within the cohort into high or low risk of disease specific death as well as the Stage II subpopulation.

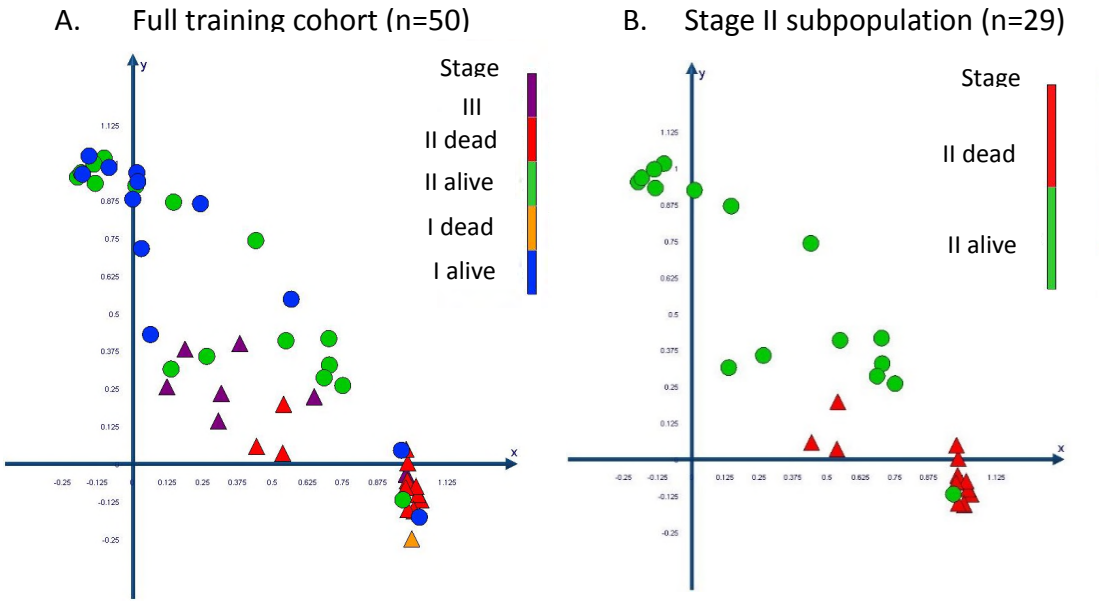

Figure 96. Visualisation of the phenotypic fingerprint through PCA. The data from a 2D principal component analysis is plotted in a scatter plot for the full training cohort (A) and for the stage II subpopulation (B). Patients who died specifically of CRC are plotted as triangles and patients who survived follow up are plotted as circles. The phenotypic fingerprint allows the significant stratification of good and poor prognosis patients.

Those patients who had a poor outcome, namely died of disease specific CRC during follow up, cluster in the lower right section of the scatter plots while the majority of those with a good outcome cluster within the top left section of the graph. In the Stage II subpopulation there is only one outlier patient with good outcome which clusters in

the poor outcome section and no patients with poor outcome cluster with those with good outcome. The clustering of the phenotypic fingerprint allows the robust patient stratification across the whole cohort with 100% specificity, 76.7% sensitivity and an area under the receiver operator curve (ROC) curve of 0.89. The sensitivity increased to 92.85% when stratifying the stage II subpopulation (Table 14). The PCA based clustering of the full exported parameter set is an excellent quality control checkpoint within the Tissue Phenomics pipeline. It allows the user to ascertain if the data captured allows meaningful patient clustering, with regards to his/her hypothesis, before performing parameter reduction statistics.

	Method Comparison					
	Full Training cohort			Stage II subpopulation		
Method	Specificity	Sensitivity	Area under ROC	Specificity	Sensitivity	Area under ROC
Phenotypic fingerprint (PCA)	100%	76.7%	0.89	100%	92.85%	0.94
ALTB (CART)	96.3%	82.6%	0.90	100%	93.75%	0.96

Table 14. Comparison of full phenotypic fingerprint and ALTB patient stratification. ALTB reports more accuracy in stage II patient stratification into good and poor prognosis categories than the full phenotypic fingerprint. ALTB is also amenable to translation into the clinic due to being a single parameter with an associated absolute cut-off calculated from continuous data.

1.2.2.2.1 Exclusion of fluorescence parameters

As with all immunofluorescence experiments there is a high likelihood of batch variation when carrying out the experiment over multiple days. There are several sources for the batch variation in fluorescence intensities and it can originate in discrepancies in reagents (volume, shelf-life or exposure to light) or imaging equipment (bulb and optics lifetimes). Although there are statistical methods to allow for batch variation, the most robust method to ensure no variation in intensities is to exclude all fluorescence intensity parameters from the phenotypic fingerprint. The remaining shape, texture and spatial density measurements will remain a constant across all batch processing. PCA was performed again after excluding all fluorescence parameters from the training set's phenotypic fingerprint. There was no change in the results from the data and the clustering of each patient's fingerprint was identical from

when the full parameter set was utilised which allows the conclusion to be drawn that fluorescence does not factor significantly in the PCA results (Figure 97).

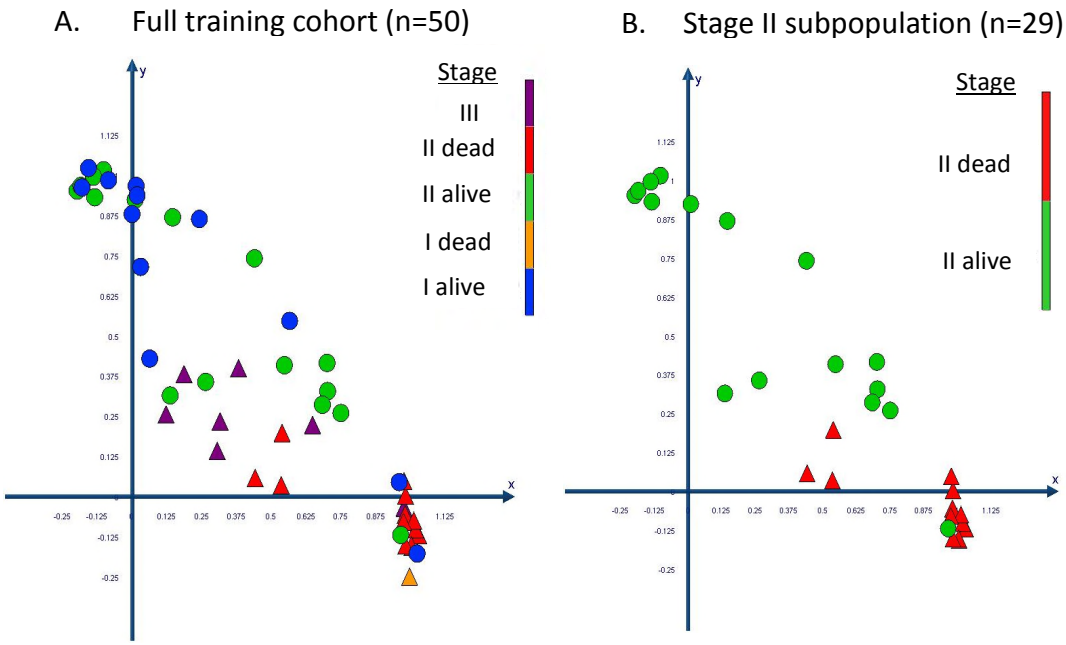

Figure 97. Visualisation of the phenotypic fingerprint through PCA after exclusion of fluorescence based parameters. The data from a 2D principal component analysis is plotted in a scatter plot for the full training cohort and for the stage II subpopulation. Patients who died specifically of CRC are plotted as triangles and patients who survived follow up are plotted as circles. The phenotypic fingerprint allows the significant stratification of good and poor prognosis patients. There is no alteration in significance of patient stratification upon the removal of fluorescence based parameters.

1.2.2.3 The identification of significant parameters through decision tree models.

1.2.2.3.1 Random Forest parameter reduction

Although the multi-parametric phenotypic fingerprint allows the significant clustering of good and poor outcome patient subgroups, there may be parameter redundancy within the model and it is not possible to ascertain which of the parameters are most significant from the PCA analysis. To allow the elimination of redundant parameters, while retaining a robust stratification model, RF was performed (Figure 92D). The RF analysis also ranks the parameters by associated Gini score which is based on variable

importance and the extent to which each variable contributes to optimal separation of good and poor outcome patients.

The 123 parameters (listed in Appendix 13) utilised to create the prognostic phenotypic fingerprint are the input for the RF analysis. The fluorescence parameters were included to assess their significance in the model. After analysis the 123 parameters were ranked by their associated Gini score and the least significant parameter was removed from the phenotypic fingerprint. This process was performed iteratively until the removal of a parameter affected the statistical significance of the model for the worse. The method resulted in a set of 37 parameters (Appendix 13) which had the ability to stratify the patients within the training cohort into high and low risk of CRC disease specific death with the same statistical significance as the full parameter set (100% specificity, 76.7% sensitivity, area under the ROC curve of 0.89). The top 20 parameters are listed in Table 15. Of these parameters 9 were involved in LVI, 7 were involved in tumour budding and all 3 parameters involved in the relative area of tumor ROIs (Necrosis/Lumen, Stroma, Tumour) within the images were present. No fluorescence associated parameters were in the top 20 significant parameters and only 6 were present in the 37 most significant parameters while 5 of these were in the bottom 7 parameters. This confirms that immunofluorescence parameters do not feature highly when stratifying the patient cohort through decision tree modelling.

Variable	Collation method	Gini Score
AREA_OF_LARGE_TUMOUR_BUDS_PXL	Sum	3.1
AREA_LVI	Sum	2.93
AREA_OCCULT_LVI	Sum	2.58
No_OF_VESSEL_BORDER_TO_OCCULT_LVI	Sum	2.56
No_OF_LARGE_TUMOUR_BUDS	Sum	2.43
No_OF_LVI	Sum	2.21
No_OF_OCCULT_LVI	Sum	2.14
No_OF_BORDERING_BUD_AND_VESSEL	Sum	2.05
No_OF_BORDERING_TUMOUR_GLAND_AND_VESSEL	Sum	1.95
BUD_WITH_≥3_NUC	Sum	1.94
TUMOUR_RELATIVE_AREA	Mean	1.92
BUD_WITH_≤2_NUC	Sum	1.92
AREA_OF_VESSEL_BORDER_TO_OCCULT_LVI_PXL	Sum	1.9
STROMA_RELATIVE_AREA	Mean	1.86
No_OF_BUDS	Sum	1.81
AREA_OF_BUDS	Sum	1.8
NUC_IN_STROMA_MEAN_DENSITY	Mean	1.78
No_OF_IRRELEVANT_MARKER	Sum	1.64
AREA_OF_VESSEL_BORDER_TO_LVI	Sum	1.64
NECROSIS_RELATIVE_AREA	Mean	1.62

Table 15. Top 20 most significant parameters exported from Random Forest analysis. Blue circle: parameters associated with tumour budding. Red circle: parameters associated with the lymphatic vasculature. Green circle: parameters associated with percentage area of each ROI within an image.

Random Forest analysis is a very robust method in which to perform parameter reduction, as the model builds 5000 decision trees within the 'forest' and out of the bag validation is performed across the model.

1.2.2.3.2 Identification of a novel histopathological feature through CART modelling

The resultant 37 most significant parameters from the RF were used as input for Classification And Regression Tree analysis (CART) to construct the decision tree model. The CART decision tree reports optimal cut-offs and parameters which best explain or stratify the data (Figure 92E).

In this study, only a single parameter was exported as the optimal terminal node. Therefore one parameter alone can optimally and significantly stratify the patient subpopulation into high and low risk of disease specific death. This parameter was the "sum area of large tumour buds" (ALTB) across each tissue section (Figure 98) and is measured in digital pixels (number of pixels within an object).

ALTB was also the most significant parameter reported from the Random Forest model. This single parameter has the ability to robustly stratify patients from the training cohort into good or poor outcome with a specificity of 96.3%, a sensitivity of 82.6% and an area under the ROC of 0.9. When analysing the Stage II subpopulation the results become even more significant with a specificity of 100%, a sensitivity of 93.75% and an area under the ROC of 0.96 (Table 14). The CART model performs a 10 fold self-test validation on the data-set using the optimal cut-off reported from the original data (self-test specificity 83.3%, sensitivity 75%, ROC 0.8).

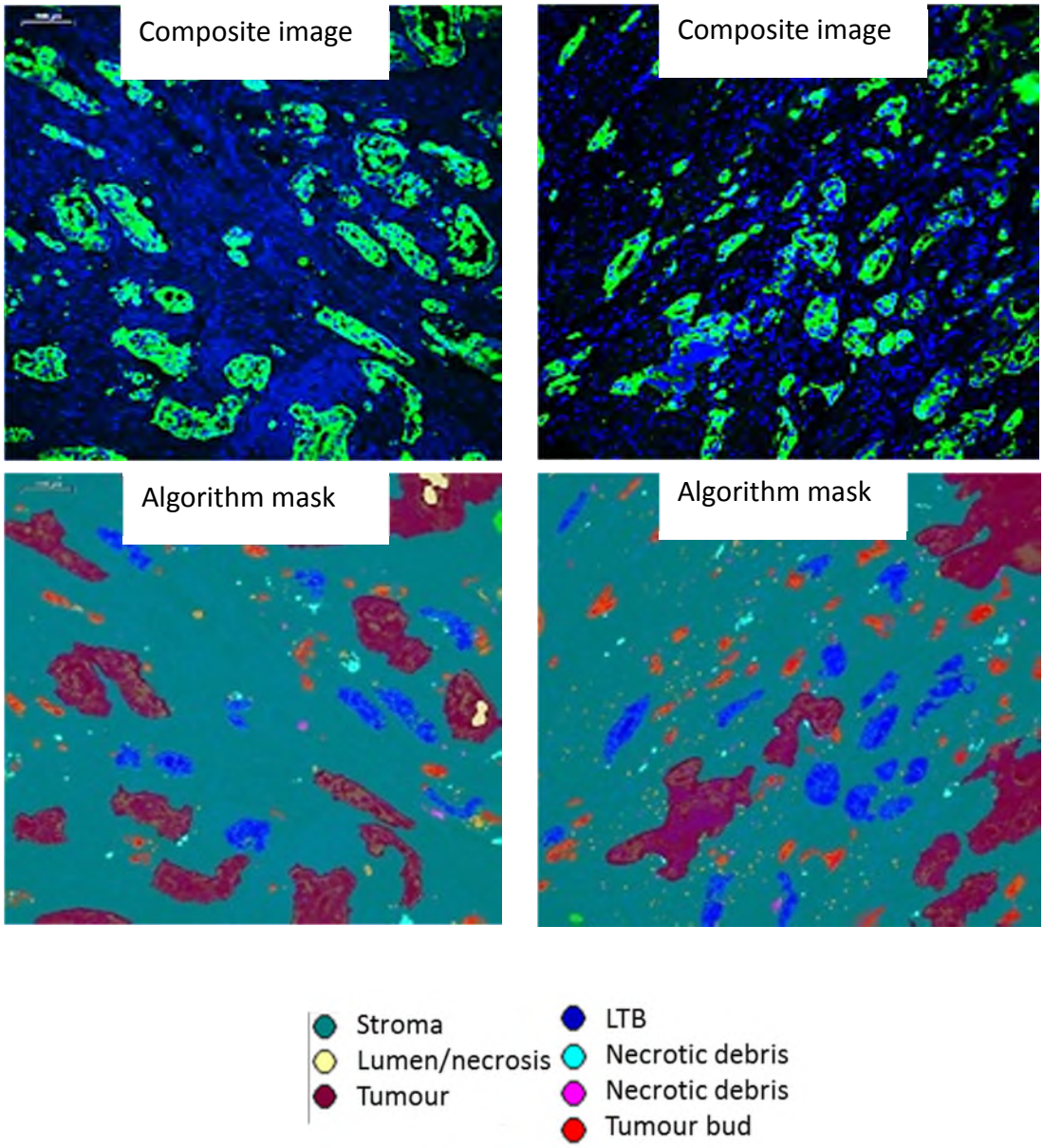

Figure 98. Examples of large tumour buds (LTB). The composite raw images (panCK: green, DAPI: blue) of two examples of tissue containing large tumour buds at the invasive front of the cancer and the associated algorithm mask. LTBs are classified with a blue object mask. The area of each LTB is calculated in pixels for each object and summed across the 15 images taken per patient sample.

The CART terminal node provides the optimal cut-off from the continuous data captured within the parameter ALTB (Figure 99). For the parameters ALTB the optimal cut-off was 161482 pixels.

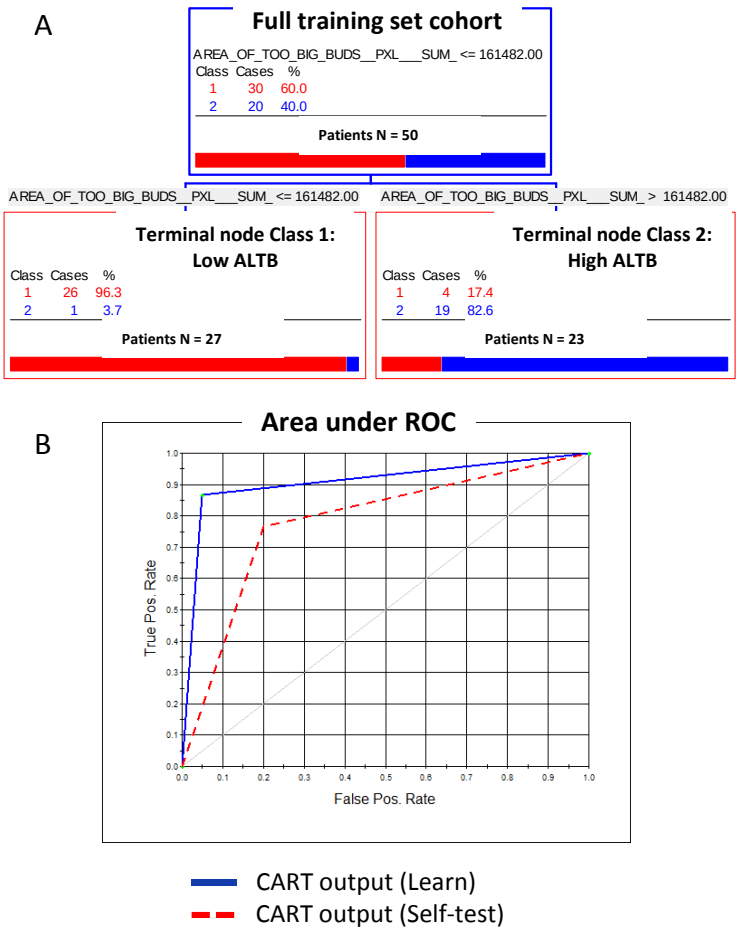

Figure 99. CART terminal node and cut-off and Area under ROC for full training cohort. A) CART terminal branch point and optimal cut-off. All patients represented in the full training cohort are assigned to class 1 or 2 dependent on their ALTB cut-off (161482 pixels) (enclosed by top blue box). Terminal node class 1 (left red box) contains patients with low ALTB (n= 27) of which 96.3% experienced disease free survival. Terminal node class 2 (right red box) contains patients with high ALTB (n= 23) of which 82.6% died specifically of CRC. B) Area under the receiver operator curve on the full data set (blue line) and after 10-fold cross-validation (red dotted line).

Using the exported cut-off of 161482 pixels, it is possible to categorise patients into groups of high and low risk of disease specific death which allows Kaplan-Meier curves to be plotted to visualise the stratification and calculate the significance of the outcome of patients over time. ALTB is a predictor of poor survival and shorter disease specific survival times in both the training cohort ($p<0.0001$) and the Stage II subpopulation ($p<0.0001$) (Figure 100). In the Stage II subpopulation no patients in the below cut-off group die of CRC specific disease.

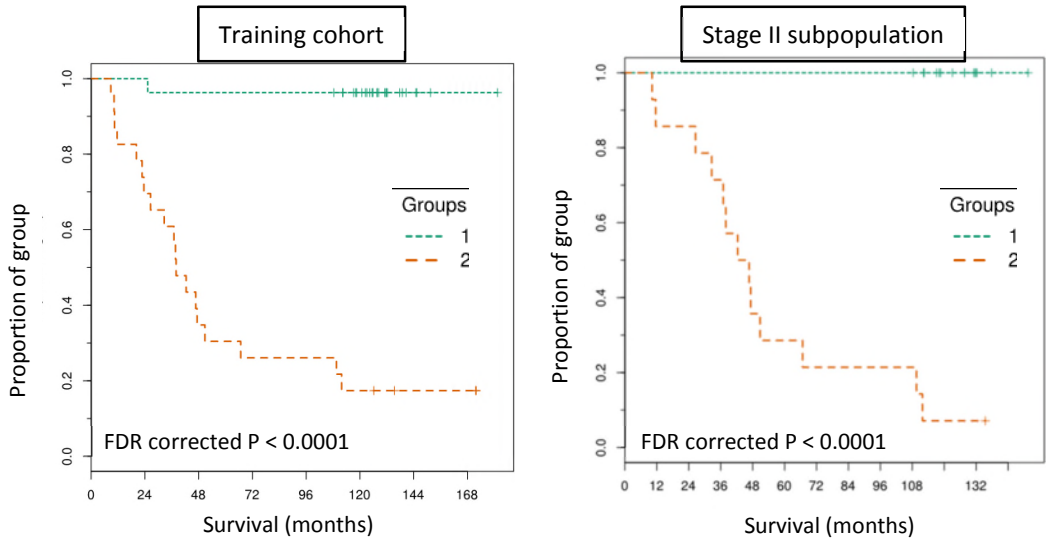

Figure 100. Kaplan-Meier curves for ALTB within the full training cohort and the stage II subpopulation. Group 1 patients are below cut-off and Group 2 patients are above cut-off for ALTB (161482 pixels). ALTB was highly significant in stratifying patients within the full training cohort and the stage II subpopulation into high and low risk of disease specific death.

1.2.3 Validation of ALTB as a prognostic parameter

1.2.3.1 Stratification of validation set utilising the training set cut-off

The Tissue Phenomics pipeline reported a highly significant and novel histopathological feature from the multi-parametric phenotypic fingerprint. In order to validate the prognostic significance of ALTB, the training set cut-off of an area of 161482 pixels was applied to the validation cohort results for the parameter. The patients were separated into categorical groups of either above or below the 161482 pixels ALTB and disease specific survival statistics were calculated.

1.2.3.1.1 Cox-regression analysis

Univariate Cox-regression analysis was performed on the validation cohort results to assess the hazard ratio and associated significance in survival prediction of ALTB. The analysis reported the novel histopathological feature to be a significant predictor of disease specific death (HR = 4; 95% CI, 1.5 – 11.1) (Table 16). The novel parameter of the ALTB had a higher hazard ratio with more significance associated (p = 0.007) than the literature based histopathological parameters of LVI (p = 0.05) and TB (p = 0.04).

Clinicopathological Parameters	patient number (n)	Univariate			
		HR	95% CI		P value
			lower	upper	
Area large tumour buds		4	1.5	11.1	0.007
High	65				
Low	69				

Table 16. Univariate Cox-regression for ALTB across the validation cohort utilising the CART exported training cohort cut-off of 161482 pixels.

1.2.3.1.2 Kaplan-Meier survival analysis

Kaplan-Meier (KM) curves were plotted through TMA Navigator and patients in the high cut-off group for ALTB had significantly shorter survival times than patients in the low cut-off group (p = 0.0026) (Figure 101). Applying the training cohort cut-off directly to the validation cohort showed that this parameter is more significant in KM patient stratification than the two prognostic parameters of LVI (p = 0.05) and TB (p = 0.04) which are both reported in the literature.

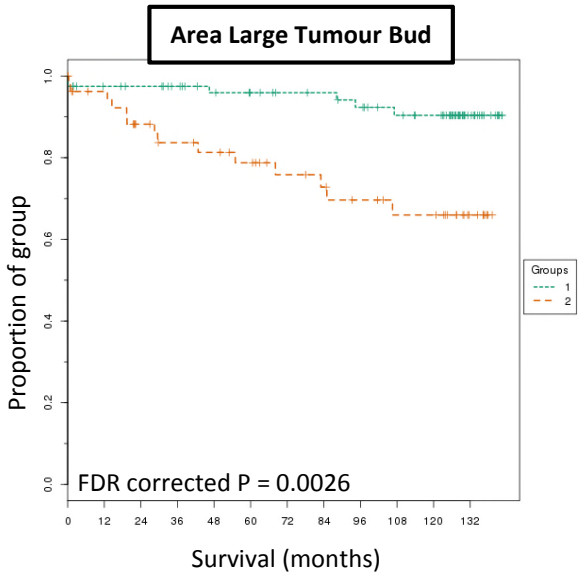

Figure 101. Kaplan-Meier curves for ALTB across the validation cohort utilising the training set cut-off of 161482 pixels. Group 1 patients are below cut-off and Group 2 patients are above cut-off for ALTB. ALTB significantly stratified the validation cohort into high and low risk of disease specific death.

1.2.3.2 Stratification of validation cohort utilising optimal cut-off for ALTB

Plotting all possible cut-offs of the training cohort and their associated *p* values reported a large range of highly significant (p = 0.001 or less) cut-offs within the training cohort. The cut-off exported from the CART analysis, although being highly significant for the training cohort, may not have been the optimal cut-off for subsequent validation cohort. Similar to results in Chapters 3 and 4 the entire range of validation cohort cut-offs and *p* values were plotted alongside those of the training cohort to identify a cut-off which was highly significant for both. The mutually significant cut-off for the stratification of patients based on ALTB was found to be 195806 pixels. By applying the new optimal cut-off to the validation cohort and plotting the results as a KM curve there was only a slight increase in the stratification of patients into high and low risk of disease specific death and the significance of patient survival over time (training cohort cut-off; p = 0.002 and optimised cut-off; p = 0.001) (Figure 102).

Univariate cox-regression results for the optimal cut-off increased the prediction of disease specific survival when applying the optimal cut-off compared to the training cohort cut-off (HR = 5.6; 95% CI, 2 – 15.5 and HR = 4; 95% CI, 1.5 – 11.1 respectively) (Table 17). The increase in significance from the training cohort cut-off to the optimal cut-off was less than when this methodology was applied to LVI or TB parameters, suggesting that the training cohort cut-off calculated from CART analysis was an extremely effective and significant one. Applying the optimal cut-off to the novel parameter ALTB places it higher in significance in disease specific death prediction compared to classical T stage (HR = 4.26; 95% CI, 1.76 – 10.33).

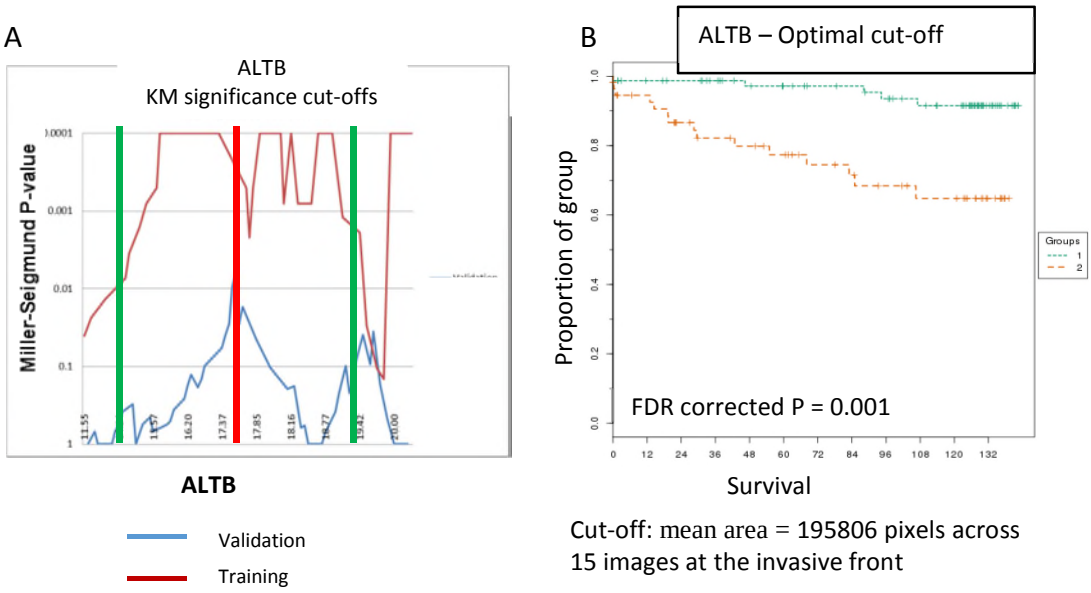

Figure 102. Assessment of optimal cut-offs within the training and validation cohorts for ALTB. A) *p* values for all possible cut-offs within the training cohort and validation cohort were plotted on the same graph. An optimal cut-off of 195806 pixels was selected which reported significant values for both cohorts (red line). The green lines mark the area containing 80% of the training cohort. B) The optimal cut-off of 195806 was utilised to plot Kaplan-Meier curves which significantly stratified the validation cohort into high and low risk of disease specific death.

Clinicopathological parameters	patient number (n)	Univariate			
		HR	95% CI		P value
			lower	upper	
Area large tumour buds		5.6	2	15.5	0.001
High	56				
Low	78				

Table 17. Univariate Cox-regression for ALTB utilising the optimal cut-off on the validation cohort.

1.3 Discussion

Morphometry is not a new science; nuclear morhpometry and tumour grade have been shown to be prognostic not only in colorectal cancer(167, 304, 346) but renal(347), ovarian(348) and bladder(349) cancer. Similarly, CRC tumour gland morphology and phenotype have been utilised to subtype an individual's cancer into clinical categories such as signet cell, serrated adenoma and mucinous as well as the assessment of the invasive edge's morphology, whether infiltrating and containing tumour buds or a pushing border(68). Recently there is growing evidence for the prognostic value of quantifying the stromal morphometric and phenotypic cellular and histological make up -- from quantifying vessel density(292), stromal cell types(350) and immune infiltrate(49, 50) as well as their spatial distribution(339, 351). After taking all of the above features into consideration, the resultant cancer tissue milieu is a complex mix of multiple histopathological features and their interactions, some easy to quantify and others not so. Although some of these histological features may be mentioned within the colorectal pathology report(237, 241) they do not regularly factor in final prognostic and treatment decisions(102). The reason for this is due to the difficulty in manually quantifying even a handful of these features in a reproducible and robust manner. In addition, assessing multiple serial sections, each stained specifically for a host or tumour cell or phenotype, is a drain on both lab resource and analysis time.

In this study, digitised tumour tissue is segmented from the stroma through image based machine learning which allows the automated measurement of multiple tumour gland associated morphometric parameters. The tumour gland morphometric

parameters were tested for significance by KM analysis across the 50-patient whole slide imaging training cohort. The two morphometric parameters which were significant for disease specific death were 'Perimeter' (M-S corrected p =0.04) and 'Rel. border to stroma' (M-S corrected p =0.004). These parameters are associated with, and could reflect, an infiltrative invasion pattern as suggested by Jass(68) (2007). Infiltrating extensions of tumour would increase the surface area, or perimeter, of the tumour gland as well as the relative border of the gland to the stroma. The prognostic relevance of stroma and tumour density percentages reflect results published in the literature(343, 344). It would be expected that there was a higher percent of stroma in images which contained a high volume of tumour buds compared to a high volume of tumour glands and so could reflect an infiltrative invasive pattern. A factor to highlight in all stroma percentage calculation is observer bias and variability with regard to sample area. Mesker and Hujbers(343, 344) manually identify an area of high infiltrative pattern at the invasive front in which to manually score tumour and stroma percentages. Although our methodology endeavours to image the entire invasive margin and quantify those with highest tumour budding, there is still scope for variability of image collection. A higher percentage of lumen and dirty necrosis was also significantly associated with better survival in the training set. Larger areas of lumen could be representative of a well-differentiated tumour which correlates with better survival(304) (Compton 1999) while a higher percentage of necrosis could represent a tumour under attack by the host immune system or within an unfavourable microenvironment; such as a hypoxic one.

The tissue phenomics approach adopted in this study employs an unbiased "measure everything" approach to data capture. Each object within the tissue is segmented and quantified with no *a priori* knowledge of which feature is prognostic. This is performed in order to build up a phenotypic fingerprint of the invasive front of the tumour for each patient. Data mining techniques are then employed to identify the significant parameters captured and to calculate robust cut-offs for novel histopathological features for patient stratification. Tissue phenomics may also add further complexity to its multi-parametric data by the quantification of *in situ* biomarkers although this was not undertaken in the present study. The novel methodology presented in this study can be utilised in combination with any image

analysis based segmented tissue to identify significant phenotypic parameters from the exported big-data fingerprint. This study utilises immunofluorescence to aid tissue segmentation, though various tissue markers coupled with image capture methodologies may be employed to create a multi-parametric phenotypic fingerprint amenable to the tissue phenomics pipeline showcased here.

For post capture and export of the multi-parametric phenotypic fingerprint one needs to employ bioinformatics to mine the big-data. Data collation is the first step toward biomarker discovery. Single cell and subcellular level segmentation creates a wealth of data per tissue section. This data must be collated before the relevant bioinformatics can be employed. Dependent on the parameter's nature this study summed or averaged each parameter to ensure a single row of data per patient. This approach is simplistic and it can be argued that heterogeneity, such as stromal cell morphometrics, is lost, however, in *in vitro* high content assays the mean of parameters has proven to be an accurate method to analyse single cell data(148, 352). It is further possible to export the multi-parametric intensity, texture and morphometric data alongside their 'x, y' coordinates within the image for each single segmented object. Although this would create a complete heterogeneous map of each nucleus and subpopulation object it would simultaneously create an extremely large and complex data set which would need cutting-edge spatial and heterogeneity statistics to analyse. Researchers have begun to map the spatial heterogeneity of the microenvironment(197) and employed image analysis techniques from astronomy(353) to analyse protein expression in TMAs, however the full potential to integrate astro-physics' statistics to explain big-data sets remains unexplored. Spatial density and patterns of the proximity and interaction of objects could yield exciting results and create another layer of complexity to the image-based big-data field. Additional cell type specific markers can be introduced to segment the heterotypic milieu of the stromal microenvironment. The combination of extra stromal or cancer markers coupled to spatial statistics could allow the capture of the complexity of the tumour micoenvironment and the cellular interactions between host and tumour thereby providing further data to input into a systems pathology mode.

Principal component analysis effectively clustered high and low risk CRC subgroups based on their phenotypic fingerprint, and allowed the evaluation of the robustness of the model through area under ROC calculations. PCA is, however, not amenable to clinical translation and does not inform on which parameters are significant or which are redundant in the model. Therefore each new patient would need to be analysed against the growing historical cohort in order to evaluate to which cluster they match the closest. To overcome this shortfall we employed decision tree ensemble models to identify the significant parameters in the model.

Random Forest (RF) is performed to rank and reduce the parameters according to their Gini score and significance in the model. Random Forest is extremely robust as it performs 5000 decision trees within the forest and validates each tree with out of the bag bootstrapping. RF is utilised to discard the non-significant parameters from the model, however it is still not applicable to a clinical prognostic score as it does not inform on cut-offs or combinations of parameters which yield the optimal output to stratify patients into high and low risk. On the contrary CART produces a single regression tree, and so is less robust than RF, however it provides optimal cut-offs for each parameter at each decision point within the model and is therefore amenable to the identification of a novel clinical histopathological marker. The CART model becomes much more efficient if only significant parameters are used for input and therefore the RF step is essential for the exclusion of non-significant parameters. In this experiment a single parameter (ALTB) and thus a single CART decision point was needed to optimally stratify the patient population. Future tissue phenomic experiments could be made up of several decision points resulting in a combination of parameters to optimally stratify patients on a predictive or prognostic query.

Large poorly differentiated cancer clusters disseminated from tumour glands are generally ignored by the majority of tumour bud researchers who have historically stated that tumour buds must be 1-5 cells in size(270). There is no obvious data within the literature which evidences the significance of tumour budding having a cut-off of 1-5 cells in size. Ueno *et al* have, however, more recently analysed the prognostic significance of larger undifferentiated tumour clusters >5 cells in size(90, 259, 269). The majority of previous studies in TB have concentrated on their count(288, 313,

354) and not the area of budding clusters, although Ueno has also proposed that the area of poor differentiation may play a prognostic role(269, 355). This measurement could be difficult to standardise and observer variability is bound to be great as it relies on the observer's judgement of the area containing the poorest differentiation within the tumour section. Our methodology can accurately quantify the area of specifically segmented objects through computer based analysis.

Ueno *et al* (269, 355) do not calculate the area of individual budding clusters but the general area of poor differentiation and show it is an independent prognostic parameter. They showed that poorly differentiated clusters, which they describe as similar to the large tumour buds reported here, were more significant at stratifying patients' outcome than the tumour bud count. They attribute this fact to the easier identification of larger islands of cells in H&E than TB which therefore results in a lower observer variability and higher quantification rates. Interestingly their results mirror those reported in this chapter in that the ALTB (HR = 5.6; 95% CI, 2-15.5) is a more significant predictor of disease specific death in the stage II patient validation cohort than tumour bud count (HR =4.5; 95% CI, 1.2-11.2). This result will need to be verified through large and independent validation cohorts. Ueno *et al's* findings may not be due to the lower observation rate of buds but to the significance of histolopathological feature itself.

A further advantage of automated image analysis is the capture of continuous feature data from a field which historically relied on manual semi-quantitative categorical clustering of histological features. Continuous data capture allows more accurate cut-offs to be applied to novel histopathological features identified through tissue phenomics as well as more robust quantification applied during validation testing due to the lack of observer variability associated with categorical manual classifications.

This study has attempted to create a tissue phenomics pipeline which is amenable to most research labs without the need for bespoke bioinformatics solutions for each image based assay. Random Forest and CART can, for example, both be run in open source software such as R (http://www.statmethods.net/advstats/cart.html) and the multi-parametric input can be exported from any image analysis software such as open source Image J (http://imagej.nih.gov/ij/) or Cell Profiler

(http://www.cellprofiler.org/). Furthermore the methodology reported here is not solely limited to image based morphometrics but is amenable to a systems pathology and integrated pathology approach(191, 356, 357). Multi-modal omics data may be added to the multi-parametric patient fingerprint in order to identify novel prognostic or predictive signatures.

Chapter 6: Integrative pathology

1.4 Introduction

Novel image based quantification techniques will more than likely not replace classical pathology, at least in the near future, but rather add to the value which is already present within the established clinical guidelines or along with biomarkers reported in the literature. Combining omics based data with classical pathology, into a modern pathology toolbox, could create more significant multi-parametric prognostic or predictive signatures. The integrative signature theory is that this methodology should be capable of more accurate and significant patient stratification than single parameters or the gold standard TNM staging. Patient stratification can take the form of high and low risk of disease specific death or inform the oncologist on personalised medical regimens.

Medical research is already beginning to embrace big-data science especially in the form of genomics, transcriptomics and proteomics(189, 190, 358, 359). A novel gene expression signature for a rectal cancer recurrence score, for example, was developed by integrating a 12 gene model to predict recurrence and disease specific survival(360). The big-data disciplines are also being integrated(361) and being input into systems medicine models(362, 363). There is less literature integrating disparate omics or emerging histopathological data strands along with the original classical core clinical pathology data items; although the value of clinical and omics integration is beginning to be recognised(364, 365). Foulis' group recently implemented a more classical pathology integrative approach to stratify high and low risk CRC patients. They integrated the manual quantification of BVI through elastic staining with T stage and found a small increase in prognostic power for early stage CRC patients than TNM staging alone(280). Similarly Japanese researchers of PDC have also integrated this novel grading system with a desmoplastic reaction score from manually semi-quantified classically H&E stained CRC tissue sections(27).

Although the general consensus of systems pathology is that it must include dynamic computational modelling, another definition states that integrative systems pathology

is the inclusion of data from multiple strands: proteomic, transcriptomic, genomic, epigenetic and tissue phenomic, into a mathematical model which selects those parameters, which when combined, infer optimal information to the pathologist or oncologist about the treatment or prognosis of individual patients. This definition (which still allows for the inclusion of dynamic modelling) of systems pathology was set out by Saidi et al(366);

> Systems Pathology seeks to integrate all levels of functional and morphological information into a coherent model that enables the understanding of perturbed physiological systems and complex pathologies in their entirety.

Although this allows for a more simplistic view of systems pathology it has the potential to include robust and clinically transferable methods of analysing data from multiple streams of tissue datafication.

This integrative pathology method is demonstrated in this chapter by combining novel histopathological features, discovered within this study through tissue phenomics and image analysis, with parameters exported from the original clinical pathology reports into a prognostic integrative model. The model informs on which individual parameters, when combined, add value to the significance of the prediction of disease specific death in the stage II CRC patient validation cohort. These parameters are then included in a novel prognostic signature and its significance is tested across the stage II validation set.

This study will test two approaches in selecting the optimal individual image-based and core clinical data-set parameters for incorporation into the integrative model. The integrative model will be tested on the validation set (n=134) due to its clinical relevance consisting of sequential stage II CRC patients collected across 2 full years.

The first method will incorporate the main image-based parameters which were significant in the validation cohort and which were reported in each of the previous chapters: Occult LVI, TB and ALTB.

The second method will select the top three most significant parameters reported from the Random Forest model which were ranked according to their Gini score. These three parameters are: 'ALTB', 'Area of LVI' and 'Area of occult LVI.

1.5 Results.

A summary of all the individual parameters, and their corresponding hazard ratios, to be investigated in this chapter are listed in Table 18 A & B.

Clinicopathological parameters	Univariate Training set cut-off				Univariate Optimal cut-off			
	HR	95% CI		P value	HR	95% CI		P value
		lower	upper			lower	upper	
Area large tumour buds*§	4	1.5	11.1	0.007	5.6	2	15.5	0.001
Tumour Budding*	2.49	1.03	5.99	0.04	4.5	1.8	11.2	0.002
Occult LVI*	2.46	1	6.05	0.05	2.9	1.2	7.1	0.02
Area LVI§	1.8	0.74	4.41	0.2	2.15	0.9	5.2	0.08
Area Occult LVI§	1.4	0.45	4.09	0.57	2.48	1.03	5.99	0.04

Parameters utilised in method one annotated with *****
Parameters utilised in method two annotated with **§**

Table 18 A. Significant image-based parameters.

Clinicopathological parameters	Univariate			
	HR	95% CI		P value
		lower	upper	
pT	4.26	1.76	10.33	0.001
Differentiation	2.17	1.14	4.13	0.02

Table 18 B. Significant clinical pathology report parameters.

1.5.1 Method 1: Integrating TB, Occult LVI, ALTB, T stage and Differentiation

This method incorporated the significant parameters quantified from Chapter 3 (TB), Chapter 4 (Occult LVI) and Chapter 5 (ALTB) with the two significant parameters located within the clinical pathology report (pT stage and Differentiation).

To identify which parameters add value to the prediction of disease specific death they were added into a forward step-wise conditional Cox-regression model. This calculation adds, in a step-wise fashion, parameters which add significance to the model and discards those parameters which do not. The model was executed across the validation cohort for both the training set cut-offs and the optimal cut-offs for each image-based parameter. The significant and non-significant parameters within the model were the same when using the training set cut-offs and for the optimal cut-offs, although significance was improved upon in the latter. The three parameters which added significance to the model of CRC specific death in the stage II clinical validation cohort were: ALTB (training set cut-off $p = 0.03$, optimal cut-off $p = 0.004$), pT stage (training set cut-off $p = 0.03$, optimal cut-off $p = 0.04$), and differentiation (training-set cut-off $p = 0.05$, optimal cut-off $p = 0.04$), (Table 19). The parameters of TB (training set cut-off $p = 0.84$, optimal cut-off $p = 0.4$), and Occult LVI (training set cut-off $p = 0.85$ optimal cut-off $p = 0.9$), were discarded as they did not add significance to the final predictive model (Table 19).

Variables in the equation	Training set cut-off				Optimal cut-off			
	HR	95% CI		P value	HR	95% CI		P value
		lower	upper			lower	upper	
ALTB	3.3	1.1	9.5	0.03	4.7	1.6	13.6	0.004
pT stage	2.8	1.1	7.3	0.03	2.7	1.1	6.9	0.04
Differentiation	2.2	1	4.9	0.05	2.3	1	5	0.04
Variables not in the equation								
TB				0.84				0.4
Occult LVI				0.85				0.9

Table 19.Forward cox-regression results for method 1. Parameters which do or do not add significant value to the integrative prognostic signature in method 1 are listed. Parameters were reported by executing forward step-wise Cox-regression on the validation cohort after categorising the patients by applying the training cohort or optimal cut-offs.

1.5.2 Method 2: Integrating ALTB, Area LVI, Area Occult LVI, T stage and Differentiation

The input parameters for the integrative forward conditional Cox regression model in method 2 were selected from the top 3 significant parameters reported from the RF result in Chapter 5 (ALTB, Area Occult LVI and Area LVI) alongside the significant parameters from the clinical core data-set (pT stage and Differentiation).

As in method 1, the model was executed across the data from the validation set after applying the training set cut-off and the optimal cut-off. Method 2 reported the same three significant parameters which added value to the prediction of disease specific death as in Method 1: ALTB (training set cut-off $p = 0.03$, optimal cut-off $p = 0.004$), pT stage (training set cut-off $p = 0.03$, optimal cut-off $p = 0.04$), and Differentiation (training set cut-off $p = 0.05$, optimal cut-off $p = 0.04$), while Area of occult LVI (training set cut-off $p = 0.6$, optimal cut-off $p = 0.75$) and Area LVI (training set cut-off $p = 0.73$, optimal cut-off $p = 0.88$) added no significant value (Table 20).

Variables in the equation	Training set cut-off				Optimal cut-off			
	HR	95% CI		P value	HR	95% CI		P value
		lower	upper			lower	upper	
ALTB	3.3	1.1	9.5	0.03	4.7	1.6	13.6	0.004
pT stage	2.8	1.1	7.3	0.03	2.7	1.1	6.9	0.04
Differentiation	2.2	1	4.9	0.05	2.3	1	5	0.04
Variables not in the equation								
Area Occult LVI				0.6				0.75
Occult LVI				0.73				0.88

Table 20. Forward Cox-regression results for method 2. Parameters which do or do not add significant value to the integrative prognostic signature in method 2 are listed. Parameters were reported by executing forward step-wise Cox-regression on the validation cohort after categorising the patients by applying the training cohort or optimal cut-offs.

1.5.3 Creation of an Integrative Pathology Signature

The three significant parameters within the forward conditional model were compiled into a final novel integrative prognostic signature (IPS). Patients with an above cut-off score in two or more of the three significant parameters within the IPS were classified as a "high-risk" group and the remainder of the patients were classified with a "low-risk" score. The IPS was the only significant parameter to predict disease specific death (training cut-off HR = 7.5; 95% CI, 3 – 18.5, p = 0.00001, optimal cut-off HR = 7.8; 95% CI, 3.2 – 19.2, p = 0.00001) when it is entered into a multivariate forward conditional Cox regression model along with its composite parts (Table 21). The composite parameters added no individual significance to the regression model in their own right: ALTB (training set cut-off p = 0.21, optimal cut-off p =0.26), pT stage (training set cut-off p = 0.49, optimal cut-off p =0.66) and differentiation (training set cut-off p = 0.62, optimal cut-off p =0.72). The IPS prognostic prediction of CRC specific death is an improvement on classical TNM staging (HR = 4.26; 95% CI, 1.76 – 10.33, p = 0.001) within this stage II CRC patient cohort.

Variables in the equation	Training cut-off				Optimal cut-off			
	HR	95% CI		P value	HR	95% CI		P value
		lower	upper			lower	upper	
IPS	7.5	3	18.5	0.00001	7.8	3.2	19.2	0.000008
Variables not in the equation								
ALTB				0.2				0.3
pT stage				0.5				0.9
Differentiation				0.6				0.4

Table 21.Forward cox-regression results upon inputting the IPS and its composite parameters into the model. Parameters were reported by executing forward step-wise Cox-regression on the validation cohort after categorising the patients by applying the training cohort or optimal cut-offs.

Kaplan-Meier curves were plotted to assess the significance of the IPS in patient survival over time (Figure 103). The IPS significantly stratifies stage II CRC patients with a high risk of CRC specific death over an 11.5 year follow up. An IPS which

consisted of either the parameters with the training set cut-off (Figure 103 A) or optimal cut-off (Figure 103 B) were tested and both the final results had a high significance in patient stratification ($p < 0.00001$).

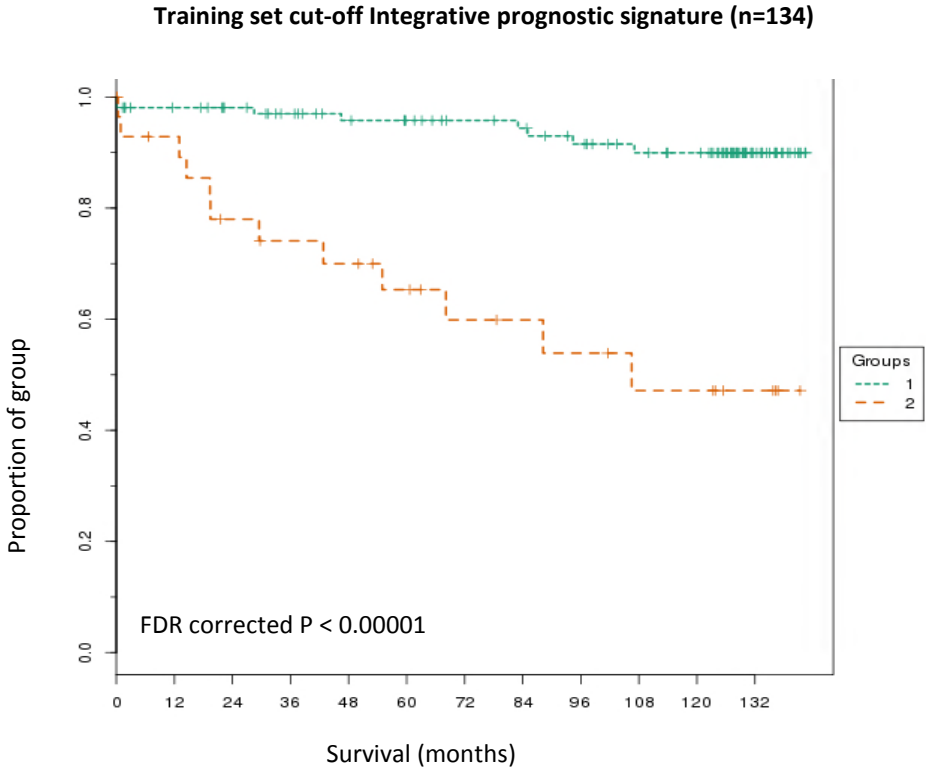

Figure 103 A) Kaplan-Meier survival curve for IPS with parameters categorised by the training set cut-offs (green: below cut-off, orange: above cut-off. The IPS was highly significant in stratifying the stage II CRC validation cohort into high and low risk of disease specific death.

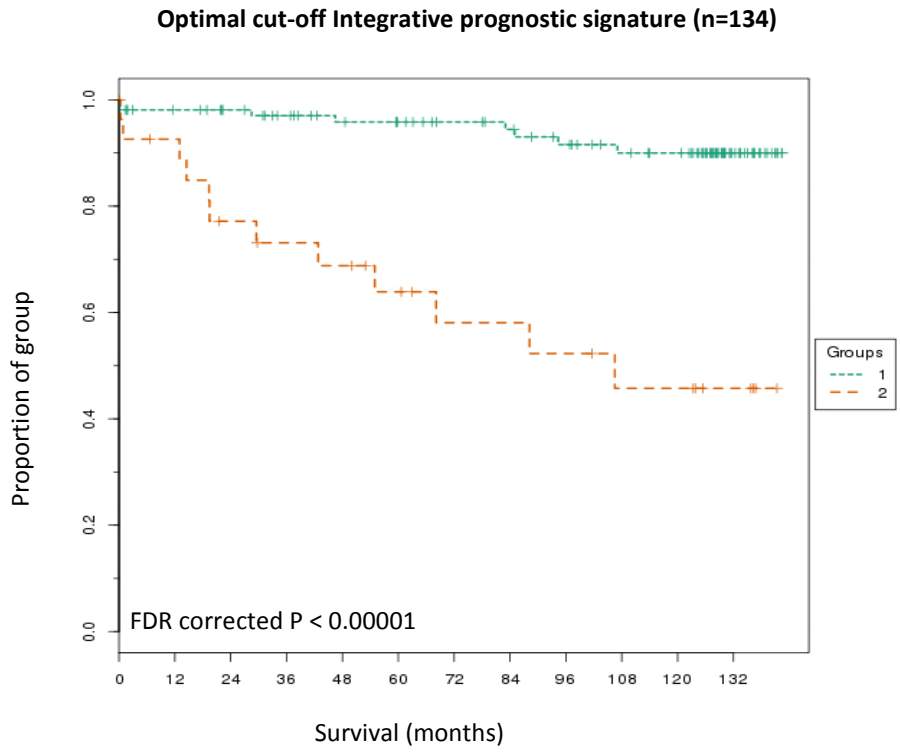

Figure 103 B) Kaplan-Meier survival curve for IPS with parameters categorised by the optimal cut-offs. The IPS was highly significant in stratifying the stage II CRC validation cohort into high and low risk of disease specific death.

1.6 Discussion

Pathology is now adept at creating large and complex data sources from across the omics fields and more recently including histopathology morphometrics and spatial heterogeneity(186, 191, 197). The challenge ahead is how to incorporate this integrated data into models which can identify the optimal combinations of parameters to answer clinical questions in a robust manner(367). TNM staging of CRC has long been the gold-standard to predict disease progression and stratify high risk sub-groups. Although many biomarkers and histopathological features have been reported in the literature none have improved upon classical pathology and replaced TNM staging or the core clinical data-set(102). Therefore it would seem pertinent to include the pathological reporting which already exists into novel integrative models. In this chapter the significant parameters from the original pathology report were added alongside the significant parameters quantified through image analysis from previous

chapters into a step-wise regressional model. Two separate methods were tested to identify which image based parameters added value to the prediction of disease specific death. Both models reported the same significant parameters: ALTB, differentiation and pT stage. The three significant parameters were then integrated to form a novel prognostic signature which reported the highest hazard ratio and significance (HR = 7.8; 95% CI, 3.2 – 19.2, p = 0.00001) compared to its composite parts and improved upon classical TNM staging (HR = 4.26; 95% CI, 1.76 – 10.33, p = 0.001).

Although the parameters of the percent of stroma and percent of tumour per image were highly significant in the training cohort and validation cohort (Table 13) they were not in the top 3 RF parameters and therefore not included in the selection of parameters to integrate. Further investigation may be beneficial in identifying the optimal model to identify which parameters are used as input for the regression analysis. There is some question on the reproducibility of the percent ROI in each image due to manual selection of the invasive front, as discussed in Chapter 5. This manual selection is open to observer variability and bias. Some impartiality is included in image selection as it was endeavoured to image the entire invasive front and only select the images with highest tumour budding for further analysis. It would be prudent, therefore, to exclude these parameters from any integrative model until an automated method of identifying the invasive front through image analysis can be programmed and thereby standardising the sample area.

Differentiation has been shown to be an independent variable in multiple studies(254) however it also shows a high degree of observer variability(368). Furthermore some studies show it to be non-significant(369). High observer variability and non-standardised reporting may result in a higher proportion of moderate differentiation being input to the patient database as extremely low and high grade cancers are easier to classify. To overcome this, a two-tiered grading system is proposed by CAP which involves either low grade or high grade(370). In the validation cohort of this study 81.4% of patients had moderately differentiated cancer whereas only 16.4% had poor and 2.2% well differentiated cancer. This small percentage of cancers at either spectrum of the grading system will account for the inclusion of differentiation as an

independently significant parameter. Implementing the two tiered system proposed by The College of American Pathologists (CAP) may improve on this parameter's prognostic significance.

TB and LVI have been shown to be significant predictors of disease specific death in univariate analysis, however, they both fall out of significance and add no extra prognostic value when the model is altered for pT stage, differentiation and ALTB. The novel parameter of ALTB therefore holds the highest prognostic significance of all image segmented objects at the invasive front and this is reflected by the output of both the Random Forest and CART decision tree models within chapter 5.

The integrative prognostic signature reported here includes information on the depth of local invasion (pT stage), the morphometry and architecture of gland formation and the invasive pattern at the tumour-stroma interface. These parameters describe the cancer's aggressiveness within the primary neoplastic site as well as giving insight into the dynamic nature of its progression. Integration of molecular profiles of the invasive subpopulations at the invasive front, such as the large tumour buds, could add to the knowledge of an individual cancer's invasive mechanism and lead to drug targets at the personalised level. The future of pathology and its holistic and integrative nature should move prognosis and prediction away from population statistics and towards P4 medicine(207).

This study adds proof to the theory that combining novel pathological parameters with classical pathology returns more significant results than either the single novel parameter or classical parameter individually, although this methodology must be further validated in large inter-institutional cohorts.

Chapter 7: Conclusion

Translational research must always start with a clinical question. The clinical question in this thesis is how to sub-stratify stage II CRC patients. Although TNM classification is the gold standard of CRC prognosis, it is not able to successfully stratify stage II patients into high and low risk of disease recurrence and disease specific death(102, 235). On average ~30% of Stage II CRC patients experience poor outcome and there is therefore a clinical need to be able to identify these patients(243, 244, 295). Whether chemotherapy will significantly increase disease free survival is yet to be determined(242, 247, 295). The hypothesis of this thesis is that stage II CRC patients can be stratified into high and low risk of disease specific death through automated image analysis.

Although there is increasing evidence of lymphatic vessel invasion and tumour budding being significantly associated with lymph node metastasis and disease specific death, they have not been included in core clinical guidelines, due to a lack of standardisation and poor reproducibility(20, 102, 238, 250, 257, 258, 270, 284). These rare and sometimes obscure events are difficult to observe in classical H&E stained tissue sections. Utilising specific antibodies through immunofluorescence coupled with automated image analysis allows the standardisation of quantification of these histopathological features. Upon applying this methodology to a training and validation set of CRC patients, the stage II patients could be significantly stratified on risk of death from CRC. Image analysis does not only segment histopathological features for quantification, but allows us to profile molecularly these heterogeneous subpopulations, such as tumour glands at the centre of a tumour and tumour buds at the invasive edge. In doing so tumour buds in some patients were found to lose certain epithelial markers such as E-Cadherin, decrease their proliferation index and show an increase in the mesenchymal protein Vimentin.

The invasive edge of CRC holds a wealth of prognostic information within, amongst other features, the tumour's invasive pattern(90, 91, 265) and the vasculature(250, 258, 262, 276, 279, 368). Although pathologists are good at identifying histopathological patterns between patients, it is a difficult task to accurately quantify each feature within

the invasive front without the use of automated image analysis. Image analysis was employed to identify the most significant of these parameters, for stage II prognosis, from this complex and heterogeneous interface. All objects within immunofluorescence images of the invasive front were segmented and multiple morphometric and texture parameters extracted for each. These parameters built up a hierarchical phenotypic fingerprint for each patient sample. The phenotypic fingerprint was mined through ensemble decision tree models to identify which parameters best predicted disease specific death. It was discovered that a single parameter was optimal at stratifying the stage II CRC patient population. This parameter was the sum area of the large tumour buds (ALTB) across 15 images captured at the invasive front of the CRC tissue section. Image analysis, in the form of tissue phenomics, not only identified this novel feature but allows its robust and standardised quantification in future validation studies. This standardised quantification also makes the methodology highly transferable to clinical practice.

As previously mentioned, TNM staging is utilised for the prognosis of CRC and has stood the test of time since no other biomarker has yet to replace it. Therefore image analysis and modern pathological data extraction techniques should aim to augment this classical staging rather than replace it. The only two parameters significantly associated with disease specific death from the original clinical report were differentiation and pT stage. Integrating the novel parameter ALTB with these two classical parameters was found to be the most significant prognostic signature captured across all parameters quantified within this thesis. This signature therefore reports on the depth of local invasion (pT stage), the morphometry and architecture of gland formation and the invasive pattern at the tumour-stroma interface. Implementing this signature allowed the significant prediction of disease specific death for a clinically relevant stage II CRC patient cohort (n=134).

In conclusion image analysis can standardise the quantification of histopathological features and probe their molecular profile. Novel image analysis methodology can also discover novel prognostic features and integrate these to augment classical clinical pathology.

Potential impact of Thesis:

The IPS improved upon current clinical staging by almost 1.5 fold. Large international validation cohorts must be applied to ensure that this result is reproducible. A major advantage of image analysis is the objective quantification of histopathological features which negates observer variability. Observer variability and poor reproducibility is a major roadblock in the translation of candidate prognostic features into the clinic. Once further validated the IPS is highly translatable to the clinic upon where high risk Stage II CRC patients may be identified more accurately than current practice. This would impact patient care as high risk Stage II patients would be assigned more detailed follow up and intervention in an attempt to extend their disease free survival and possibly prevent disease specific death.

Implementation to the clinic:

In order to implement the IPS into routine clinical practice it must, as previously stated, be further validated. Digital pathology is becoming common place in laboratory medicine although image analysis has been slower in its adoption. Studies such as this are needed to validate image analysis for clinical practice and will overcome the scepticism of the technology which currently exists. Once a digital pathology IT infrastructure is in place it would be a simple alteration to bolt on image analysis processing workstations to automatically quantify the ALTB in a standardised fashion. The full Tissue Phenomics pipeline would be difficult to implement but it is in fact not needed in a clinical setting. The research aspect of this study, and for other future studies, would identify the most significant parameters and their optimal cut-offs to answer the clinical question. Once these are identified only a far more simplistic assay and image analysis solution would be required. In this case an image analysis algorithm would only need to report a single parameter: ALTB. This end result is readily transferable to the clinic and would require little training once the immunofluorescence kit and algorithm was rolled out as a fully automated packaged.

The first two aims and objectives of the thesis were successfully mapped to the results by the development of image analysis algorithms which:

1. Quantified the histopathological features of tumour budding, lymphatic vasculature invasion and density in a standardised manner and the result of

which allowed the significant stratification of high risk of disease specific death Stage II CRC patients.

2. Automatically segmented and exported a multi-parametric image-based data set captured in an unbiased manner and which formed part of a pipeline which employed decision tree models to identify the most significant parameter to stratify high risk of disease specific death Stage II CRC patients. Once identified this novel parameter (ALTB) was able to significantly categorise a validation cohort of 134 Stage II CRC patients into high and low risk of disease specific death.

The final aim and objective was completed by identifying the significant parameters in the clinical pathology report of the validation cohort patients through univariate Cox-regression. The significant clinical and image-based parameters were entered into a forward step-wise Cox-regression model to identify which added value to a novel Integrative Pathology Signature (IPS). The IPS improved upon conventional clinical staging and was more significant at identifying high risk of disease specific death Stage II CRC patients.

Future work:

1. Validate the integrative prognostic signature in large international cohorts.
2. Profile the immune response at the invasive front through image analysis. Calculate the spatial heterogeneity of the heterotypic immune cells with tumour histopathological features and the cancer microenvironment.
3. Incorporate multi-omics data to the hierarchical clinical and phenotypic signature so as to capture a holistic and complex data-set for CRC prognosis and drug prediction enabling a systems pathology approach to be applied (Figure 104). In doing so the field of pathology could move from population statistics toward clinical decision making at the truly personalised level.

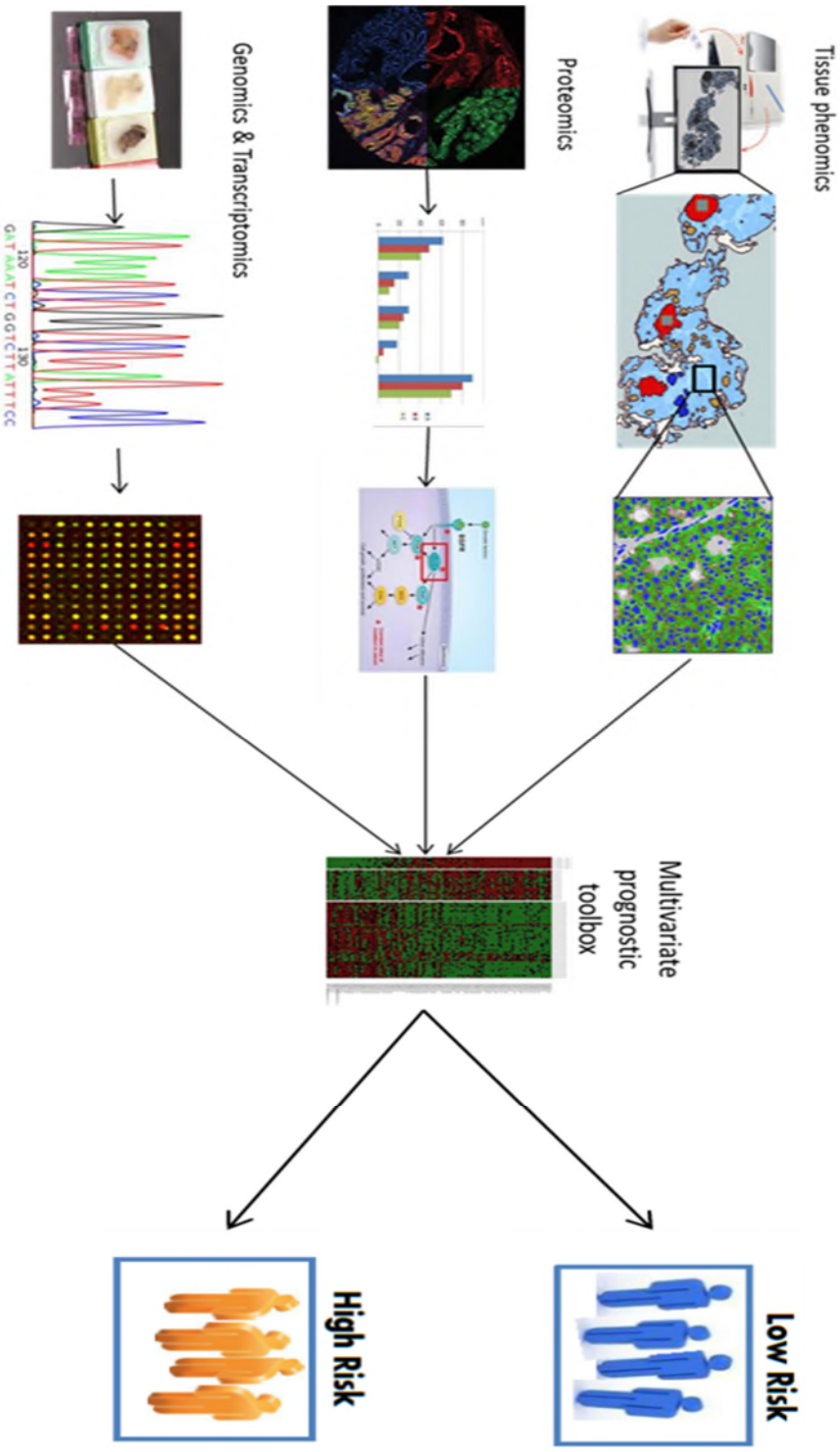

Figure 104 – Multi-omics integration into a systems pathology model.

Chapter 8: References

1. Wild BWSCP. World Cancer Report: IARC; 2014 01/28/2014.
2. Barbara Young WS, Geraldine O'Dowd. Wheater's basic pathology 5th edition: Elsevier; 2011.
3. Strayer DS. Rubin's Pathology: Clinicopathologic Foundations of Medicine: Lippincott Williams and Wilkins; 2014 31 July 2014.
4. Nguyen DX, Bos PD, Massague J. Metastasis: from dissemination to organ-specific colonization. Nature reviews Cancer. 2009;9(4):274-84.
5. Seyfried TN, Huysentruyt LC. On the origin of cancer metastasis. Critical reviews in oncogenesis. 2013;18(1-2):43-73.
6. Visvader JE. Cells of origin in cancer. Nature. 2011;469(7330):314-22.
7. Steeg PS. Tumor metastasis: mechanistic insights and clinical challenges. Nature medicine. 2006;12(8):895-904.
8. Vogelstein B, Kinzler KW. The multistep nature of cancer. Trends in genetics : TIG. 1993;9(4):138-41.
9. Hanahan D, Weinberg RA. Hallmarks of cancer: the next generation. Cell. 2011;144(5):646-74.
10. Stratton MR, Campbell PJ, Futreal PA. The cancer genome. Nature. 2009;458(7239):719-24.
11. Friedl P, Alexander S. Cancer invasion and the microenvironment: plasticity and reciprocity. Cell. 2011;147(5):992-1009.
12. Magee JA, Piskounova E, Morrison SJ. Cancer stem cells: impact, heterogeneity, and uncertainty. Cancer cell. 2012;21(3):283-96.
13. Valent P, Bonnet D, De Maria R, Lapidot T, Copland M, Melo JV, et al. Cancer stem cell definitions and terminology: the devil is in the details. Nature reviews Cancer. 2012;12(11):767-75.
14. Islam F, Qiao B, Smith RA, Gopalan V, Lam AK. Cancer stem cell: Fundamental experimental pathological concepts and updates. Experimental and molecular pathology. 2015.
15. Cabrera MC, Hollingsworth RE, Hurt EM. Cancer stem cell plasticity and tumor hierarchy. World journal of stem cells. 2015;7(1):27-36.
16. Scheel C, Weinberg RA. Cancer stem cells and epithelial-mesenchymal transition: concepts and molecular links. Seminars in cancer biology. 2012;22(5-6):396-403.
17. Nieto MA, Cano A. The epithelial-mesenchymal transition under control: global programs to regulate epithelial plasticity. Seminars in cancer biology. 2012;22(5-6):361-8.
18. Tsai JH, Yang J. Epithelial-mesenchymal plasticity in carcinoma metastasis. Genes & development. 2013;27(20):2192-206.
19. Schmalhofer O, Brabletz S, Brabletz T. E-cadherin, beta-catenin, and ZEB1 in malignant progression of cancer. Cancer Metastasis Rev. 2009;28(1-2):151-66.
20. Lugli A, Karamitopoulou E, Zlobec I. Tumour budding: a promising parameter in colorectal cancer. Br J Cancer. 2012;106(11):1713-7.
21. Gao ZH, Lu C, Wang MX, Han Y, Guo LJ. Differential beta-catenin expression levels are associated with morphological features and prognosis of colorectal cancer. Oncology letters. 2014;8(5):2069-76.

22. Vannier C, Mock K, Brabletz T, Driever W. Zeb1 regulates E-cadherin and Epcam (epithelial cell adhesion molecule) expression to control cell behavior in early zebrafish development. The Journal of biological chemistry. 2013;288(26):18643-59.
23. Fuxe J, Karlsson MC. TGF-beta-induced epithelial-mesenchymal transition: a link between cancer and inflammation. Seminars in cancer biology. 2012;22(5-6):455-61.
24. De Wever O, Mareel M. Role of tissue stroma in cancer cell invasion. J Pathol. 2003;200(4):429-47.
25. Leibovich-Rivkin T, Liubomirski Y, Bernstein B, Meshel T, Ben-Baruch A. Inflammatory factors of the tumor microenvironment induce plasticity in nontransformed breast epithelial cells: EMT, invasion, and collapse of normally organized breast textures. Neoplasia (New York, NY). 2013;15(12):1330-46.
26. Nistico P, Bissell MJ, Radisky DC. Epithelial-mesenchymal transition: general principles and pathological relevance with special emphasis on the role of matrix metalloproteinases. Cold Spring Harbor perspectives in biology. 2012;4(2).
27. Ueno H, Shinto E, Kajiwara Y, Fukazawa S, Shimazaki H, Yamamoto J, et al. Prognostic impact of histological categorisation of epithelial-mesenchymal transition in colorectal cancer. Br J Cancer. 2014;111(11):2082-90.
28. Koukourakis MI, Giatromanolaki A, Harris AL, Sivridis E. Comparison of metabolic pathways between cancer cells and stromal cells in colorectal carcinomas: a metabolic survival role for tumor-associated stroma. Cancer Res. 2006;66(2):632-7.
29. Kelly H, Goldberg RM. Systemic therapy for metastatic colorectal cancer: current options, current evidence. J Clin Oncol. 2005;23(20):4553-60.
30. Schiller JH. Current standards of care in small-cell and non-small-cell lung cancer. Oncology. 2001;61 Suppl 1:3-13.
31. Bayoudh L, Afrit M, Daldoul O, Zarrad M, Boussen H. Trastuzumab (herceptine) in medical therapy in breast cancer. Tunis Med. 2012;90(1):6-12.
32. Bareschino MA, Schettino C, Rossi A, Maione P, Sacco PC, Zeppa R, et al. Treatment of advanced non small cell lung cancer. J Thorac Dis. 2011;3(2):122-33.
33. Fox SB, Gasparini G, Harris AL. Angiogenesis: pathological, prognostic, and growth-factor pathways and their link to trial design and anticancer drugs. Lancet Oncol. 2001;2(5):278-89.
34. Shiao SL, Ganesan AP, Rugo HS, Coussens LM. Immune microenvironments in solid tumors: new targets for therapy. Genes Dev. 2011;25(24):2559-72.
35. Albini A, Sporn MB. The tumour microenvironment as a target for chemoprevention. Nat Rev Cancer. 2007;7(2):139-47.
36. Damasceno M. Bevacizumab for the first-line treatment of human epidermal growth factor receptor 2-negative advanced breast cancer. Curr Opin Oncol. 2011;23 Suppl:S3-9.
37. Kollmannsberger C, Bjarnason G, Burnett P, Creel P, Davis M, Dawson N, et al. Sunitinib in metastatic renal cell carcinoma: recommendations for management of noncardiovascular toxicities. Oncologist. 2011;16(5):543-53.
38. Hirschhorn-Cymerman D, Rizzuto GA, Merghoub T, Cohen AD, Avogadri F, Lesokhin AM, et al. OX40 engagement and chemotherapy combination provides potent antitumor immunity with concomitant regulatory T cell apoptosis. J Exp Med. 2009;206(5):1103-16.

39. Beatty GL, Chiorean EG, Fishman MP, Saboury B, Teitelbaum UR, Sun W, et al. CD40 agonists alter tumor stroma and show efficacy against pancreatic carcinoma in mice and humans. Science. 2011;331(6024):1612-6.
40. Marimastat: BB 2516, TA 2516. Drugs R D. 2003;4(3):198-203.
41. Dredge K. AE-941 (AEterna). Curr Opin Investig Drugs. 2004;5(6):668-77.
42. Arnes JB, Stefansson IM, Straume O, Baak JP, Lonning PE, Foulkes WD, et al. Vascular proliferation is a prognostic factor in breast cancer. Breast Cancer Res Treat. 2011.
43. Des Guetz G, Uzzan B, Nicolas P, Cucherat M, Morere JF, Benamouzig R, et al. Microvessel density and VEGF expression are prognostic factors in colorectal cancer. Meta-analysis of the literature. Br J Cancer. 2006;94(12):1823-32.
44. Mohammed RA, Ellis IO, Elsheikh S, Paish EC, Martin SG. Lymphatic and angiogenic characteristics in breast cancer: morphometric analysis and prognostic implications. Breast Cancer Res Treat. 2009;113(2):261-73.
45. Mohammed RA, Martin SG, Mahmmod AM, Macmillan RD, Green AR, Paish EC, et al. Objective assessment of lymphatic and blood vascular invasion in lymph node-negative breast carcinoma: findings from a large case series with long-term follow-up. J Pathol. 2011;223(3):358-65.
46. Storr SJ, Safuan S, Mitra A, Elliott F, Walker C, Vasko MJ, et al. Objective assessment of blood and lymphatic vessel invasion and association with macrophage infiltration in cutaneous melanoma. Mod Pathol. 2011.
47. Suzuki A, Togashi K, Nokubi M, Koinuma K, Miyakura Y, Horie H, et al. Evaluation of venous invasion by Elastica van Gieson stain and tumor budding predicts local and distant metastases in patients with T1 stage colorectal cancer. Am J Surg Pathol. 2009;33(11):1601-7.
48. Lundqvist L, Stenlund H, Laurell G, Nylander K. The importance of stromal inflammation in squamous cell carcinoma of the tongue. J Oral Pathol Med. 2011.
49. Roxburgh CS, Richards CH, Macdonald AI, Powell AG, McGlynn LM, McMillan DC, et al. The in situ local immune response, tumour senescence and proliferation in colorectal cancer. Br J Cancer. 2013;109(8):2207-16.
50. Galon J, Mlecnik B, Bindea G, Angell HK, Berger A, Lagorce C, et al. Towards the introduction of the Immunoscore in the classification of malignant tumors. J Pathol. 2013.
51. Shekarian T, Valsesia-Wittmann S, Caux C, Marabelle A. Paradigm shift in oncology: targeting the immune system rather than cancer cells. Mutagenesis. 2015;30(2):205-11.
52. Abba M, Laufs S, Aghajany M, Korn B, Benner A, Allgayer H. Look who's talking: deregulated signaling in colorectal cancer. Cancer Genomics Proteomics. 2012;9(1):15-25.
53. Phipps AI, Limburg PJ, Baron JA, Burnett-Hartman AN, Weisenberger DJ, Laird PW, et al. Association between molecular subtypes of colorectal cancer and patient survival. Gastroenterology. 2015;148(1):77-87.e2.
54. Reis-Filho JS, Lakhani SR. Breast cancer special types: why bother? J Pathol. 2008;216(4):394-8.
55. Sanz-García E, Elez E, Macarulla T, Dienstmann R, Salazar R, Tabernero J. Prognosis and Therapeutic Implications for Emerging Colorectal Cancer Subtypes. Curr Colorectal Cancer Rep. 2014;10(1):55-61.

56. Inamura K, Yamauchi M, Nishihara R, Kim SA, Mima K, Sukawa Y, et al. Prognostic significance and molecular features of signet-ring cell and mucinous components in colorectal carcinoma. Ann Surg Oncol. 2015;22(4):1226-35.
57. Goldberg RM, Sargent DJ, Morton RF, Fuchs CS, Ramanathan RK, Williamson SK, et al. A randomized controlled trial of fluorouracil plus leucovorin, irinotecan, and oxaliplatin combinations in patients with previously untreated metastatic colorectal cancer. Journal of clinical oncology : official journal of the American Society of Clinical Oncology. 2004;22(1):23-30.
58. Tournigand C, Andre T, Achille E, Lledo G, Flesh M, Mery-Mignard D, et al. FOLFIRI followed by FOLFOX6 or the reverse sequence in advanced colorectal cancer: a randomized GERCOR study. Journal of clinical oncology : official journal of the American Society of Clinical Oncology. 2004;22(2):229-37.
59. Jonker DJ, O'Callaghan CJ, Karapetis CS, Zalcberg JR, Tu D, Au HJ, et al. Cetuximab for the treatment of colorectal cancer. N Engl J Med. 2007;357(20):2040-8.
60. Karapetis CS, Khambata-Ford S, Jonker DJ, O'Callaghan CJ, Tu D, Tebbutt NC, et al. K-ras mutations and benefit from cetuximab in advanced colorectal cancer. N Engl J Med. 2008;359(17):1757-65.
61. Amado RG, Wolf M, Peeters M, Van Cutsem E, Siena S, Freeman DJ, et al. Wild-type KRAS is required for panitumumab efficacy in patients with metastatic colorectal cancer. J Clin Oncol. 2008;26(10):1626-34.
62. Loupakis F, Ruzzo A, Cremolini C, Vincenzi B, Salvatore L, Santini D, et al. KRAS codon 61, 146 and BRAF mutations predict resistance to cetuximab plus irinotecan in KRAS codon 12 and 13 wild-type metastatic colorectal cancer. Br J Cancer. 2009;101(4):715-21.
63. Di Nicolantonio F, Martini M, Molinari F, Sartore-Bianchi A, Arena S, Saletti P, et al. Wild-type BRAF is required for response to panitumumab or cetuximab in metastatic colorectal cancer. J Clin Oncol. 2008;26(35):5705-12.
64. Sartore-Bianchi A, Martini M, Molinari F, Veronese S, Nichelatti M, Artale S, et al. PIK3CA mutations in colorectal cancer are associated with clinical resistance to EGFR-targeted monoclonal antibodies. Cancer Res. 2009;69(5):1851-7.
65. Therkildsen C, Bergmann TK, Henrichsen-Schnack T, Ladelund S, Nilbert M. The predictive value of KRAS, NRAS, BRAF, PIK3CA and PTEN for anti-EGFR treatment in metastatic colorectal cancer: A systematic review and meta-analysis. Acta oncologica (Stockholm, Sweden). 2014;53(7):852-64.
66. Douillard JY, Siena S, Cassidy J, Tabernero J, Burkes R, Barugel M, et al. Randomized, phase III trial of panitumumab with infusional fluorouracil, leucovorin, and oxaliplatin (FOLFOX4) versus FOLFOX4 alone as first-line treatment in patients with previously untreated metastatic colorectal cancer: the PRIME study. J Clin Oncol. 2010;28(31):4697-705.
67. Sinicrope FA, Shi Q, Smyrk TC, Thibodeau SN, Dienstmann R, Guinney J, et al. Molecular markers identify subtypes of stage III colon cancer associated with patient outcomes. Gastroenterology. 2015;148(1):88-99.
68. Jass JR. Classification of colorectal cancer based on correlation of clinical, morphological and molecular features. Histopathology. 2007;50(1):113-30.
69. De Stefano A, Carlomagno C. Beyond KRAS: Predictive factors of the efficacy of anti-EGFR monoclonal antibodies in the treatment of metastatic colorectal cancer. World J Gastroenterol. 2014;20(29):9732-43.

70. Wang Y, Cao S, Chen Y. Molecular Treatment of Different Breast Cancers. Anti-cancer agents in medicinal chemistry. 2015.
71. Litzenburger BC, Brown PH. Advances in Preventive Therapy for Estrogen-Receptor-Negative Breast Cancer. Current breast cancer reports. 2014;6:96-109.
72. Chau CH, Figg WD. Molecular and phenotypic heterogeneity of metastatic prostate cancer. Cancer Biol Ther. 2005;4(2):166-7.
73. Barbieri CE, Demichelis F, Rubin MA. Molecular genetics of prostate cancer: emerging appreciation of genetic complexity. Histopathology. 2012;60(1):187-98.
74. Gershenson DM. The heterogeneity of epithelial ovarian cancer: getting it right. Cancer. 2010;116(6):1400-2.
75. Faratian D, Um I, Wilson DS, Mullen P, Langdon SP, Harrison DJ. Phosphoprotein pathway profiling of ovarian carcinoma for the identification of potential new targets for therapy. Eur J Cancer. 2011;47(9):1420-31.
76. Bellmunt J, Eisen T, Szczylik C, Mulders P, Porta C. A new patient-focused approach to the treatment of metastatic renal cell carcinoma: establishing customized treatment options. BJU Int. 2011;107(8):1190-9.
77. Novara G, Martignoni G, Artibani W, Ficarra V. Grading systems in renal cell carcinoma. J Urol. 2007;177(2):430-6.
78. Diaz LA, Jr., Williams RT, Wu J, Kinde I, Hecht JR, Berlin J, et al. The molecular evolution of acquired resistance to targeted EGFR blockade in colorectal cancers. Nature. 2012;486(7404):537-40.
79. Hiley C, de Bruin EC, McGranahan N, Swanton C. Deciphering intratumor heterogeneity and temporal acquisition of driver events to refine precision medicine. Genome biology. 2014;15(8):453.
80. Fidler IJ. Tumor heterogeneity and the biology of cancer invasion and metastasis. Cancer Res. 1978;38(9):2651-60.
81. Hanahan D, Weinberg Robert A. Hallmarks of Cancer: The Next Generation. Cell. 2011;144(5):646-74.
82. Shinto E, Tsuda H, Ueno H, Hashiguchi Y, Hase K, Tamai S, et al. Prognostic implication of laminin-5 gamma 2 chain expression in the invasive front of colorectal cancers, disclosed by area-specific four-point tissue microarrays. Lab Invest. 2005;85(2):257-66.
83. Kajiwara Y, Ueno H, Hashiguchi Y, Shinto E, Shimazaki H, Mochizuki H, et al. Heterogeneity of metalloproteinase expression in colorectal cancer - relation of molecular findings to basic morphology. Anticancer Res. 2011;31(5):1567-75.
84. Rohwer N, Lobitz S, Daskalow K, Jons T, Vieth M, Schlag PM, et al. HIF-1alpha determines the metastatic potential of gastric cancer cells. Br J Cancer. 2009;100(5):772-81.
85. Choi YP, Shim HS, Gao MQ, Kang S, Cho NH. Molecular portraits of intratumoral heterogeneity in human ovarian cancer. Cancer Lett. 2011;307(1):62-71.
86. Karamitopoulou E, Zlobec I, Panayiotides I, Patsouris ES, Peros G, Rallis G, et al. Systematic analysis of proteins from different signaling pathways in the tumor center and the invasive front of colorectal cancer. Hum Pathol. 2011;42(12):1888-96.
87. Baldus SE, Schaefer KL, Engers R, Hartleb D, Stoecklein NH, Gabbert HE. Prevalence and heterogeneity of KRAS, BRAF, and PIK3CA mutations in primary colorectal adenocarcinomas and their corresponding metastases. Clin Cancer Res. 2010;16(3):790-9.

88. Richman SD, Chambers P, Seymour MT, Daly C, Grant S, Hemmings G, et al. Intra-tumoral heterogeneity of KRAS and BRAF mutation status in patients with advanced colorectal cancer (aCRC) and cost-effectiveness of multiple sample testing. Anal Cell Pathol (Amst). 2011;34(1-2):61-6.
89. Yancovitz M, Litterman A, Yoon J, Ng E, Shapiro RL, Berman RS, et al. Intra- and inter-tumor heterogeneity of BRAF(V600E))mutations in primary and metastatic melanoma. PLoS One. 2012;7(1):e29336.
90. Ueno H, Hase K, Hashiguchi Y, Shimazaki H, Tanaka M, Miyake O, et al. Site-specific tumor grading system in colorectal cancer: multicenter pathologic review of the value of quantifying poorly differentiated clusters. Am J Surg Pathol. 2014;38(2):197-204.
91. Betge J, Kornprat P, Pollheimer MJ, Lindtner RA, Schlemmer A, Rehak P, et al. Tumor Budding is an Independent Predictor of Outcome in AJCC/UICC Stage II Colorectal Cancer. Ann Surg Oncol. 2012.
92. Horcic M, Koelzer VH, Karamitopoulou E, Terracciano L, Puppa G, Zlobec I, et al. Tumor budding score based on 10 high-power fields is a promising basis for a standardized prognostic scoring system in stage II colorectal cancer. Hum Pathol. 2013;44(5):697-705.
93. Puppa G, Senore C, Sheahan K, Vieth M, Lugli A, Zlobec I, et al. Diagnostic reproducibility of tumour budding in colorectal cancer: a multicentre, multinational study using virtual microscopy. Histopathology. 2012;61(4):562-75.
94. Richards CH, Mohammed Z, Qayyum T, Horgan PG, McMillan DC. The prognostic value of histological tumor necrosis in solid organ malignant disease: a systematic review. Future Oncol. 2011;7(10):1223-35.
95. Richards CH, Roxburgh CS, Anderson JH, McKee RF, Foulis AK, Horgan PG, et al. Prognostic value of tumour necrosis and host inflammatory responses in colorectal cancer. Br J Surg. 2012;99(2):287-94.
96. Hector S, Prehn JH. Apoptosis signaling proteins as prognostic biomarkers in colorectal cancer: a review. Biochim Biophys Acta. 2009;1795(2):117-29.
97. Villar E, Redondo M, Rodrigo I, Garcia J, Avila E, Matilla A. bcl-2 Expression and apoptosis in primary and metastatic breast carcinomas. Tumour Biol. 2001;22(3):137-45.
98. Aleskandarany MA, Green AR, Benhasouna AA, Barros FF, Neal KR, Reis-Filho JS, et al. Prognostic value of proliferation assay in the luminal, HER2 positive and triple negative biological classes of breast cancer. Breast Cancer Res. 2012;14(1):R3.
99. Ladstein RG, Bachmann IM, Straume O, Akslen LA. Prognostic Importance of the Mitotic Marker Phosphohistone H3 in Cutaneous Nodular Melanoma. J Invest Dermatol. 2012.
100. Kopetz S, Tabernero J, Rosenberg R, Jiang ZQ, Moreno V, Bachleitner-Hofmann T, et al. Genomic Classifier ColoPrint Predicts Recurrence in Stage II Colorectal Cancer Patients More Accurately Than Clinical Factors. The oncologist. 2015;20(2):127-33.
101. Srivastava G, Renfro LA, Behrens RJ, Lopatin M, Chao C, Soori GS, et al. Prospective multicenter study of the impact of oncotype DX colon cancer assay results on treatment recommendations in stage II colon cancer patients. The oncologist. 2014;19(5):492-7.

102. Maurice B Loughrey PQ, Neil A Shepherd. Final Standards and datasets for reporting cancers Dataset for colorectal cancer histopathology reports July 2014 2014 [updated July 2014; cited 2014 04/03/2015]. 2014:[Available from: http://www.rcpath.org/Resources/RCPath/Migrated%20Resources/Documents/G/G049_ColorectalDataset_July14.pdf.
103. Fleming M, Ravula S, Tatishchev SF, Wang HL. Colorectal carcinoma: Pathologic aspects. Journal of gastrointestinal oncology. 2012;3(3):153-73.
104. Compton CC, Greene FL. The staging of colorectal cancer: 2004 and beyond. CA: a cancer journal for clinicians. 2004;54(6):295-308.
105. Nambiar PR, Gupta RR, Misra V. An "Omics" based survey of human colon cancer. Mutation research. 2010;693(1-2):3-18.
106. Hansen KD, Timp W, Bravo HC, Sabunciyan S, Langmead B, McDonald OG, et al. Increased methylation variation in epigenetic domains across cancer types. Nature genetics. 2011;43(8):768-75.
107. Hinoue T, Weisenberger DJ, Lange CP, Shen H, Byun HM, Van Den Berg D, et al. Genome-scale analysis of aberrant DNA methylation in colorectal cancer. Genome research. 2012;22(2):271-82.
108. Evangelou E, Ioannidis JP. Meta-analysis methods for genome-wide association studies and beyond. Nature reviews Genetics. 2013;14(6):379-89.
109. Galvan JA, Helbling M, Koelzer VH, Tschan MP, Berger MD, Hadrich M, et al. TWIST1 and TWIST2 promoter methylation and protein expression in tumor stroma influence the epithelial-mesenchymal transition-like tumor budding phenotype in colorectal cancer. Oncotarget. 2015;6(2):874-85.
110. Lipson D, Capelletti M, Yelensky R, Otto G, Parker A, Jarosz M, et al. Identification of new ALK and RET gene fusions from colorectal and lung cancer biopsies. Nat Med. 2012.
111. Jones S, Wang TL, Shih Ie M, Mao TL, Nakayama K, Roden R, et al. Frequent mutations of chromatin remodeling gene ARID1A in ovarian clear cell carcinoma. Science. 2010;330(6001):228-31.
112. Kohlmann A, Grossmann V, Haferlach T. Integration of next-generation sequencing into clinical practice: are we there yet? Semin Oncol. 2012;39(1):26-36.
113. Vakiani E, Janakiraman M, Shen R, Sinha R, Zeng Z, Shia J, et al. Comparative genomic analysis of primary versus metastatic colorectal carcinomas. Journal of clinical oncology : official journal of the American Society of Clinical Oncology. 2012;30(24):2956-62.
114. Cooke SL, Temple J, Macarthur S, Zahra MA, Tan LT, Crawford RA, et al. Intra-tumour genetic heterogeneity and poor chemoradiotherapy response in cervical cancer. Br J Cancer. 2011;104(2):361-8.
115. Sawada T, Yamamoto E, Suzuki H, Nojima M, Maruyama R, Shioi Y, et al. Association between genomic alterations and metastatic behavior of colorectal cancer identified by array-based comparative genomic hybridization. Genes, chromosomes & cancer. 2013;52(2):140-9.
116. Michels E, De Preter K, Van Roy N, Speleman F. Detection of DNA copy number alterations in cancer by array comparative genomic hybridization. Genet Med. 2007;9(9):574-84.
117. Malone JH, Oliver B. Microarrays, deep sequencing and the true measure of the transcriptome. BMC Biol. 2011;9:34.

118. van 't Veer LJ, Dai H, van de Vijver MJ, He YD, Hart AA, Mao M, et al. Gene expression profiling predicts clinical outcome of breast cancer. Nature. 2002;415(6871):530-6.
119. Slodkowska EA, Ross JS. MammaPrint 70-gene signature: another milestone in personalized medical care for breast cancer patients. Expert Rev Mol Diagn. 2009;9(5):417-22.
120. Lo SS, Mumby PB, Norton J, Rychlik K, Smerage J, Kash J, et al. Prospective multicenter study of the impact of the 21-gene recurrence score assay on medical oncologist and patient adjuvant breast cancer treatment selection. J Clin Oncol. 2010;28(10):1671-6.
121. Kelley RK, Venook AP. Prognostic and predictive markers in stage II colon cancer: is there a role for gene expression profiling? Clin Colorectal Cancer. 2011;10(2):73-80.
122. Lapointe LC, Pedersen SK, Dunne R, Brown GS, Pimlott L, Gaur S, et al. Discovery and validation of molecular biomarkers for colorectal adenomas and cancer with application to blood testing. PLoS One. 2012;7(1):e29059.
123. Mosig RA, Lin L, Senturk E, Shah H, Huang F, Schlosshauer P, et al. Application of RNA-Seq Transcriptome Analysis: CD151 is an Invasion/Migration Target in All Stages of Epithelial Ovarian Cancer. J Ovarian Res. 2012;5(1):4.
124. Dawson JC, Carragher NO. Quantitative phenotypic and pathway profiling guides rational drug combination strategies. Frontiers in pharmacology. 2014;5:118.
125. Lin JC. Protein microarrays for cancer diagnostics and therapy. Medical principles and practice : international journal of the Kuwait University, Health Science Centre. 2010;19(4):247-54.
126. Malinowsky K, Nitsche U, Janssen KP, Bader FG, Spath C, Drecoll E, et al. Activation of the PI3K/AKT pathway correlates with prognosis in stage II colon cancer. Br J Cancer. 2014;110(8):2081-9.
127. Mueller C, Liotta LA, Espina V. Reverse phase protein microarrays advance to use in clinical trials. Mol Oncol. 2010;4(6):461-81.
128. Liao CC, Ward N, Marsh S, Arulampalam T, Norton JD. Mass spectrometry protein expression profiles in colorectal cancer tissue associated with clinico-pathological features of disease. BMC cancer. 2010;10:410.
129. Espina V, Heiby M, Pierobon M, Liotta LA. Laser capture microdissection technology. Expert Rev Mol Diagn. 2007;7(5):647-57.
130. Espina V, Wulfkuhle J, Liotta LA. Application of laser microdissection and reverse-phase protein microarrays to the molecular profiling of cancer signal pathway networks in the tissue microenvironment. Clin Lab Med. 2009;29(1):1-13.
131. Paweletz CP, Charboneau L, Bichsel VE, Simone NL, Chen T, Gillespie JW, et al. Reverse phase protein microarrays which capture disease progression show activation of pro-survival pathways at the cancer invasion front. Oncogene. 2001;20(16):1981-9.
132. Rothberg JM, Hinz W, Rearick TM, Schultz J, Mileski W, Davey M, et al. An integrated semiconductor device enabling non-optical genome sequencing. Nature. 2011;475(7356):348-52.
133. Voshol H, Ehrat M, Traenkle J, Bertrand E, van Oostrum J. Antibody-based proteomics: analysis of signaling networks using reverse protein arrays. FEBS J. 2009;276(23):6871-9.

134. Dabbs DJ. Diagnostic Immunohistochemistry, 4th Edition: Saunders; 2013 3rd December 2013.
135. Giger OT, Comtesse SC, Lugli A, Zlobec I, Kurrer MO. Intra-tumoral budding in preoperative biopsy specimens predicts lymph node and distant metastasis in patients with colorectal cancer. Mod Pathol. 2012;25(7):1048-53.
136. Kazama S, Watanabe T, Ajioka Y, Kanazawa T, Nagawa H. Tumour budding at the deepest invasive margin correlates with lymph node metastasis in submucosal colorectal cancer detected by anticytokeratin antibody CAM5.2. Br J Cancer. 2006;94(2):293-8.
137. Hammond ME, Hayes DF, Wolff AC, Mangu PB, Temin S. American society of clinical oncology/college of american pathologists guideline recommendations for immunohistochemical testing of estrogen and progesterone receptors in breast cancer. J Oncol Pract. 2010;6(4):195-7.
138. Wolff AC, Hammond ME, Schwartz JN, Hagerty KL, Allred DC, Cote RJ, et al. American Society of Clinical Oncology/College of American Pathologists guideline recommendations for human epidermal growth factor receptor 2 testing in breast cancer. J Clin Oncol. 2007;25(1):118-45.
139. Bayani J, Squire JA. Fluorescence in situ Hybridization (FISH). Current protocols in cell biology / editorial board, Juan S Bonifacino [et al]. 2004;Chapter 22:Unit 22.4.
140. Sato-Kuwabara Y, Neves JI, Fregnani JH, Sallum RA, Soares FA. Evaluation of gene amplification and protein expression of HER-2/neu in esophageal squamous cell carcinoma using Fluorescence in situ Hybridization (FISH) and immunohistochemistry. BMC Cancer. 2009;9:6.
141. Dekanic A, Dintinjan RD, Budisavljevic I, Pecanic S, Butorac MZ, Jonjic N. Strong nuclear EGFR expression in colorectal carcinomas is associated with cyclin-D1 but not with gene EGFR amplification. Diagn Pathol. 2011;6:108.
142. Yang J, Luo H, Li Y, Li J, Cai Z, Su X, et al. Intratumoral heterogeneity determines discordant results of diagnostic tests for human epidermal growth factor receptor (HER) 2 in gastric cancer specimens. Cell Biochem Biophys. 2012;62(1):221-8.
143. Rubakhin SS, Sweedler JV. Quantitative measurements of cell-cell signaling peptides with single-cell MALDI MS. Analytical chemistry. 2008;80(18):7128-36.
144. Reindl W, Bowen BP, Balamotis MA, Green JE, Northen TR. Multivariate analysis of a 3D mass spectral image for examining tissue heterogeneity. Integrative biology : quantitative biosciences from nano to macro. 2011;3(4):460-7.
145. Casadonte R, Caprioli RM. Proteomic analysis of formalin-fixed paraffin-embedded tissue by MALDI imaging mass spectrometry. Nature protocols. 2011;6(11):1695-709.
146. Korn K, Krausz E. Cell-based high-content screening of small-molecule libraries. Curr Opin Chem Biol. 2007;11(5):503-10.
147. Gasparri F, Cappella P, Galvani A. Multiparametric cell cycle analysis by automated microscopy. J Biomol Screen. 2006;11(6):586-98.
148. Caie PD, Walls RE, Ingleston-Orme A, Daya S, Houslay T, Eagle R, et al. High-content phenotypic profiling of drug response signatures across distinct cancer cells. Molecular cancer therapeutics. 2010;9(6):1913-26.
149. Puppa G, Risio M, Sheahan K, Vieth M, Zlobec I, Lugli A, et al. Standardization of whole slide image morphologic assessment with definition of a new

application: Digital slide dynamic morphometry. Journal of pathology informatics. 2011;2:48.
150. Ghaznavi F, Evans A, Madabhushi A, Feldman M. Digital imaging in pathology: whole-slide imaging and beyond. Annual review of pathology. 2013;8:331-59.
151. Webster JD, Dunstan RW. Whole-slide imaging and automated image analysis: considerations and opportunities in the practice of pathology. Vet Pathol. 2014;51(1):211-23.
152. Pantanowitz L, Sinard JH, Henricks WH, Fatheree LA, Carter AB, Contis L, et al. Validating whole slide imaging for diagnostic purposes in pathology: guideline from the College of American Pathologists Pathology and Laboratory Quality Center. Arch Pathol Lab Med. 2013;137(12):1710-22.
153. Titus K. Regulators scanning the digital scanners. CAP Today. 2012:56-62.
154. Kux L. Technical Performance Assessment of Digital Pathology Whole Slide Imaging Devices; Draft Guidance for Industry and Food and Drug Administration Staff; Availability 2015 [25/02/15]. Available from: https://federalregister.gov/a/2015-03843.
155. The Canadian Association of Pathologists Telepathology Guidelines C, Bernard C, Chandrakanth SA, Cornell IS, Dalton J, Evans A, et al. Guidelines from the Canadian Association of Pathologists for establishing a telepathology service for anatomic pathology using whole-slide imaging. Journal of pathology informatics. 2014;5:15.
156. Romero Lauro G, Cable W, Lesniak A, Tseytlin E, McHugh J, Parwani A, et al. Digital Pathology Consultations—a New Era in Digital Imaging, Challenges and Practical Applications. Journal of Digital Imaging. 2013;26(4):668-77.
157. Brachtel E, Yagi Y. Digital imaging in pathology--current applications and challenges. Journal of biophotonics. 2012;5(4):327-35.
158. Potts SJ. Digital pathology in drug discovery and development: multisite integration. Drug discovery today. 2009;14(19-20):935-41.
159. Pantanowitz L, Szymas J, Yagi Y, Wilbur D. Whole slide imaging for educational purposes. Journal of pathology informatics. 2012;3:46.
160. Laurent C, Guérin M, Frenois F-X, Thuries V, Jalabert L, Brousset P, et al. Whole-slide imaging is a robust alternative to traditional fluorescent microscopy for fluorescence in situ hybridization imaging using break-apart DNA probes. Human Pathology.44(8):1544-55.
161. van der Post RS, van der Laak JA, Sturm B, Clarijs R, Schaafsma HE, van Krieken JH, et al. The evaluation of colon biopsies using virtual microscopy is reliable. Histopathology. 2013;63(1):114-21.
162. Stathonikos N, Veta M, Huisman A, van Diest PJ. Going fully digital: Perspective of a Dutch academic pathology lab. Journal of pathology informatics. 2013;4:15.
163. Rojo MG, Bueno G, Slodkowska J. Review of imaging solutions for integrated quantitative immunohistochemistry in the Pathology daily practice. Folia histochemica et cytobiologica / Polish Academy of Sciences, Polish Histochemical and Cytochemical Society. 2009;47(3):349-54.
164. O'Mahony FC, Faratian D, Varley J, Nanda J, Theodoulou M, Riddick AC, et al. The use of automated quantitative analysis to evaluate epithelial-to-mesenchymal

transition associated proteins in clear cell renal cell carcinoma. PloS one. 2012;7(2):e31557.
165. Eynard HG, Soria EA, Cuestas E, Rovasio RA, Eynard AR. Assessment of colorectal cancer prognosis through nuclear morphometry. J Surg Res. 2009;154(2):345-8.
166. Ikeguchi M, Sakatani T, Endo K, Makino M, Kaibara N. Computerized nuclear morphometry is a useful technique for evaluating the high metastatic potential of colorectal adenocarcinoma. Cancer. 1999;86(10):1944-51.
167. Mitmaker B, Begin LR, Gordon PH. Nuclear shape as a prognostic discriminant in colorectal carcinoma. Dis Colon Rectum. 1991;34(3):249-59.
168. Camp RL, Chung GG, Rimm DL. Automated subcellular localization and quantification of protein expression in tissue microarrays. Nature medicine. 2002;8(11):1323-7.
169. Mansfield JR, Hoyt C, Levenson RM. Visualization of microscopy-based spectral imaging data from multi-label tissue sections. Curr Protoc Mol Biol. 2008;Chapter 14:Unit 14 9.
170. Fiore C, Bailey D, Conlon N, Wu X, Martin N, Fiorentino M, et al. Utility of multispectral imaging in automated quantitative scoring of immunohistochemistry. J Clin Pathol. 2012;65(6):496-502.
171. Liu J, Lau SK, Varma VA, Moffitt RA, Caldwell M, Liu T, et al. Molecular mapping of tumor heterogeneity on clinical tissue specimens with multiplexed quantum dots. ACS Nano. 2010;4(5):2755-65.
172. Friedenberger M, Bode M, Krusche A, Schubert W. Fluorescence detection of protein clusters in individual cells and tissue sections by using toponome imaging system: sample preparation and measuring procedures. Nature protocols. 2007;2(9):2285-94.
173. Schubert W, Gieseler A, Krusche A, Serocka P, Hillert R. Next-generation biomarkers based on 100-parameter functional super-resolution microscopy TIS. New biotechnology. 2012;29(5):599-610.
174. Amin W, Srinivasan M, Song SY, Parwani AV, Becich MJ. Use of automated image analysis in evaluation of Mesothelioma Tissue Microarray (TMA) from National Mesothelioma Virtual Bank. Pathol Res Pract. 2014;210(2):79-82.
175. Rizzardi AE, Johnson AT, Vogel RI, Pambuccian SE, Henriksen J, Skubitz AP, et al. Quantitative comparison of immunohistochemical staining measured by digital image analysis versus pathologist visual scoring. Diagn Pathol. 2012;7:42.
176. Barsky S, Gentchev L, Basu A, Jimenez R, Boussaid K, Gholap A. Use and validation of epithelial recognition and fields of view algorithms on virtual slides to guide TMA construction. BioTechniques. 2009;47(5):927-38.
177. McKenna SJ, Amaral T, Akbar S, Jordan L, Thompson A. Immunohistochemical analysis of breast tissue microarray images using contextual classifiers. Journal of pathology informatics. 2013;4(Suppl):S13.
178. Yang DT, Quann PJ, Petrich AM, Leith CP, Young KH, Kahl BS. Use of tissue microarray and automated quantitative analysis for screening and validation of potential biomarkers in mantle cell lymphoma. Appl Immunohistochem Mol Morphol. 2011;19(1):62-9.
179. Pennanen M, Heiskanen I, Sane T, Remes S, Mustonen H, Haglund C, et al. Helsinki score-a novel model for prediction of metastases in adrenocortical carcinomas. Hum Pathol. 2014.

180. Fleischmann A, Huland H, Mirlacher M, Wilczak W, Simon R, Erbersdobler A, et al. Prognostic relevance of Bcl-2 overexpression in surgically treated prostate cancer is not caused by increased copy number or translocation of the gene. Prostate. 2011.
181. Scrima M, De Marco C, Fabiani F, Franco R, Pirozzi G, Rocco G, et al. Signaling Networks Associated with AKT Activation in Non-Small Cell Lung Cancer (NSCLC): New Insights on the Role of Phosphatydil-Inositol-3 kinase. PLoS One. 2012;7(2):e30427.
182. Belhomme P, Toralba S, Plancoulaine B, Oger M, Gurcan MN, Bor-Angelier C. Heterogeneity assessment of histological tissue sections in whole slide images. Computerized medical imaging and graphics : the official journal of the Computerized Medical Imaging Society. 2014.
183. Webster JD, Dunstan RW. Whole-Slide Imaging and Automated Image Analysis: Considerations and Opportunities in the Practice of Pathology. Vet Pathol. 2013.
184. Kumar A, Rao A, Bhavani S, Newberg JY, Murphy RF. Automated analysis of immunohistochemistry images identifies candidate location biomarkers for cancers. Proceedings of the National Academy of Sciences of the United States of America. 2014;111(51):18249-54.
185. Veta M, van Diest PJ, Willems SM, Wang H, Madabhushi A, Cruz-Roa A, et al. Assessment of algorithms for mitosis detection in breast cancer histopathology images. Medical image analysis. 2015;20(1):237-48.
186. Yuan Y. Modelling the spatial heterogeneity and molecular correlates of lymphocytic infiltration in triple-negative breast cancer. Journal of the Royal Society, Interface / the Royal Society. 2015;12(103).
187. Balsat C, Signolle N, Goffin F, Delbecque K, Plancoulaine B, Sauthier P, et al. Improved computer-assisted analysis of the global lymphatic network in human cervical tissues. Mod Pathol. 2014;27(6):887-98.
188. Isse K, Lesniak A, Grama K, Roysam B, Minervini MI, Demetris AJ. Digital transplantation pathology: combining whole slide imaging, multiplex staining and automated image analysis. American journal of transplantation : official journal of the American Society of Transplantation and the American Society of Transplant Surgeons. 2012;12(1):27-37.
189. Khoury MJ, Ioannidis JP. Medicine. Big data meets public health. Science (New York, NY). 2014;346(6213):1054-5.
190. Issa NT, Byers SW, Dakshanamurthy S. Big data: the next frontier for innovation in therapeutics and healthcare. Expert review of clinical pharmacology. 2014;7(3):293-8.
191. Cooper LA, Kong J, Gutman DA, Dunn WD, Nalisnik M, Brat DJ. Novel genotype-phenotype associations in human cancers enabled by advanced molecular platforms and computational analysis of whole slide images. Laboratory investigation; a journal of technical methods and pathology. 2015.
192. Beck AH, Sangoi AR, Leung S, Marinelli RJ, Nielsen TO, van de Vijver MJ, et al. Systematic analysis of breast cancer morphology uncovers stromal features associated with survival. Sci Transl Med. 2011;3(108):108ra13.
193. Kong J, Cooper LA, Wang F, Gao J, Teodoro G, Scarpace L, et al. Machine-based morphologic analysis of glioblastoma using whole-slide pathology images uncovers clinically relevant molecular correlates. PloS one. 2013;8(11):e81049.

194. Miller WR, Larionov A, Renshaw L, Anderson TJ, Walker JR, Krause A, et al. Gene expression profiles differentiating between breast cancers clinically responsive or resistant to letrozole. Journal of clinical oncology : official journal of the American Society of Clinical Oncology. 2009;27(9):1382-7.
195. Rimm DL. Next-gen immunohistochemistry. Nature methods. 2014;11(4):381-3.
196. Angelo M, Bendall SC, Finck R, Hale MB, Hitzman C, Borowsky AD, et al. Multiplexed ion beam imaging of human breast tumors. Nature medicine. 2014;20(4):436-42.
197. Heindl A, Nawaz S, Yuan Y. Mapping spatial heterogeneity in the tumor microenvironment: a new era for digital pathology. Laboratory investigation; a journal of technical methods and pathology. 2015.
198. Zoratto F, Rossi L, Verrico M, Papa A, Basso E, Zullo A, et al. Focus on genetic and epigenetic events of colorectal cancer pathogenesis: implications for molecular diagnosis. Tumour biology : the journal of the International Society for Oncodevelopmental Biology and Medicine. 2014;35(7):6195-206.
199. Almendro V, Kim HJ, Cheng YK, Gonen M, Itzkovitz S, Argani P, et al. Genetic and phenotypic diversity in breast tumor metastases. Cancer Res. 2014;74(5):1338-48.
200. Karagoz K, Sinha R, Arga KY. Triple negative breast cancer: a multi-omics network discovery strategy for candidate targets and driving pathways. Omics : a journal of integrative biology. 2015;19(2):115-30.
201. Roden AC, Garcia JJ, Wehrs RN, Colby TV, Khoor A, Leslie KO, et al. Histopathologic, immunophenotypic and cytogenetic features of pulmonary mucoepidermoid carcinoma. Mod Pathol. 2014;27(11):1479-88.
202. Le Cao KA, Gonzalez I, Dejean S. integrOmics: an R package to unravel relationships between two omics datasets. Bioinformatics (Oxford, England). 2009;25(21):2855-6.
203. Day RS, McDade KK, Chandran UR, Lisovich A, Conrads TP, Hood BL, et al. Identifier mapping performance for integrating transcriptomics and proteomics experimental results. BMC bioinformatics. 2011;12:213.
204. Miyoshi NS, Pinheiro DG, Silva WA, Jr., Felipe JC. Computational framework to support integration of biomolecular and clinical data within a translational approach. BMC bioinformatics. 2013;14:180.
205. Bronsert P, Enderle-Ammour K, Bader M, Timme S, Kuehs M, Csanadi A, et al. Cancer cell invasion and EMT marker expression: a three-dimensional study of the human cancer-host interface. J Pathol. 2014;234(3):410-22.
206. Faratian D, Clyde RG, Crawford JW, Harrison DJ. Systems pathology--taking molecular pathology into a new dimension. Nature reviews Clinical oncology. 2009;6(8):455-64.
207. Hood L, Friend SH. Predictive, personalized, preventive, participatory (P4) cancer medicine. Nature reviews Clinical oncology. 2011;8(3):184-7.
208. Goltsov A, Faratian D, Langdon SP, Mullen P, Harrison DJ, Bown J. Features of the reversible sensitivity-resistance transition in PI3K/PTEN/AKT signalling network after HER2 inhibition. Cellular signalling. 2012;24(2):493-504.
209. Gomez-Cabrero D, Lluch-Ariet M, Tegner J, Cascante M, Miralles F, Roca J, et al. Synergy-COPD: a systems approach for understanding and managing chronic diseases. Journal of Translational Medicine. 2014;12(Suppl 2):S2.

210. Faratian D, Goltsov A, Lebedeva G, Sorokin A, Moodie S, Mullen P, et al. Systems biology reveals new strategies for personalizing cancer medicine and confirms the role of PTEN in resistance to trastuzumab. Cancer Res. 2009;69(16):6713-20.
211. Almendro V, Cheng YK, Randles A, Itzkovitz S, Marusyk A, Ametller E, et al. Inference of tumor evolution during chemotherapy by computational modeling and in situ analysis of genetic and phenotypic cellular diversity. Cell reports. 2014;6(3):514-27.
212. Madhavan S, Gusev Y, Natarajan TG, Song L, Bhuvaneshwar K, Gauba R, et al. Genome-wide multi-omics profiling of colorectal cancer identifies immune determinants strongly associated with relapse. Frontiers in genetics. 2013;4:236.
213. Colorectal Cancer

Estimated Incidence, Mortality and Prevalence Worldwide in 2012 GLOBOCAN 20122012 [23/02/15]. Available from: http://globocan.iarc.fr/Pages/fact_sheets_cancer.aspx.
214. Cancer Statistics Colorectal Cancer NHS Scotland: ISD Scotland; 2014 [cited 2015 23/02/15]. Available from: http://www.isdscotland.org/Health-Topics/Cancer/Cancer-Statistics/Colorectal/.
215. ISD Scotland Cancer Statistics Colorectal cancer [Internet]. 2010. Available from: http://www.isdscotland.org/Health-Topics/Cancer/Cancer-Statistics/Colorectal/#summary.
216. Shah R, Jones E, Vidart V, Kuppen PJ, Conti JA, Francis NK. Biomarkers for early detection of colorectal cancer and polyps: systematic review. Cancer epidemiology, biomarkers & prevention : a publication of the American Association for Cancer Research, cosponsored by the American Society of Preventive Oncology. 2014;23(9):1712-28.
217. Worthley DL, Leggett BA. Colorectal cancer: molecular features and clinical opportunities. Clin Biochem Rev. 2010;31(2):31-8.
218. Siegel R, Ward E, Brawley O, Jemal A. Cancer statistics, 2011: the impact of eliminating socioeconomic and racial disparities on premature cancer deaths. CA: a cancer journal for clinicians. 2011;61(4):212-36.
219. Brenner H, Kloor M, Pox CP. Colorectal cancer. Lancet. 2014;383(9927):1490-502.
220. Fearon ER, Vogelstein B. A genetic model for colorectal tumorigenesis. Cell. 1990;61(5):759-67.
221. Soreide K, Nedrebo BS, Knapp JC, Glomsaker TB, Soreide JA, Korner H. Evolving molecular classification by genomic and proteomic biomarkers in colorectal cancer: potential implications for the surgical oncologist. Surgical oncology. 2009;18(1):31-50.
222. Armaghany T, Wilson JD, Chu Q, Mills G. Genetic alterations in colorectal cancer. Gastrointestinal cancer research : GCR. 2012;5(1):19-27.
223. Vilar E, Gruber SB. Microsatellite instability in colorectal cancer-the stable evidence. Nat Rev Clin Oncol. 2010;7(3):153-62.
224. Fearon ER. Molecular genetics of colorectal cancer. Annual review of pathology. 2011;6:479-507.
225. Geiersbach KB, Samowitz WS. Microsatellite instability and colorectal cancer. Arch Pathol Lab Med. 2011;135(10):1269-77.

226. Lee KH, Lee JS, Nam JH, Choi C, Lee MC, Park CS, et al. Promoter methylation status of hMLH1, hMSH2, and MGMT genes in colorectal cancer associated with adenoma-carcinoma sequence. Langenbeck's archives of surgery / Deutsche Gesellschaft fur Chirurgie. 2011;396(7):1017-26.
227. Weisenberger DJ, Siegmund KD, Campan M, Young J, Long TI, Faasse MA, et al. CpG island methylator phenotype underlies sporadic microsatellite instability and is tightly associated with BRAF mutation in colorectal cancer. Nature genetics. 2006;38(7):787-93.
228. Leggett B, Whitehall V. Role of the serrated pathway in colorectal cancer pathogenesis. Gastroenterology. 2010;138(6):2088-100.
229. Shen L, Toyota M, Kondo Y, Lin E, Zhang L, Guo Y, et al. Integrated genetic and epigenetic analysis identifies three different subclasses of colon cancer. Proceedings of the National Academy of Sciences of the United States of America. 2007;104(47):18654-9.
230. Compton CC. Colorectal carcinoma: diagnostic, prognostic, and molecular features. Mod Pathol. 2003;16(4):376-88.
231. Jain P, Mondal SK, Sinha SK, Mukhopadhyay M, Chakraborty I. Diagnostic and prognostic significance of different mucin expression, preoperative CEA, and CA-125 in colorectal carcinoma: A clinicopathological study. Journal of natural science, biology, and medicine. 2014;5(2):404-8.
232. Purdie CA, Piris J. Histopathological grade, mucinous differentiation and DNA ploidy in relation to prognosis in colorectal carcinoma. Histopathology. 2000;36(2):121-6.
233. Marzouk O, Schofield J. Review of histopathological and molecular prognostic features in colorectal cancer. Cancers. 2011;3(2):2767-810.
234. Makino T, Tsujinaka T, Mishima H, Ikenaga M, Sawamura T, Nakamori S, et al. Primary signet-ring cell carcinoma of the colon and rectum: report of eight cases and review of 154 Japanese cases. Hepato-gastroenterology. 2006;53(72):845-9.
235. Bosman FT, Carneiro, F., Hruban, R.H., Theise, N.D. WHO Classification of Tumours of the Digestive System, Fourth Edition. 4th ed: IACR; 2010 2010.
236. Jass JR, Love SB, Northover JM. A new prognostic classification of rectal cancer. Lancet. 1987;1(8545):1303-6.
237. Lea D, Haland S, Hagland HR, Soreide K. Accuracy of TNM staging in colorectal cancer: a review of current culprits, the modern role of morphology and stepping-stones for improvements in the molecular era. Scandinavian journal of gastroenterology. 2014;49(10):1153-63.
238. Compton CC. Optimal pathologic staging: defining stage II disease. Clin Cancer Res. 2007;13(22 Pt 2):6862s-70s.
239. Ueno H, Mochizuki H, Akagi Y, Kusumi T, Yamada K, Ikegami M, et al. Optimal Colorectal Cancer Staging Criteria in TNM Classification. Journal of Clinical Oncology. 2012.
240. Puppa G. TNM staging system of colorectal carcinoma: surgical pathology of the seventh edition. Diagnostic Histopathology.17(6):243-62.
241. Quirke P, Morris E. Reporting colorectal cancer. Histopathology. 2007;50(1):103-12.
242. Poston GJ, Tait D, O'Connell S, Bennett A, Berendse S. Diagnosis and management of colorectal cancer: summary of NICE guidance. BMJ. 2011;343:d6751.

243. Dotan E, Cohen SJ. Challenges in the management of stage II colon cancer. Seminars in oncology. 2011;38(4):511-20.
244. Morris EJ, Maughan NJ, Forman D, Quirke P. Who to treat with adjuvant therapy in Dukes B/stage II colorectal cancer? The need for high quality pathology. Gut. 2007;56(10):1419-25.
245. O'Connell JB, Maggard MA, Ko CY. Colon cancer survival rates with the new American Joint Committee on Cancer sixth edition staging. J Natl Cancer Inst. 2004;96(19):1420-5.
246. Zaniboni A, Labianca R. Adjuvant therapy for stage II colon cancer: an elephant in the living room? Annals of Oncology. 2004;15(9):1310-8.
247. Gray R, Barnwell J, McConkey C, Hills RK, Williams NS, Kerr DJ. Adjuvant chemotherapy versus observation in patients with colorectal cancer: a randomised study. Lancet. 2007;370(9604):2020-9.
248. Urquhart R, Bu J, Grunfeld E, Dewar R, MacIntyre M, Porter GA. Examining stage IIB survival in a population-based cohort of patients with colorectal cancer. Cancer. 2012;118(23):5973-81.
249. Lombardi L, Morelli F, Cinieri S, Santini D, Silvestris N, Fazio N, et al. Adjuvant colon cancer chemotherapy: where we are and where we'll go. Cancer treatment reviews. 2010;36 Suppl 3:S34-41.
250. Baxter NN, Virnig DJ, Rothenberger DA, Morris AM, Jessurun J, Virnig BA. Lymph node evaluation in colorectal cancer patients: a population-based study. J Natl Cancer Inst. 2005;97(3):219-25.
251. Mescoli C, Albertoni L, Pucciarelli S, Giacomelli L, Russo VM, Fassan M, et al. Isolated tumor cells in regional lymph nodes as relapse predictors in stage I and II colorectal cancer. Journal of clinical oncology : official journal of the American Society of Clinical Oncology. 2012;30(9):965-71.
252. Barresi V, Reggiani Bonetti L, Vitarelli E, Di Gregorio C, Ponz de Leon M, Barresi G. Immunohistochemical assessment of lymphovascular invasion in stage I colorectal carcinoma: prognostic relevance and correlation with nodal micrometastases. Am J Surg Pathol. 2012;36(1):66-72.
253. Chen SL, Steele SR, Eberhardt J, Zhu K, Bilchik A, Stojadinovic A. Lymph node ratio as a quality and prognostic indicator in stage III colon cancer. Ann Surg. 2011;253(1):82-7.
254. Compton. Prognostic Factors in Cancer 3rd edition ed: Wiley&Blackwell; 2006 6/1/2006.
255. de la Cruz-Merino L, Henao Carrasco F, Vicente Baz D, Nogales Fernandez E, Reina Zoilo JJ, Codes Manuel de Villena M, et al. Immune microenvironment in colorectal cancer: a new hallmark to change old paradigms. Clin Dev Immunol. 2011;2011:174149.
256. Huh JW, Lee JH, Kim HR, Kim YJ. Prognostic significance of lymphovascular or perineural invasion in patients with locally advanced colorectal cancer. Am J Surg. 2013.
257. Yang Y, Huang X, Sun J, Gao P, Song Y, Chen X, et al. Prognostic Value of Perineural Invasion in Colorectal Cancer: A Meta-Analysis. J Gastrointest Surg. 2015.
258. Glasgow SC, Bleier JI, Burgart LJ, Finne CO, Lowry AC. Meta-analysis of histopathological features of primary colorectal cancers that predict lymph node metastases. J Gastrointest Surg. 2012;16(5):1019-28.

259. Ueno H, Hase K, Hashiguchi Y, Shimazaki H, Yoshii S, Kudo SE, et al. Novel risk factors for lymph node metastasis in early invasive colorectal cancer: a multi-institution pathology review. Journal of gastroenterology. 2014;49(9):1314-23.
260. Lin M, Ma SP, Lin HZ, Ji P, Xie D, Yu JX. Intratumoral as well as peritumoral lymphatic vessel invasion correlates with lymph node metastasis and unfavourable outcome in colorectal cancer. Clin Exp Metastasis. 2010;27(3):123-32.
261. Williams GT, Quirke P, Shephard NA. Standards and Datasets for Reporting Cancers Dataset for colorectal cancer (2nd edition) - September 2007 2007 [26/09/2013]. Available from: http://www.rcpath.org/Resources/RCPath/Migrated%20Resources/Documents/G/G049-ColorectalDataset-Sep07.pdf.
262. Mou S, Soetikno R, Shimoda T, Rouse R, Kaltenbach T. Pathologic predictive factors for lymph node metastasis in submucosal invasive (T1) colorectal cancer: a systematic review and meta-analysis. Surg Endosc. 2013;27(8):2692-703.
263. Doyle B, Hagan S, Al-Mulla F, Scott L, Harden S, Paul J, et al. Raf kinase inhibitor protein expression combined with peritoneal involvement and lymphovascular invasion predicts prognosis in Dukes' B colorectal cancer patients. Histopathology. 2013;62(3):505-10.
264. Chang S-C, Lin C-C, Wang H-S, Yang S-H, Jiang J-K, Lan Y-T, et al. Lymphovascular invasion determines the outcome of stage I colorectal cancer patients. Formosan Journal of Surgery. 2012;45(5):141-5.
265. Ohtsuki K, Koyama F, Tamura T, Enomoto Y, Fujii H, Mukogawa T, et al. Prognostic value of immunohistochemical analysis of tumor budding in colorectal carcinoma. Anticancer Res. 2008;28(3B):1831-6.
266. Kingston EF, Goulding H, Bateman AC. Vascular invasion is underrecognized in colorectal cancer using conventional hematoxylin and eosin staining. Dis Colon Rectum. 2007;50(11):1867-72.
267. Jass JR, Ajioka Y, Allen JP, Chan YF, Cohen RJ, Nixon JM, et al. Assessment of invasive growth pattern and lymphocytic infiltration in colorectal cancer. Histopathology. 1996;28(6):543-8.
268. Zlobec I, Baker K, Minoo P, Hayashi S, Terracciano L, Lugli A. Tumor border configuration added to TNM staging better stratifies stage II colorectal cancer patients into prognostic subgroups. Cancer. 2009;115(17):4021-9.
269. Ueno H, Kajiwara Y, Shimazaki H, Shinto E, Hashiguchi Y, Nakanishi K, et al. New criteria for histologic grading of colorectal cancer. Am J Surg Pathol. 2012;36(2):193-201.
270. Ueno H, Murphy J, Jass JR, Mochizuki H, Talbot IC. Tumour 'budding' as an index to estimate the potential of aggressiveness in rectal cancer. Histopathology. 2002;40(2):127-32.
271. Barresi V, Branca G, Ieni A, Reggiani Bonetti L, Baron L, Mondello S, et al. Poorly differentiated clusters (PDCs) as a novel histological predictor of nodal metastases in pT1 colorectal cancer. Virchows Arch. 2014;464(6):655-62.
272. Mitrovic B, Schaeffer DF, Riddell RH, Kirsch R. Tumor budding in colorectal carcinoma: time to take notice. Mod Pathol. 2012;25(10):1315-25.
273. Barnetson RA, Tenesa A, Farrington SM, Nicholl ID, Cetnarskyj R, Porteous ME, et al. Identification and survival of carriers of mutations in DNA mismatch-repair genes in colon cancer. N Engl J Med. 2006;354(26):2751-63.

274. Kononen J, Bubendorf L, Kallioniemi A, Barlund M, Schraml P, Leighton S, et al. Tissue microarrays for high-throughput molecular profiling of tumor specimens. Nat Med. 1998;4(7):844-7.
275. Camp RL, Dolled-Filhart M, Rimm DL. X-tile: a new bio-informatics tool for biomarker assessment and outcome-based cut-point optimization. Clin Cancer Res. 2004;10(21):7252-9.
276. Lubbock AL, Katz E, Harrison DJ, Overton IM. TMA Navigator: Network inference, patient stratification and survival analysis with tissue microarray data. Nucleic Acids Res. 2013;41(Web Server issue):W562-8.
277. Stacker SA, Williams SP, Karnezis T, Shayan R, Fox SB, Achen MG. Lymphangiogenesis and lymphatic vessel remodelling in cancer. Nature reviews Cancer. 2014;14(3):159-72.
278. Betge J, Pollheimer MJ, Lindtner RA, Kornprat P, Schlemmer A, Rehak P, et al. Intramural and extramural vascular invasion in colorectal cancer: prognostic significance and quality of pathology reporting. Cancer. 2012;118(3):628-38.
279. Roxburgh CS, McMillan DC, Anderson JH, McKee RF, Horgan PG, Foulis AK. Elastica staining for venous invasion results in superior prediction of cancer-specific survival in colorectal cancer. Ann Surg. 2010;252(6):989-97.
280. Roxburgh CS, McMillan DC, Richards CH, Atwan M, Anderson JH, Harvey T, et al. The clinical utility of the combination of T stage and venous invasion to predict survival in patients undergoing surgery for colorectal cancer. Ann Surg. 2014;259(6):1156-65.
281. Matsumoto K, Nakayama Y, Inoue Y, Minagawa N, Katsuki T, Shibao K, et al. Lymphatic microvessel density is an independent prognostic factor in colorectal cancer. Dis Colon Rectum. 2007;50(3):308-14.
282. Chen Y, Yan J, Wang Z, Yu S, Yuan Z, Yang C, et al. A meta-analysis of the relationship between lymphatic microvessel density and the survival of patient with colorectal cancer. Lymphology. 2013;46(1):42-51.
283. Cacchi C, Arnholdt HM, Jahnig H, Anthuber M, Probst A, Oruzio DV, et al. Clinical significance of lymph vessel density in T3 colorectal carcinoma. Int J Colorectal Dis. 2012;27(6):721-6.
284. Uribarrena AR, Ortego J, Fuentes J, Raventos N, Parra P, Uribarrena ER. Prognostic value of microvascular density in dukes a and B (t1-t4, n0, m0) colorectal carcinomas. Gastroenterol Res Pract. 2009;2009:679830.
285. Talbot IC, Ritchie S, Leighton M, Hughes AO, Bussey HJ, Morson BC. Invasion of veins by carcinoma of rectum: method of detection, histological features and significance. Histopathology. 1981;5(2):141-63.
286. Harris EI, Lewin DN, Wang HL, Lauwers GY, Srivastava A, Shyr Y, et al. Lymphovascular invasion in colorectal cancer: an interobserver variability study. Am J Surg Pathol. 2008;32(12):1816-21.
287. Zaorsky NG, Patil N, Freedman GM, Tuluc M. Differentiating lymphovascular invasion from retraction artifact on histological specimen of breast carcinoma and their implications on prognosis. Journal of breast cancer. 2012;15(4):478-80.
288. Karamitopoulou E, Zlobec I, Kolzer V, Kondi-Pafiti A, Patsouris ES, Gennatas K, et al. Proposal for a 10-high-power-fields scoring method for the assessment of tumor budding in colorectal cancer. Mod Pathol. 2013;26(2):295-301.
289. Hasan J, Byers R, Jayson GC. Intra-tumoural microvessel density in human solid tumours. Br J Cancer. 2002;86(10):1566-77.

290. Cserni G, Sejben I, Bori R. Diagnosing vascular invasion in colorectal carcinomas: improving reproducibility and potential pitfalls. Journal of Clinical Pathology. 2013.
291. Kirsch R, Messenger DE, Riddell RH, Pollett A, Cook M, Al-Haddad S, et al. Venous invasion in colorectal cancer: impact of an elastin stain on detection and interobserver agreement among gastrointestinal and nongastrointestinal pathologists. Am J Surg Pathol. 2013;37(2):200-10.
292. Barresi V, Reggiani-Bonetti L, Di Gregorio C, De Leon MP, Barresi G. Lymphatic vessel density and its prognostic value in stage I colorectal carcinoma. J Clin Pathol. 2011;64(1):6-12.
293. Webster JD, Simpson ER, Michalowski AM, Hoover SB, Simpson RM. Quantifying histological features of cancer biospecimens for biobanking quality assurance using automated morphometric pattern recognition image analysis algorithms. Journal of biomolecular techniques : JBT. 2011;22(3):108-18.
294. Kayser K, Gortler J, Bogovac M, Bogovac A, Goldmann T, Vollmer E, et al. AI (artificial intelligence) in histopathology--from image analysis to automated diagnosis. Folia histochemica et cytobiologica / Polish Academy of Sciences, Polish Histochemical and Cytochemical Society. 2009;47(3):355-61.
295. Kojima M, Shimazaki H, Iwaya K, Kage M, Akiba J, Ohkura Y, et al. Pathological diagnostic criterion of blood and lymphatic vessel invasion in colorectal cancer: a framework for developing an objective pathological diagnostic system using the Delphi method, from the Pathology Working Group of the Japanese Society for Cancer of the Colon and Rectum. Journal of Clinical Pathology. 2013;66(7):551-8.
296. Sato T, Ueno H, Mochizuki H, Shinto E, Hashiguchi Y, Kajiwara Y, et al. Objective criteria for the grading of venous invasion in colorectal cancer. Am J Surg Pathol. 2010;34(4):454-62.
297. Midgley R, Kerr DJ. Adjuvant chemotherapy for stage II colorectal cancer: the time is right! Nat Clin Pract Oncol. 2005;2(7):364-9.
298. Angell HK, Gray N, Womack C, Pritchard DI, Wilkinson RW, Cumberbatch M. Digital pattern recognition-based image analysis quantifies immune infiltrates in distinct tissue regions of colorectal cancer and identifies a metastatic phenotype. Br J Cancer. 2013;109(6):1618-24.
299. Tretiakova M, Antic T, Binder D, Kocherginsky M, Liao C, Taxy JB, et al. Microvessel density is not increased in prostate cancer: digital imaging of routine sections and tissue microarrays. Hum Pathol. 2013;44(4):495-502.
300. Wang TB, Chen ZG, Wei XQ, Wei B, Dong WG. Serum vascular endothelial growth factor-C and lymphoangiogenesis are associated with the lymph node metastasis and prognosis of patients with colorectal cancer. ANZ J Surg. 2011;81(10):694-9.
301. Gao J, Knutsen A, Arbman G, Carstensen J, Franlund B, Sun XF. Clinical and biological significance of angiogenesis and lymphangiogenesis in colorectal cancer. Dig Liver Dis. 2009;41(2):116-22.
302. Longatto-Filho A, Pinheiro C, Ferreira L, Scapulatempo C, Alves VA, Baltazar F, et al. Peritumoural, but not intratumoural, lymphatic vessel density and invasion correlate with colorectal carcinoma poor-outcome markers. Virchows Arch. 2008;452(2):133-8.

303. Alexander D, Jhala N, Chatla C, Steinhauer J, Funkhouser E, Coffey CS, et al. High-Grade Tumor Differentiation Is an Indicator of Poor Prognosis in African Americans with Colonic Adenocarcinomas. Cancer. 2005;103(10):2163-70.
304. Compton CC, Fielding LP, Burgart LJ, Conley B, Cooper HS, Hamilton SR, et al. Prognostic factors in colorectal cancer. College of American Pathologists Consensus Statement 1999. Arch Pathol Lab Med. 2000;124(7):979-94.
305. Deans GT, Heatley M, Anderson N, Patterson CC, Rowlands BJ, Parks TG, et al. Jass' classification revisited. Journal of the American College of Surgeons. 1994;179(1):11-7.
306. Morodomi T, Isomoto H, Shirouzu K, Kakegawa K, Irie K, Morimatsu M. An index for estimating the probability of lymph node metastasis in rectal cancers. Lymph node metastasis and the histopathology of actively invasive regions of cancer. Cancer. 1989;63(3):539-43.
307. Hase K, Shatney C, Johnson D, Trollope M, Vierra M. Prognostic value of tumor "budding" in patients with colorectal cancer. Dis Colon Rectum. 1993;36(7):627-35.
308. Wohlke M, Schiffmann L, Prall F. Aggressive colorectal carcinoma phenotypes of invasion can be assessed reproducibly and effectively predict poor survival: interobserver study and multivariate survival analysis of a prospectively collected series of 299 patients after potentially curative resections with long-term follow-up. Histopathology. 2011;59(5):857-66.
309. Hayes BD, Maguire A, Conlon N, Gibbons D, Wang LM, Sheahan K. Reproducibility of the rapid bud count method for assessment of tumor budding in stage II colorectal cancer. Am J Surg Pathol. 2010;34(5):746-8.
310. Prall F, Ostwald C, Linnebacher M. Tubular invasion and the morphogenesis of tumor budding in colorectal carcinoma. Hum Pathol. 2009;40(10):1510-2.
311. Yamauchi H, Togashi K, Kawamura YJ, Horie H, Sasaki J, Tsujinaka S, et al. Pathological predictors for lymph node metastasis in T1 colorectal cancer. Surgery today. 2008;38(10):905-10.
312. Nakamura T, Mitomi H, Kanazawa H, Ohkura Y, Watanabe M. Tumor budding as an index to identify high-risk patients with stage II colon cancer. Dis Colon Rectum. 2008;51(5):568-72.
313. Lai YH, Wu LC, Li PS, Wu WH, Yang SB, Xia P, et al. Tumour budding is a reproducible index for risk stratification of patients with stage II colon cancer. Colorectal disease : the official journal of the Association of Coloproctology of Great Britain and Ireland. 2014;16(4):259-64.
314. Yusra, Semba S, Yokozaki H. Biological significance of tumor budding at the invasive front of human colorectal carcinoma cells. International journal of oncology. 2012;41(1):201-10.
315. Brabletz T, Hlubek F, Spaderna S, Schmalhofer O, Hiendlmeyer E, Jung A, et al. Invasion and metastasis in colorectal cancer: epithelial-mesenchymal transition, mesenchymal-epithelial transition, stem cells and beta-catenin. Cells, tissues, organs. 2005;179(1-2):56-65.
316. Zlobec I, Lugli A, Baker K, Roth S, Minoo P, Hayashi S, et al. Role of APAF-1, E-cadherin and peritumoral lymphocytic infiltration in tumour budding in colorectal cancer. J Pathol. 2007;212(3):260-8.

317. Gosens MJ, van Kempen LC, van de Velde CJ, van Krieken JH, Nagtegaal ID. Loss of membranous Ep-CAM in budding colorectal carcinoma cells. Mod Pathol. 2007;20(2):221-32.
318. Zlobec I, Gunthert U, Tornillo L, Iezzi G, Baumhoer D, Terracciano L, et al. Systematic assessment of the prognostic impact of membranous CD44v6 protein expression in colorectal cancer. Histopathology. 2009;55(5):564-75.
319. Dawson H, Koelzer VH, Karamitopoulou E, Economou M, Hammer C, Muller DE, et al. The apoptotic and proliferation rate of tumour budding cells in colorectal cancer outlines a heterogeneous population of cells with various impacts on clinical outcome. Histopathology. 2014;64(4):577-84.
320. Moreno-Bueno G, Portillo F, Cano A. Transcriptional regulation of cell polarity in EMT and cancer. Oncogene. 0000;27(55):6958-69.
321. Wodarz A, Nathke I. Cell polarity in development and cancer. Nature cell biology. 2007;9(9):1016-24.
322. Guzinska-Ustymowicz K. MMP-9 and cathepsin B expression in tumor budding as an indicator of a more aggressive phenotype of colorectal cancer (CRC). Anticancer Res. 2006;26(2b):1589-94.
323. Shinto E, Baker K, Tsuda H, Mochizuki H, Ueno H, Matsubara O, et al. Tumor buds show reduced expression of laminin-5 gamma 2 chain in DNA mismatch repair deficient colorectal cancer. Dis Colon Rectum. 2006;49(8):1193-202.
324. Hostettler l, Zlobec I, Terracciano L, Lugli A. ABCG5-positivity in tumor buds is an indicator of poor prognosis in node-negative colorectal cancer patients. World Journal of Gastroenterology : WJG. 2010;16(6):732-9.
325. Hamilton PW, Allen DC, Watt PC, Patterson CC, Biggart JD. Classification of normal colorectal mucosa and adenocarcinoma by morphometry. Histopathology. 1987;11(9):901-11.
326. Deans GT, Hamilton PW, Watt PC, Heatley M, Williamson K, Patterson CC, et al. Morphometric analysis of colorectal cancer. Dis Colon Rectum. 1993;36(5):450-6.
327. Nakashima Y, Yao T, Hirahashi M, Aishima S, Kakeji Y, Maehara Y, et al. Nuclear atypia grading score is a useful prognostic factor in papillary gastric adenocarcinoma. Histopathology. 2011;59(5):841-9.
328. Zlobec I, Lugli A. Epithelial mesenchymal transition and tumor budding in aggressive colorectal cancer: tumor budding as oncotarget. Oncotarget. 2010;1(7):651-61.
329. Kim MA, Lee HS, Yang H-K, Kim WH. Cytokeratin expression profile in gastric carcinomas. Human Pathology.35(5):576-81.
330. Garcia-Solano J, Conesa-Zamora P, Trujillo-Santos J, Torres-Moreno D, Makinen MJ, Perez-Guillermo M. Immunohistochemical expression profile of beta-catenin, E-cadherin, P-cadherin, laminin-5gamma2 chain, and SMAD4 in colorectal serrated adenocarcinoma. Hum Pathol. 2012;43(7):1094-102.
331. Kevans D, Wang LM, Sheahan K, Hyland J, O'Donoghue D, Mulcahy H, et al. Epithelial-mesenchymal transition (EMT) protein expression in a cohort of stage II colorectal cancer patients with characterized tumor budding and mismatch repair protein status. Int J Surg Pathol. 2011;19(6):751-60.
332. Harbaum L, Pollheimer MJ, Kornprat P, Lindtner RA, Schlemmer A, Rehak P, et al. Keratin 7 expression in colorectal cancer--freak of nature or significant finding? Histopathology. 2011;59(2):225-34.

333. Gurzu S, Jung I. Aberrant pattern of the cytokeratin 7/cytokeratin 20 immunophenotype in colorectal adenocarcinomas with BRAF mutations. Pathol Res Pract. 2012;208(3):163-6.
334. Ngan CY, Yamamoto H, Seshimo I, Tsujino T, Man-i M, Ikeda JI, et al. Quantitative evaluation of vimentin expression in tumour stroma of colorectal cancer. Br J Cancer. 2007;96(6):986-92.
335. Lugli A, Iezzi G, Hostettler I, Muraro MG, Mele V, Tornillo L, et al. Prognostic impact of the expression of putative cancer stem cell markers CD133, CD166, CD44s, EpCAM, and ALDH1 in colorectal cancer. Br J Cancer. 2010;103(3):382-90.
336. Takahashi H, Ishii H, Nishida N, Takemasa I, Mizushima T, Ikeda M, et al. Significance of Lgr5(+ve) cancer stem cells in the colon and rectum. Ann Surg Oncol. 2011;18(4):1166-74.
337. Dotse E, Bian Y. Isolation of colorectal cancer stem-like cells. Cytotechnology. 2014.
338. Caie PD, Schuur K, Oniscu A, Mullen P, Reynolds PA, Harrison DJ. Human tissue in systems medicine. The FEBS journal. 2013;280(23):5949-56.
339. Edin S, Wikberg ML, Dahlin AM, Rutegard J, Oberg A, Oldenborg PA, et al. The distribution of macrophages with a M1 or M2 phenotype in relation to prognosis and the molecular characteristics of colorectal cancer. PLoS One. 2012;7(10):e47045.
340. Mei Z, Liu Y, Liu C, Cui A, Liang Z, Wang G, et al. Tumour-infiltrating inflammation and prognosis in colorectal cancer: systematic review and meta-analysis. British journal of cancer. 2014;110(6):1595-605.
341. Angell H, Galon J. From the immune contexture to the Immunoscore: the role of prognostic and predictive immune markers in cancer. Current Opinion in Immunology. 2013;25(2):261-7.
342. Forrest R, Guthrie GJ, Orange C, Horgan PG, McMillan DC, Roxburgh CS. Comparison of visual and automated assessment of tumour inflammatory infiltrates in patients with colorectal cancer. European journal of cancer (Oxford, England : 1990). 2014;50(3):544-52.
343. Huijbers A, Tollenaar RA, v Pelt GW, Zeestraten EC, Dutton S, McConkey CC, et al. The proportion of tumor-stroma as a strong prognosticator for stage II and III colon cancer patients: validation in the VICTOR trial. Ann Oncol. 2013;24(1):179-85.
344. Mesker WE, Junggeburt JM, Szuhai K, de Heer P, Morreau H, Tanke HJ, et al. The carcinoma-stromal ratio of colon carcinoma is an independent factor for survival compared to lymph node status and tumor stage. Cell Oncol. 2007;29(5):387-98.
345. Park JH, Richards CH, McMillan DC, Horgan PG, Roxburgh CSD. The relationship between tumour stroma percentage, the tumour microenvironment and survival in patients with primary operable colorectal cancer. Annals of Oncology. 2014.
346. Buhmeida A, Ristamaki R, Lamlum H, Bendardaf R, Heikkila S, Collan Y, et al. Nuclear area is a prognostic determinant in advanced colorectal cancer. Anticancer Res. 2005;25(4):3083-8.
347. Carducci MA, Piantadosi S, Pound CR, Epstein JI, Simons JW, Marshall FF, et al. Nuclear morphometry adds significant prognostic information to stage and grade for renal cell carcinoma. Urology. 1999;53(1):44-9.
348. Katsoulis M, Lekka J, Vlachonikolis I, Delides GS. The prognostic value of morphometry in advanced epithelial ovarian cancers. Br J Cancer. 1995;72(4):958-63.

349. Fukuzawa S, Hashimura T, Sasaki M, Yamabe H, Yoshida O. Nuclear morphometry for improved prediction of the prognosis of human bladder carcinoma. Cancer. 1995;76(10):1790-6.
350. Nakagawa H, Liyanarachchi S, Davuluri RV, Auer H, Martin EW, Jr., de la Chapelle A, et al. Role of cancer-associated stromal fibroblasts in metastatic colon cancer to the liver and their expression profiles. Oncogene. 2004;23(44):7366-77.
351. Galon J, Costes A, Sanchez-Cabo F, Kirilovsky A, Mlecnik B, Lagorce-Pages C, et al. Type, density, and location of immune cells within human colorectal tumors predict clinical outcome. Science (New York, NY). 2006;313(5795):1960-4.
352. Ljosa V, Caie PD, Ter Horst R, Sokolnicki KL, Jenkins EL, Daya S, et al. Comparison of Methods for Image-Based Profiling of Cellular Morphological Responses to Small-Molecule Treatment. J Biomol Screen. 2013.
353. Ali HR, Irwin M, Morris L, Dawson SJ, Blows FM, Provenzano E, et al. Astronomical algorithms for automated analysis of tissue protein expression in breast cancer. Br J Cancer. 2013;108(3):602-12.
354. Betge J, Kornprat P, Pollheimer MJ, Lindtner RA, Schlemmer A, Rehak P, et al. Tumor budding is an independent predictor of outcome in AJCC/UICC stage II colorectal cancer. Ann Surg Oncol. 2012;19(12):3706-12.
355. Ueno H, Mochizuki H, Hashiguchi Y, Ishiguro M, Kajiwara Y, Sato T, et al. Histological grading of colorectal cancer: a simple and objective method. Ann Surg. 2008;247(5):811-8.
356. Costa J. Systems pathology: a critical review. Molecular oncology. 2012;6(1):27-32.
357. Werner HM, Mills GB, Ram PT. Cancer Systems Biology: a peek into the future of patient care? Nature reviews Clinical oncology. 2014;11(3):167-76.
358. Gu J, Taylor CR. Practicing Pathology in the Era of Big Data and Personalized Medicine. Applied Immunohistochemistry & Molecular Morphology. 2014;22(1):1-9.
359. Raghupathi W, Raghupathi V. Big data analytics in healthcare: promise and potential. Health Information Science and Systems. 2014;2(1):3.
360. Reimers MS, Kuppen PJK, Lee M, Lopatin M, Tezcan H, Putter H, et al. Validation of the 12-Gene Colon Cancer Recurrence Score as a Predictor of Recurrence Risk in Stage II and III Rectal Cancer Patients. Journal of the National Cancer Institute. 2014;106(11).
361. Almendro V, Kim HJ, Cheng Y-K, Gönen M, Itzkovitz S, Argani P, et al. Genetic and Phenotypic Diversity in Breast Tumor Metastases. Cancer Research. 2014;74(5):1338-48.
362. Li J, Shi M, Ma Z, Zhao S, Euskirchen G, Ziskin J, et al. Integrated systems analysis reveals a molecular network underlying autism spectrum disorders. Molecular Systems Biology. 2014;10(12):n/a-n/a.
363. Chen R, Mias George I, Li-Pook-Than J, Jiang L, Lam Hugo YK, Chen R, et al. Personal Omics Profiling Reveals Dynamic Molecular and Medical Phenotypes. Cell. 2012;148(6):1293-307.
364. Canuel V, Rance B, Avillach P, Degoulet P, Burgun A. Translational research platforms integrating clinical and omics data: a review of publicly available solutions. Briefings in Bioinformatics. 2014.
365. Choi IY, Kim TM, Kim MS, Mun SK, Chung YJ. Perspectives on clinical informatics: integrating large-scale clinical, genomic, and health information for clinical care. Genomics & informatics. 2013;11(4):186-90.

366. Saidi O, Cordon-Cardo C, Costa J. Technology insight: will systems pathology replace the pathologist? Nature clinical practice Urology. 2007;4(1):39-45.
367. Gomez-Cabrero D, Abugessaisa I, Maier D, Teschendorff A, Merkenschlager M, Gisel A, et al. Data integration in the era of omics: current and future challenges. BMC systems biology. 2014;8 Suppl 2:I1.
368. Jass JR, Atkin WS, Cuzick J, Bussey HJ, Morson BC, Northover JM, et al. The grading of rectal cancer: historical perspectives and a multivariate analysis of 447 cases. Histopathology. 1986;10(5):437-59.
369. Ratto C, Sofo L, Ippoliti M, Merico M, Doglietto GB, Crucitti F. Prognostic factors in colorectal cancer. Literature review for clinical application. Dis Colon Rectum. 1998;41(8):1033-49.
370. Washington MK, Berlin J, Branton P, Burgart LJ, Carter DK, Fitzgibbons PL, et al. Protocol for the Examination of Specimens From Patients With Primary Carcinoma of the Colon and Rectum. Archives of Pathology & Laboratory Medicine. 2009;133(10):1539-51.

Chapter 9: Appendices

Appendix A. Royal College of Pathologists (RCPath) clinical data items

RCPath Core data items:

Macroscopic core data items:

- Site of tumour.
- Maximum tumour diameter.
- Distance to the nearer longitudinal resection margin.
- Tumour perforation.
- Relation of the tumour to the peritoneal reflection (rectal tumours only).
- Grade of the plane(s) of surgical excision (AR and APE specimens).
- Distance of the tumour from the dentate line (for APE specimens only).

Microscopic core data items:

- Histological tumour type.
- Histological differentiation.
- Maximum extent of local invasion (pT stage) and maximum distance of extramural
- spread.
- Grade of tumour regression following pre-operative (neoadjuvant) therapy.
- Resection margins (longitudinal and circumferential margins).
- Lymph node status (number present, number involved, highest lymph node status).
- Venous invasion.
- Histologically confirmed distant metastatic disease.

RCPath non-core data items:

- Nature of advancing margin (infiltrative versus expansive).
- Tumour budding.
- Lymphatic invasion.
- Extramural tumour nodules less than 3 mm in diameter.
- Perineural infiltration

Appendix 1 Brightfield vessel detect algorithm settings

series_name	Parameter	Value
Setting 1	Action	General Settings
Setting 2	Magnification	20
Setting 3	µm/pixel	0.43
Setting 4	Stain Combination	IHC Brown chromogen (e.g. DAB)
Setting 5	IHC Marker	Cytoplasm
Setting 6	ROI Subset Export	TRUE
Setting 7	Stitch Tiles	FALSE
Setting 8	Analyze % of tissue	100
Setting 9	Action	Manual ROI Selection (Select Segments)
Setting 10	Resolution (x)	0.88
Setting 20	Magnification	10
Setting 30	Action	Vessel Detection
Setting 31	IHC Threshold	0.14
Setting 32	Gap to close (µm)	4
Setting 37	Action	Vessel Classification
Setting 38	IHC Threshold	0.14
Setting 39	Select Feature	Area (µm²)
Setting 40	Threshold Small/Medium	100
Setting 41	Threshold Medium/Large	300
Setting 53	Action	Custom Export
Setting 54	Class	Vessel
Setting 55	Per Single Objects	FALSE
Setting 56	Per Single Objects	FALSE
Setting 57	Standard Deviaion	TRUE
Setting 58	Minimum	FALSE
Setting 59	Maximum	FALSE
Setting 60	Sum	FALSE
Setting 61	Number	TRUE

Appendix 2. Brightfield vessel detect algorithm export parameters

Histological Score Nuclei
All Nucleus
Nucleus Small
Nucleus Medium
Nucleus Large
% Nucleus Small
% Nucleus Medium
% Nucleus Large
Vessel density (1/mm²)
Vessel with lumen density (1/mm²)
Vessel
Vessel with Lumen
Average vessel size (µm²)
Average vessel with lumen size (µm²)
Average Vessel Wall thickness (µm)
% Vessel Small
% Vessel Medium
% Vessel Large
# Vessel Small
# Vessel Medium
# Vessel Large
% Vessel with Lumen Small
% Vessel with Lumen Medium
% Vessel with Lumen Large
# Vessel with Lumen Small
# Vessel with Lumen Medium
# Vessel with Lumen Large

Appendix 3. Brightfield vessel detect and host cell exclusion algorithm settings

Parameter	Value
Action	General Settings
Magnification	20
µm/pixel	0.43
Stain Combination	IHC Brown chromogen (e.g. DAB)
IHC Marker	Cytoplasm
ROI Subset Export	TRUE
Stitch Tiles	FALSE
Analyze % of tissue	100
Action	Manual ROI Selection (Select

	Segments)
Resolution (x)	0.88
Action	Initialize Cellular Analysis
Analyze ROI 1	TRUE
Analyze ROI 2	FALSE
Analyze ROI 3	FALSE
Analyze ROI 4	FALSE
Analyze ROI 5	FALSE
Analyze ROI 6	FALSE
Analyze ROI 7	FALSE
Analyze ROI 8	FALSE
Magnification	10
Action	Nucleus Detection
Hematoxylin Threshold	0.03
Typical Nucleus Size (µm²)	55
Action	Nucleus Morphology and Filter
Use Exclusion	TRUE
Condition 1	Length/Width >= 3
Condition 2	Hematoxylin Intensity <= 0.0001
Condition 2	Area < 50
Remove Excluded Nuclei	TRUE
Action	Vessel Detection
IHC Threshold	0.14
Gap to close (µm)	8
Action	Nucleus Classification
Select Feature	Area (µm²)
Threshold Small/Medium (µm²)	60
Threshold Medium/Large (µm²)	110
Action	Vessel Classification
IHC Threshold	0.14
Select Feature	Area (µm²)
Threshold Small/Medium	100
Threshold Medium/Large	300
Threshold Small/Medium	TRUE
Condition 1	Hematoxylin Intensity >= 0.2
Condition 2	Circularity < 0.1
Remove excluded vessels	FALSE
Action	Default Export
ROI: Screenshot 1	Overlay
ROI: Screenshot 2	Overlay with Outlines
ROI Statistics	TRUE
Cellular Analysis: Screenshot 1	Original
Cellular Analysis: Screenshot 2	Overlay with Outlines
Cellular Analysis Statistics	TRUE

Action	Custom Export
Class	Vessel
Per Single Objects	FALSE
Per Single Objects	FALSE
Standard Deviaion	TRUE
Minimum	FALSE
Maximum	FALSE
Sum	FALSE
Number	TRUE

Appendix 4. ROI Tissue Segmentation algorithm settings.

Parameter	Value
Portal	IF Tissue
Action	General Settings
Magnification	20
µm/pixel	0.47
Bit depth	12 bit
Layer 1	CK
Layer 2	D240
Layer 3	DAPI
Production Mode	FALSE
Action	Tissue - Background Separation
Select Image Layers	CK, D240, DAPI,
Use Autothresholds	FALSE
Homogeneity Threshold	0
Brightness Threshold	0
Tissue Min Size (1000 µm²)	0
Action	Composer: Initialization
Magnification	10
Action	Composer: Training
Use Layers	CK, D240, DAPI,
Action	Composer: Reclassify Region
Source Class	Tumour
Target Class	Stroma
Use Condition	TRUE
Condition 1	Area < 5000
Action	Composer: Reclassify Region
Source Class	Stroma
Source Class	Necrosis
Use Condition	TRUE

Condition 1	Mean Layer 1 >= 7.7
Condition 2	Roundness <= 1
Interrupt on Server	FALSE

Appendix 5. IF Vessel Detect algorithm settings

Parameter	Value
Action	Initialize Cellular Analysis
Analyze Tumour	TRUE
Analyze ROI 2	FALSE
Analyze Necrosis	FALSE
Analyze ROI 4	FALSE
Analyze Stroma	TRUE
Analyze ROI 6	FALSE
Analyze ROI 7	FALSE
Analyze ROI 8	FALSE
Magnification	20
Action	Nucleus Detection
Nuclues Layer	DAPI
Membrane Mask	
Nucleus Region	0.4
Typical Nucleus Size (µm²)	47
Export a Screenshot	TRUE
Action	Nucleus Morphology and Filter
Use Exclusion	TRUE
Condition 1	Mean PanCK < 50
Condition 2	Area < 5
Remove Excluded Nuclei	TRUE
Action	Vessel Detection
Image Layer	D240
Stain Threshold	6
Gap to close (µm)	4
Export a Screenshot	TRUE
Action	Nucleus Classification
Select Feature	Marker Intensity
in Channel	D240
Threshold None/Low	18
Threshold Low/Medium	18
Threshold Medium/High	18
Export a Screenshot	FALSE
Action	Vessel Classification
Select Feature	Area (µm²)

Image Layer	Layer 4	
Threshold Small/Medium		50
Threshold Medium/Large		300
Threshold Small/Medium	FALSE	
Action	Default Export	
Export a Screenshot	TRUE	
ROI Statistics	TRUE	
Cellular Analysis Statistics	TRUE	
Action	Custom Export	
Class	Nucleus Positive	
Per Single Objects	TRUE	
Per Single Objects	FALSE	
Standard Deviaion	FALSE	
Minimum	FALSE	
Maximum	FALSE	
Sum	FALSE	
Number	FALSE	

Appendix 6. IF Marker Area algorithm settings

Action	Initialize Cellular Analysis	
Analyze ROI 1	FALSE	
Analyze ROI 2	FALSE	
Analyze ROI 3	FALSE	
Analyze ROI 4	FALSE	
Analyze Stroma	TRUE	
Analyze ROI 6	FALSE	
Analyze ROI 7	FALSE	
Analyze ROI 8	FALSE	
Magnification		20
Action	Marker Area Detection	
Marker 1	PanCk	
Threshold		35
Marker 2	D240	
Threshold		30
Marker 3		
Minimum Area (µm²)		11
Export a Screenshot	FALSE	
Action	Default Export	
Export a Screenshot	TRUE	
ROI Statistics	TRUE	
Cellular Analysis Statistics	TRUE	

Action	Custom Export
Class	Marker 2
Per Single Objects	TRUE
Per Single Objects	FALSE
Standard Deviaion	FALSE
Minimum	FALSE
Maximum	FALSE
Sum	FALSE
Number	FALSE
Action	Custom Export
Class	Markers 1 and 2
Per Single Objects	TRUE
Per Single Objects	FALSE
Standard Deviaion	FALSE
Minimum	FALSE
Maximum	FALSE
Sum	FALSE
Number	FALSE

Appendix 7. IF TMA ROI Tissue segmentation algorithm settings

Parameter	Value
Action	General Settings
Magnification	20
µm/pixel	0.47
Bit depth	12 bit
Layer 1	CK
Layer 2	D240
Layer 3	DAPI
Production Mode	FALSE
Action	Tissue - Background Separation
Select Image Layers	CK, D240, DAPI,
Use Autothresholds	FALSE
Homogeneity Threshold	0
Brightness Threshold	0
Tissue Min Size (1000 µm²)	0
Action	Composer: Initialization
Magnification	10
Action	Composer: Training
Use Layers	CK, D240, DAPI,
Action	Composer: Create Region

Select Class	Tumour
Select Distance (µm)	2
Simple Region Grow	TRUE
Action	Composer: Reclassify Region
Source Class	Tumour
Target Class	Stroma
Use Condition	TRUE
Condition 1	Area < 5000
Action	Composer: Reclassify Region
Source Class	no tissue
Target Class	stroma
Use Condition	TRUE
Condition 1	Circularity > 0.7
Condition 2	Rel. Border to Image Border = 0
Interrupt on Server	FALSE

Appendix 8. Brightfield Tumour Bud Algorithm settings

Parameter	Value
Portal	BF Tissue
Action	General Settings
Magnification	10
µm/pixel	0.6
Stain Combination	IHC Brown chromogen (e.g. DAB)
IHC Marker	Cytoplasm
Production Mode	FALSE
Action	Tissue - Background Separation
Use Autothresholds	TRUE
Tissue Min Size (1000 µm²)	0
Action	Composer: Initialization
Magnification	2
Action	Composer: Training
Action	Composer: Reclassify Region
Source Class	Tumour
Target Class	Stroma
Use Condition	TRUE
Condition 1	Area < 5000
Action	ROI Correction
Interrupt on Server	FALSE
Store ROI classification	FALSE

Action	Initialize Cellular Analysis
Analyze ROI 1	FALSE
Analyze ROI 2	FALSE
Analyze ROI 3	FALSE
Analyze Lumen	TRUE
Analyze ROI 5	FALSE
Analyze Stroma	TRUE
Analyze Tumour	TRUE
Analyze ROI 8	FALSE
Magnification	10
Action	Nucleus Detection
Hematoxylin Threshold	0.1
Typical Nucleus Size (µm²)	56.65982157
Action	Marker Area Detection
Threshold Marker	0.76
Minimum Area (µm²)	8
Action	Marker Area Classification
Select Feature	IHC Marker Intensity
Threshold Low/Medium	0.6
Threshold Medium/High	1
Use Condition	FALSE
Remove Excluded Areas	FALSE
Action	Default Export
ROI: Screenshot 1	Original
ROI: Screenshot 2	Overlay with Outlines
ROI Statistics	TRUE
Cellular Analysis: Screenshot 1	Original
Cellular Analysis: Screenshot 2	Overlay with Outlines
Cellular Analysis Statistics	TRUE

Appendix 9. IHA algorithm settings (Developer LVI, LVD & TB)

optimisation of tumour bud and LVI

reset

delete map: on tumour bud map : delete map

delete map: on vessel map : delete map

delete map: on copy of main : delete map

delete map: on LVI colocalisation map : delete map

delete map: on ROI and bud map : delete map

copy map: copy map to 'tumour bud map'

copy map: copy map to 'vessel map'

remove all objects but marker one on tumour bud

on tumour bud map

delete image object level: delete 'NucleusLevel'

remove objects: loop: Marker 2 at MarkerLevel: remove objects into unclassified (merge by shape)

assign class: Markers 1 and 2 at MarkerLevel: Marker 1

merge region: Marker 1 at MarkerLevel: merge region

assign class: Marker 2 at MarkerLevel: unclassified

convert image objects: at MarkerLevel: convert image objects -> Connected 2D

merge region: unclassified at MarkerLevel: merge region

assign class: Marker 1 with Existence of super objects Tumour (1) = 1 at MarkerLevel: marker 1 in tumour

assign class: Marker 1 with Existence of super objects necrosis (1) = 1 at MarkerLevel: marker 1 in tumour

assign class: Marker 1 with Existence of super objects no tissue (1) = 1 at MarkerLevel: marker 1 in no tissue

copy image object level: at TissueLevel: copy creating 'CopyofTissueLevel' above

assign class: with Classified as no tissue = 0 at CopyofTissueLevel: _TempClass1

convert image objects: at CopyofTissueLevel: convert image objects -> Connected 2D

merge region: _TempClass1, Tumour at CopyofTissueLevel: merge region

distance map: at CopyofTissueLevel: distance to no tissue(distance map)

delete image object level: delete 'CopyofTissueLevel'

convert to sub-objects: at TissueLevel: convert to sub-objects

assign class: with Existence of sub objects Marker 1 (1) = 1 at TissueLevel: Marker 1

convert image objects: at TissueLevel: convert image objects -> Disconnected (fusion up)

convert image objects: at TissueLevel: convert image objects -> Connected 2D

update variable: Marker 1 at TissueLevel: distance to no tissue = Mean distance map

assign class: Marker 1 with distance to no tissue <= 50 at TissueLevel: edge effect

assign class: Marker 1 with Area <= 55 µm² at TissueLevel: necrotic debris

remove all objects but marker two on vessel map

on vessel map

delete image object level: delete 'NucleusLevel'

remove objects: loop: Marker 1 at MarkerLevel: remove objects into unclassified (merge by shape)

assign class: Markers 1 and 2 at MarkerLevel: Marker 2

pixel-based object resizing: loop: on vessel map Marker 2 at MarkerLevel: grow into unclassified where D240>=40

find enclosed by class: on vessel map at MarkerLevel: enclosed by Marker 2: Marker 2 +

merge region: on vessel map Marker 2 at MarkerLevel: merge region

assign class: Marker 1 at MarkerLevel: unclassified

convert image objects: at MarkerLevel: convert image objects -> Connected 2D

merge region: unclassified at MarkerLevel: merge region

assign class: Marker 2 with Existence of super objects Tumour (1) = 1 at MarkerLevel: marker 2 in tumour

assign class: Marker 2 with Existence of super objects necrosis (1) = 1 at MarkerLevel: marker 2 in tumour

assign class: Marker 2 with Existence of super objects no tissue (1) = 1 at MarkerLevel: marker 2 in no tissue

copy image object level: at TissueLevel: copy creating 'CopyofTissueLevel' above

assign class: with Classified as no tissue = 0 at CopyofTissueLevel: _TempClass2

convert image objects: at CopyofTissueLevel: convert image objects -> Connected 2D

merge region: _TempClass2, Tumour at CopyofTissueLevel: merge region

distance map: at CopyofTissueLevel: distance to no tissue(distance map)

delete image object level: delete 'CopyofTissueLevel'

convert to sub-objects: at TissueLevel: convert to sub-objects

assign class: with Existence of sub objects Marker 2 (1) = 1 at TissueLevel: Marker 2

convert image objects: at TissueLevel: convert image objects -> Disconnected (fusion up)

convert image objects: at TissueLevel: convert image objects -> Connected 2D

update variable: Marker 2 at TissueLevel: distance to no tissue = Mean distance map

assign class: Marker 2 with distance to no tissue <= 50 at TissueLevel: edge effect

assign class: on vessel map Marker 2 at TissueLevel: D240

evaluate tumour buds

fill holes in buds and evaluate nuclei in buds

pixel-based object resizing: on tumour bud map Marker 1 at TissueLevel: grow into Stroma

find enclosed by class: on tumour bud map at TissueLevel: enclosed by Marker 1: _TempClass1 +

grow region: on tumour bud map Marker 1 at TissueLevel: <- _TempClass1

merge region: on tumour bud map Marker 1 at TissueLevel: merge region

pixel-based object resizing: on tumour bud map Marker 1 at TissueLevel: shrink using Stroma

convert image objects: at TissueLevel: convert image objects -> Connected 2D

merge region: on tumour bud map Stroma at TissueLevel: merge region

copy image object level: on tumour bud map at TissueLevel: copy creating 'Nucleus level' below

synchronize map: on main at NucleusLevel: synchronize map 'tumour bud map'

assign class: on tumour bud map Nucleus with Area < 16 µm² at Nucleus level: Nucelar debris

assign class: on tumour bud map Nucleus with Standard deviation DAPI < 6 and Mean DAPI < 40 at Nucleus level: false nucleus

assign class: on tumour bud map Marker 1 with Mean CK <= 50 at TissueLevel: Non specific CK

assign class: on tumour bud map Marker 1 with Standard deviation CK <= 10 at TissueLevel: Non specific CK

assign class: on tumour bud map Marker 1 with Number of sub objects Nucleus (1) > 5 at TissueLevel: too big buds

assign class: on tumour bud map Marker 1 with Number of sub objects Nucelar debris (1) >= 1 and Existence of sub objects Nucleus (1) < 1 at TissueLevel: bud with debris nulceus

remove irrelevant marker 1 areas

assign class: on tumour bud map Marker 1 with Existence of sub objects Nucleus (1) < 1 at TissueLevel: irrelevant marker

remainder of marker 1 = tumour bud

on tumour bud map

assign class: Marker 1 at TissueLevel: tumour bud

create ROI and Tumour bud map and calculate distance to tumour

copy map: on tumour bud map : copy map to 'ROI and bud map'

on ROI and bud map

delete image object level: on ROI and bud map : delete 'Nucleus level'

copy image object level: at TissueLevel: copy creating 'vessel level' below

synchronize map: on vessel map at TissueLevel: synchronize map 'ROI and bud map'

delete layer: delete image layer 'distance map'

copy image object level: at TissueLevel: copy creating 'CopyofTissueLevel' above

assign class: with Classified as Tumour = 0 at CopyofTissueLevel: _TempClass1

convert image objects: at CopyofTissueLevel: convert image objects -> Connected 2D

merge region: _TempClass1 at CopyofTissueLevel: merge region

distance map: _TempClass1 at CopyofTissueLevel: distance to Tumour(distance map)

delete image object level: delete 'CopyofTissueLevel'

LVI and colocalisation

convert to sub-objects: at TissueLevel: convert to sub-objects

assign class: Stroma with Existence of sub objects D240 (1) = 1 at TissueLevel: D240

assign class: tumour bud with Existence of sub objects D240 (1) = 1 at TissueLevel: Markers 1 and 2

assign class: bud with debris nulceus, irrelevant marker, too big buds with Existence of sub objects D240 (1) = 1 at TissueLevel: non bud invasion

assign class: tumour bud with Existence of D240 (0) = 1 at TissueLevel: tumour bud border to marker 2

assign class: bud with debris nulceus, irrelevant marker, too big buds with Existence of D240 (0) = 1 at TissueLevel: tumour border to marker 2

assign class: D240 with Existence of Markers 1 and 2 (0) = 1 at TissueLevel: vessel border to bud invasion

convert image objects: at TissueLevel: convert image objects -> Disconnected (fusion up)

convert image objects: at TissueLevel: convert image objects -> Connected 2D

assign class: D240 with Existence of Tumour (0) = 1 at TissueLevel: vessel border to tumour mass

calculate bud distance to tumour

on ROI and bud map

update variable: on ROI and bud map bud with debris nulceus, D240, irrelevant marker, Markers 1 and 2, too big buds, tumour border to marker 2, tumour bud, tumour bud border to marker 2, vessel border to bud invasion at TissueLevel: distance to tumour = Mean distance map

update variable: D240 mean distance to tumour = 0

compute statistical value: on ROI and bud map D240 at TissueLevel: D240 mean distance to tumour = mean(distance to tumour)

update variable: M1&2 mean distance to tumour = 0

compute statistical value: on ROI and bud map Markers 1 and 2 at TissueLevel: M1&2 mean distance to tumour = mean(distance to tumour)

update variable: bud mean distance to tumour = 0

compute statistical value: on ROI and bud map tumour bud at TissueLevel: bud mean distance to tumour = mean(distance to tumour)

update variable: debris bud mean distance to tumour = 0

compute statistical value: on ROI and bud map bud with debris nulceus at TissueLevel: debris bud mean distance to tumour = mean(distance to tumour)

update variable: irrelevant mean distance to tumour = 0

compute statistical value: on ROI and bud map irrelevant marker at TissueLevel: irrelevant mean distance to tumour = mean(distance to tumour)

update variable: big bud mean distance to tumour = 0

compute statistical value: on ROI and bud map too big buds at TissueLevel: big bud mean distance to tumour = mean(distance to tumour)

update variable: tumour border to D240 mean distance to tumour = 0

compute statistical value: on ROI and bud map tumour border to marker 2 at TissueLevel: tumour border to D240 mean distance to tumour = mean(distance to tumour)

update variable: vessel border to bud invasion mean distance to tumour = 0

compute statistical value: on ROI and bud map vessel border to bud invasion at TissueLevel: vessel border to bud invasion mean distance to tumour = mean(distance to tumour)

update variable: bud border to D240 mean distance to tumour = 0

compute statistical value: on ROI and bud map tumour bud border to marker 2 at TissueLevel: bud border to D240 mean distance to tumour = mean(distance to tumour)

statistical export of invasive eptihelial bodies

export object statistics: on ROI and bud map bud with debris nulceus, D240, irrelevant marker, Markers 1 and 2, tumour bud, tumour bud border to marker 2, vessel border to bud invasion at TissueLevel: export object statistics

export object statistics: on ROI and bud map vessel border to tumour mass at MarkerLevel: export object statistics

export object statistics: on tumour bud map bud with debris nulceus, irrelevant marker, too big buds, tumour bud at TissueLevel: export object statistics

export object statistics: on tumour bud map Nucleus with Existence of super objects tumour bud (1) = 1 at Nucleus level: export object statistics

export object statistics: on tumour bud map Nucleus with Existence of super objects tumour bud (1) = 0 and Existence of super objects Stroma (1) = 1 at Nucleus level: export object statistics

export object statistics: on tumour bud map Nucleus with Existence of super objects Tumour (1) = 1 at Nucleus level: export object statistics

calculate colocalisation stat

update variable: sum of area bud and vessel coloc = 0

compute statistical value: on ROI and bud map Markers 1 and 2 at TissueLevel: sum of area bud and vessel coloc = sum(Area)

update variable: sum of area non-bud and vessel coloc = 0

compute statistical value: on ROI and bud map non bud invasion at TissueLevel: sum of area non-bud and vessel coloc = sum(Area)

update variable: number of marker 1 and 2 = 0

compute statistical value: on ROI and bud map Markers 1 and 2 at TissueLevel: number of marker 1 and 2 = number

update variable: number of non bud invasion = 0

compute statistical value: on ROI and bud map non bud invasion at TissueLevel: number of non bud invasion = number

calculate tumour bud stat

update variable: number of buds = 0

compute statistical value: on tumour bud map tumour bud at TissueLevel: number of buds = number

update variable: no. of big buds = 0

compute statistical value: on tumour bud map too big buds at TissueLevel: no. of big buds = number

update variable: bud with <=2 nuc = 0

compute statistical value: on tumour bud map tumour bud with Number of sub objects Nucleus (1) <= 2 at TissueLevel: bud with <=2 nuc = number

update variable: bud with >=3 nuc = 0

compute statistical value: on tumour bud map tumour bud with Number of sub objects Nucleus (1) >= 3 at TissueLevel: bud with >=3 nuc = number

update variable: sum area of buds = 0

calculate vessel stat

update variable: number of vessels = 0

compute statistical value: on vessel map D240 with Existence of Stroma (0) = 1 at TissueLevel: number of vessels = number

update variable: sum area of vessels = 0

compute statistical value: on vessel map D240 at TissueLevel: sum area of vessels = sum(Area)

update variable: on vessel map D240 at TissueLevel: Individual vessel area = Area

export project statistics: on ROI and bud map : export project statistics

export project statistics: on tumour bud map : export project statistics

calculate LVD and export vessel stats

export project statistics: on vessel map : export project statistics

export object statistics: on vessel map D240 at TissueLevel: export object statistics

Appendix 10. Nuclear morphometric export parameters

tumour subpopulation parameter
nuc in bud_asymmetry
nuc in bud_border index
nuc in bud_meanCK
nuc in bud_meanDAPI
nuc in bud_mean_Area
nuc in bud_mean_Ellipticity
nuc in bud_mean_Ratio_CK
nuc in bud_mean_Ratio_DAPI
nuc in bud_mean_Roundness
nuc in bud_mean_Shape index
nuc in bud_mean_borderlength
nuc in bud_mean_circularity
nuc in bud_mean_compactness
nuc in bud_mean_density
nuc in bud_mean_length
nuc in bud_mean_lengthwidth
nuc in bud_mean_perimeter
nuc in bud_mean_stdev_CK

nuc in bud_mean_stdev_DAPI
nuc in bud_mean_width
nuc in tumour_asymmetry
nuc in tumour_border index
nuc in tumour_meanCK
nuc in tumour_meanD240
nuc in tumour_meanDAPI
nuc in tumour_mean_Area
nuc in tumour_mean_Elliptic fit
nuc in tumour_mean_Ellipticity

nuc in tumour_mean_Ratio_CK
nuc in tumour_mean_Ratio_DAPI
nuc in tumour_mean_Roundness
nuc in tumour_mean_Shape index
nuc in tumour_mean_borderlength
nuc in tumour_mean_circularity
nuc in tumour_mean_compactness
nuc in tumour_mean_density
nuc in tumour_mean_length
nuc in tumour_mean_lengthwidth
nuc in tumour_mean_perimeter
nuc in tumour_mean_stdev_CK
nuc in tumour_mean_stdev_DAPI
nuc in tumour_mean_width
Average CK Intensity (Tumour Area) (mean)
Layer mean of CK tumour bud (mean)
Layer mean of CK Large tumour buds (mean)

Appendix 11. TMA Tumour subpopulation algorithm settings

Part 1: Tissue Studio cell simulation and segmentation

Parameter	Value
Portal	IF Tissue
Image Type	FOV
panCK	G:\TB TMA protein\TBA_B-Cat\grayscale\CY3_00002.tif
B-Cat	G:\TB TMA protein\TBA_B-Cat\grayscale\CY5_00002.tif
DAPI	G:\TB TMA protein\TBA_B-Cat\grayscale\DAPI_00002.tif

Layer 4	G:\TB TMA protein\TBA_B-Cat\grayscale\CY3_00002.tif	
Layer 5	G:\TB TMA protein\TBA_B-Cat\grayscale\CY5_00002.tif	
Layer 6	G:\TB TMA protein\TBA_B-Cat\grayscale\DAPI_00002.tif	
Layer 7	G:\TB TMA protein\TBA_B-Cat\grayscale\CY3_00002.tif	
Layer 8	G:\TB TMA protein\TBA_B-Cat\grayscale\CY5_00002.tif	
Layer 9	G:\TB TMA protein\TBA_B-Cat\grayscale\DAPI_00002.tif	
Layer 10	G:\TB TMA protein\TBA_B-Cat\grayscale\CY3_00002.tif	
Layer 11	G:\TB TMA protein\TBA_B-Cat\grayscale\CY5_00002.tif	
Layer 12	G:\TB TMA protein\TBA_B-Cat\grayscale\DAPI_00002.tif	
Action	General Settings	
Magnification		10
µm/pixel		0.6
Bit depth	10 bit	
Layer 1	panCK	
Layer 2	B-Cat	
Layer 3	DAPI	
Layer 4	Layer 4	
Layer 5	Layer 5	
Layer 6	Layer 6	
Layer 7	Layer 7	
Layer 8	Layer 8	
Layer 9	Layer 9	
Layer 10	Layer 10	
Layer 11	Layer 11	
Layer 12	Layer 12	
Production Mode	FALSE	
Action	Tissue - Background Separation	
Select Image Layers	panCK, B-Cat, DAPI,	
Use Autothresholds	FALSE	
Homogeneity Threshold		0
Brightness Threshold		0
Tissue Min Size (1000 µm²)		0
Action	Composer: Initialization	
Magnification		5
Action	Composer: Training	
Use Layers	panCK, B-Cat, DAPI,	

Action	Composer: Create Region	
Select Class	Tumour	
Select Distance (µm)		2
Simple Region Grow	TRUE	
Action	Composer: Reclassify Region	
Source Class	Tumour	
Target Class	Stroma	
Use Condition	TRUE	
Condition 1	Area < 3500	
Action	ROI Correction	
Interrupt on Server	FALSE	
Store ROI classification	TRUE	
Action	Initialize Cellular Analysis	
Analyze ROI 1	FALSE	
Analyze ROI 2	FALSE	
Analyze ROI 3	FALSE	
Analyze Necrosis	TRUE	
Analyze no tissue	TRUE	
Analyze Stroma	TRUE	
Analyze Tumour	TRUE	
Analyze ROI 8	FALSE	
Magnification		10
Action	Nucleus Detection	
Nucleus Layer	DAPI	
Membrane Mask		
Nucleus Region		0.22
Typical Nucleus Size (µm²)		60
Export a Screenshot	TRUE	
Action	Cell Simulation	
Simulation Mode	Simulate inside cytoplasmic stain	
Select Cytoplasm Layer	panCK,	
Marker Threshold		44.87
Typical Cell Size (µm²)		132
Export a Screenshot	TRUE	
Action	Cell Classification	
Select Feature	Marker Intensity	
in Channel	panCK	
Measurement in	Cytoplasm	
Threshold None/Low		62.8
Threshold Low/Medium		89.7
Threshold Medium/High		116.7
Use Condition	FALSE	
Remove Excluded Cells	FALSE	

Export a Screenshot		TRUE
Action	Default Export	
Export a Screenshot		FALSE
ROI Statistics		TRUE
Cellular Analysis Statistics		TRUE

Part 2. Developer XD tumour subpopulation creation and biomarker quantification.

Process: Main:

Creation of CK subpopulations

reset

delete map: on subpopulation map : delete map

delete map: on false cell map : delete map

copy map: copy map to 'subpopulation map'

copy map: copy map to 'false cell map'

negate stromal cells from buds

grow cytoplam into CK areas

delete image object level: on false cell map : delete 'CellLevel'

pixel-based object resizing: loop: on false cell map Cytoplasm at NucleusLevel: grow into unclassified where CK>=35

clean up false CK positive cells

assign class: Nucleus with Rel. border to Cytoplasm <= 0.3 and Existence of super objects Stroma (1) = 1 at NucleusLevel: Negative Nucleus

assign class: Nucleus with Mean CK <= 16 and Existence of super objects Stroma (1) = 1 at NucleusLevel: Negative Nucleus

assign class: Nucleus with Existence of super objects Stroma (2) = 1 and Area <= 60 µm² at NucleusLevel: tempclass02

assign class: tempclass02 with Mean CK <= 40 at NucleusLevel: tempclass4

assign class: tempclass4 with Rel. border to Cytoplasm >= 0.4 at NucleusLevel: Nucleus

assign class: tempclass02 with Rel. border to Cytoplasm >= 0.45 at NucleusLevel: Nucleus

assign class: tempclass02 at NucleusLevel: Negative Nucleus

assign class: tempclass4 at NucleusLevel: Negative Nucleus

merge maps together for correct cell segmentation

delete image object level: delete 'NucleusLevel'

copy image object level: at CellLevel: copy creating 'NucleusLevel' below

synchronize map: on false cell map at NucleusLevel: synchronize map 'subpopulation map'

assign class: Cell Stained Subclasses (excl. Negative) with Existence of sub objects Negative Nucleus (1) = 1 and Existence of sub objects Nucleus (1) = 0 at CellLevel: Cell Negative

grow cells into CK areas

pixel-based object resizing: loop: on subpopulation map Cell Stained Subclasses (excl. Negative) at CellLevel: grow into all where CK>=35

find enclosed by class: loop: unclassified at CellLevel: enclosed by Cell High: Temp class01 +

grow region: loop: Cell High at CellLevel: <- Temp class01

find enclosed by class: loop: on subpopulation map unclassified at CellLevel: enclosed by Cell Medium: Temp class01 +

grow region: loop: Cell Medium at CellLevel: <- Temp class01

find enclosed by class: loop: on subpopulation map unclassified at CellLevel: enclosed by Cell Low: Temp class01 +

grow region: loop: Cell Low at CellLevel: <- Temp class01

find enclosed by class: loop: on subpopulation map unclassified at CellLevel: enclosed by Cell Negative: Temp class01 +

grow region: loop: Cell Negative at CellLevel: <- Temp class01

clean up false nuclei

assign class: on subpopulation map Nucleus with Area <= 14 µm² at NucleusLevel: debris nucleus

assign class: Nucleus with Mean Layer 3 <= 40 and Standard deviation Layer 3 <= 6 at NucleusLevel: false nucleus

\\ Merge panCk positive cells to create subpopulations in stroma and in tumour depending on low, medium and high CK intensity

merge subpopulations

merge stromal subpopulations

copy image object level: at CellLevel: copy creating 'subpop level' above

merge region: Cell Stained Subclasses (excl. Negative) with Existence of super objects Stroma (1) = 1 at subpop level: merge region

assign regions on subpopulation map

assign class: Cell Stained Subclasses (excl. Negative) with Number of sub objects Cell (1) <= 5 and Existence of super objects Stroma (1) = 1 at subpop level: tumour bud

assign class: Cell Stained Subclasses (excl. Negative) with Number of sub objects Cell (1) >= 6 at subpop level: BigTumour bud

merge tumour subpopulations

merge region: Cell High with Existence of super objects Tumour (1) = 1 at subpop level: merge region

merge region: Cell Low, Cell Negative with Existence of super objects Tumour (1) = 1 at subpop level: merge region

merge region: Cell Medium with Existence of super objects Tumour (1) = 1 at subpop level: merge region

assign class: Cell High with Existence of super objects Tumour (1) = 1 at subpop level: Tumour high CK

assign class: Cell Medium with Existence of super objects Tumour (1) = 1 at subpop level: Tumour medium CK

assign class: Cell Low, Cell Negative with Existence of super objects Tumour (1) = 1 at subpop level: Tumour low CK

Export results

export nuclear morphometry in subpops

export object statistics: Nucleus with Existence of super objects tumour bud (2) = 1 at NucleusLevel: export object statistics

export object statistics: Nucleus with Existence of super objects BigTumour bud (2) = 1 at NucleusLevel: export object statistics

export object statistics: Negative Nucleus with Existence of super objects Cell Negative (2) = 1 at NucleusLevel: export object statistics

export object statistics: Nucleus with Existence of super objects Tumour high CK (2) = 1 at NucleusLevel: export object statistics

export object statistics: Nucleus with Existence of super objects Tumour medium CK (2) = 1 at NucleusLevel: export object statistics

export object statistics: Cytoplasm with Existence of super objects Tumour low CK (2) = 1 at NucleusLevel: export object statistics

calculate mean nuclear stats in stroma

update variable: nuc in stroma_meanTarget = 0

compute statistical value: on subpopulation map Negative Nucleus with Existence of super objects Cell Negative (2) = 1 and Existence of super objects Stroma (3) = 0 at NucleusLevel: nuc in stroma_meanTarget = mean(Mean Layer 2)

update variable: Cyto in stroma_meanTarget = 0

compute statistical value: on subpopulation map Cytoplasm with Existence of super objects Cell Negative (2) = 1 and Existence of super objects Stroma (3) = 0 at NucleusLevel: Cyto in stroma_meanTarget = mean(Mean Layer 2)

update variable: nuc in stroma_meanCK = 0

compute statistical value: on subpopulation map Negative Nucleus with Existence of super objects Cell Negative (2) = 1 at NucleusLevel: nuc in stroma_meanCK = mean(Mean CK)

update variable: cyto in stroma_meanCK = 0

compute statistical value: on subpopulation map Cytoplasm with Existence of super objects Cell Negative (2) = 1 and Existence of super objects Stroma (3) = 1 at NucleusLevel: cyto in stroma_meanCK = mean(Mean CK)

update variable: nuc in stroma_meanDAPI = 0

compute statistical value: on subpopulation map Negative Nucleus with Existence of super objects Cell Negative (2) = 1 at NucleusLevel: nuc in stroma_meanDAPI = mean(Mean Layer 3)

update variable: nuc in stroma_mean_stdev_CK = 0

compute statistical value: on subpopulation map Negative Nucleus with Existence of super objects Cell Negative (2) = 1 at NucleusLevel: nuc in stroma_mean_stdev_CK = mean(Standard deviation CK)

update variable: nuc in stroma_mean_stdev_D240 = 0

compute statistical value: on subpopulation map Negative Nucleus, Nucleus with Existence of super objects Cell Negative (2) = 1 at NucleusLevel: nuc in stroma_mean_stdev_D240 = mean(Standard deviation Layer 2)

update variable: nuc in stroma_mean_stdev_DAPI = 0

compute statistical value: on subpopulation map Negative Nucleus with Existence of super objects Cell Negative (2) = 1 at NucleusLevel: nuc in stroma_mean_stdev_DAPI = mean(Standard deviation Layer 3)

update variable: nuc in stroma_mean_Ratio_CK = 0

compute statistical value: on subpopulation map Negative Nucleus with Existence of super objects Cell Negative (2) = 1 at NucleusLevel: nuc in stroma_mean_Ratio_CK = mean(Ratio CK)

update variable: nuc in stroma_mean_Ratio_D240 = 0

compute statistical value: on subpopulation map Negative Nucleus with Existence of super objects Cell Negative (2) = 1 at NucleusLevel: nuc in stroma_mean_Ratio_D240 = mean(Ratio Layer 2)

update variable: nuc in stroma_mean_Ratio_DAPI = 0

compute statistical value: on subpopulation map Negative Nucleus with Existence of super objects Cell Negative (2) = 1 at NucleusLevel: nuc in stroma_mean_Ratio_DAPI = mean(Ratio Layer 3)

update variable: nuc in stroma_mean_Area = 0

compute statistical value: on subpopulation map Negative Nucleus with Existence of super objects Cell Negative (2) = 1 at NucleusLevel: nuc in stroma_mean_Area = mean(Area)

update variable: nuc in stroma_mean_borderlength = 0

compute statistical value: on subpopulation map Negative Nucleus with Existence of super objects Cell Negative (2) = 1 at NucleusLevel: nuc in stroma_mean_borderlength = mean(Border length)

update variable: nuc in stroma_mean_length = 0

compute statistical value: on subpopulation map Negative Nucleus with Existence of super objects Cell Negative (2) = 1 at NucleusLevel: nuc in stroma_mean_length = mean(Length)

update variable: nuc in stroma_asymmetry = 0

compute statistical value: on subpopulation map Negative Nucleus with Existence of super objects Cell Negative (2) = 1 at NucleusLevel: nuc in stroma_asymmetry = mean(Asymmetry)

update variable: nuc in stroma_border index = 0

compute statistical value: on subpopulation map Negative Nucleus with Existence of super objects Cell Negative (2) = 1 at NucleusLevel: nuc in stroma_border index = mean(Border index)

update variable: nuc in stroma_mean_lengthwidth = 0

compute statistical value: on subpopulation map Negative Nucleus with Existence of super objects Cell Negative (2) = 1 at NucleusLevel: nuc in stroma_mean_lengthwidth = mean(Length\Width)

update variable: nuc in stroma_mean_perimeter = 0

compute statistical value: on Screenshot Negative Nucleus with Existence of super objects Cell Negative (2) = 1 at NucleusLevel: nuc in stroma_mean_perimeter = mean(Perimeter)

update variable: nuc in stroma_mean_width = 0

compute statistical value: on subpopulation map Negative Nucleus with Existence of super objects Cell Negative (2) = 1 at NucleusLevel: nuc in stroma_mean_width = mean(Width)

update variable: nuc in stroma_mean_circularity = 0

compute statistical value: on subpopulation map Negative Nucleus with Existence of super objects Cell Negative (2) = 1 at NucleusLevel: nuc in stroma_mean_circularity = mean(Circularity)

update variable: nuc in stroma_mean_compactness = 0

compute statistical value: on subpopulation map Negative Nucleus with Existence of super objects Cell Negative (2) = 1 at NucleusLevel: nuc in stroma_mean_compactness = mean(Compactness)

update variable: nuc in stroma_mean_density = 0

compute statistical value: on subpopulation map Negative Nucleus with Existence of super objects Cell Negative (2) = 1 at NucleusLevel: nuc in stroma_mean_density = mean(Density)

update variable: nuc in stroma_mean_Ellipticity = 0

compute statistical value: on subpopulation map Negative Nucleus with Existence of super objects Cell Negative (2) = 1 at NucleusLevel: nuc in stroma_mean_Ellipticity = mean(Ellipticity)

update variable: nuc in stroma_mean_Roundness = 0

compute statistical value: on subpopulation map Negative Nucleus with Existence of super objects Cell Negative (2) = 1 at NucleusLevel: nuc in stroma_mean_Roundness = mean(Roundness)

update variable: nuc in stroma_mean_Shape index = 0

compute statistical value: on subpopulation map Negative Nucleus with Existence of super objects Cell Negative (2) = 1 at NucleusLevel: nuc in stroma_mean_Shape index = mean(Shape index)

calculate mean intensities tum buds

update variable: nuc in tumourbud_meanTarget = 0

compute statistical value: on subpopulation map Nucleus with Existence of super objects tumour bud (2) = 1 at NucleusLevel: nuc in tumourbud_meanTarget = mean(Mean Layer 2)

update variable: Cyto in tumourbud_meanTarget = 0

compute statistical value: on subpopulation map Cytoplasm with Existence of super objects tumour bud (2) = 1 at NucleusLevel: Cyto in tumourbud_meanTarget = mean(Mean Layer 2)

update variable: nuc in tumourbud_meanCK = 0

compute statistical value: on subpopulation map Nucleus with Existence of super objects tumour bud (2) = 1 at NucleusLevel: nuc in tumourbud_meanCK = mean(Mean CK)

update variable: Cyto in tumourbud_meanCK = 0

compute statistical value: on subpopulation map Cytoplasm with Existence of super objects tumour bud (2) = 1 at NucleusLevel: Cyto in tumourbud_meanCK = mean(Mean CK)

update variable: Nuc in tumourbud_meanDAPI = 0

compute statistical value: on subpopulation map Nucleus with Existence of super objects tumour bud (2) = 1 at NucleusLevel: Nuc in tumourbud_meanDAPI = mean(Mean Layer 3)

calculate mean intensities large tum buds

update variable: nuc in BIGtumourbud_meanTarget = 0

compute statistical value: on subpopulation map Nucleus with Existence of super objects BigTumour bud (2) = 1 at NucleusLevel: nuc in BIGtumourbud_meanTarget = mean(Mean Layer 2)

update variable: Cyto in BIGtumourbud_meanTarget = 0

compute statistical value: on subpopulation map Cytoplasm with Existence of super objects BigTumour bud (2) = 1 at NucleusLevel: Cyto in BIGtumourbud_meanTarget = mean(Mean Layer 2)

update variable: nuc in BIGtumourbud_meanCK = 0

compute statistical value: on subpopulation map Nucleus with Existence of super objects BigTumour bud (2) = 1 at NucleusLevel: nuc in BIGtumourbud_meanCK = mean(Mean CK)

update variable: Cyto in BIGtumourbud_meanCK = 0

compute statistical value: on subpopulation map Cytoplasm with Existence of super objects BigTumour bud (2) = 1 at NucleusLevel: Cyto in BIGtumourbud_meanCK = mean(Mean CK)

update variable: nuc in BIGtumourbud_meanDAPI = 0

compute statistical value: on subpopulation map Nucleus with Existence of super objects BigTumour bud (2) = 1 at NucleusLevel: nuc in BIGtumourbud_meanDAPI = mean(Mean Layer 3)

calculate mean intensities tumour HIGH

update variable: nuc in TumHIGH_meanTarget = 0

compute statistical value: on subpopulation map Nucleus with Existence of super objects Tumour high CK (2) = 1 at NucleusLevel: nuc in TumHIGH_meanTarget = mean(Mean Layer 2)

update variable: Cyto in TumHIGH_meanTarget = 0

compute statistical value: on subpopulation map Cytoplasm with Existence of super objects Tumour high CK (2) = 1 at NucleusLevel: Cyto in TumHIGH_meanTarget = mean(Mean Layer 2)

update variable: nuc in TumHIGH_meanCK = 0

compute statistical value: on subpopulation map Nucleus with Existence of super objects Tumour high CK (2) = 1 at NucleusLevel: nuc in TumHIGH_meanCK = mean(Mean CK)

update variable: Cyto in TumHIGH_meanCK = 0

compute statistical value: on subpopulation map Cytoplasm with Existence of super objects Tumour high CK (2) = 1 at NucleusLevel: Cyto in TumHIGH_meanCK = mean(Mean CK)

update variable: nuc in TumHIGH_meanDAPI = 0

compute statistical value: on subpopulation map Nucleus with Existence of super objects Tumour high CK (2) = 1 at NucleusLevel: nuc in TumHIGH_meanDAPI = mean(Mean Layer 3)

calculate mean intensities tumour MED

update variable: nuc in TumMED_meanTarget = 0

compute statistical value: on subpopulation map Nucleus with Existence of super objects Tumour medium CK (2) = 1 at NucleusLevel: nuc in TumMED_meanTarget = mean(Mean Layer 2)

update variable: Cyto in TumMED_meanTarget = 0

compute statistical value: on subpopulation map Cytoplasm with Existence of super objects Tumour medium CK (2) = 1 at NucleusLevel: Cyto in TumMED_meanTarget = mean(Mean Layer 2)

update variable: nuc in TumMED_meanCK = 0

compute statistical value: on subpopulation map Nucleus with Existence of super objects Tumour medium CK (2) = 1 at NucleusLevel: nuc in TumMED_meanCK = mean(Mean CK)

update variable: Cyto in TumMED_meanCK = 0

compute statistical value: on subpopulation map Cytoplasm with Existence of super objects Tumour medium CK (2) = 1 at NucleusLevel: Cyto in TumMED_meanCK = mean(Mean CK)

update variable: nuc in TumMED_meanDAPI = 0

compute statistical value: on subpopulation map Nucleus with Existence of super objects Tumour medium CK (2) = 1 at NucleusLevel: nuc in TumMED_meanDAPI = mean(Mean Layer 3)

calculate mean intensities tumour LOW

update variable: nuc in TumLOW_meanTarget = 0

compute statistical value: on subpopulation map Nucleus with Existence of super objects Tumour low CK (2) = 1 at NucleusLevel: nuc in TumLOW_meanTarget = mean(Mean Layer 2)

update variable: Cyto in TumLOW_meanTarget = 0

compute statistical value: on subpopulation map Cytoplasm with Existence of super objects Tumour low CK (2) = 1 at NucleusLevel: Cyto in TumLOW_meanTarget = mean(Mean Layer 2)

update variable: nuc in TumLOW_meanCK = 0

compute statistical value: on subpopulation map Nucleus with Existence of super objects Tumour low CK (2) = 1 at NucleusLevel: nuc in TumLOW_meanCK = mean(Mean CK)

update variable: Cyto in TumLOW_meanCK = 0

compute statistical value: on subpopulation map Cytoplasm with Existence of super objects Tumour low CK (2) = 1 at NucleusLevel: Cyto in TumLOW_meanCK = mean(Mean CK)

update variable: nuc in TumLOW_meanDAPI = 0

compute statistical value: on subpopulation map Nucleus with Existence of super objects Tumour low CK (2) = 1 at NucleusLevel: nuc in TumLOW_meanDAPI = mean(Mean Layer 3)

export subpopulation stats

export object statistics: Cell Negative at subpop level: export object statistics

export object statistics: tumour bud at subpop level: export object statistics

export object statistics: BigTumour bud at subpop level: export object statistics

export object statistics: Tumour high CK at subpop level: export object statistics

export object statistics: Tumour medium CK at subpop level: export object statistics

export object statistics: Tumour low CK at subpop level: export object statistics

export cytoplasmic intensity in subpops

export object statistics: Cytoplasm with Existence of super objects tumour bud (2) = 1 at NucleusLevel: export object statistics

export object statistics: Cytoplasm with Existence of super objects BigTumour bud (2) = 1 at NucleusLevel: export object statistics

export object statistics: Cytoplasm with Existence of super objects Cell Negative (2) = 1 at NucleusLevel: export object statistics

export object statistics: Cytoplasm with Existence of super objects Tumour high CK (2) = 1 at NucleusLevel: export object statistics

export object statistics: Cytoplasm with Existence of super objects Tumour medium CK (2) = 1 at NucleusLevel: export object statistics

export nuclear intensity in subpops

export object statistics: Nucleus with Existence of super objects tumour bud (2) = 1 at NucleusLevel: export object statistics

export object statistics: Nucleus with Existence of super objects BigTumour bud (2) = 1 at NucleusLevel: export object statistics

export object statistics: Nucleus with Existence of super objects Cell Negative (2) = 1 at NucleusLevel: export object statistics

export object statistics: Nucleus with Existence of super objects Tumour high CK (2) = 1 at NucleusLevel: export object statistics

export object statistics: Nucleus with Existence of super objects Tumour medium CK (2) = 1 at NucleusLevel: export object statistics

export mean nuc stats

export project statistics: on subpopulation map : export project statistics

Appendix 12. Tissue Phenomics Aanalyser algorithm settings

optimisation of tumour bud and LVI

reset

delete map: on tumour bud map : delete map

delete map: on vessel map : delete map

delete map: on copy of main : delete map

delete map: on LVI colocalisation map : delete map

delete map: on ROI and bud map : delete map

copy map: copy map to 'tumour bud map'

copy map: copy map to 'vessel map'

remove all objects but marker one on tumour bud

on tumour bud map

delete image object level: delete 'NucleusLevel'

remove objects: loop: Marker 2 at MarkerLevel: remove objects into unclassified (merge by shape)

assign class: Markers 1 and 2 at MarkerLevel: Marker 1

merge region: Marker 1 at MarkerLevel: merge region

assign class: Marker 2 at MarkerLevel: unclassified

convert image objects: at MarkerLevel: convert image objects -> Connected 2D

merge region: unclassified at MarkerLevel: merge region

assign class: Marker 1 with Existence of super objects Tumour (1) = 1 at MarkerLevel: marker 1 in tumour

assign class: Marker 1 with Existence of super objects necrosis (1) = 1 at MarkerLevel: marker 1 in tumour

assign class: Marker 1 with Existence of super objects no tissue (1) = 1 at MarkerLevel: marker 1 in no tissue

copy image object level: at TissueLevel: copy creating 'CopyofTissueLevel' above

assign class: with Classified as no tissue = 0 at CopyofTissueLevel: _TempClass1

convert image objects: at CopyofTissueLevel: convert image objects -> Connected 2D

merge region: _TempClass1, Tumour at CopyofTissueLevel: merge region

distance map: at CopyofTissueLevel: distance to no tissue(distance map)

delete image object level: delete 'CopyofTissueLevel'

convert to sub-objects: at TissueLevel: convert to sub-objects

assign class: with Existence of sub objects Marker 1 (1) = 1 at TissueLevel: Marker 1

convert image objects: at TissueLevel: convert image objects -> Disconnected (fusion up)

convert image objects: at TissueLevel: convert image objects -> Connected 2D

update variable: Marker 1 at TissueLevel: distance to no tissue = Mean distance map

assign class: Marker 1 with distance to no tissue <= 50 at TissueLevel: edge effect

assign class: Marker 1 with Area <= 55 µm² at TissueLevel: necrotic debris

remove all objects but marker two on vessel map

on vessel map

delete image object level: delete 'NucleusLevel'

remove objects: loop: Marker 1 at MarkerLevel: remove objects into unclassified (merge by shape)

assign class: Markers 1 and 2 at MarkerLevel: Marker 2

pixel-based object resizing: loop: on vessel map Marker 2 at MarkerLevel: grow into unclassified where D240>=40

find enclosed by class: on vessel map at MarkerLevel: enclosed by Marker 2: Marker 2 +

merge region: on vessel map Marker 2 at MarkerLevel: merge region

assign class: Marker 1 at MarkerLevel: unclassified

convert image objects: at MarkerLevel: convert image objects -> Connected 2D

merge region: unclassified at MarkerLevel: merge region

assign class: Marker 2 with Existence of super objects Tumour (1) = 1 at MarkerLevel: marker 2 in tumour

assign class: Marker 2 with Existence of super objects necrosis (1) = 1 at MarkerLevel: marker 2 in tumour

assign class: Marker 2 with Existence of super objects no tissue (1) = 1 at MarkerLevel: marker 2 in no tissue

copy image object level: at TissueLevel: copy creating 'CopyofTissueLevel' above

assign class: with Classified as no tissue = 0 at CopyofTissueLevel: _TempClass2

convert image objects: at CopyofTissueLevel: convert image objects -> Connected 2D

merge region: _TempClass2, Tumour at CopyofTissueLevel: merge region

distance map: at CopyofTissueLevel: distance to no tissue(distance map)

delete image object level: delete 'CopyofTissueLevel'

convert to sub-objects: at TissueLevel: convert to sub-objects

assign class: with Existence of sub objects Marker 2 (1) = 1 at TissueLevel: Marker 2

convert image objects: at TissueLevel: convert image objects -> Disconnected (fusion up)

convert image objects: at TissueLevel: convert image objects -> Connected 2D

update variable: Marker 2 at TissueLevel: distance to no tissue = Mean distance map

assign class: Marker 2 with distance to no tissue <= 50 at TissueLevel: edge effect

assign class: on vessel map Marker 2 at TissueLevel: D240

evaluate tumour buds

fill holes in buds and evaluate nuclei in buds

pixel-based object resizing: on tumour bud map Marker 1 at TissueLevel: grow into Stroma

find enclosed by class: on tumour bud map at TissueLevel: enclosed by Marker 1: _TempClass1 +

grow region: on tumour bud map Marker 1 at TissueLevel: <- _TempClass1

merge region: on tumour bud map Marker 1 at TissueLevel: merge region

pixel-based object resizing: on tumour bud map Marker 1 at TissueLevel: shrink using Stroma

convert image objects: at TissueLevel: convert image objects -> Connected 2D

merge region: on tumour bud map Stroma at TissueLevel: merge region

copy image object level: on tumour bud map at TissueLevel: copy creating 'Nucleus level' below

synchronize map: on main at NucleusLevel: synchronize map 'tumour bud map'

assign class: on tumour bud map Nucleus with Area < 16 µm² at Nucleus level: Nucelar debris

assign class: on tumour bud map Nucleus with Standard deviation DAPI < 6 and Mean DAPI < 40 at Nucleus level: false nucleus

assign class: on tumour bud map Marker 1 with Mean CK <= 50 at TissueLevel: Non specific CK

assign class: on tumour bud map Marker 1 with Standard deviation CK <= 10 at TissueLevel: Non specific CK

assign class: on tumour bud map Marker 1 with Number of sub objects Nucleus (1) > 5 at TissueLevel: too big buds

assign class: on tumour bud map Marker 1 with Number of sub objects Nucelar debris (1) >= 1 and Existence of sub objects Nucleus (1) < 1 at TissueLevel: bud with debris nulceus

remove irrelevant marker 1 areas

assign class: on tumour bud map Marker 1 with Existence of sub objects Nucleus (1) < 1 at TissueLevel: irrelevant marker

remainder of marker 1 = tumour bud

on tumour bud map

assign class: Marker 1 at TissueLevel: tumour bud

create ROI and Tumour bud map and calculate distance to tumour

copy map: on tumour bud map : copy map to 'ROI and bud map'

on ROI and bud map

delete image object level: on ROI and bud map : delete 'Nucleus level'

copy image object level: at TissueLevel: copy creating 'vessel level' below

synchronize map: on vessel map at TissueLevel: synchronize map 'ROI and bud map'

delete layer: delete image layer 'distance map'

copy image object level: at TissueLevel: copy creating 'CopyofTissueLevel' above

assign class: with Classified as Tumour = 0 at CopyofTissueLevel: _TempClass1

convert image objects: at CopyofTissueLevel: convert image objects -> Connected 2D

merge region: _TempClass1 at CopyofTissueLevel: merge region

distance map: _TempClass1 at CopyofTissueLevel: distance to Tumour(distance map)

delete image object level: delete 'CopyofTissueLevel'

LVI and colocalisation

convert to sub-objects: at TissueLevel: convert to sub-objects

assign class: Stroma with Existence of sub objects D240 (1) = 1 at TissueLevel: D240

assign class: tumour bud with Existence of sub objects D240 (1) = 1 at TissueLevel: Markers 1 and 2

assign class: bud with debris nulceus, irrelevant marker, too big buds with Existence of sub objects D240 (1) = 1 at TissueLevel: non bud invasion

assign class: tumour bud with Existence of D240 (0) = 1 at TissueLevel: tumour bud border to marker 2

assign class: bud with debris nulceus, irrelevant marker, too big buds with Existence of D240 (0) = 1 at TissueLevel: tumour border to marker 2

assign class: D240 with Existence of Markers 1 and 2 (0) = 1 at TissueLevel: vessel border to bud invasion

convert image objects: at TissueLevel: convert image objects -> Disconnected (fusion up)

convert image objects: at TissueLevel: convert image objects -> Connected 2D

assign class: D240 with Existence of Tumour (0) = 1 at TissueLevel: vessel border to tumour mass

calculate bud distance to tumour

on ROI and bud map

update variable: on ROI and bud map bud with debris nulceus, D240, irrelevant marker, Markers 1 and 2, too big buds, tumour border to marker 2, tumour bud, tumour bud border to marker 2, vessel border to bud invasion at TissueLevel: distance to tumour = Mean distance map

update variable: D240 mean distance to tumour = 0

compute statistical value: on ROI and bud map D240 at TissueLevel: D240 mean distance to tumour = mean(distance to tumour)

update variable: M1&2 mean distance to tumour = 0

compute statistical value: on ROI and bud map Markers 1 and 2 at TissueLevel: M1&2 mean distance to tumour = mean(distance to tumour)

update variable: bud mean distance to tumour = 0

compute statistical value: on ROI and bud map tumour bud at TissueLevel: bud mean distance to tumour = mean(distance to tumour)

update variable: debris bud mean distance to tumour = 0

compute statistical value: on ROI and bud map bud with debris nulceus at TissueLevel: debris bud mean distance to tumour = mean(distance to tumour)

update variable: irrelevant mean distance to tumour = 0

compute statistical value: on ROI and bud map irrelevant marker at TissueLevel: irrelevant mean distance to tumour = mean(distance to tumour)

update variable: big bud mean distance to tumour = 0

compute statistical value: on ROI and bud map too big buds at TissueLevel: big bud mean distance to tumour = mean(distance to tumour)

update variable: tumour border to D240 mean distance to tumour = 0

compute statistical value: on ROI and bud map tumour border to marker 2 at TissueLevel: tumour border to D240 mean distance to tumour = mean(distance to tumour)

update variable: vessel border to bud invasion mean distance to tumour = 0

compute statistical value: on ROI and bud map vessel border to bud invasion at TissueLevel: vessel border to bud invasion mean distance to tumour = mean(distance to tumour)

update variable: bud border to D240 mean distance to tumour = 0

compute statistical value: on ROI and bud map tumour bud border to marker 2 at TissueLevel: bud border to D240 mean distance to tumour = mean(distance to tumour)

statistical export of invasive eptihelial bodies

export object statistics: on ROI and bud map bud with debris nulceus, D240, irrelevant marker, Markers 1 and 2, tumour bud, tumour bud border to marker 2, vessel border to bud invasion at TissueLevel: export object statistics

export object statistics: on ROI and bud map vessel border to tumour mass at MarkerLevel: export object statistics

export object statistics: on tumour bud map bud with debris nulceus, irrelevant marker, too big buds, tumour bud at TissueLevel: export object statistics

export object statistics: on tumour bud map Nucleus with Existence of super objects tumour bud (1) = 1 at Nucleus level: export object statistics

export object statistics: on tumour bud map Nucleus with Existence of super objects tumour bud (1) = 0 and Existence of super objects Stroma (1) = 1 at Nucleus level: export object statistics

export object statistics: on tumour bud map Nucleus with Existence of super objects Tumour (1) = 1 at Nucleus level: export object statistics

calculate colocalisation stat

update variable: sum of area bud and vessel coloc = 0

compute statistical value: on ROI and bud map Markers 1 and 2 at TissueLevel: sum of area bud and vessel coloc = sum(Area)

update variable: sum of area non-bud and vessel coloc = 0

compute statistical value: on ROI and bud map non bud invasion at TissueLevel: sum of area non-bud and vessel coloc = sum(Area)

update variable: sum of area of vessel border to bud invasion = 0

compute statistical value: on ROI and bud map vessel border to bud invasion at TissueLevel: sum of area of vessel border to bud invasion = sum(Area)

update variable: number of bordering bud and vessel = 0

compute statistical value: on ROI and bud map tumour bud border to marker 2 at TissueLevel: number of bordering bud and vessel = number

update variable: number of bordering tumour and vessel = 0

compute statistical value: on ROI and bud map tumour border to marker 2 at TissueLevel: number of bordering tumour and vessel = number

update variable: number of vessel border to bud invasion = 0

compute statistical value: on ROI and bud map vessel border to bud invasion at TissueLevel: number of vessel border to bud invasion = number

update variable: number of marker 1 and 2 = 0

compute statistical value: on ROI and bud map Markers 1 and 2 at TissueLevel: number of marker 1 and 2 = number

update variable: number of non bud invasion = 0

compute statistical value: on ROI and bud map non bud invasion at TissueLevel: number of non bud invasion = number

calculate tumour bud stat

update variable: number of buds = 0

compute statistical value: on tumour bud map tumour bud at TissueLevel: number of buds = number

update variable: no. of big buds = 0

compute statistical value: on tumour bud map too big buds at TissueLevel: no. of big buds = number

update variable: bud with <=2 nuc = 0

compute statistical value: on tumour bud map tumour bud with Number of sub objects Nucleus (1) <= 2 at TissueLevel: bud with <=2 nuc = number

update variable: bud with >=3 nuc = 0

compute statistical value: on tumour bud map tumour bud with Number of sub objects Nucleus (1) >= 3 at TissueLevel: bud with >=3 nuc = number

update variable: sum area of buds = 0

compute statistical value: on tumour bud map tumour bud at TissueLevel: sum area of buds = sum(Area)

update variable: on tumour bud map tumour bud at TissueLevel: Individual bud area = Area

calculate vessel stat

update variable: number of vessels = 0

compute statistical value: on vessel map D240 with Existence of Stroma (0) = 1 at TissueLevel: number of vessels = number

update variable: sum area of vessels = 0

compute statistical value: on vessel map D240 at TissueLevel: sum area of vessels = sum(Area)

update variable: on vessel map D240 at TissueLevel: Individual vessel area = Area

calculate mean nuclear stats in stroma

update variable: nuc in stroma_meanD240 = 0

compute statistical value: on tumour bud map Nucleus with Existence of super objects Stroma (1) = 1 at Nucleus level: nuc in stroma_meanD240 = mean(Mean D240)

update variable: nuc in stroma_meanCK = 0

compute statistical value: on tumour bud map Nucleus with Existence of super objects Stroma (1) = 1 at Nucleus level: nuc in stroma_meanCK = mean(Mean CK)

update variable: nuc in stroma_meanDAPI = 0

compute statistical value: on tumour bud map Nucleus with Existence of super objects Stroma (1) = 1 at Nucleus level: nuc in stroma_meanDAPI = mean(Mean DAPI)

update variable: nuc in stroma_mean_stdev_CK = 0

compute statistical value: on tumour bud map Nucleus with Existence of super objects Stroma (1) = 1 at Nucleus level: nuc in stroma_mean_stdev_CK = mean(Standard deviation CK)

update variable: nuc in stroma_mean_stdev_D240 = 0

compute statistical value: on tumour bud map Nucleus with Existence of super objects Stroma (1) = 1 at Nucleus level: nuc in stroma_mean_stdev_D240 = mean(Standard deviation D240)

update variable: nuc in stroma_mean_stdev_DAPI = 0

compute statistical value: on tumour bud map Nucleus with Existence of super objects Stroma (1) = 1 at Nucleus level: nuc in stroma_mean_stdev_DAPI = mean(Standard deviation DAPI)

update variable: nuc in stroma_mean_Ratio_CK = 0

compute statistical value: on tumour bud map Nucleus with Existence of super objects Stroma (1) = 1 at Nucleus level: nuc in stroma_mean_Ratio_CK = mean(Ratio CK)

update variable: nuc in stroma_mean_Ratio_D240 = 0

compute statistical value: on tumour bud map Nucleus with Existence of super objects Stroma (1) = 1 at Nucleus level: nuc in stroma_mean_Ratio_D240 = mean(Ratio D240)

update variable: nuc in stroma_mean_Ratio_DAPI = 0

compute statistical value: on tumour bud map Nucleus with Existence of super objects Stroma (1) = 1 at Nucleus level: nuc in stroma_mean_Ratio_DAPI = mean(Ratio DAPI)

update variable: nuc in stroma_mean_Area = 0

compute statistical value: on tumour bud map Nucleus with Existence of super objects Stroma (1) = 1 at Nucleus level: nuc in stroma_mean_Area = mean(Area)

update variable: nuc in stroma_mean_borderlength = 0

compute statistical value: on tumour bud map Nucleus with Existence of super objects Stroma (1) = 1 at Nucleus level: nuc in stroma_mean_borderlength = mean(Border length)

update variable: nuc in stroma_mean_length = 0

compute statistical value: on tumour bud map Nucleus with Existence of super objects Stroma (1) = 1 at Nucleus level: nuc in stroma_mean_length = mean(Length)

update variable: nuc in stroma_asymmetry = 0

compute statistical value: on tumour bud map Nucleus with Existence of super objects Stroma (1) = 1 at Nucleus level: nuc in stroma_asymmetry = mean(Asymmetry)

update variable: nuc in stroma_border index = 0

compute statistical value: on tumour bud map Nucleus with Existence of super objects Stroma (1) = 1 at Nucleus level: nuc in stroma_border index = mean(Border index)

update variable: nuc in stroma_mean_lengthwidth = 0

compute statistical value: on tumour bud map Nucleus with Existence of super objects Stroma (1) = 1 at Nucleus level: nuc in stroma_mean_lengthwidth = mean(Length\Width)

update variable: nuc in stroma_mean_perimeter = 0

compute statistical value: on tumour bud map Nucleus with Existence of super objects Stroma (1) = 1 at Nucleus level: nuc in stroma_mean_perimeter = mean(Perimeter)

update variable: nuc in stroma_mean_width = 0

compute statistical value: on tumour bud map Nucleus with Existence of super objects Stroma (1) = 1 at Nucleus level: nuc in stroma_mean_width = mean(Width)

update variable: nuc in stroma_mean_circularity = 0

compute statistical value: on tumour bud map Nucleus with Existence of super objects Stroma (1) = 1 at Nucleus level: nuc in stroma_mean_circularity = mean(Circularity)

update variable: nuc in stroma_mean_compactness = 0

compute statistical value: on tumour bud map Nucleus with Existence of super objects Stroma (1) = 1 at Nucleus level: nuc in stroma_mean_compactness = mean(Compactness)

update variable: nuc in stroma_mean_density = 0

compute statistical value: on tumour bud map Nucleus with Existence of super objects Stroma (1) = 1 at Nucleus level: nuc in stroma_mean_density = mean(Density)

update variable: nuc in stroma_mean_Ellipticity = 0

compute statistical value: on tumour bud map Nucleus with Existence of super objects Stroma (1) = 1 at Nucleus level: nuc in stroma_mean_Ellipticity = mean(Ellipticity)

update variable: nuc in stroma_mean_Roundness = 0

compute statistical value: on tumour bud map Nucleus with Existence of super objects Stroma (1) = 1 at Nucleus level: nuc in stroma_mean_Roundness = mean(Roundness)

update variable: nuc in stroma_mean_Shape index = 0

compute statistical value: on tumour bud map Nucleus with Existence of super objects Stroma (1) = 1 at Nucleus level: nuc in stroma_mean_Shape index = mean(Shape index)

calculate mean nuclear stats in bud

update variable: nuc in bud_meanD240 = 0

compute statistical value: on tumour bud map Nucleus with Existence of super objects tumour bud (1) = 1 at Nucleus level: nuc in bud_meanD240 = mean(Mean D240)

update variable: nuc in bud_meanCK = 0

compute statistical value: on tumour bud map Nucleus with Existence of super objects tumour bud (1) = 1 at Nucleus level: nuc in bud_meanCK = mean(Mean CK)

update variable: nuc in bud_meanDAPI = 0

compute statistical value: on tumour bud map Nucleus with Existence of super objects tumour bud (1) = 1 at Nucleus level: nuc in bud_meanDAPI = mean(Mean DAPI)

update variable: nuc in bud_mean_stdev_CK = 0

compute statistical value: on tumour bud map Nucleus with Existence of super objects tumour bud (1) = 1 at Nucleus level: nuc in bud_mean_stdev_CK = mean(Standard deviation CK)

update variable: nuc in bud_mean_stdev_D240 = 0

compute statistical value: on tumour bud map Nucleus with Existence of super objects tumour bud (1) = 1 at Nucleus level: nuc in bud_mean_stdev_D240 = mean(Standard deviation D240)

update variable: nuc in bud_mean_stdev_DAPI = 0

compute statistical value: on tumour bud map Nucleus with Existence of super objects tumour bud (1) = 1 at Nucleus level: nuc in bud_mean_stdev_DAPI = mean(Standard deviation DAPI)

update variable: nuc in bud_mean_Ratio_CK = 0

compute statistical value: on tumour bud map Nucleus with Existence of super objects tumour bud (1) = 1 at Nucleus level: nuc in bud_mean_Ratio_CK = mean(Ratio CK)

update variable: nuc in bud_mean_Ratio_D240 = 0

compute statistical value: on tumour bud map Nucleus with Existence of super objects tumour bud (1) = 1 at Nucleus level: nuc in bud_mean_Ratio_D240 = mean(Ratio D240)

update variable: nuc in bud_mean_Ratio_DAPI = 0

compute statistical value: on tumour bud map Nucleus with Existence of super objects tumour bud (1) = 1 at Nucleus level: nuc in bud_mean_Ratio_DAPI = mean(Ratio DAPI)

update variable: nuc in bud_mean_Area = 0

compute statistical value: on tumour bud map Nucleus with Existence of super objects tumour bud (1) = 1 at Nucleus level: nuc in bud_mean_Area = mean(Area)

update variable: nuc in bud_mean_borderlength = 0

compute statistical value: on tumour bud map Nucleus with Existence of super objects tumour bud (1) = 1 at Nucleus level: nuc in bud_mean_borderlength = mean(Border length)

update variable: nuc in bud_mean_length = 0

compute statistical value: on tumour bud map Nucleus with Existence of super objects tumour bud (1) = 1 at Nucleus level: nuc in bud_mean_length = mean(Length)

update variable: nuc in bud_asymmetry = 0

compute statistical value: on tumour bud map Nucleus with Existence of super objects tumour bud (1) = 1 at Nucleus level: nuc in bud_asymmetry = mean(Asymmetry)

update variable: nuc in bud_border index = 0

compute statistical value: on tumour bud map Nucleus with Existence of super objects tumour bud (1) = 1 at Nucleus level: nuc in bud_border index = mean(Border index)

update variable: nuc in bud_mean_lengthwidth = 0

compute statistical value: on tumour bud map Nucleus with Existence of super objects tumour bud (1) = 1 at Nucleus level: nuc in bud_mean_lengthwidth = mean(Length\Width)

update variable: nuc in bud_mean_perimeter = 0

compute statistical value: on tumour bud map Nucleus with Existence of super objects tumour bud (1) = 1 at Nucleus level: nuc in bud_mean_perimeter = mean(Perimeter)

update variable: nuc in bud_mean_width = 0

compute statistical value: on tumour bud map Nucleus with Existence of super objects tumour bud (1) = 1 at Nucleus level: nuc in bud_mean_width = mean(Width)

update variable: nuc in bud_mean_circularity = 0

compute statistical value: on tumour bud map Nucleus with Existence of super objects tumour bud (1) = 1 at Nucleus level: nuc in bud_mean_circularity = mean(Circularity)

update variable: nuc in bud_mean_compactness = 0

compute statistical value: on tumour bud map Nucleus with Existence of super objects tumour bud (1) = 1 at Nucleus level: nuc in bud_mean_compactness = mean(Compactness)

update variable: nuc in bud_mean_density = 0

compute statistical value: on tumour bud map Nucleus with Existence of super objects tumour bud (1) = 1 at Nucleus level: nuc in bud_mean_density = mean(Density)

update variable: nuc in bud_mean_Ellipticity = 0

compute statistical value: on tumour bud map Nucleus with Existence of super objects tumour bud (1) = 1 at Nucleus level: nuc in bud_mean_Ellipticity = mean(Ellipticity)

update variable: nuc in bud_mean_Roundness = 0

compute statistical value: on tumour bud map Nucleus with Existence of super objects tumour bud (1) = 1 at Nucleus level: nuc in bud_mean_Roundness = mean(Roundness)

update variable: nuc in bud_mean_Shape index = 0

compute statistical value: on tumour bud map Nucleus with Existence of super objects tumour bud (1) = 1 at Nucleus level: nuc in bud_mean_Shape index = mean(Shape index)

calculate mean nuclear stats in tumour

update variable: nuc in tumour_meanD240 = 0

compute statistical value: on tumour bud map Nucleus with Existence of super objects Tumour (1) = 1 at Nucleus level: nuc in tumour_meanD240 = mean(Mean D240)

update variable: nuc in tumour_meanCK = 0

compute statistical value: on tumour bud map Nucleus with Existence of super objects Tumour (1) = 1 at Nucleus level: nuc in tumour_meanCK = mean(Mean CK)

update variable: nuc in tumour_meanDAPI = 0

compute statistical value: on tumour bud map Nucleus with Existence of super objects Tumour (1) = 1 at Nucleus level: nuc in tumour_meanDAPI = mean(Mean DAPI)

update variable: nuc in tumour_mean_stdev_CK = 0

compute statistical value: on tumour bud map Nucleus with Existence of super objects Tumour (1) = 1 at Nucleus level: nuc in tumour_mean_stdev_CK = mean(Standard deviation CK)

update variable: nuc in tumour_mean_stdev_D240 = 0

compute statistical value: on tumour bud map Nucleus with Existence of super objects Tumour (1) = 1 at Nucleus level: nuc in tumour_mean_stdev_D240 = mean(Standard deviation D240)

update variable: nuc in tumour_mean_stdev_DAPI = 0

compute statistical value: on tumour bud map Nucleus with Existence of super objects Tumour (1) = 1 at Nucleus level: nuc in tumour_mean_stdev_DAPI = mean(Standard deviation DAPI)

update variable: nuc in tumour_mean_Ratio_CK = 0

compute statistical value: on tumour bud map Nucleus with Existence of super objects Tumour (1) = 1 at Nucleus level: nuc in tumour_mean_Ratio_CK = mean(Ratio CK)

update variable: nuc in tumour_mean_Ratio_D240 = 0

compute statistical value: on tumour bud map Nucleus with Existence of super objects Tumour (1) = 1 at Nucleus level: nuc in tumour_mean_Ratio_D240 = mean(Ratio D240)

update variable: nuc in tumour_mean_Ratio_DAPI = 0

compute statistical value: on tumour bud map Nucleus with Existence of super objects Tumour (1) = 1 at Nucleus level: nuc in tumour_mean_Ratio_DAPI = mean(Ratio DAPI)

update variable: nuc in tumour_mean_Area = 0

compute statistical value: on tumour bud map Nucleus with Existence of super objects Tumour (1) = 1 at Nucleus level: nuc in tumour_mean_Area = mean(Area)

update variable: nuc in tumour_mean_borderlength = 0

compute statistical value: on tumour bud map Nucleus with Existence of super objects Tumour (1) = 1 at Nucleus level: nuc in tumour_mean_borderlength = mean(Border length)

update variable: nuc in tumour_mean_length = 0

compute statistical value: on tumour bud map Nucleus with Existence of super objects Tumour (1) = 1 at Nucleus level: nuc in tumour_mean_length = mean(Length)

update variable: nuc in tumour_asymmetry = 0

compute statistical value: on tumour bud map Nucleus with Existence of super objects Tumour (1) = 1 at Nucleus level: nuc in tumour_asymmetry = mean(Asymmetry)

update variable: nuc in tumour_border index = 0

compute statistical value: on tumour bud map Nucleus with Existence of super objects Tumour (1) = 1 at Nucleus level: nuc in tumour_border index = mean(Border index)

update variable: nuc in tumour_mean_lengthwidth = 0

compute statistical value: on tumour bud map Nucleus with Existence of super objects Tumour (1) = 1 at Nucleus level: nuc in tumour_mean_lengthwidth = mean(Length\Width)

update variable: nuc in tumour_mean_perimeter = 0

compute statistical value: on tumour bud map Nucleus with Existence of super objects Tumour (1) = 1 at Nucleus level: nuc in tumour_mean_perimeter = mean(Perimeter)

update variable: nuc in tumour_mean_width = 0

compute statistical value: on tumour bud map Nucleus with Existence of super objects Tumour (1) = 1 at Nucleus level: nuc in tumour_mean_width = mean(Width)

update variable: nuc in tumour_mean_circularity = 0

compute statistical value: on tumour bud map Nucleus with Existence of super objects Tumour (1) = 1 at Nucleus level: nuc in tumour_mean_circularity = mean(Circularity)

update variable: nuc in tumour_mean_compactness = 0

compute statistical value: on tumour bud map Nucleus with Existence of super objects Tumour (1) = 1 at Nucleus level: nuc in tumour_mean_compactness = mean(Compactness)

update variable: nuc in tumour_mean_density = 0

compute statistical value: on tumour bud map Nucleus with Existence of super objects Tumour (1) = 1 at Nucleus level: nuc in tumour_mean_density = mean(Density)

update variable: nuc in tumour_mean_Ellipticity = 0

compute statistical value: on tumour bud map Nucleus with Existence of super objects Tumour (1) = 1 at Nucleus level: nuc in tumour_mean_Ellipticity = mean(Ellipticity)

update variable: nuc in tumour_mean_Roundness = 0

compute statistical value: on tumour bud map Nucleus with Existence of super objects Tumour (1) = 1 at Nucleus level: nuc in tumour_mean_Roundness = mean(Roundness)

update variable: nuc in tumour_mean_Shape index = 0

compute statistical value: on tumour bud map Nucleus with Existence of super objects Tumour (1) = 1 at Nucleus level: nuc in tumour_mean_Shape index = mean(Shape index)

export LVI and bud stats

export project statistics: on ROI and bud map : export project statistics

export project statistics: on tumour bud map : export project statistics

export object statistics: on ROI and bud map Markers 1 and 2, non bud invasion, tumour border to marker 2, tumour bud border to marker 2, vessel border to bud invasion at TissueLevel: export object statistics

export object statistics: on tumour bud map unclassified at Nucleus level: export object statistics

export object statistics: on tumour bud map Stroma at Nucleus level: export object statistics

calculate LVD and export vessel stats

export project statistics: on vessel map : export project statistics

export object statistics: on vessel map D240 at TissueLevel: export object statistics

Appendix 13. Phenotypic fingerprint parameters

Variable	Collation method	Gini Score
AREA_OF_LARGE_TUMOUR_BUDS_PXL	Sum	3.1
AREA_LVI	Sum	2.93
AREA_OCCULT_LVI	Sum	2.58
No_OF_VESSEL_BORDER_TO_OCCULT_LVI	Sum	2.56
No_OF_LARGE_TUMOUR_BUDS	Sum	2.43
No_OF_LVI	Sum	2.21
No_OF_OCCULT_LVI	Sum	2.14
No_OF_BORDERING_BUD_AND_VESSEL	Sum	2.05
No_OF_BORDERING_TUMOUR_GLAND_AND_VESSEL	Sum	1.95
BUD_WITH_≥3_NUC	Sum	1.94
TUMOUR_RELATIVE_AREA	Mean	1.92
BUD_WITH_≤2_NUC	Sum	1.92
AREA_OF_VESSEL_BORDER_TO_OCCULT_LVI_PXL	Sum	1.9
STROMA_RELATIVE_AREA	Mean	1.86
No_OF_BUDS	Sum	1.81
AREA_OF_BUDS	Sum	1.8
NUC_IN_STROMA_MEAN_DENSITY	Mean	1.78
No_OF_IRRELEVANT_MARKER	Sum	1.64
AREA_OF_VESSEL_BORDER_TO_LVI	Sum	1.64
NECROSIS_RELATIVE_AREA	Mean	1.62
TUMOUR_BUD_AREA_PERCENTAGE_OF_STROMA	Mean	1.57
AREA_OF_DEBRIS_MARKER_PXL	Sum	1.49
NUC_IN_BUD_MEAN_LENGTH	Mean	1.44
No_OF_VESSELS	Sum	1.43
NUC_IN_STROMA_MEAN_STDEV_CK	Mean	1.42
AREA_OF_VESSELS	Sum	1.39
AREA_OF_IRRELEVANT_MARKER_PXL	Sum	1.36
No_OF_DEBRIS_MARKER	Sum	1.32
NUC_IN_BUD_MEAN_AREA	Mean	1.26

D240_AREA_PERCENTAGE_OF_STROMA	Mean	1.25
AVERAGE_CK_INTENSITY_STROMA	Mean	1.23
NUC_IN_STROMA_ASYMMETRY	Mean	1.12
NUC_IN_STROMA_MEAN_LENGTHWIDTH	Mean	1.11
NUC_IN_TUMOUR_MEAN_STDEV_CK	Mean	1.08
NUC_IN_TUMOUR_MEAN_RATIO_D240	Mean	1.04
LAYER_MEAN_OF_CK_BIG_BUDS	Mean	1.04
NUC_IN_BUD_MEANDAPI	Mean	0.99
NUC_IN_BUD_MEAN_WIDTH	Mean	0.95
MEAN_PERIMETER_TUMOUR	Mean	0.91
NUC_IN_BUD_MEAN_BORDERLENGTH	Mean	0.91
REL_BORDER_TO_STROMA_TUMOUR	Mean	0.83
No_OF_VESSEL_BORDER_TO_TUMOUR_GLAND	Sum	0.8
BORDER_TO_STROMA_TUMOUR	Mean	0.8
BORDER_INDEX_TUMOUR	Mean	0.8
MEAN_CK_TUMOUR	Mean	0.74
NUC_IN_STROMA_MEAN_COMPACTNESS	Mean	0.74
AREA_OF_VESSEL_BORDER_TO_TUMOUR_MASS_PXL	Sum	0.72
NUC_IN_STROMA_MEAN_SHAPE_INDEX	Mean	0.71
WIDTH_TUMOUR	Mean	0.69
NUC_IN_STROMA_MEANCK	Mean	0.69
NUC_IN_BUD_MEAN_STDEV_DAPI	Mean	0.69
AREA_TUMOUR	Mean	0.67
NUC_IN_TUMOUR_MEAN_RATIO_DAPI	Mean	0.67
NUC_IN_STROMA_MEAN_CIRCULARITY	Mean	0.63
NUC_IN_STROMA_MEAN_RATIO_CK	Mean	0.63
NUC_IN_BUD_MEAN_STDEV_D240	Mean	0.62
NUC_IN_STROMA_MEAN_ROUNDNESS	Mean	0.58
NUC_IN_BUD_MEAN_DENSITY	Mean	0.56
NUC_IN_STROMA_MEAN_D240	Mean	0.54
AVERAGE_CK_INTENSITY_TUMOUR_AREA	Mean	0.54
NUC_IN_TUMOUR_MEAN_STDEV_DAPI	Mean	0.53
NUC_IN_TUMOUR_MEAN_RATIO_CK	Mean	0.52
NUC_IN_STROMA_MEAN_ELLIPTICITY	Mean	0.49
NUC_IN_BUD_MEANCK	Mean	0.48
ASYMMETRY__TUMOUR	Mean	0.48
NUC_IN_STROMA_MEAN_RATIO_D240	Mean	0.47
NUC_IN_STROMA_MEAN_STDEV_DAPI	Mean	0.44
NUC_IN_TUMOUR_MEAN_COMPACTNESS	Mean	0.43
NUC_IN_STROMA_MEAN_STDEV_D240	Mean	0.43
NUC_IN_TUMOUR_MEANCK	Mean	0.43
NUC_IN_BUD_MEAN_RATIO_D240	Mean	0.43
NUC_IN_BUD_MEAN_RATIO_CK	Mean	0.42
MEAN_DAPI_TUMOUR	Mean	0.4

NUC_IN_BUD_MEAND240	Mean	0.4
NUC_IN_STROMA_MEAN_RATIO_DAPI	Mean	0.4
LAYER_MEAN_OF_CK_TUMOUR_BUD	Mean	0.39
NUC_IN_TUMOUR_MEAN_LENGTHWIDTH	Mean	0.39
NUC_IN_STROMA_BORDER_INDEX	Mean	0.38
NUC_IN_TUMOUR_MEANDAPI	Mean	0.38
NUC_IN_BUD_MEAN_SHAPE_INDEX	Mean	0.37
NUC_IN_STROMA_MEANDAPI	Mean	0.37
ELLIPTIC_FIT__TUMOUR	Mean	0.37
LENGTH_WIDTH__TUMOUR	Mean	0.36
NUC_IN_TUMOUR_MEAN_STDEV_D240	Mean	0.35
NUC_IN_BUD_MEAN_RATIO_DAPI	Mean	0.35
NUC_IN_TUMOUR_ASYMMETRY	Mean	0.34
NUC_IN_STROMA_MEAN_WIDTH	Mean	0.33
LENGTH_TUMOUR	Mean	0.31
MEAN_D240_TUMOUR	Mean	0.31
NUC_IN_BUD_MEAN_COMPACTNESS	Mean	0.3
NUC_IN_BUD_MEAN_STDEV_CK	Mean	0.3
NUC_IN_TUMOUR_MEAN_CIRCULARITY	Mean	0.3
LAYER_MEAN_OF_CK_DEBRIS_MARKER_NUCLEUS	Mean	0.3
NUC_IN_TUMOUR_MEAN_SHAPE_INDEX	Mean	0.29
AVERAGE_DAPI_INTENSITY_TUMOUR_AREA	Mean	0.28
NUC_IN_BUD_MEAN_ELLIPTICITY	Mean	0.28
MEAN_COMPACTNESS_TUMOUR	Mean	0.27
MEAN_OF_D240_VESSEL	Mean	0.27
DAPI_INTENSITY_STROMA	Mean	0.26
ROUNDNESS_TUMOUR	Mean	0.26
NUC_IN_TUMOUR_MEAN_DENSITY	Mean	0.26
NUC_IN_TUMOUR_MEAN_D240	Mean	0.26
NUC_IN_BUD_MEAN_CIRCULARITY	Mean	0.25
NUC_IN_BUD_MEAN_LENGTHWIDTH	Mean	0.25
NUC_IN_TUMOUR_MEAN_LENGTH	Mean	0.25
MEAN_ELLIPTICITY_TUMOUR	Mean	0.25
AREA_OF_TUMOUR_INVADING_VESSEL	Sum	0.25
NUC_IN_BUD_ASYMMETRY	Mean	0.24
MEAN_RECTANGULAR_FIT_TUMOUR	Mean	0.24
NUC_IN_STROMA_MEAN_AREA	Mean	0.24
NUMBER_OF_TUMOUR_INVADING_VESSEL	Sum	0.24
NUC_IN_TUMOUR_BORDER_INDEX	Mean	0.24
NUC_IN_BUD_BORDER_INDEX	Mean	0.23
MEAN_OF_CK_IRRELEVANT_MARKER	Mean	0.23
NUC_IN_BUD_MEAN_ROUNDNESS	Mean	0.23
NUC_IN_STROMA_MEAN_LENGTH	Mean	0.23
NUC_IN_TUMOUR_MEAN_WIDTH	Mean	0.22
NUC_IN_TUMOUR_MEAN_ELLIPTICITY	Mean	0.22

CIRCULARITY_TUMOUR	Mean	0.22
NUC_IN_TUMOUR_MEAN_BORDERLENGTH	Mean	0.22
NUC_IN_TUMOUR_MEAN_ROUNDNESS	Mean	0.21
NUC_IN_STROMA_MEAN_BORDERLENGTH	Mean	0.19
NUC_IN_TUMOUR_MEAN_AREA	Mean	0.19

Parameters in bold and above the line are the 37 significant parameters reported from the Random Forest model

American Joint Committee on Cancer

Colon and Rectum Cancer Staging

7th EDITION

Appendix B

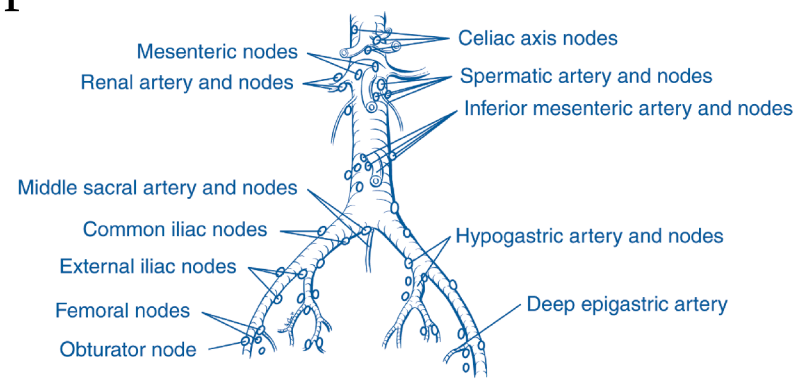

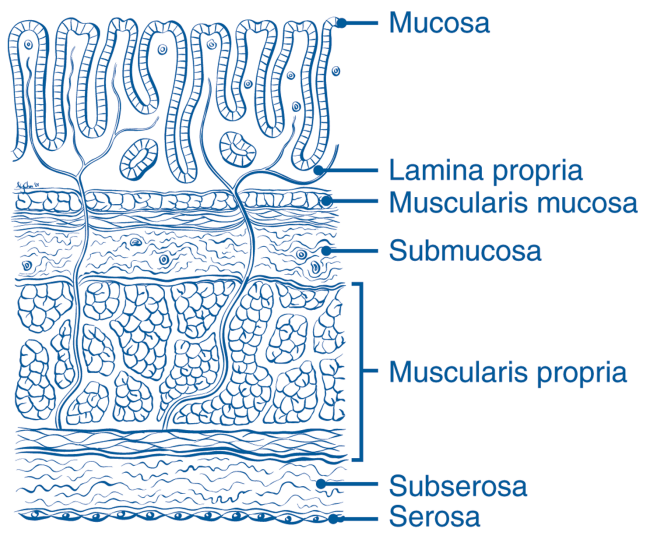

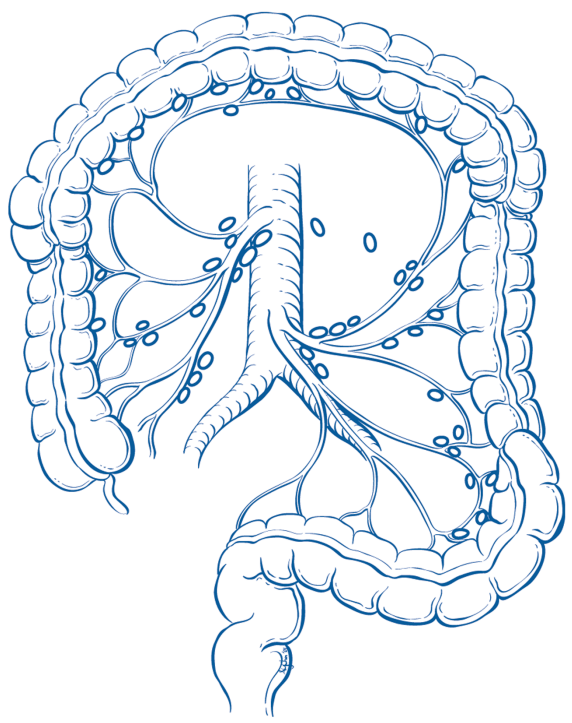

Definitions

Primary Tumor (T)

- **TX** Primary tumor cannot be assessed
- **T0** No evidence of primary tumor
- **Tis** Carcinoma in situ: intraepithelial or invasion of lamina propria[1]
- **T1** Tumor invades submucosa
- **T2** Tumor invades muscularis propria
- **T3** Tumor invades through the muscularis propria into pericolorectal tissues
- **T4a** Tumor penetrates to the surface of the visceral peritoneum[2]
- **T4b** Tumor directly invades or is adherent to other organs or structures[2,3]

Regional Lymph Nodes (N)[4]

- **NX** Regional lymph nodes cannot be assessed
- **N0** No regional lymph node metastasis
- **N1** Metastasis in 1–3 regional lymph nodes
- **N1a** Metastasis in one regional lymph node
- **N1b** Metastasis in 2–3 regional lymph nodes
- **N1c** Tumor deposit(s) in the subserosa, mesentery, or nonperitonealized pericolic or perirectal tissues without regional nodal metastasis
- **N2** Metastasis in 4 or more regional lymph nodes
- **N2a** Metastasis in 4–6 regional lymph nodes
- **N2b** Metastasis in 7 or more regional lymph nodes

Distant Metastasis (M)

- **M0** No distant metastasis
- **M1** Distant metastasis
- **M1a** Metastasis confined to one organ or site (for example, liver, lung, ovary, nonregional node)
- **M1b** Metastases in more than one organ/site or the peritoneum

ANATOMIC STAGE/PROGNOSTIC GROUPS

Stage	T	N	M	Dukes*	MAC*
0	Tis	N0	M0	–	–
I	T1	N0	M0	A	A
	T2	N0	M0	A	B1
IIA	T3	N0	M0	B	B2
IIB	T4a	N0	M0	B	B2
IIC	T4b	N0	M0	B	B3
IIIA	T1–T2	N1/N1c	M0	C	C1
	T1	N2a	M0	C	C1
IIIB	T3–T4a	N1/N1c	M0	C	C2
	T2–T3	N2a	M0	C	C1/C2
	T1–T2	N2b	M0	C	C1
IIIC	T4a	N2a	M0	C	C2
	T3–T4a	N2b	M0	C	C2
	T4b	N1–N2	M0	C	C3
IVA	Any T	Any N	M1a	–	–
IVB	Any T	Any N	M1b	–	–

NOTE: cTNM is the clinical classification, pTNM is the pathologic classification. The y prefix is used for those cancers that are classified after neoadjuvant pretreatment (for example, ypTNM). Patients who have a complete pathologic response are ypT0N0cM0 that may be similar to Stage Group 0 or I. The r prefix is to be used for those cancers that have recurred after a disease-free interval (rTNM).
* Dukes B is a composite of better (T3 N0 M0) and worse (T4 N0 M0) prognostic groups, as is Dukes C (any TN1 M0 and Any T N2 M0). MAC is the modified Astler-Coller classification.

Notes

[1] Tis includes cancer cells confined within the glandular basement membrane (intraepithelial) or mucosal lamina propria (intramucosal) with no extension through the muscularis mucosae into the submucosa.

[2] Direct invasion in T4 includes invasion of other organs or other segments of the colorectum as a result of direct extension through the serosa, as confirmed on microscopic examination (for example, invasion of the sigmoid colon by a carcinoma of the cecum) or, for cancers in a retroperitoneal or subperitoneal location, direct invasion of other organs or structures by virtue of extension beyond the muscularis propria (that is, a tumor on the posterior wall of the descending colon invading the left kidney or lateral abdominal wall; or a mid or distal rectal cancer with invasion of prostate, seminal vesicles, cervix, or vagina).

[3] Tumor that is adherent to other organs or structures, grossly, is classified cT4b. However, if no tumor is present in the adhesion, microscopically, the classification should be pT1-4a depending on the anatomical depth of wall invasion. The V and L classifications should be used to identify the presence or absence of vascular or lymphatic invasion, whereas the PN site-specific factor should be used for perineural invasion.

[4] A satellite peritumoral nodule in the pericolorectal adipose tissue of a primary carcinoma without histologic evidence of residual lymph node in the nodule may represent discontinuous spread, venous invasion with extravascular spread (V1/2), or a totally replaced lymph node (N1/2). Replaced nodes should be counted separately as positive nodes in the N category, whereas discontinuous spread or venous invasion should be classified and counted in the Site-Specific Factor category Tumor Deposits (TD).

Financial support for AJCC 7th Edition Staging Posters provided by the American Cancer Society